Technische Universität München
Department Physik
E19a – Chemische Physik fern vom Gleichgewicht

Synchronization Phenomena in Temporally Forced Electrochemical Oscillating Media

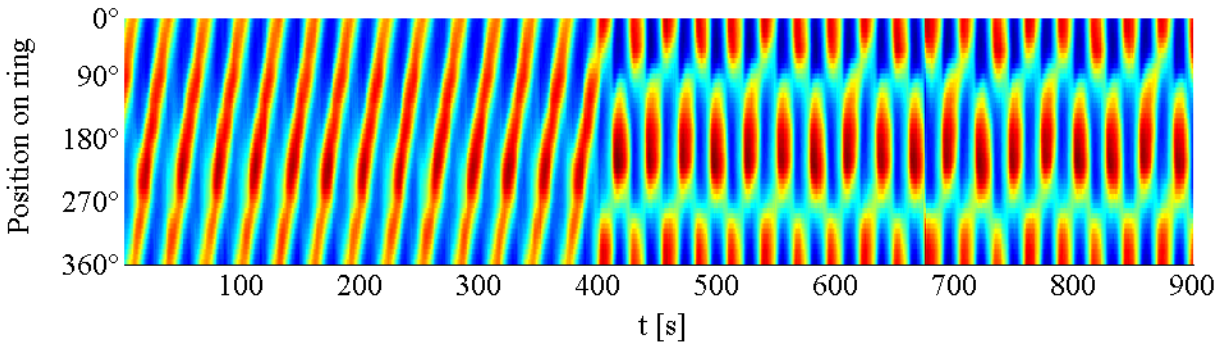

Doktorarbeit von Tahmineh Pourrostami
Januar 2013

Technische Universität München
Department Physik
E19a – Chemische Physik fern vom Gleichgewicht

Synchronization Phenomena in Temporally Forced Electrochemical Oscillating Media

Tahmineh Pourrostami

Vollständiger Abdruck der von der Fakultät für Physik der Technischen Universität München zur Erlangung des akademischen Grades eines

Doktors der Naturwissenschaften (Dr. rer. nat.)

genehmigten Dissertation.

Vorsitzende: Univ.-Prof. Dr. Nora Brambilla

Prüferinnen der Dissertation:

1. Univ.-Prof. Dr. Katharina Krischer

2. Univ.-Prof. Christine Papadakis, Ph.D.

Die Dissertation wurde am 31.01.2013 bei der Technischen Universität München eingereicht und durch die Fakultät für Physik am 06.03.2013 angenommen.

Contents

Abstract

Experiments on the time-periodic uniform forcing of an oscillating quasi-1D medium close to a nontrivial Hopf bifurcation were performed. The oscillatory system is the oxidation of H_2 on a Pt ring-electrode in the presence of poisons and negative global coupling. The results were compared to simulations based on the forced complex Ginzburg-Landau equation. Besides, stochastic oscillations occurring at different conditions for the unforced system are reported and their stability range is studied.

Chapter 1

Introduction

Synchronization phenomena are widely encountered in nature and various fields of science. Examples of oscillators which adjust their frequency and phase as a response of their interaction with other oscillators or an external periodic force range from a simple system such as a driven damped pendulum to swarms of fireflies where groups of flies light up in synchrony as a result of mutual interactions. In many cases, this external influence appears in the form of a time-periodic external forcing. Circadian rhythms in our body with frequencies close to 24 hours, which are entrained by the 24-h day-night periodicity provide well known examples of forced systems. Hence, understanding the influence of extrinsic perturbation on autonomous oscillators is of great theoretical and practical importance.

The history of studying synchronization dates back to the 17^{th} century when Christiaan Huygens described a synchronization process of two pendulum clocks on the wall [1]. Since then, the investigation of the interaction of two or more coupled oscillators or the influence of an external perturbation on self-sustained oscillators has been the focus of many experimental and theoretical works in various fields of science [2–4]. An oscillating system subject to an external time-periodic forcing exhibit predominantly two types of behavior. The driven dynamical system may be *entrained* by the external forcing. In this case the ratio of the response frequency to the driving frequency are (small) rational numbers. Or, the system may exhibit a quasiperiodic or so-called *unlocked* behavior. The parameter regions of the entrained and unlocked responses depend sensitively on two parameters: on the ratio of the natural frequency of the unperturbed oscillator and the forcing frequency and the forcing strength. In the parameter plane spanned by the frequency ratio-forcing strength, the entrained regions have a tongue-like form that starts with zero width at all rational numbers $\frac{m}{n}$ for zero forcing strength and opens up with increasing strength. These regions are often referred to as *Arnold tongues*. Most of the investigations of forced oscillating systems have been focused on the response of single

oscillators, which are well understood [5–9]. However, in comparison, there has been little analysis of synchronization phenomena in spatially extended oscillating media. An spatially extended system can be thought of as being composed of several individually acting single oscillators, which exchange information among each other via a coupling in space. Examples of investigations of frequency locking in spatially distributed systems include cardiac activity [10], autocatalytic surface reaction [11], liquid crystals [12] and chemical reactions [13].

As far as chemical oscillators are concerned, many studies in theory and experiment have been focused on reaction-diffusion systems. About two decades ago Swinney et al. published a report on spatiotemporal patterns that appear when subjecting the quasi-two dimensional light-sensitive Belousov-Zhabotinsky (BZ) reaction, to periodic optical forcing [13]. Their studies were motivated by a theoretical analysis showing that an array of coupled nonlinear oscillators under external forcing can exhibit spatial reorganization [14]. Later, Anna Lin et al. performed a detailed study of various resonance regions such as 2:1, 3:1 and 4:1 entrainment bands, resulting from the periodic forcing the of the light-sensitive BZ reaction [15–17]. Moreover, the resonant responses around the 2:1, 3:1 and 4:1 forcing parameters were also theoretically investigated [17–20]. The theoretical studies are based on the assumption that the unforced dynamical system is close to the onset of oscillations more precisely close to a Hopf bifurcation. In the vicinity of the Hopf bifurcation, the spatially extended oscillating system is governed by a universal equation for the complex amplitude of the oscillations, called the *complex Ginzburg-Landau equation* (CGLE). In this equation a diffusion term accounts for the diffusive spatial coupling among the different locations, or oscillators of the spatially extended system. Furthermore, for theoretical studies of frequency locking in spatially distributed systems, a term that accounts for the externally applied forcing is added to the CGLE.

The unforced oscillations in the works mentioned above are caused by a 'trivial' Hopf bifurcation where a spatially uniform mode starts oscillating around an unstable stationary state. The resulting uniform oscillations can be either stable or unstable. In the first case, the system is called 'Benjamin-Feir (BF)' stable. In the second case, a spatiotemporal incoherent BF-unstable state develops. When BF-stable systems are subject to a time-periodic forcing the oscillations establish a defined phase relation to the forcing signal and around the 1:1 resonance their response is similar to the behavior of single oscillators subject to external forcing. In other resonance regions, the entrained state might be patterned.

In the above mentioned examples the spatially extended system is coupled through diffusion. The influence of the spatial coupling present in the system has been the

subject of extensive studies [21–24]. These studies of pattern formation phenomena in spatially distributed systems have shown that dynamics of the system and thus, the pattern formation phenomena are strongly influenced by the nature and strength of the spatial coupling. In addition to the diffusion coupling, whose influence is local, electrochemical systems can be coupled non-locally and globally. A spatial coupling is termed local when a perturbation at a specific location on the electrode, is only *felt* by the neighboring sites. The non-local coupling, on the other hand, acts in such a way that also the locations further away from the perturbation are affected. However, this influence decreases with the distance from the location of perturbation. In other words, positions close to the perturbation are affected with a higher strength than those further away. The dominant coupling in the electrochemical systems is non-local. The non-local coupling is mediated by the electric potential in the electrolyte and is termed as migration coupling. In contrast, in the presence of a global coupling the perturbation affects all locations of the electrode equally, independent of their relative position to the location of the perturbation. Global coupling can be induced by the operation mode of an electrochemical measurement. Performing measurements under galvanostatic control induces a synchronizing or positive global coupling, whereas compensating part of the cell resistance during measurements under potentiostatic control induces a negative or desynchronizing global coupling to the system [25, 26]. A wide range of studies on electrochemical pattern formation in the presence of negative global coupling have shown that it may lead to the appearance of a rich variety of patterns such as stationary domains [26, 27], standing waves [28, 29] and pulses [28, 30, 31]. The negative global coupling causes the occurrence of wave instabilities which break both the temporal and spatial symmetry of the homogeneous state, in contrast to the (uniform) Hopf bifurcation which only breaks the temporal symmetry of this state. Since a wave instability is related to a pair of complex eigenvalues corresponding to eigenmodes, it might be referred to as 'non-trivial' Hopf bifurcation.

Depending on the reaction dynamics, a non-trivial Hopf bifurcation leads to standing or traveling wave solutions. When a traveling wave is subject to a spatially uniform periodic forcing, it is easy to see that there are qualitative difference to systems close to a trivial Hopf bifurcation. If the system is viewed as being composed of infinitely many local oscillators, the phase of the oscillators of the base state are 2π distributed. If one of these oscillators adjusts its phase such that the phase difference to the forcing signal is the 'preferred one', all the other locations has to accommodate less favorable phase differences. When viewing the traveling wave as being the result of the superposition of a spatial sine-mode and its $90\,^\circ$ shifted cosine-mode, the problem can be expressed in terms of phase relations between the two time dependent coefficients of the modes and the forcing signal. Again, only

one of the coefficients can adjust as expected for a driven oscillator while the other one is forced to take on a less favorable phase difference. Thus, it is not obvious at all how the traveling wave solution responds to a uniform external forcing. Experiments such as those performed by forcing the traveling waves that appear in liquid crystals [12] or the traveling waves produced by a long hot wire located underneath and parallel to the free surface of a liquid [32], have addressed this problem. Theoretical studies have also followed these experiments [33]. Yet, we are far from deeper understanding of forced traveling waves.

A major focus of this work is dedicated to the to investigation of the influence of a time-periodic external signal on the traveling pulses that appear in an electrochemical oscillating system in the presence of a negative global coupling. During the experiments of this work, we try to provide an answer to the question of how the interplay between an externally applied forcing and a desynchronizing global coupling can affect the existing patterns or result in the formation of new spatiotemporal patterns. The unforced oscillating system of this work is a prototype electrochemical oscillator in the presence of negative global coupling. The system is the electrooxidation of H_2 on a Pt ring-electrode in the presence of poisons, namely Cu^{2+}, as cation, and Cl^- or Br^- as anion. The potentiostatic current oscillations in this system result from the competition of the cation and anion for free sites on the Pt electrode, which is due to the overlap of their adsorption isotherms. This, in turn, causes a decrease in the H_2 oxidation on the electrode surface. In the absence of negative global coupling the system is coupled by migration. The homogeneous dynamics of this system in the presence of migration coupling has been studied in detail before [34]. When compensating part of the cell resistance in the measurements a negative global coupling is induced to the system. The reference state of the system was adjusted where phase pulses prevail that travel around the ring-electrode with a constant velocity. The phenomena of frequency locking in this system were then investigated by adding a small sinusoidal variation to the applied voltage. The responses of this oscillating system around the 1:1, 2:1 and 1:2 resonance regions were measured experimentally. Specific features of each entrainment band and the resonant patterns that appear were studied and characterized.

When replacing the Cl^- anions by Br^- anions, the dynamic behavior of the unforced system changed qualitatively. During the non-stationary measurements several different types of oscillations occurred. Furthermore, stationary measurements indicated that contrary to the oscillations observed in the presence of Cl^-, these oscillations possess no intrinsic frequency and are of a stochastic nature. These stochastic oscillations provide a second interesting reference state for the study of the response of the system to a global coupling as well as periodic forcing. Appealing

questions are here whether the global coupling suppresses the localized oscillation events and in which frequency range applying a periodic forcing results in a periodic response. Since this dynamic reference state has to my knowledge not been reported in the literature, these problems present a completely open area of research.

The structure of the thesis is as follows. In chapter 2 the basic concepts necessary for understanding the experimental results are presented. Chapter 3 gives a description of the experimental setup and the parameters used for performing the measurements. In chapter 4 the focus lies on the influence of external forcing on the dynamics of hydrogen oxidation on a Pt ring-electrode in the presence of a negative global coupling. In addition to depicting the experimentally measured 1:1, 2:1 and 1:2 entrainment bands and a detailed discussion of the resonance patterns in each parameter regime, a theoretical model is presented which reproduced many features of the experimental results. Chapter 5 describes the phenomena observed during the oxidation of H_2 on Pt ring-electrode in the presence of Cu^{2+} and Br^-. A summary of the main results is given in chapter 6.

Chapter 2

Background

This chapter provides a brief introduction into the concepts required to understand the experiments and results in the following chapters. The first section shortly describes the properties of electrochemical cells and the metal/liquid interface. In the second section some basic concepts of nonlinear phenomena in electrochemistry such as the occurrence of bistability and oscillations are summarized. The third section introduces the different mechanisms of spatial coupling in electrochemical systems. In the fourth section the electrochemical system which has been studied in this work is presented, and the last section gives a brief insight into the basic concepts of external forcing.

2.1 Electrochemistry

2.1.1 The electrochemical setup

Figure 2.1(a) depicts a general setup of an electrochemical experiment with three electrodes. The electrochemical reactions of interest occur at the surface of the working electrode (WE), and the interface between the working electrode and the electrolyte is the focus of our interest. In a three electrode cell arrangement the current flows between the working and the counter electrode (CE). Faradaic reactions at the WE and CE mediate a transition between an ionic current in the electrolyte and an electronic current through the electrical circuit. The potential of the WE is measured with respect to the reference electrode (RE) which provides a fixed potential. The potential difference between the WE and the RE is controlled by a potentiostat (which will be explained later) and is ideally not affected by the current flowing between the working and the counter electrode. The set voltage, U, is composed of the double layer potential, Φ_{dl} , and the ohmic drop in the electrolyte. Figure 2.1(b) shows an equivalent circuit of an electrochemical cell. The potential drop at the electrode/electrolyte interface is called the double layer potential or the

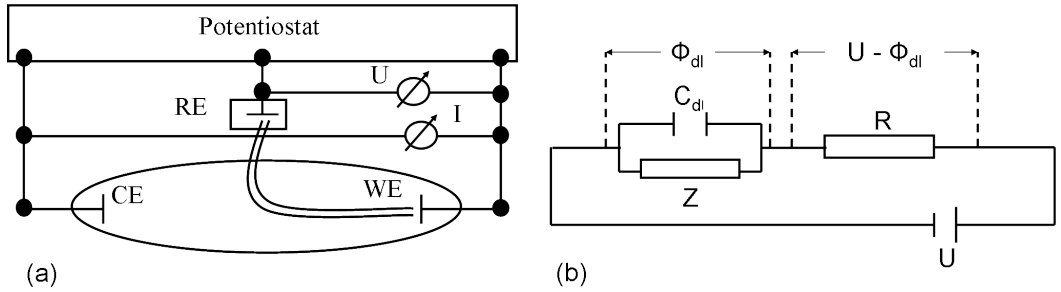

Figure 2.1: *(a) Schematic setup of a three electrode electrochemical cell. (b) Equivalent circuit of the electrochemical cell, Φ_{dl} is the potential drop at the WE, C_{dl} the double layer capacitance, Z a general faradaic impedance and R, the ohmic resistance of the electrolyte between WE and RE.*

interfacial potential. The double layer potential will be described in detail in the next section. From figure 2.1(b) it is obvious that across the electrode/electrolyte interface the current can take two pathways, a capacitive or a faradaic route. The electrolyte behaves like an ohmic resistor. In many situations only the resistance between the WE and the RE is important. This resistance is often called the uncompensated cell resistance, R_u, while the entire cell resistance is called R_Ω and the difference between R_Ω and R_u is the compensated resistance: $R_c = R_\Omega - R_u$. Throughout this thesis, whenever distinguishing between R_u and R_Ω is not essential for the discussion, R_u is referred to as R.

2.1.2 The double layer potential

Different electronic properties of a metal and a liquid give rise to the redistribution of ions and charges at the interface between the metal and the electrolyte. At the electrode side, the high conductivity of the metal prevents the formation of an extended charge region and depending on excess or deficiency of electrons, a thin charge layer of less than 0.1 Å forms. In the electrolyte, on the other hand, the rearrangement of ions changes the electrostatic properties at the interface in such a way that an excess of positive or negative ions accumulate close to the electrode surface, compensating for the charge on the electrode.

Helmholz was the first who introduced a model of the double layer. In this model Helmholtz assumes that the ions in the electrolyte can be considered as parallel layers.

Figure 2.2 displays the electrode/electrolyte interface with the ionic layers on the electrolyte side. The closest layer to the metal surface, called the inner Helmholtz

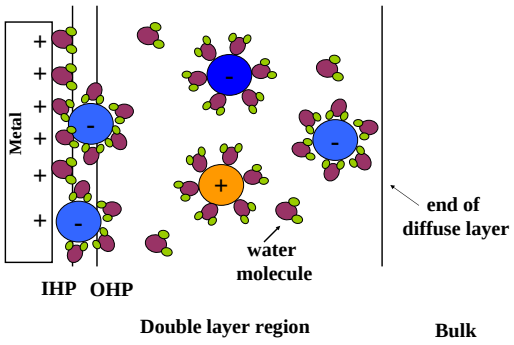

Figure 2.2: *Schematic picture of different layers at the metal/electrolyte interface. The orange and blue circles indicate cations and anions respectively.*

plane (IHP), is composed of solvent molecules and specifically adsorbed species. The IHP is defined by an imaginary plane going through the center of charge of the specifically adsorbed ions. The next nearest plane, the outer Helmholtz plane (OHP), is defined by the center of the closest solvated ions. The region between OHP and the bulk, where the electrolyte properties are still affected by the presence of the metal electrode, is called the diffuse layer. The thickness of this third layer depends on the charge carrier density, i.e., the concentration of the electrolyte. For highly concentrated electrolytes the diffuse layer almost vanishes.

The charge redistribution causes a potential drop across the compact and diffuse layers in the electrolyte which is called the double layer potential, Φ_{dl}. This variable plays an important role in the study of most electrochemical systems far from equilibrium [35–38]. Also in this work potential patterns at the electrode/electrolyte interface and their time evolution are studied.

2.2 Homogeneous dynamics

When discussing nonlinear phenomena in electrochemical systems it is necessary to include the interfacial electrode kinetics. The reason is that almost all pattern forming electrochemical systems show a region of *negative differential resistance* (NDR) in their current-voltage characteristic curve, and most instabilities encountered in these systems are associated with the NDR. The most frequent type of NDR is the N-NDR which possesses an the N-shaped NDR in its I/Φ_{dl} characteristics. Koper [38] has shown that the NDR can have three origins:
1. $dA/d\Phi_{dl} < 0$, A being the active electrode area. This could be due to potential-dependent adsorption of a species that increases with increasing overpotential and

blocks the surface and inhibits the reaction.
2. $dk/d\Phi_{dl} < 0$, k being the rate constant. When adsorption of a certain species that increases the activation energy is favored at higher overpotentials the electron transfer rate decreases with increasing polarization.
3. $dc/d\Phi_{dl} < 0$, c being the concentration of the active species. The depletion of the electro-active species involves more complex models of the double layer potential, as at first pointed out by Frumkin [39, 40].

In the electrochemical system discussed here, different adsorbing species compete and block the active surface area and give rise to the occurrence of an N-shaped NDR in the I/Φ_{dl} curve.

Figure 2.3(a) displays schematically the I-Φ_{dl} characteristic of an N-NDR system. In some electrochemical systems the NDR is only observed in a subsystem and the negative differential resistance is partially or completely hidden by a second potential dependent process in the stationary polarization curve. These systems are called HN-NDR (H for hidden) systems.

2.2.1 Bistability

The dynamic behavior of N-NDR systems that exhibit bistability can be determined by the time evolution of the double layer potential. In these systems the NDR branch (or the middle branch) of the N-shaped I/Φ_{dl} polarization curve gives rise to a self-enhancing process or a positive feedback loop, in which every change in Φ_{dl} is enhanced. In N-NDR systems bistability is encountered both under galvanostatic and potentiostatic control, provided R is larger than a critical value in the potentiostatic case. Here, we consider the situation under potentiostatic control. Considering the equivalent circuit in figure 2.1(b), the potential control keeps U i.e., the sum of Φ_{dl} and I*R constant. Eq. 2.1 shows the charge balance of this circuit that is obtained by applying Kirchhoff's law.

$$C_{dl}\frac{d\Phi_{dl}}{dt} + I_F = \frac{U - \Phi_{dl}}{R} \tag{2.1}$$

Here C_{dl} is the capacitance of the double layer, Φ_{dl} the double layer potential, U the externally applied voltage, R the sum of all external ohmic resistances and I_F the faradaic current. Any fluctuation of Φ_{dl} on the NDR branch to larger values leads to a decrease of I_F, on the one hand, and of I, the total current through the electrolyte, on the other hand. If the decrease of the faradaic current exceeds the positive capacitive current, Φ_{dl} is driven towards larger values and the fluctuation is enhanced, otherwise it decays. Therefore the stability of the branch depends on

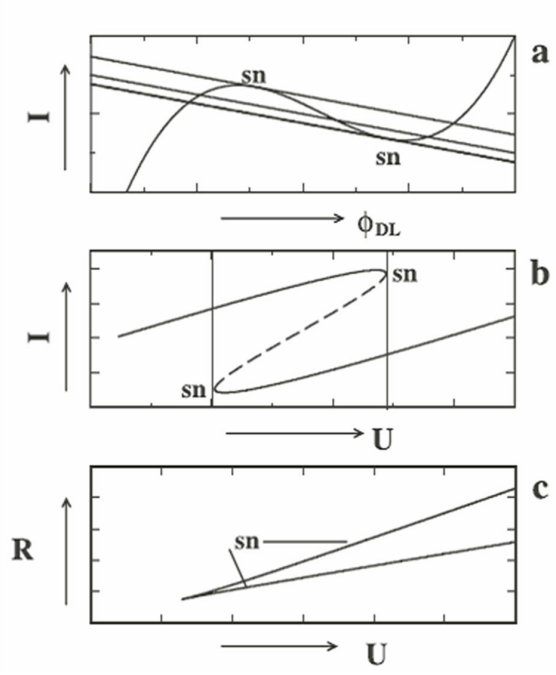

Figure 2.3: *(a) N-shaped I/Φ_{dl} curve with three load lines for three different U values. The bistable region is bounded by the two outer load lines. (b) The characteristic current-voltage curve corresponding to (a). The system goes through a saddle-node (sn) bifurcation to enter the bistable region. (c) The two parameter bifurcation diagram of an N-NDR system, in the external resistance vs. applied voltage plane. The sn bifurcations show the boarders of the bistable region. Taken from [41].*

the ohmic resistance value.

The steady state solutions ($d\Phi_{dl}/dt = 0$) of Eq. 2.1 can be obtained graphically by plotting the load lines and I/Φ_{dl} in the same graph, as it is shown in figure 2.3(a). The intersections of the load lines with the current-potential characteristic curve of the electrode/electrolyte interface are the fixed points of the system. From figure 2.3(a) it is obvious that the system has three steady states in a certain parameter range. The stability analysis of these fixed points shows that the system is stable unless:

$$Z < 0 \quad and \quad R > |Z| \tag{2.2}$$

where Z is the zero frequency faradaic impedance. From the first inequality of Eq. 2.2 it can be seen easily that instabilities can arise in a region with a negative differential resistance on the I/Φ_{dl} curve. The second one shows that when the sum of the external resistances is larger than the faradaic impedance the steady states become

unstable. Applying these stability criteria to the system shown in figure 2.3(a) we see that the system possesses two stable fixed points on the outer branches of the I/Φ_{dl} curve with a positive slope and one unstable fixed point on the middle branch with the negative slope. Depending on the direction of the perturbation, the system is driven from the unstable fixed point to either of the two stable steady states.

Figures 2.3(b) and (c) depict the current-voltage curve and the location of the bistable parameter region in the R-U plane, respectively. Two saddle-node (sn) bifurcations mark the boarder of the bistability region. Figure 2.3(c) shows the saddle-node bifurcations separating the monostable and bistable regions. At higher U and with increasing resistance the bistable region becomes broader.

2.2.2 Oscillations

As discussed above, bistable systems are characterized by a positive feedback loop in Φ_{dl}. For oscillations to occur, the system requires at least another degree of freedom. If a second slow process introduces a negative feedback loop to the system, with Φ_{dl} being a member of the loop, it will start oscillating. Often oscillatory systems can be described as so-called activator-inhibitor systems. The autocatalytic species, in general the activator and in our case Φ_{dl}, activates the production of the inhibitor species which, in turn, slows down or inhibits the growth of the activator and establishes the negative feedback loop.

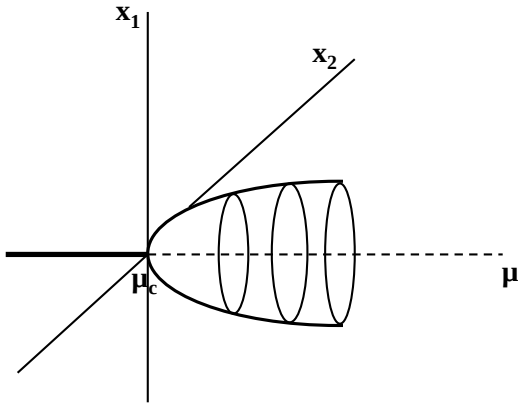

Figure 2.4: *Bifurcation diagram of a supercritical Hopf bifurcation.*

The occurrence of oscillations in a system points to the existence of a *limit cycle* in phase space. A limit cycle is an isolated closed loop in phase space which is stable if the neighboring phase space points are attracted to it and unstable if they are repelled from it. The most common mechanism leading to the emergence of a limit cycle is called a *Hopf bifurcation*. To understand the occurrence of a Hopf bifurcation in activator-inhibitor system, consider the following set of ordinary differential equations

$$\begin{aligned} \dot{u} &= f(u, v, \mu) \\ \dot{v} &= g(u, v, \mu) \end{aligned} \tag{2.3}$$

with u the activator variable and v the inhibitor variable.

Let us assume that $(u^*, v^*) = (0, 0)$ is the steady state of the system. Linearizion of Eq. 2.3 around the steady state gives

$$\begin{aligned} \frac{\partial u}{\partial t} &= f_u u + f_v v + h.o.t. \\ \frac{\partial v}{\partial t} &= g_u u + g_v v + h.o.t. \end{aligned} \tag{2.4}$$

with the Jacobian matrix

$$J = \begin{pmatrix} \frac{\partial f}{\partial u} & \frac{\partial f}{\partial v} \\ \frac{\partial g}{\partial u} & \frac{\partial g}{\partial v} \end{pmatrix} \Big|_{0,0} \equiv \begin{pmatrix} f_u & f_v \\ g_u & g_v \end{pmatrix} \tag{2.5}$$

The system undergoes a Hopf bifurcation at the parameter value $\mu = \mu_c$ if at μ_c the Jacobian has purely imaginary eigenvalues

$$\begin{aligned} &\lambda_{1,2} = \pm i\omega \quad and \\ &\frac{\partial \lambda_i}{\partial \mu}\Big|_{\mu=\mu_c} \neq 0 \end{aligned} \tag{2.6}$$

Figure 2.4 illustrates the bifurcation diagram of a *supercritical* Hopf bifurcation where due to the variation of the parameter μ a limit cycle is born at the bifurcation point, μ_c. The radius of the limit cycle and thus the amplitude of the oscillations, grows proportional to $\sqrt{\mu - \mu_c}$ in the vicinity of the bifurcation point.

Figure 2.5(a) shows a typical schematic picture of oscillations in an N-NDR system. The R/U bifurcation diagram of an N-NDR system, which is depicted in figure 2.5(b) shows that in an N-NDR system oscillations are observed in a certain parameter region, at comparatively low values of U and R while for increasing resistance

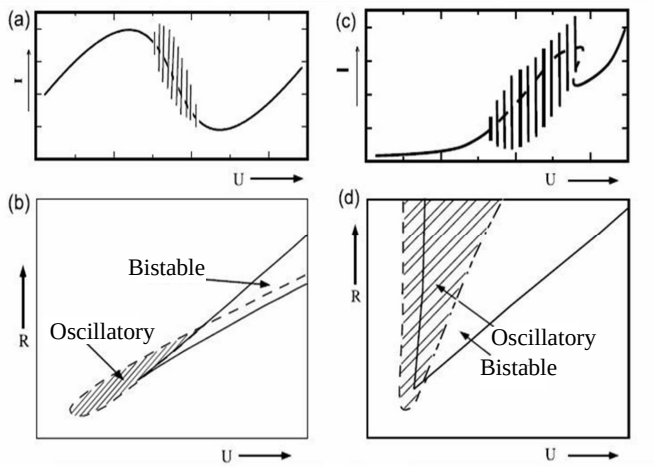

Figure 2.5: *(a) Current oscillations of an N-NDR system on a branch with negative slope. (b) Two parameter bifurcation diagram of (a) showing the oscillatory, bistable and monostable regions. Oscillations arise only in a certain parameter range and are absent under galvanostatic control. (c) A typical I/U curve of an HN-NDR system where the NDR is hidden. (d) Bifurcation diagram corresponding to (c) showing that above a certain threshold of R, oscillations exist. Taken from [41].*

and voltage the system becomes bistable. For HN-NDR systems, where the NDR is partially hidden (figure 2.5(c)), the bifurcation diagram looks qualitatively different. Figure 2.5(d) shows that for such systems, in a suitable potential window, the oscillatory region is unbounded from above which implies that when the total resistance becomes large enough and the system enters the oscillatory regime, the oscillations continue as the resistance increases. Hence, HN-NDR systems can oscillate under galvanostatic control where the resistance is infinitely high. This characteristic of HN-NDR systems marks a significant difference to N-NDR systems which do not oscillate under galvanostatic conditions.

Close to the Hopf bifurcation point, the oscillatory dynamics of an individual oscillator can be mapped to the Stuart-Landau equation [42] shown in Eq. 2.7.

$$\dot{W} = W - (1 + ic_2)\,|W|^2\,W \tag{2.7}$$

where W is a complex order parameter and c_2 is a measure of the dependence of the oscillation frequency on the amplitude of the oscillation.

2.3 Spatial coupling in electrochemical systems

Spatially extended systems can be assumed to be composed of many individual oscillators which are coupled by some means. The collective behavior of these oscillators has been the subject of many different studies. For such distributed oscillatory systems it is important to know how individual oscillators 'communicate' among each other or how they are *coupled*.

The electric field in the solution induces the basic spatial coupling mechanism in electrochemical systems, the so-called migration coupling. However, in many cases, this is not the only way in which the oscillators are coupled. The external control, for instance, can introduce an additional coupling between different sites of the electrode. Due to the control of the experiment the dynamics of different locations on the electrode may depend on the average double layer potential which means that any local variation in the double layer potential is 'felt' *with the same strength* by all other locations along the electrode, independent of their distance to the position of the perturbation. This type of coupling is called global coupling. Diffusion is another coupling mechanism in electrochemical systems which acts locally and will be explained in the last section. In this section migration coupling and positive and negative global coupling will be briefly introduced.

2.3.1 Migration coupling

When the system is coupled through the electric field of the electrolyte, reaction-migration equations describe the local evolution of the double layer potential where the dynamic equation for $\Phi_{dl}(x,t)$ can be written as the local charge balance at the WE:

$$C_{sp}\frac{\partial \Phi_{dl}}{\partial t} = -i_F - \sigma \frac{\partial \Phi_e}{\partial z}\bigg|_{z=-w} \tag{2.8}$$

In Eq. 2.8 C_{sp} stands for the specific double layer capacitance (capacitance per unit area), i_F is the faradaic current density, σ the specific conductivity of the electrolyte, z the spatial coordinate perpendicular to the working electrode and Φ_e represents the electrical potential within the electrolyte. The last term on the right hand side represents the migration current flowing into the double layer at the position -w, which is at the WE. In the bulk solution it can be assumed that the concentration and the conductivity are uniform and therefore the distribution of electric potential is described by Laplace's equation. The boundary conditions required for Laplace's equation bring about that the geometry of the system plays an important role for

pattern formation in electrochemical systems [43].

Migration coupling is non-local which means that a local change affects different locations at the electrode with different strength, depending on their distance from the location of the perturbation, whereas in local or diffusive coupling only the neighboring positions are affected by the changes. The non-locality can be understood intuitively for migration coupling: due to the tendency of the electrolyte to stay electroneutral any local variation in the interfacial potential influences the potential distribution, and thus the electric field, in the whole electrolyte which, in turn, affects different locations on the electrode. The coupling range decreases with decreasing WE/CE distance [43] which is another evidence of the effect of the cell geometry. For a laterally homogeneous potential distribution between the WE and the CE, the last term in Eq. 2.8 can be reformulated:

$$-\sigma \frac{\partial \Phi_e}{\partial z}\bigg|_{z=-w} = \frac{\sigma}{w}(\Phi_e|_{z=0} - \Phi_e|_{z=-w}) = \frac{\sigma}{w}(U - \Phi_{dl}) \tag{2.9}$$

where $\Phi_e|_{z=0} = 0$.

with Eq. 2.9, Eq. 2.8 can be written as

$$C_{sp}\frac{\partial \Phi_{dl}}{\partial t} = f(u, \Phi_{dl}) - \sigma(\frac{\partial \Phi_e}{\partial z}\bigg|_{z=-w} + \frac{U - \Phi_{dl}}{w}) \tag{2.10}$$

In Eqs. 2.9 and 2.10, z = 0 is at the position of the CE (and the RE accordingly, since it is assumed to be in the same height as the CE). The function $f(u, \Phi_{dl})$ accounts for the homogeneous dynamics.

Christoph et al. [44,45] have described the migration coupling by introducing a coupling function H that only depends on the geometry of the cell. With the help of a Green function formalism they have expressed the potential distribution in the electrolyte in terms of the boundary conditions of the electrode. The spatial coupling is expressed in terms of the integral of the coupling function over the electrode area. For a homogeneous ring-electrode the spatial coupling term vanishes whereas for an inhomogeneous situation the coupling function, H(x-x′), expresses the effect that any position x′ has on the dynamics of the system at location x. For a ring-electrode with negligible width of the ring, the spatial coupling function, H(x-x′), is visualized in figure 2.6.

In figure 2.6 the non-local nature of the coupling is evident. Since every point along the electrode contributes to the temporal evolution of every other point, the coupling function is positive everywhere; in other words, migration coupling is synchronizing and evens out any potential profile tangential to the WE. In case of a local coupling

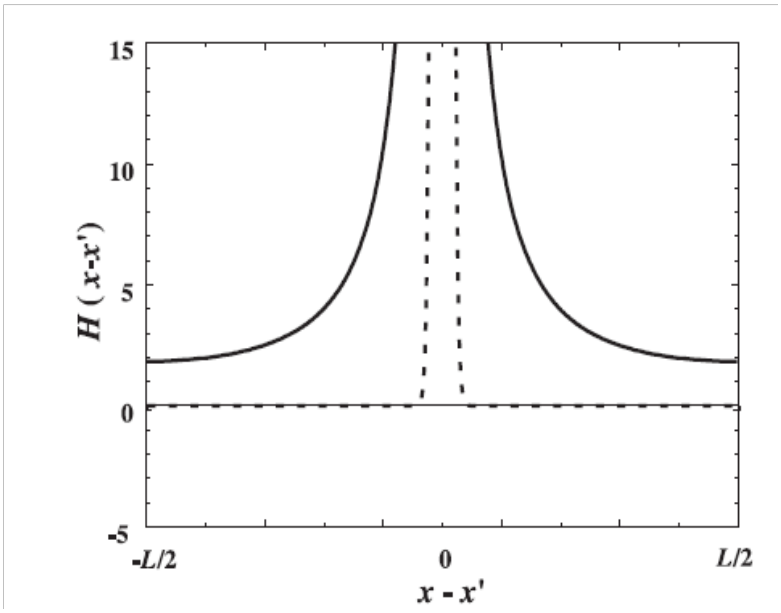

Figure 2.6: *The coupling functions H(x-x′) of a one-dimensional ring-electrode with circumference L for migration coupling (solid line) and local, diffusive coupling (dotted line). Taken from [31].*

(the dashed line in figure 2.6) the coupling function is zero except for locations in the immediate neighborhood of the point x.

2.3.2 Global coupling

Migration coupling as explained above is a non-local spatial coupling, which is present in all electrochemical systems. Depending on the relative arrangement of WE, CE and RE, as well as the experimental operation mode, different positions on the electrode can be additionally coupled by a positive or a negative *global coupling*. Through a global coupling the dynamics of every location on the electrode is affected by any local perturbation of Φ_{dl}, independent of its distance to the perturbation. Both potentiostatic and galvanostatic modes can give rise to a global coupling. The global coupling caused by a galvanostatic control is a positive global coupling while compensating part of the cell resistance under potentiostatic control induces a negative global coupling. Since all the experiments of this work are performed under potentiostatic control, the positive global coupling is not further discussed here.[1].

To understand how the potentiostatic control can induce a negative global coupling, first one should recall that the boundary conditions and therefore the potential dis-

[1]For details of the global coupling under galvanostatic control see ref [25, 46]

tribution at the electrode determine the potential within the electrolyte. Here we assume that at some position on the electrode Φ_{dl} has changed. This alters the electric potential distribution in the entire electrolyte to keep the electrolyte electroneutral. The changes of the electric potential in the electrolyte are the larger the closer a location is to the WE. If the RE is close to the WE, the electric potential in the electrolyte at the position of the RE changes noticeably due to a local fluctuation of Φ_{dl}. To compensate for the change in the potential difference between the WE and the RE and to keep it at the set value, the potentiostat changes the potential at the WE until the set value is reached again. This, in turn, affects the interfacial potential everywhere along the electrode/electrolyte interface. In this manner, a local perturbation of the double layer potential has changed the interfacial potential at any location of the electrolyte, independent of its distance to the potential fluctuation. However, it should be noted that this requirement can be only fulfilled with a symmetric cell geometry where the WE is a thin ring-electrode and the RE is placed on the axis of the ring. This condition is in agreement with the experimental setup of this work. In case of asymmetric setups and specially 2-dimensional electrodes such as disc electrodes, the distance of different locations on the WE to the RE are not equal, in addition to the migration coupling, the system is affected by an 'asymmetry effect' [47].

Considering the global coupling in the case of a ring WE, the evolution equation of the double layer potential can be written as follows [48, 49]:

$$C_{sp}\frac{\partial \Phi_{dl}}{\partial t} = -i_F + \frac{U-\Phi_{dl}}{AR_\Omega(1+\gamma)} - \sigma(\frac{\partial \Phi_e}{\partial z} - \Phi_e)\Big|_{z=-w} + \frac{1}{AR_\Omega}\frac{\gamma}{1+\gamma}(<\Phi_{dl}> - \Phi_{dl}) \tag{2.11}$$

with

$\gamma = -R_c/R_\Omega$

Here the cornered brackets indicate the spatial average and the remaining symbols have been defined previously.

In Eq. 2.11 the first two terms on the rhs account for the homogeneous dynamics, the third one describes the migration coupling and the last term expresses the global coupling introduced to the system by compensating part of the cell resistance. The coefficient of the last term determines the coupling strength.

From this equation, we can observe that when compensating part of the cell resistance (i.e., $R_c \neq 0$) a global coupling with a negative sign is introduced into the

system. For a ring shaped WE where the RE (or the tip of the Luggin-Haber capillary) is placed on the axis of the WE, decreasing the distance between working and reference electrodes is one method of compensating the cell resistance. Using an external negative impedance device, which compensates part of the resistance, can also introduce a negative global coupling (NGC) to the system. Global coupling has a decisive influence on the stability of uniform states but positive and negative GCs affect the dynamics of the system differently. The coupling induced by partial compensation of the cell resistance under potentiostatic control, for instance, gives rise to a NGC which is desynchronizing. The desynchronizing effect of the NGC can be intuitively understood from Eq. 2.11. For negative coefficients of the global coupling term, the coupling enhances the difference between $<\Phi_{dl}>$ and Φ_{dl} and hence a perturbation in Φ_{dl}.

An instructive way to understand the influence of the global coupling on the dynamic behavior is to investigate its effect on the stability of the linearized homogeneous steady state of the system. Consider an activator-inhibitor system with global coupling of the form

$$\begin{aligned} \frac{\partial \Phi_{dl}}{\partial t} &= f(\Phi_{dl}, \theta) + \sigma(\frac{\partial \Phi_e}{\partial z} - \Phi_e)\Big|_{z=-w} + \alpha(<\Phi_{dl}> - \Phi_{dl}) \\ \frac{\partial \theta}{\partial t} &= g(\Phi_{dl}, \theta) + \frac{\partial^2 \theta}{\partial x^2} \end{aligned} \tag{2.12}$$

where Φ_{dl} is the double layer potential and θ a chemical variable. Here α stands for the strength of the global coupling which is equal to the coefficient of the last term in Eq. 2.11 and is negative for a negative global coupling.

The Jacobi matrix of this system is shown in Eq. 2.13.

$$J = \begin{pmatrix} f_{\Phi_{dl}} + \alpha & f_\theta \\ g_{\Phi_{dl}} & g_\theta \end{pmatrix} \tag{2.13}$$

In Eq. 2.13 $f_{\Phi_{dl}}$ ($g_{\Phi_{dl}}$) and f_θ (g_θ) denote the partial derivatives of f(g) with respect to Φ_{dl} and θ, respectively. For $\alpha = 0$ the matrix corresponds to the Jacobi matrix of the homogeneous steady state with respect to homogeneous perturbations, in the absence of the global coupling. For our periodic boundary condirions, the eigen functions $\hat{\theta}$ of the spatial eigenvalue problem

$$\frac{\partial^2 \hat{\theta}}{\partial x^2} = -n^2 \hat{\theta} \tag{2.14}$$

are Fourier functions

$\theta(x,t) = a_n cos(nx) + b_n sin(nx), \quad n = 0, 1, 2, ...$

where n takes the role of the wave number.

The spatial eigenvalue problem regarding the spatial operator in the time evolution of Φ_{dl} (for $\alpha = 0$) is defined by

$$\left.\frac{\partial \Phi_e}{\partial z}\right|_{z=-w} = m\ \Phi_e|_{z=-w} \tag{2.15}$$

The time-dependent solution of this spatial eigenvalue problem is

$\Phi_e(x,z,t) = (c_n(t)cos(nx) + d_n(t)sin(nx))sinh(nz) + c_0(t)z, \quad n = 1, 2, ...$

The sign of the eigenvalues of the Jacobi matrix, J, determines the stability of the homogeneous steady state. Eq. 2.16 reveals how the eigenvalues of the J are determined by the trace (Tr) and determinant (Det) of it.

$$\lambda_{1,2} = \frac{Tr_J}{2} \pm \sqrt{\frac{(Tr_J)^2}{4} - Det_J} \tag{2.16}$$

The steady state is stable if the real part of the eigenvalues are negative, which will be realized if $Tr_J < 0$ and $Det_J > 0$.

For $\alpha = 0$ the real part of the eigenvalues $Re(\lambda(n))$ are negative for any n and the perturbations decay exponentially in time. In the presence of a global coupling the $Re(\lambda(n))$ is shifted by the value of α. Eq. 2.17 shows how Tr_J and Det_J of the globally coupled system are related to that of the homogeneous steady state in the absence of the global coupling:

$$\begin{aligned} Tr_J(\alpha) &= Tr_J(0) + \alpha \\ Det_J(\alpha) &= Det_J(0) + g_\theta \alpha \end{aligned} \tag{2.17}$$

In an (H)N-NDR system where the double layer potential takes the role of the activator, g_θ is negative. Hence, a positive global coupling with $\alpha > 0$ can stabilize the homogeneous stationary state and has a synchronizing effect. However, the presence of negative global coupling where $\alpha < 0$, acts in the opposite way.

When treating n as a continuous variable, the growth rate of the real part of $\lambda(n)$ versus n for the zeroth mode (n = 0) is identical to the case for $\alpha = 0$. However, for wave numbers larger than 0 ($n > 0$) the growth rate of the perturbation is shifted

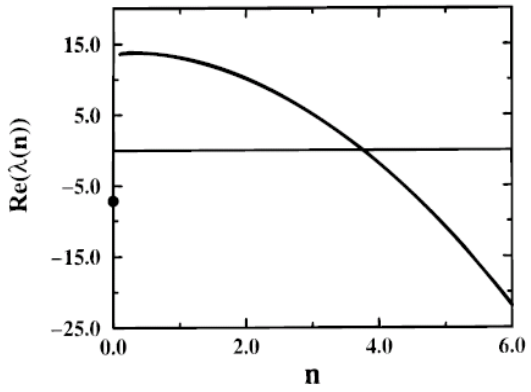

Figure 2.7: *Schematic dispersion relation showing the growth rate of the perturbations $Re(\lambda(n))$ vs. the wave number, n in the presence of a negative global coupling in the system. Taken from [50].*

by α due to the addition of the global coupling [50]. Hence, for globally coupled systems, the dispersion relation possesses a discontinuity at $n = 0$. Figure 2.7 presents the dispersion relation for a negatively globally coupled system.

Since any variations in parameters which does not affect $< \Phi_{dl} >$, and correspondingly the global coupling, will not affect the discontinuity of the dispersion relation at $n = 0$, whenever a change of the value of a parameter makes the homogeneous steady state unstable, the mode with wave number 1 will be the first to become unstable, if $\alpha < 0$. This means that, in the absence of the NGC, the 0-mode oscillations destabilize before the higher modes, whereas for a globally coupled system the Hopf bifurcation point for the 0-mode oscillations is delayed and hence, the modes with wave number $n = 1$ (or $n = -1$) will be the first to destabilize and, give rise to the appearance of spatially non-uniform oscillations for sufficiently large systems.

In this situation two instabilities can be distinguished. If the eigenvalue is real and the eigenvalues corresponding to $n = 1$ have different signs, the bifurcation drives the system to a stationary patterned state with two stationary domains. Examples of such patterns are observed during the electrochemical reduction of peroxidisulfate [26] or the oxidation of H_2 on a Pt electrode with experimental conditions other than those used in this work [25, 27]. The second situation is observed when $\mathrm{Im}(\lambda(n)) \neq 0$ and the variations in the parameters cause a wave bifurcation where at

the bifurcation point the real part of the complex conjugate eigenvalues crosses zero. This bifurcation leads to a state whose symmetry is broken in space and time. The resulting patterns are standing waves which consist of two domains which oscillate 180 ° out of phase or phase pulses which propagate on the electrode.

A standing wave can be understood as the superposition of two traveling waves or a spatially fixed spatial profile whose amplitude oscillates in time.

$$U_{standing}(x,t) = Ae^{i\omega t}e^{ikx} + Ae^{i\omega t}e^{-ikx} \tag{2.18}$$

where A is constant, k is equal to $\frac{2\pi}{\mathrm{L}}$ and L stands for the length of the system. The first term on the right hand side in Eq. 2.18 presents a traveling wave propagating in the right direction with $n = 1$ and the second term stands for a waves traveling in the left direction, with $n = -1$. Accordingly, Eq. 2.18 is equivalent to $U_{standing}(x,t) = a(t)sin(kx)$, assuming that we are sufficiently close to the bifurcation. These are two equivalent mathematical formulations and depending on the context, we will make use of both formalisms.

Correspondingly, there exist two equivalent formulations for traveling waves, which will be both employed below

$$\begin{aligned} U_{traveling}(x,t) &= Be^{i\omega t}e^{ikx} \\ U_{traveling}(x,t) &= Be^{i(\omega t - T/4)}sin(kx) + Be^{i\omega t}cos(kx) \end{aligned} \tag{2.19}$$

The second equation in 2.19 can also be written as

$$U_{traveling}(x,t) = b_1(t)sin(kx) + b_2(t)cos(kx) \tag{2.20}$$

where $b_1(t) = b_2(t + T/4)$ or $b_1(t) = b_2(t - T/4)$, with T the period of the traveling wave.

Fukushima et al. [51] have investigated pattern selection principles for standing and traveling waves that are induced by a global coupling. They have shown that, the prediction of the selected spatiotemporal pattern can be achieved with a weakly nonlinear bifurcation analysis, in which the second and third order terms are taken into account.

The traveling pulses described above have also been investigated experimentally. For electrochemical systems, traveling pulses were first observed by Otterstedt et al. during cobalt electrodissolution [31, 52] where they observed traveling domains of high activity on an otherwise passive surface. Similar phenomena were later observed for other systems, e.g. formic acid electrooxidation [28,53], H_2O_2 reduction on

platinum electrodes [54] and oxidation of H_2 on Pt in the presence of poisons [23,30].

In most of the experimental work of this thesis traveling pulses constitute our reference state. By choosing a suitable global coupling strength and in the presence of Cl^- ions, whose role in the electrochemistry of the system will be discussed in the next section, the system possesses stable traveling pulses. Experimental examples of phase pulses observed with the electrochemical system of this thesis will be presented in chapter 4.

2.4 The electrochemical system

The electrochemical system studied in this work is the hydrogen electrooxidation reaction (HOR) in the presence of strongly adsorbing cations and anions. This is a prototypical HN-NDR electrochemical oscillator whose dynamics is well understood [34]. The oscillation mechanisms of this system will be presented in this section.

The hydrogen oxidation reaction (HOR) on a platinum surface is a widely studied system [55–58]. Addition of electrosorbing metals such as Cu^{2+} and strongly adsorbing anions like Cl^- and Br^- changes the system to a HN-NDR oscillator which exhibits oscillations in a wide parameter range. The N-shaped NDR in the I/U characteristic curve of this system is caused by the presence of the halide ions which inhibit the oxidation of hydrogen by occupying active Pt sites. Adding Cu^{2+} ions to the solution hides the NDR branch partially and results in oscillations around the hidden N-shaped NDR branch. These oscillations occur under both potentiostatic and galvanostatic conditions, provided that under potentiostatic control the uncompensated resistance is larger than a critical value (see figure 2.5(d)). Throughout this work Cu^{2+}, Cl^- or Br^- are used as the electrosorbing cation and anion, respectively.

The I/Φ_{dl} curve of H_2 oxidation in a pure H_2-saturated sulfuric acid solution shows a steep increase in the current followed by a plateau (solid line in figure 2.8). Here we observe diffusion-controlled reaction rates at relatively low potentials which are caused by the high rate constant of hydrogen oxidation on Pt. This makes the oxidation current almost independent of the potential. Addition of Cl^- ions to the solution leads to the decrease of the current with increasing potential as a result of Cl^- adsorption on the Pt surface (dashed line in figure 2.8). Further addition of the Cu^{2+} ions to the electrolyte suppresses the reaction almost completely and decreases the oxidation current to zero in the potential region where copper deposits. Desorption of the Cu^{2+} is marked by the increase in the current (dotted line in fig-

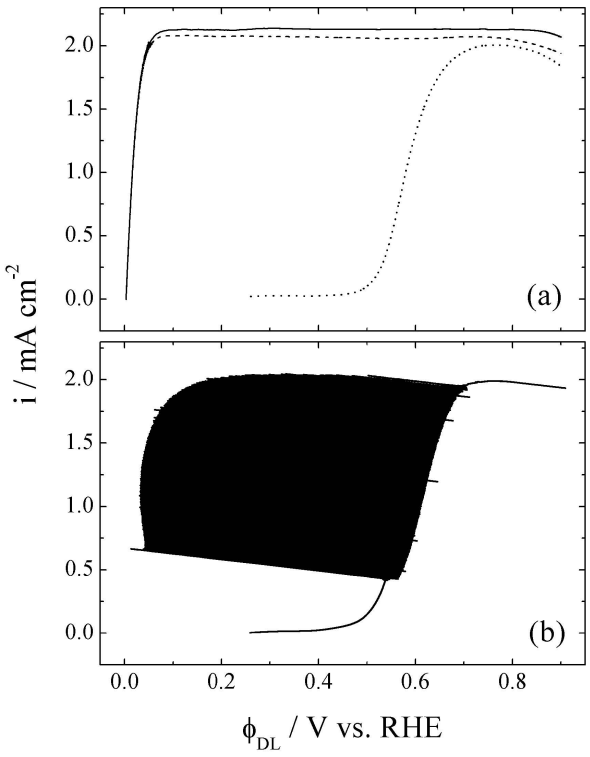

Figure 2.8: *(a) I-Φ_{dl} characteristics of a Pt electrode in H_2 saturated H_2SO_4 electrolyte (solid curve), in H_2 saturated H_2SO_4 electrolyte after addition of small amounts of Cl^- ions (dashed curve) and after addition of a small amount of Cl^- and Cu^{2+} ions (dotted curve), (b) the same as the dotted curve as in (a), but with a large series resistance. For experimental details see [24, 34]. Taken from [24].*

ure 2.8). The oxidation current then takes on the values of the Cu^{2+} free electrolyte.

Adsorption of both Cu^{2+} and Cl^- ions inhibits hydrogen oxidation on the surface. However, since ad- and desorption of these ions possess different potential dependences, they establish the positive and negative feedback loops in the system. Adsorption of metal ions occurs at low potentials, while above a critical potential they desorb from the surface. The specific adsorption of the anions, on the contrary, is favored with increasing potentials. It is also necessary that the Cl^- ad- and desorption process that gives rise to the negative impedance is faster than the Cu^{2+} deposition and dissolution which hides the negative impedance region. As discussed in section 2.2, in the presence of both feedback loops the system starts oscillating.

These feedback loops are shown in figure 2.9. In the positive feedback loop (the upper circle in figure 2.9), any change of the double layer potential to more positive values leads to its further increase. As the potential increases, the Cl^- ions adsorb

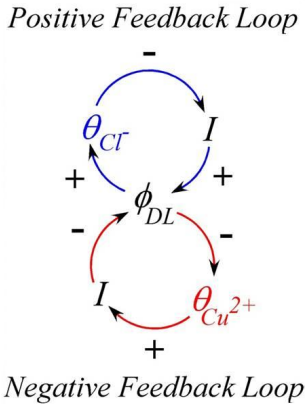

Figure 2.9: *Schematic picture of the positive (upper) and negative (lower) feedback loops of the HOR system in the presence of Cl^- and Cu^{2+} ions.*

on the Pt surface and block free Pt surface sites. The increase in chloride coverage, θ_{Cl}, with increasing potential initiates an autocatalytic process. Higher θ_{Cl} decreases the oxidation current and under potentiostatic control, where U = Φ_{dl} + IR, the potentiostat shifts Φ_{dl} to more positive values to keep the voltage constant. In the negative feedback loop, on the other hand, an initial increase in Φ_{dl} is suppressed. The decrease in the Cu^{2+} coverage at higher potentials increases the oxidation current which in turn, drives Φ_{dl} to lower values and inhibits its further increase. This general mechanism applies to measurements under galvanostatic control too.

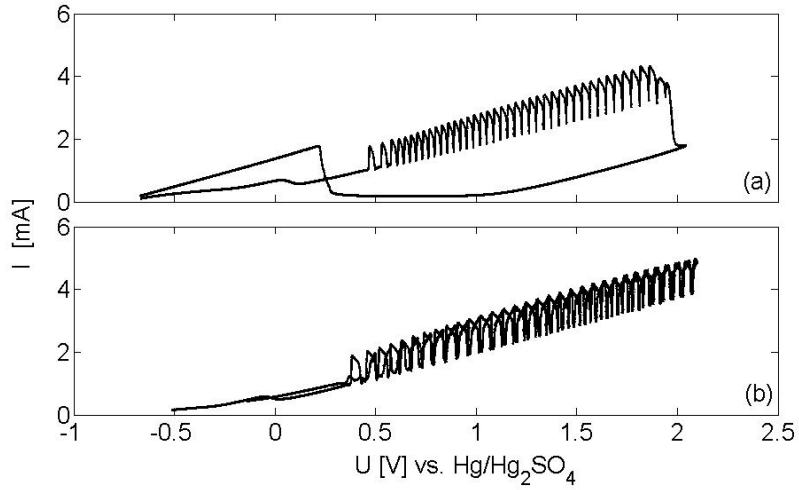

Figure 2.10: *(a) Cyclic voltammogram of HOR in H_2 saturated 0.5 mM H_2SO_4, 0.05 mM $CuSO_4$ and 0.06 mM HCl. $\gamma = 0$. Rotation rate = 20 Hz. (b) Anodic turning point in the oscillatory regime. Oscillations continue on the negative sweep.*

Figure 2.10 displays two cyclic voltammograms obtained during HOR in the presence of Cu^{2+} and Cl^{-} ions and a sufficiently large external resistance. In figure 2.10(a) it can be observed that the oscillatory region begins at about 0.5 V during the positive sweep. The oscillations continue until about 1.87 V where a bifurcation destroys the limit cycle and stops the oscillations. Further increase of the voltage gives rise to oxide formation that prevents the oxidation of hydrogen by blocking the surface. The residual current at these potentials is caused by oxygen evolution. In the negative sweep the current decreases and goes to zero at about 1 V and remains close to zero until 0.37 V where the oxide is reduced and dissolved. It is shown [24] that the formation and reduction of oxides roughens the Pt surface. Hence, for the experiments in this thesis, we have avoided entering that region and measured only within the oscillatory regime. Figure 2.10(b) shows an example of a cyclic voltammogram where the sweep direction was reversed before the occurrence of the bifurcation, the oscillations continue on the negative sweep.

2.5 External Forcing

The influence of a spatially uniform time-periodic external forcing on the dynamics of a single oscillating system and spatially extended oscillators will be discussed here.

Homogeneous systems

The governing equations in an oscillatory system with limit cycle behavior contain no explicit time dependence. Hence, there exists a continuous time translation symmetry. Introducing a periodic external forcing to the system, makes the time shifts only symmetric in multiples of the forcing frequency. In other words, inducing the external perturbation breaks the time translational symmetry of the system and leaves a discrete symmetry where $t \rightarrow \mathrm{t} + \dfrac{2\pi}{f_f}$, where f_f denotes the frequency of the externally applied signal. The difference between the natural frequency of the oscillating system, f_0, and the forcing frequency, f_f, f_0-f_f, is called the frequency detuning and is designated by ν. To determine the effect of the external forcing on the systems dynamics, it is convenient to study the phase difference between both signals, where the phase of the sinusoidal forcing signal is defined as $\Phi_f(t) = 2\pi f_f t + \phi_f$ and of a response with the dominant frequency f_r is $\Phi_r(t) = 2\pi f_r t + \phi_r$. ϕ_r and ϕ_f are the initial phase shifts. At small positive or negative detuning, the frequency of the forced oscillating system adjusts itself to the externally applied frequency and hence, the frequency of the driven oscillator or the response frequency, f_r, becomes equal to the forcing frequency or a rational multiple of it [8]:

$$\frac{f_f}{f_r} = \frac{m}{n} \tag{2.21}$$

where n and m are integers without a common divisor. At this state, the response of the system is periodic and *synchronous* and the system is *entrained* or *frequency locked*. The phases of the external perturbation and the oscillator are not equal but the phase difference $\Delta\Phi = \Phi_f - \Phi_r$, is constant.

The range of forcing control parameters (e.g. frequency and amplitude), where only periodic responses appear is referred to as a $m : n$ *resonance* region. In a 1:1 resonance regime, for example, the forcing frequency is close to the natural frequency of the oscillator and the response frequency , f_r adjusts itself to exactly the forcing frequency.

When the frequency detuning grows and exceeds a critical value, the forcing will not be strong enough to entrain the oscillator and the response becomes *quasiperiodic*; i.e. it is characterized by oscillations with more than one frequency. The power spectrum of the driven oscillator in this parameter regime shows that in addition to f_f or one of its multiples, the so-called beat frequency is also present. The beat frequency is given by the difference between the response frequency of the system and the frequency of the externally applied signal.

In the presence of an external perturbation with a low amplitude, an attractive two-dimensional torus exists in the phase space for this system where the trajectory continually winds around the torus in the short direction (executing $f_0/2\pi$ rotations per unit time) and long direction (making $f_f/2\pi$ rotations per unit time). The average number of times that the orbit goes around the torus in the short direction during one forcing period is defined as the *winding number*. For a rational winding number, $w = \frac{n}{m}$ where m and n are integers without a common divisor, the trajectory approaches a periodic solution for n times winding during m periods whereas, for the irrational winding numbers the trajectories wind around endlessly, fill the torus but never close in exactly onto itself. In this case each trajectory comes arbitrarily close to any point on the torus and is dense on it and gives rise to quasiperiodic dynamics.

When the response of the system to an external forcing is spanned in the plane of the forcing parameters, which are commonly frequency ratio (f_f/f_0) and amplitude A, the resulting curves show that the n:m resonance regimes appear as regions with a finite width which are surrounded by parameter regimes with irrational winding numbers. The tongue-shaped regions with rational winding number are called the Arnold tongues [7]. Figure 2.11 displays a 1:1, 2:1 and a $m : n$ resonance region in an amplitude - frequency ratio plane.

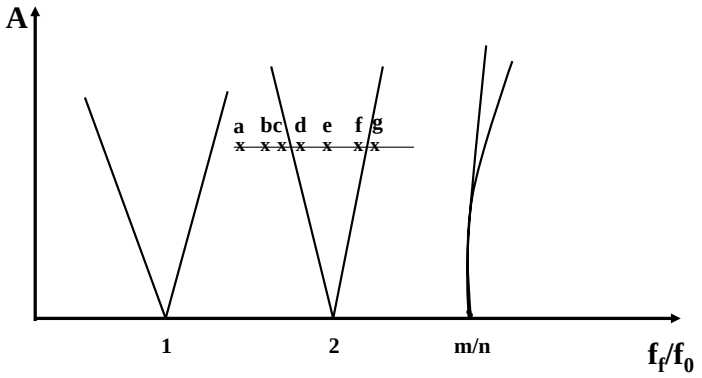

Figure 2.11: *The tongue shaped resonance regimes depicted by plotting the forcing parameters, amplitude, A, vs. the ratio of the forcing frequency, f_f to the oscillations frequency, f_0. Inside each tongue the oscillator is frequency-locked and in the area between two tongues the respond is quasiperiodic. Taken from [59].*

The two-dimensional attractive toroidal surface in phase space corresponds to an attractive invariant circle in the Poincaré (stroboscopic) map. A periodic solution on the torus becomes a fixed point of period n. From the definition of the winding number it follows that since every point of a period n orbit is mapped to itself after n forcing periods, the nth iteration of the Poincaré map of a limit cycle with period n possesses n fixed points.

Studying the stroboscopic phase portrait of the driven system inside and outside the entrainment band and at the transition point between the synchronous and asynchronous regions is helpful to understand the dynamics of the system in these parameter regimes. Figure 2.12 depicts such picture for a forced oscillatory system close to the 2:1 resonance region. This picture is obtained by following points on a 1-parameter cut through the 2:1 resonance region, as indicated in figure 2.11. The phase portrait is displayed for four of the points marked in figure 2.11. At the edges of the entrainment band a saddle-node bifurcation of limit cycles takes place on the torus, through which two limit cycles collide and disappear [60]. At the bifurcation point a half-stable limit cycle is born which splits into a pair of stable and unstable limit cycles as the bifurcation parameter grows. The saddle-node which appears on the torus at the border of the entrainment band has a period m and is attractive at one side and repulsive on the other side. At point d the saddle and the

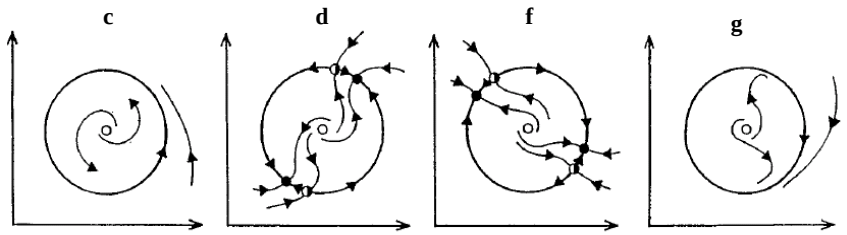

Figure 2.12: *Poincaré map of an externally forced oscillatory system (c) and (g) close to, and (d) and (f) inside the 2:1 entrainment band. The phase portraits corresponds to the parameter values marked in figure 2.11. Taken from [59].*

node have split and give rise to two limit cycles with period m that wind around the torus. Close to the other transition point (point f), the saddle and the node move in opposite directions which causes the limit cycles to collide and disappear through another saddle-node bifurcation. In the parameter region surrounding the synchronous regime the dynamics are quasiperiodic. However, in a region close to the borders of the tongue (points c and g) the iterations of the Poincaré map close to the position where the saddle-node pair is born is slowed down. This phenomenon is also called the *critical slowing down* [61, 62].

From the definition of the entrainment it is clear that inside the entrainment band where the system is locked to the forcing and $f_r = \frac{n}{m} f_f$, the phase difference between the externally applied signal and the response is either zero or constant. However, the dynamics of this phase difference changes as the frequency detuning is varied. Figure 2.13 presents the dynamics of the phase difference between the sinusoidal forcing signal and the time series of the response, $\Delta\Phi$, at the different parameter regions marked in figure 2.11. The figure shows that at zero detuning (point e) and at low detuning where the phase of the system is still locked by the phase of the driving force (points d and f) the driven system oscillates in-phase or with a constant phase difference to the driving force. When the frequency detuning becomes large enough so that the external forcing is not strong enough to entrain the system, a nonzero phase difference appears which grows infinitely in time. However, as it can be seen in figure 2.13, the growth of $\Delta\Phi$ is not uniform unless the detuning becomes very large. In the vicinity of the transition points (points c and g) the dynamics of $\Delta\Phi$ are highly nonuniform. Here, the system stays in a quasi-locked state for a long time with a nearly constant $\Delta\Phi$ which is followed by short time interval where $\Delta\Phi$ gains (or loses) $\frac{2\pi}{n}$. This jump in the phase difference between the force and the driven system is called a *phase slip*. The nonuniform growth of

$\Delta\Phi$ in the close neighborhood of the synchronization region is a manifestation of the critical slowing down which was discussed above. As the detuning increases the time intervals of the phase slip become longer than the oscillation period (point b) and finally the unbounded growth of $\Delta\Phi$ becomes uniform. Hence, studying the dynamics of $\Delta\Phi$ provides considerable insight into the behavior of the system with respect to entrainment.

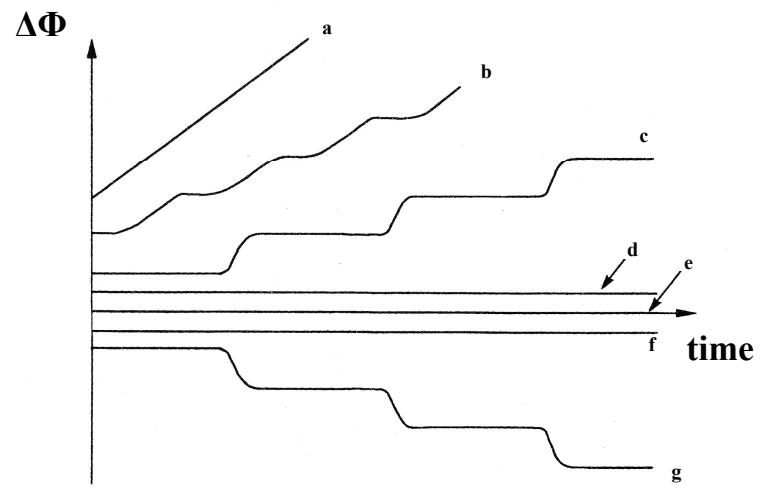

Figure 2.13: *The dynamics of the phase difference between the externally applied forcing signal and the response of the driven system at different parameter points shown in figure 2.11.*

It is intuitive that since f_r always lies between f_0 and f_f, for positive frequency detuning where f_0 is larger than f_f the phase difference between the forcing signal and the unlocked response grows in positive direction, whereas when f_0 is lower than f_f, the latter phase relation grows in negative direction.

The variations of the beat frequency, and correspondingly the response frequency, with increasing and decreasing detuning within the quasiperiodic parameter region is an important characteristic of the dynamics in this region. Figure 2.14 shows that the dependence of the beat frequency on the frequency detuning is monotonic. However, in the neighborhood of the resonance regime where the system goes through critical slowing down, the increase (decrease) is not linear anymore but obeys a square-root low and becomes proportional to $\sqrt{\nu - \nu_t}$, ν_t being the frequency mismatch at the transition point between synchronous and asynchronous regions [8]. When the mismatch between the forcing frequency and the natural frequency of the system becomes large, the response oscillates with the natural frequency of the

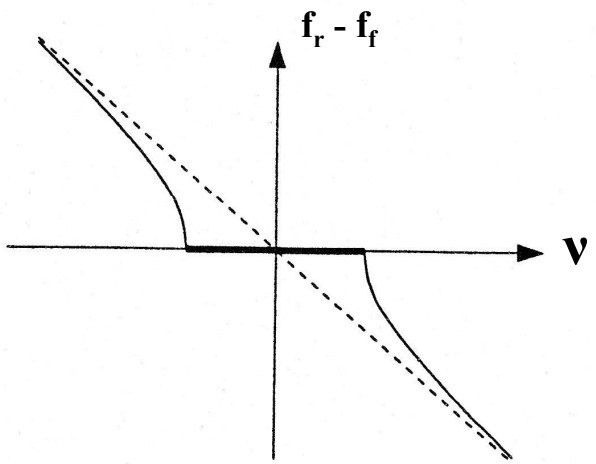

Figure 2.14: *Difference between the response and forcing frequency as a function of frequency detuning. Taken from [8].*

system. It is clear that for frequency locked responses the beat frequency is zero, which appears as a horizontal line in figure 2.14.

Spatially extended systems: Reaction-diffusion systems

Reaction-diffusion systems are an important class of the spatially extended systems which are considered as prototype examples of pattern forming systems. The spatiotemporal patterns arise due to the interaction of homogeneous dynamics and diffusive spatial coupling. In general, reaction-diffusion systems can be expressed by a system of partial differential equations of the form.

$$\frac{\partial c_i}{\partial t} = R_i(c) + D_i \nabla^2 c_i \quad i = 1, 2, ..., n \tag{2.22}$$

where D_i is the diffusion coefficient of the ith species, ∇^2 the Laplace operator and R_i is the rate law that depends on a set of concentrations $c = (c_1 ... c_i ... c_n)$. From Eq. 2.22 it is obvious that there are two ways in which the concentration of the ith species (c_i) can change, either the chemical species is produced or consumed, or it diffuses in or out. Hence, the evolution of c_i can be decomposed into a reaction term, R_i, and a diffusion term $D_i \nabla^2 c_i$. The reaction term stands for the local dependence on the value of other variables and the diffusion term accounts for the transport processes that spatially couple the different locations of the electrode. The interaction of the homogeneous or reaction part with diffusion gives rise to interesting spatiotemporal patterns [63–65].

Externally forced spatially extended systems, specially reaction-diffusion systems, have been studied theoretically and experimentally to investigate if the universal features of frequency locking that single oscillators exhibit persist for spatially extended oscillators [15–18,66]. The theoretical investigations of phase locking in spatially extended systems which suggest continuum models of forced pattern forming systems, are either based on a kinetic model or on amplitude equation. In the works of the first group, the unforced system is described by a coupled kinetic model, such as the Brusselator, Oregonator[1] or FitzHugh-Nagumo model, and then the external forcing is added to the system by modulating one of its parameters periodically in time [15, 70]. The investigations of the second group are based on the description of the unforced system with the complex Ginzburg-landau equation. The complex Ginzburg-Landau equation (CGLE) is a universal equation that describes the dynamics of a spatially extended oscillating system close to the Hopf bifurcation. Here, it is assumed that the instability of the uniform stationary state gives rise to the occurrence of oscillations. To account for the external forcing in these systems a term controlling the forcing strength is added to the CGLE [18–20, 71]. The CGLE and forced CGLE will be explained in detail in the next section.

Considering chemical reactions, one of the early experimental studies focusing on the response of a reaction-diffusion system to external time-periodic forcing was carried out by Swinney et al. [13] who reported resonant patterns arising when subjecting the light-sensitive Belousov-Zhabotinsky (BZ) reaction [2] to time-periodic illuminations as an external perturbation. Following that, Anna Lin et al. reported the formation of various resonant patterns in the light perturbed BZ reaction [15, 16]. In their experiments unforced quasi-two-dimensional oscillating system exhibited rotating spirals which after applying the external forcing resulted in the appearance of a wide range of phenomena not normally seen for single oscillators. Both Swinney et al. [13] and Anna Lin et al. [16] have shown experimentally that when applying the perturbation with 1:1 parameters, the only synchronized solution that appeared were spatially homogeneous, completely phase synchronized oscillations. This has been confirmed by the theoretical work of H.K. Park [19]. Chate and Pikovsky [74]

[1]The Brusselator model was developed by Glansdorff and Prigogine [67] and can be seen as a generic form of a chemical oscillator. It contains only the equations for two intermediary species and not for the specific components of the BZ. The most accepted description of BZ reaction is the so called FKN model [68], suggested by Field, Körös and Noyes which consists of 18 reactions. The simplified version of this mechanism which only considers the essential steps of the full model, is called the Oregonator model [69]. In Eq. 2.22, the term $R_i(c)$ contains no explicit time dependence which corresponds to an unforced dynamics. To model an externally forced reaction-diffusion system, the frequency ω, and strength of the external force, k are included in $R_i(c)$ which gives $R_i(c; k, \omega t)$, where R_i is required to be periodic with respect to ωt.

[2]A description of the BZ chemical reaction can be found in [72, 73].

and later Kim et al. [75] reported the theoretical observation of spatially homogeneous responses which change to stripes when the forcing strength is reduced below a certain threshold. However, their simulations are performed in the phase turbulent region (Benjamin-Feir unstable regime).

The responses around a 2:1 resonance are the most widely studied ones, where a variety of rich resonant patterns are observed. Experimentally, labyrinthine standing wave patterns and π-fronts were observed by Petrov et al. [13]. π-fronts consist of two oscillating spatially uniform domains which oscillate with a π phase shift. Along with the two uniform phase states, front solutions bi-asymptotic to the two stable phases exist. Later Anna Lin et al. reported about the observation of several qualitatively different standing wave patterns [15,16,66] which were also reproduced in the simulations they presented. The theoretical works which focused on the same resonance region, reproduced the experimentally observed spatiotemporal patterns and studied some of them in detail [18, 19, 76, 77]. Furthermore, other resonance regimes such as 3:1 and 4:1 were investigated too [17, 19, 75].

In all the works mentioned above, the entrained responses appear in tongue shaped structures, similar to those observed for single oscillators. However, H.K. Park showed that when a diffusively coupled oscillator is subjected to an external perturbation, both forcing and coupling term due to diffusion, affect the frequency of the driven system and depending on the forcing parameters, they can act together, resulting in the enhancement of the frequency locked region or against each other giving rise to the suppression of entrainment in different parameter regimes. Hence, although the resulting Arnold tongue structures nearly coincide with the Arnold tongues obtained for a single oscillator, the diffusive spatial coupling between different locations of a spatially extended oscillator can modify the frequency locking by reducing or increasing the range of frequency locking in the system [19]. Later, it was shown that pattern formation mechanisms can affect the extent of frequency locking. For 2:1 forcing parameters Yochelis et al. showed that mechanisms associated with phase-front instabilities result in the transition of resonant stationary patterns to non-resonant traveling waves [78]. This mechanism, called the nonequilibrium Ising-Bloch bifurcation, affects the frequency locking and hence, the width of the resonance region [76]. Moreover, appearance of a finite-wave number or Turing like instability, induced by the periodic forcing can also extend or reduce the resonance region of a spatially extended system [76, 79].

However, to my current knowledge, no reports on the response of non-uniform oscillations, that emerge through a non-trivial Hopf bifurcation of wave number one, to temporal modulation were found in the context of chemical reactions. One of

the early studies of such a driven system was presented by Rehberg et al. in 1988 in the context of liquid crystals. They investigated the influence of temporal forcing on traveling waves that appear in nematic liquid crystals and showed that this modulation can stabilize standing waves when the forcing is applied with twice their autonomous frequency [12]. Followed by that, the forced traveling waves were also studied theoretically using the complex Ginzburg-Landau equation [33].

2.6 The complex Ginzburg-Landau equation

It was mentioned in 2.2.2 that the dynamics of a single nonlinear oscillator close to the onset of oscillations can be described by a universal mathematical model called the Stuart-Landau equation, based on an ordinary differential equation of a complex order parameter W. The time evolution of W describes the dynamics of a point like system. For spatially extended systems where different locations are locally coupled by diffusion, the oscillating dynamics close to the Hopf bifurcation is described by the complex Ginzburg-Landau equation (CGLE), which reads [42, 80, 81]:

$$\partial_t \mathrm{W} = W - (1 + i\mathrm{c}_2)\,|W|^2\,W + (1 + i\mathrm{c}_1)\partial_x^2 \mathrm{W} \tag{2.23}$$

In this universal equation, except for the system length, there are only two free parameters c_1 and c_2 [82]. Here, c_2 is a measure of the dependence of the oscillation frequency on the amplitude of the oscillation and c_1 depending on the diffusion coefficients of the two variables. Hence, the first two terms on the right hand side of Eq. 2.23 describe the uniform dynamics of a point like system and the last term represents the spatial coupling through diffusion. In Eq. 2.23 the system is in a rotating reference frame, which rotates with, ω_0, the autonomous frequency of the oscillator and hence, the frequency of the autonomous oscillator does not appear in the equation.

The stability of uniform oscillations is determined by the value of $c_1c_2 + 1$. In the c_1-c_2 parameter plane the line at which $c_1c_2 = 1$ is called the Benjamin-Feir line. By crossing the Benjamin-Feir line and moving from positive values of $c_1c_2 + 1$ to negative values, the stable uniform oscillations become unstable. This parameter region is referred to as the Benjamin-Feir unstable regime [42, 81, 83, 84].

Considering the general equation describing the time evolution of W for a diffusively coupled spatially extended one-dimensional system with length L and, periodic boundary conditions, we see that the general solution can be expanded in a Fourier series:

$$W(x,t) = \sum_{n=-\infty}^{+\infty} W_n(t) e^{i2\pi nx/L} \tag{2.24}$$

where n is the Fourier mode number. Knowing that $W(x,t)$ is periodic with respect to L, i.e. $W(x,t) = W(x+L,t)$, it is clear that all solutions of Eq. 2.24 satisfy this condition, too.

The Fourier mode with $n = 0$ corresponds to the spatially homogeneous mode and every other Fourier mode with $n \neq 0$, to a periodic solution in space with the wave number $2\pi n/L$. The time evolution of W_n for each Fourier mode can be calculated by substituting Eq. 2.24 in Eq. 2.23, which after integration, gives the time dependent complex amplitude $W_n(t)$, for each n. The cubic term in the resulting equation couples the Fourier modes.

2.6.1 Forced complex Ginzburg-Landau equation

In 2.5 it was shown that when a diffusively coupled spatially extended oscillator is subjected to an externally applied force, the force breaks the continuous translational time symmetry of the systems by adding a periodicity which introduces an additional time scale. When the external forcing is incorporated, Eq. 2.23 becomes

$$\partial_t \mathrm{W} = (1 + i\nu)W - (1 + i\mathrm{c}_2)\left|W\right|^2 W + (1 + i\mathrm{c}_1)\partial_x^2 \mathrm{W} + \delta_m \cdot W^{*(m-1)} \tag{2.25}$$

In this equation, ν represents the frequency detuning of the external force and the autonomous frequency of the driven system. The last term on the rhs contains the forcing parameters where δ controls the strength of the forcing signal, the term W^* is the complex conjugate of W and m stands for the ratio of the forcing and natural frequency in a $m:1$ resonance. By introducing the forcing to the CGLE, the equation has moved to a rotating reference frame which moves with the frequency of the externally applied forcing.

Eq. 2.25 is invariant to phase transformations of the form $W \to We^{i2\pi/m}$. This can be seen by replacing $W = Re^{i\Phi}$ in Eq. 2.25 which results in n different stationary solutions which are separated by $2\pi/m$ and each corresponds to one phase locked state [14].

2.7 Characterization of spatiotemporal patterns

2.7.1 The Karhunen-Loève Decomposition

The Karhunen-Loève Decomposition (KLD) or Proper Orthogonal Decomposition (POD) is a statistical pattern analysis technique for analyzing an ensemble of spatially distributed data and finding their dominant structure. This technique decomposes the data into an orthogonal basis and time dependent coefficients. The analysis also gives a measure of the relative contribution of each basis function to the total "energy".

In 1956 Lorenz applied this technique in weather forecast context [85] and since then this method has been largely used for analyzing spatiotemporal turbulent patterns in many contexts among them chemical systems [86–88]. Using the KL decomposition, a spatiotemporally varying set of data can be decomposed into a set of time-independent spatial structures and their time dependent scalar amplitudes. This enables us to detect the spatially coherent modes, e.g. the most important spatial structures in the system.

Throughout this work the interfacial potential measured along the ring-electrode (U_{PP}(x,t)) is analyzed by the KL decomposition.

If we measure N discrete points in space at M instants in time, the elements of the correlation matrix R are:

$$r_{ij} = \frac{1}{M}\sum_{m=1}^{M}[U_{pp}(x_i,t_m)U_{pp}(x_j,t_m)] \quad i,j = 1....N. \tag{2.26}$$

The eigenvectors of this matrix, Φ_i , form a complete orthonormal set. The state of the system at any instant can be given in terms of these eigenvectors. The corresponding eigenvalues, λ_i, give a measure of the contribution of the 'modes' (eigenvectors) to the total spatiotemporal pattern and is maximized when:

$$\lambda_i =< (U_{pp},\Phi_i)^2 > \tag{2.27}$$

where the angle brackets stands for the average and the parenthesis for the inner product.

We can easily project the U_{PP}(x,t) onto these 'modes' and reduce the data to several time series. Eq. 2.28 shows how the data can be described in terms of the eigenvectors and the corresponding coefficients, Eq. 2.29, shows how the coefficients are calculated.

$$U_{pp}(x,t) = \sum_{j=1}^{M} b_j(t)\Phi_j(x) \tag{2.28}$$

$$b_i(t) = (\Phi_j(x), U_{pp}(x,t)) \tag{2.29}$$

Normalizing the values of the eigenvalues λ_i provides the values of the *energy*. Distribution of the energy between the spatial modes indicates the contribution of each KL mode in the dynamics.

2.7.2 Hilbert transform

The Hilbert transform or the analytic signal approach [8,89] is a useful approach for obtaining phase and amplitude variable of an oscillating systems whose definition of phase, according to Pikovsky et al. [90], is not unique. The Hilbert transform of a variable $\mathrm{U_{PP}(x,t)}$ can be calculated by producing a variable $\tilde{U}_{pp}$ from the experimental time series for each location on the electrode, in the following way

$$\tilde{U}_{pp}(x,t) = \pi^{-1} \int_{-\infty}^{\infty} \frac{U_{pp}(x,t\prime)}{(t-t\prime)}\, dt\prime \tag{2.30}$$

In practical implementations, the Hilbert transform is calculated by obtaining the Fourier transformation of the U_{PP} and shifting each complex Fourier coefficient by $\pi/2$. Finally the backward Fourier transform will provide the Hilbert transform. By projecting the dynamics into the plane spanned by the experimental signal and its Hilbert transform, the complex variable ζ, or the analytic signal, is obtained.

$$\zeta(x,t) = U_{pp}(x,t) + i\tilde{U}_{pp}(x,t) \tag{2.31}$$

Using the polar coordinate representation of ζ in the complex plane the instantaneous state of the dynamical system is defined by the time dependent spatial distribution of phase, ϕ and amplitude, ρ, as shown in Eq. 2.32.

$$\phi(x,t) = arg(\zeta) \quad and \quad \rho = |\zeta| \tag{2.32}$$

Here, I would like to mention that all the KL decomposition and Hilbert transform analysis of this work has been done by Prof. Dr. Adrian Bîrzu, whose collaboration is greatly appreciated.

Chapter 3

Experimental

This chapter presents a detailed description of the experimental setup, chemicals and instrumentation, which were used for carrying out the measurements of this thesis.

3.1 The electrochemical cell and the electrodes

The electrochemical cell which were used for the experiments, is depicted in figure 3.1. This cell consists of a cylindrical glass cell of 400 cm^3 volume with two gas inlets opposite to each other, a small glass cylinder inside the cell, three electrodes and a potential probe.

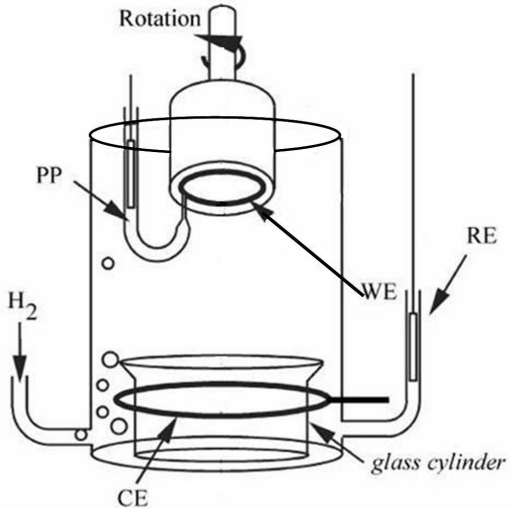

Figure 3.1: *Electrochemical cell. WE: working electrode; CE: counter electrode; RE: reference electrode; PP: potential probe.*

Working electrode

For the experiments a ring shaped polycrystalline platinum electrode, embedded into Teflon, was used as the working electrode. The inner and outer diameters of the ring were 30 mm and 32 mm, respectively. Prior to each experiment the ring was polished to a mirror finish on a polishing cloth with fine diamond pastes with a particle size down to 0.25 μm. The ring was then ultrasonically cleaned in acetone, ethanol,methanol and water respectively. Finally, the working electrode was electrochemically annealed [91] by cycling between -0.65 and 0.7 V (vs. Hg/Hg_2SO_4) with 0.1 V/s in a 0.5 M H_2SO_4 solution under Ar bubbling for 30 minutes. Figure 3.2 shows a cyclic voltammogram of the platinum ring after pretreatment.

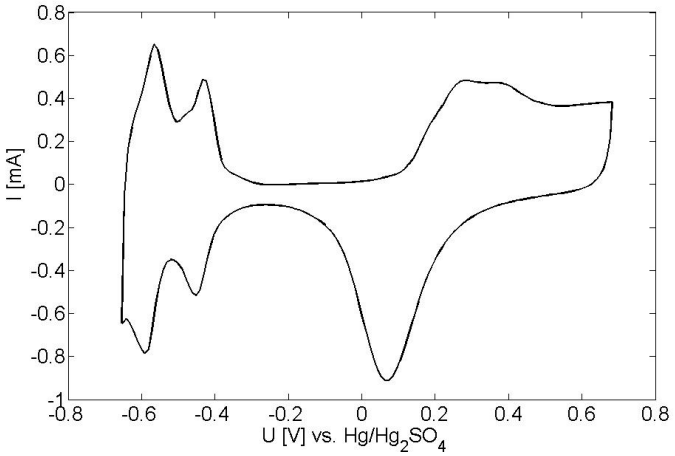

Figure 3.2: *Cyclic voltammogram of a rotating Pt ring-electrode measured in Ar saturated 0.5 M H_2SO_4, with 0.1 Vs^{-1} scan rate and 20 Hz rotation rate.*

Counter electrode

In these experiments the counter electrode was a ring shaped platinum wire (thickness 1 mm) with a diameter of 65 mm. The ring was fixed in a plane parallel to the plane of the WE and in a distance of 40 mm away from the working electrode to ensure a defined distance between the working and the counter electrodes.

Reference electrode

All the measurements in this work were done under potential control, i.e., the potential difference between the working and reference electrode was kept fix. Throughout all the experiments a mercury-mercurous sulfate (Hg/Hg_2SO_4) electrode was used as reference electrode. The electrode was placed in a separate compartment which was

connected to the main cell below the counter electrode. It was important to have the RE at the plane of the CE to avoid any geometry induced negative differential resistance.

Potential probe (PP)

Throughout the work of this thesis, we monitored the spatiotemporal pattern formation on the surface of the ring-electrode by measuring the interfacial potential drop along the angular direction of the working electrode *insitu*. To do this, a home-made Ag/AgCl electrode (for details see [92]) was put into a J-shaped glass capillary which was placed underneath the working electrode. The tip of the glass capillary was about 1 mm away from the surface of the ring. Throughout this work, the potential which was measured by the potential probe is designated by U_{PP}.

The small glass cylinder inside the cell distributes the gas and prevents the formation of bubbles on the Pt ring surface. The cell was placed in a Faraday cage, which is a conductive box connected to the ground, to reduce the current and voltage noise on the working and reference electrode, respectively.

3.2 Chemicals, electrolytes and experimental parameters

It is important to use pure chemicals for these experiments to avoid any adsorption of impurities on the surface. All electrolyte solutions for these experiments were prepared using ultra-pure water produced by a combination of a Millipore Elix 5 and Millipore Milli-Q water system. The specific resistance of water was 18.2 MΩcm and had less than 4 ppb TOC (total organic carbon). For the pre-treatment of the ring-electrode suprapure H_2SO_4 96% from Merk was used. For the rest of the electrolytes HCl 37% (Merck), $CuSO_4.5H_2O$ (Merck) and KBr (Fluka) were used as received. The purity levels of the Ar and H_2 (Westfalen) used were 99.999%.

The electrolyte which was used to performe the experiments in chapter 4 consisted of 0.5 mM H_2SO_4, 0.05 mM $CuSO_4$ and 0.06 mM HCl.

Experiments presented in chapter 5 were performed in the presence of Br^- as anion. The measurements were done using electrolytes consisting 0.5 mM H_2SO_4, 0.1 mM $CuSO_4$ and two different concentrations of the anion, 0.01 mM KBr and 0.005 mM KBr, respectively.

All the electrolytes were saturated with H_2.

The values of the other experimental parameters such as the cell resistance, R_Ω, the compensated resistance, R_c, or the fixed voltage, U_0 during the stationary measurements, are specified for each experiment in the caption of the respective figure. It should be noted that the voltage values are not IR-corrected. Moreover, since an amplifier was used to reduce noise the presented values of the potential probe are multiplied by a factor of 10.

3.3 Instrumentation and data processing

In addition to the electrochemical cell, the setup consisted of a potentiostat, a National Instrument data acquisition board, a rotating electrode system, a device to provide the negative global coupling and a function generator to generate a sinusoidal signal.

A potentiostat is an electronic device that keeps a selected potential difference between the RE and WE fix and measures the current flowing between the WE and the CE. It should be noted that in the measurement setup of this work the WE was grounded. The potentiostat employed for the experiments of this work was built by the Electronic Laboratory of the Fritz-Haber-Institute der MPG, Berlin. For further data analysis applied voltage, current, potential of the PP and a photocell signal, which will be explained later, were acquired with the data acquisition board, which was controlled by a labview program.

The rotating system is of particular importance in the setup of these experiments. It ensures a defined and efficient transport of H_2, Cu^{2+} and Cl^- from the bulk electrolyte to the surface of the working electrode and one is that it enables us to measure the interfacial potential along the working electrode by placing the tip of the stationary potential probe close to the surface of the ring. In all the experiments the working electrode was rotating over the potential probe with 20 Hz. With a data acquisition rate of 1 kHz we measured the interfacial potential with a resolution of 50 points on the ring per rotation. The rotation system consisted of a rod that connected the working electrode to a rotator with a controller and adjustable speed from Pine Research Instrumentation.

As mentioned in section 2.3.2, in electrochemical systems a negative global coupling (NGC) can be introduced to the system by compensating part of the cell resistance. In all experiments discussed in this thesis part of the electrolyte resistance is com-

pensated by means of the built-in negative impedance device of the potentiostat which is in series with the WE.

The external periodic forcing was produced by a programmable function generator with adjustable frequency and amplitude (Hameg HM 8130). By connecting the output of the function generator to the potentiostat, this sinusoidal signal was added to the external voltage so the applied voltage is describe by $U = U_0 + U_1 Sin(2\pi f_f t)$. During the stationary experiments U_0 is kept constant.

The slight imprecisions of the frequency of the rotating system causes a drift of 5 rotations in 120 seconds which should be corrected for long measurements. The precise rotation speed is measured by producing a light signal with a nontransparent marker fixed on the rotating rod which is detected by a photocell connected to the data acquisition board. This light signal was used for interpolation of the data to eliminate the drift. More details of the interpolation can be found in [93]. Since U_{PP} is subject to the same drift as the light signal, this signal can be used to correct the drift in the potential data too.

During the measurements the data points are acquired one after another which appoints a different time to each measured point. To correct this time shift for the spatial profiles at one instant in time, all the data points are interpolated along the time axis [93]. Figure 3.3 shows the change of the light signal and the interfacial potential after drift and time shift corrections.

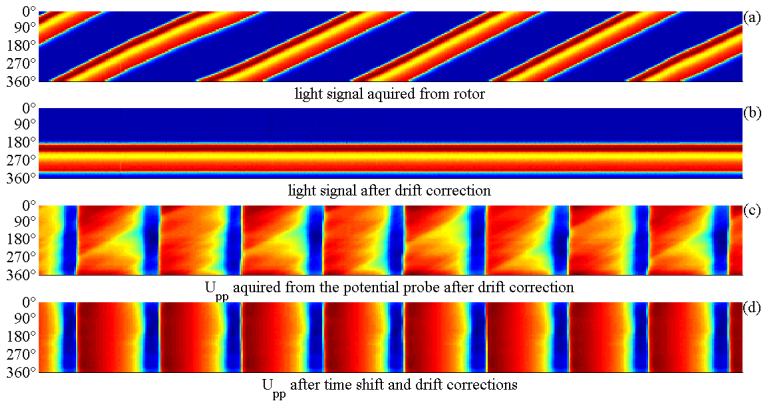

Figure 3.3: *(a) light signal acquired from the rotor, (b) light signal after drift correction, (c) signal acquired from the potential probe after drift correction, (d) signal acquired from the potential probe after drift and time shift corrections. The X axis depicts the position on the ring and the Y axis the time.*

Chapter 4

Time-periodic Forcing of a Traveling Pulse on a Ring

The impact of a time-periodic, spatially uniform external forcing on a non-uniformly oscillating system, is one of the key questions that this work addresses. The system investigated is the electrooxidation of hydrogen on a Pt ring-electrode in the presence of Cl^- and Cu^{2+} ions under NGC. The global coupling rendered the uniform oscillations unstable and induced the emergence of stable phase-pulse solutions. The results of the systematic studies of the response of the oscillatory HOR system in the presence of NGC to the external perturbation are presented in this chapter.

4.1 Introduction

As already discussed in chapter 2, the $Pt|H_2SO_4,Cl^-,Cu^{2+}|H_2$ system is a prototype example of an HN-NDR oscillator that exhibits different oscillations under potentiostatic control. Already about two decades ago Krischer et al. investigated this system and reported a rich variety of temporal patterns exhibited by this system [94–96]. Later, they reported the systems spatiotemporal dynamics in the absence and the presence of negative global coupling [23–25,30]. Before introducing a negative global coupling, the system exhibits spatially weakly modulated oscillations in the entire measured potential window. An example of such oscillations is shown in figure 4.1 where the time evolution of the inhomogeneous part of the interfacial potential, $U_{PP} - < U_{PP} >_x$, is displayed together with the corresponding current time series. These relaxation-like oscillations are characterized by fast passive/active, (low/high) and active/passive current transitions separated by a relatively long time interval in which the system is in the active or the passive region. The abrupt change of the current from a passive (low) to an active (high) state or vice versa breaks up the homogeneous interfacial potential distribution, as can be seen in figure 4.1. Here, any deviation of the colors from green, where $U_{PP} - < U_{PP} >_x$ is about zero, indi-

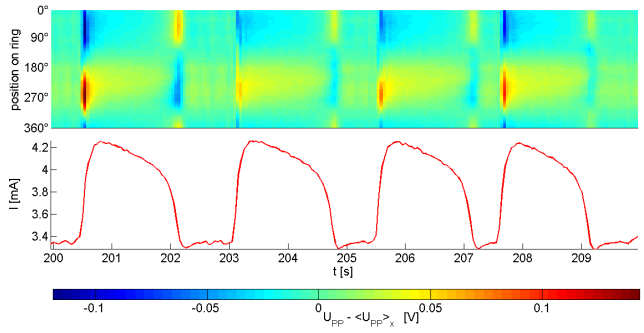

Figure 4.1: *Nearly homogeneous oscillations observed during HOR on a Pt ring-electrode in the absence of a NGC under potentiostatic control. Upper plate:* $U_{PP} - < U_{PP} >_x (x,t)$ *lower plate: I(t). The electrolyte consisted of 0.5 mM* H_2SO_4*, 0.05 mM* $CuSO_4$ *and 0.06 mM HCl saturated with* H_2*. Rotation rate of the WE:* $\omega = 20Hz$*.*

cates a spatial structure. A spatial instability of the homogeneous limit cycle gives rise to this spatial modulation.

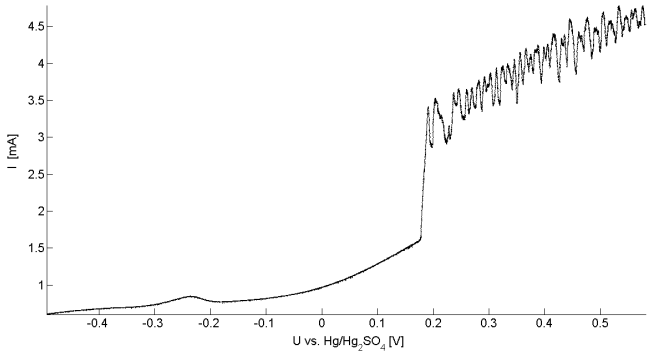

Figure 4.2: *Current-voltage characteristic in the presence of NGC during a potentiodynamic experiment. Scan rate 0.01 V/s, for* $R_c = 300\ \Omega$ *and* $R_\Omega = 540\ \Omega$*. The remaining experimental conditions are the same as in figure 4.1.*

Addition of a negative global coupling changes the dynamics of the system qualitatively. For the experiments of this work the NGC was induced by compensating a part of the total cell resistance (R_Ω), using the built-in IR compensation device of the potentiostat which is de facto a negative impedance device. The change in the dynamics due to the presence of the NGC is obvious when comparing figure 4.2, where the data were acquired in the presence of NGC with figure 2.10, where the system is only coupled through migration coupling. In figure 4.2 one can see that a jump in the current at U = 0.17 V marks the onset of irregular oscillations, which keep their irregularity during the entire potential ramp.

Different from the above discussed oscillations in the absence of NGC, shown in figure 4.1, in the presence of NGC stable large amplitude patterns with periodic dynamics establish under potentiostatic control. The type of spatiotemporal pattern that is observed depends on the strength of the NGC. At low NGC strength, first (asymmetric) target patterns emerged, at higher NGC strength traveling pulses prevailed. This sequence is in agreement with a previous report in the literature [24].

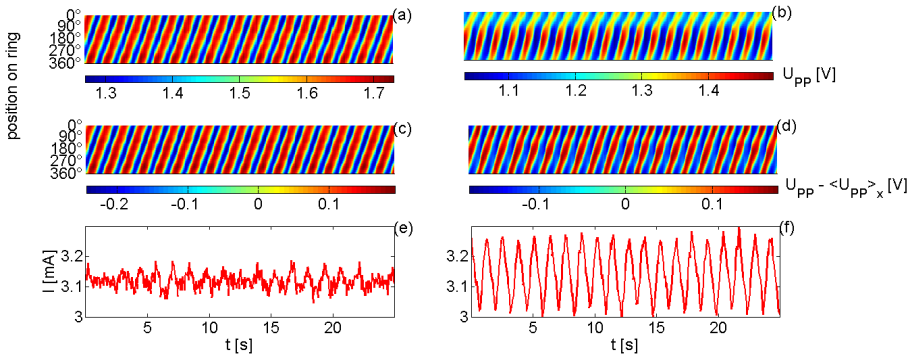

Figure 4.3: *(a) and (b) U_{PP} as a function of time and ring position, (c) and (d) $U_{PP} - < U_{PP} >_x$(x,t), (e) and (f) the current time series of (a) and (b), respectively. Measured at (a) $U_0 = 0.60$ V, $R_\Omega = 540\Omega$, $R_c = 300\Omega$ and (b) $U_0 = 0.30$ V, $R_\Omega = 550\Omega$, $R_c = 350\Omega$.*

Figure 4.3(a) and (b) show two typical space-time measurements in the oscillatory region in the presence of NGC at a constant value of the external potential. In both measurements, traveling pulse solutions establish which propagate with a constant velocity and shape such as in figure 4.3(a) or have some imperfections in the pulse shape as can be seen in figure 4.3(b). Figure 4.3(e) and (f) present the current time series of the system in these two measurements. The amplitude of the current oscillations are proportional to that of the uniform mode, $< \mathrm{U_{PP}} >_x$, thus one can see that in the experiments corresponding to 4.3(f) the spatially homogeneous mode oscillates with a higher amplitude than the measurement corresponding to 4.3(e). The period of these oscillations corresponds to the time in which the pulse travels once around the ring. In the ideal case, a constant pulse shape would exhibit stationary current and different positions on the electrode would oscillate locally. However, during the experiments of this thesis, and similar to reports of experimental observations of traveling pulses with the same electrochemical system [23,30,49], the pulses have never been 'perfect' and their width changed during propagation on the ring at each rotation. In previous works, the modulations in the pulse width have been attributed to Pt surface inhomogeneities. The electrode surface, like any other catalytic surface, contains small morphological non-uniformities which result

in slight differences in the local catalytic properties of the surface. The quality of the surface could also vary slightly with time and thus local and possibly also temporal changes of surface properties might affect the pulse propagation. The origin of the pulse width modulation and the oscillations of the spatially uniform mode will be later discussed in detail in this chapter.

To gain more insight into the spatiotemporal dynamics and to obtain more possibilities for analyzing the response of the globally coupled oscillating system to the periodic external modulation, a Karhunen-Loève decomposition is performed for all the measurements. In section 2.7.1 it was shown that with the help of the KLD, the spatially active coherent modes that govern the spatiotemporal patterns are identified and their respective contributions to the patterns is determined. Originally, the spatiotemporal data acquired consisted of a time series at 50 points in space. As will be demonstrated below KL decomposition reveals that all the measured data can be well represented by just two or three spatial modes. Hence, performing a KL decomposition on a set of data results in an enormous data compression.

With help of KL decomposition, the space-time evolution of $U_{PP}(x,t)$ is given by:

$$U_{pp}(x,t) = \sum_{j=1}^{N} b_j(t)\Phi_j(x) \tag{4.1}$$

where for each j the term $b_j(t)\Phi_j(x)$ contains the contribution of mode j at position x and time t to the signal U_{PP} at position x and time t.

Figure 4.4(a) and (b) display the results of the KL decomposition of the traveling pulse shown in figure 4.3(a). Figure 4.4(a) quantifies how much of the observed pattern is captured by the first 10 KL spatial modes by presenting the energy distribution between them. The figure reveals that the traveling pulse can be captured by the first two spatial modes only, whose contribution to the total energy are nearly equal. Figure 4.4(b) shows how the spatial profiles of these two KL modes look like, on the top as a pseudocolor representation and in the bottom row as profiles along the spatial axis. They clearly present a sine and a cosine mode with wave number k_n with $n = 1$.

Figure 4.5 depicts the time dependent coefficients, $b_1(t)$ and $b_2(t)$ that correspond to the two KL spatial modes presented in figure 4.4(b). One can see that the two time series oscillate with the same amplitude and frequency, however, they are time-shifted by $\pi/2$.

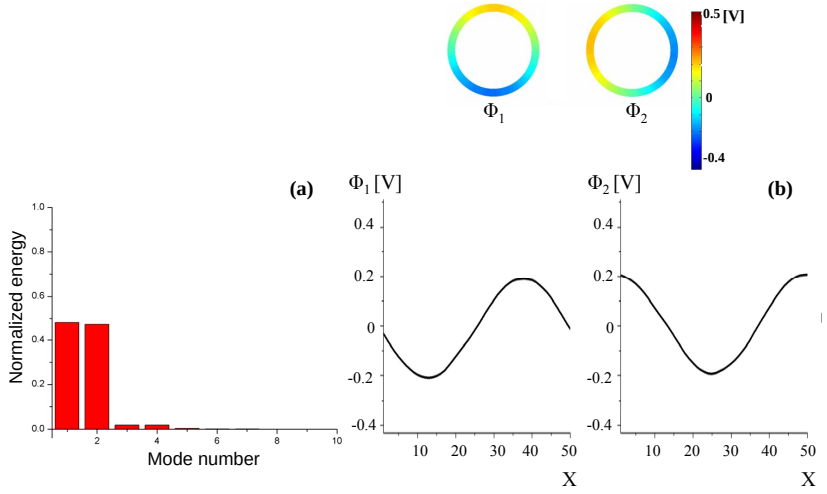

Figure 4.4: *Results of the KLD analysis of the traveling pulse presented in figure 4.3(a): (a) distribution of the normalized energy between the first 10 KL spatial modes of $U_{PP}(x,t)$, (b) the spatial profile of the first two KL spatial modes in pseudo-color representation (top) and in a Φ-x graph (bottom).*

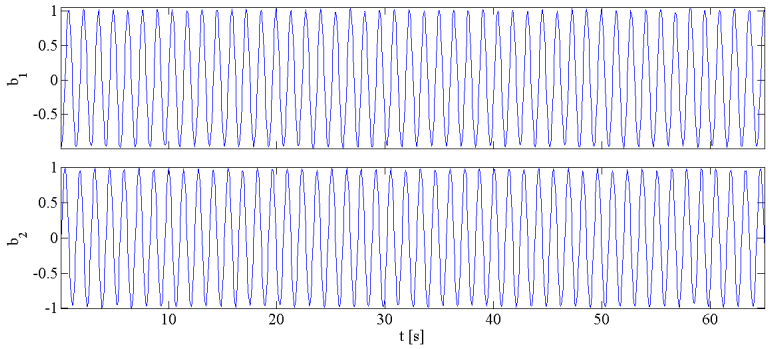

Figure 4.5: *Time dependent coefficients of the two KL spatial modes depicted in figure 4.4(b).*

The KL decomposition confirms that the pulse structures shown in figure 4.3(a) are well captured by the superposition of two spatial structures of a sine-shape and its 90 ° space-shifted version, called in the following the *pulse modes*:

$$U_{PP}(x,t) = a_1(t)sin(\frac{2\pi x}{L}) + a_2(t)cos(\frac{2\pi x}{L}) \tag{4.2}$$

where L is the circumference of the ring-electrode. Hence, the results are in agreement with the description that the pulses emerge through a non-trivial Hopf bifurcation with $n = 1$, induced by the negative global coupling.

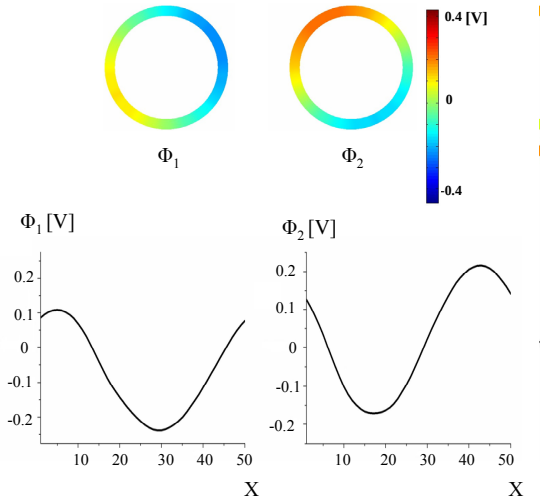

Figure 4.6: *The two KL spatial modes which describe the space-time evolution of U_{PP} for pulses shown in figure 4.3(b).*

Figure 4.6 shows the results of the KL decomposition of the traveling pulses shown in figure 4.3(b), where the spatially uniform mode oscillates with high amplitude, compared to figure 4.3(a). These results show that also here, the first two KL spatial modes of U_{PP} are sufficient to describe the spatiotemporal data, however, the sine and cosine-shaped spatial profiles are shifted by an offset caused by the spatially uniform mode. The effect of this offset appears in form of slight modulations in the width of the pulses as can be observed in figure 4.3(b). Subtracting the uniform mode from the U_{PP} decreases or eliminates the modulations in the pulse width as shown in figure 4.3(d). Also the results of the KL decomposition of the inhomogeneous part of U_{PP}, confirm that the pulse modes of $U_{PP} - < U_{PP} >_x$ do not contain an offset. Therefore, to account for the influence of the oscillations of the uniform mode in the description of U_{PP}, three terms have been considered:

$$U_{PP}(x,t) = a_1(t)sin(\frac{2\pi x}{L}) + a_2(t)cos(\frac{2\pi x}{L}) + a_0(t) \tag{4.3}$$

In Eq. 4.3, the first two terms on the right hand side stand for the inhomogeneous part of the spatiotemporal data and $a_0(t)$ represents the oscillations of the spatially uniform mode with time. Hence, analyzing the full spatiotemporal data, U_{PP}, which provides an insight into how the spatially uniform mode affects the other spatial modes of the system and the inhomogeneous part, which consists of the pulse modes, will provide a complete understanding of the response of the dynamical system. In the data analysis presented in this chapter, the time dependent coefficients

of the complete set of spatiotemporal data, resulting from the KL decomposition of U_{PP} and that of the KL spatial modes obtained from the KL decomposition of the $U_{PP} - < U_{PP} >_x$ are designated with $b_i(t)$ and $a_i(t)$, respectively, for $i = 1, 2, 3, ...$

Subjecting the pulses to external time-periodic forcing

As explained in 2.3.2, traveling pulses in a periodic domain correspond to limit cycles in phase space. Hence, when they are subjected to an external periodic perturbation, within a certain parameter region in the plane of forcing amplitude - forcing frequency, one can expect that the oscillations entrain to rational multiples of the perturbation frequency, giving rise to a variety of different spatiotemporal patterns. To experimentally measure the response of this system to different forcing parameters, first the traveling pulses which served as the reference state of the unforced system were established and followed for several periods of oscillations. Then the external sinusoidal signal was added to the voltage and the response of the driven system to the external forcing was measured. Finally, after the termination of the external forcing the unforced system continued oscillating, reestablishing the traveling pulses again, which ensured the stability of the reference state.

Similar to the unforced dynamical system, analyzing the response of the oscillating system to the external forcing by means of KL decomposition is a very helpful method. Since after subtracting the spatial average of $U_{PP}(x, t)$, the remaining, inhomogeneous part of the response consists of the same main spatial modes as the unforced pulse, the question of determining the entrainment regions of the system reduces to monitoring the behavior of these two spatial modes together with the spatially uniform mode with respect to the forcing signal.

The phase difference between the external sinusoidal modulation and each of the time series of the KLD coefficients, $\Delta\Phi$, is determined by calculating the time difference (Δt) between one maximum in the forcing signal with the corresponding maximum in the amplitudes of the time dependent KL coefficients, $a_1(t)$ and $a_2(t)$. To determine the phase difference between the spatially homogeneous mode and the forcing signal, Δt is determined between the forcing signal and $a_0(t)$. The resulting stroboscopic phase differences are denoted with $\Delta\Phi_0$, $\Delta\Phi_1$ and $\Delta\Phi_2$ for the phase difference of the spatially uniform mode and the two pulse modes to the forcing signal, respectively. It was explained in section 2.5 that entrained responses establish a bounded phase relation to the forcing signal, whereas the phase difference between the forcing signal and a quasiperiodic response grows in negative or positive direction with time.

In the framework of this thesis, the response of this globally coupled electrochemical system to external forcing was studied in three different parameter ranges. First, the external sinusoidal signal oscillated with frequencies, close or equal to the natural frequency of the system, f_0. Then, the response of the system to a time-periodic forcing where $f_f \approx 2f_0$ was studied. Finally, the patterns that prevailed as a result of applying an external modulation with a frequency close to half of the natural frequency were investigated.

In these parameter regions several different sub- and superharmonic synchronization areas are present as well, such as the 1:3 or the 2:3 tongue, which exist close to the 1:2 tongue. However, the focus of this work will be on studying the three mentioned Arnold tongues which are the largest ones in the measured parameter regime.

4.2 The 1:1 Arnold Tongue

In this section we explore the pattern formation within a regime in which the forcing frequency is slightly detuned with respect to the natural frequency of the system and, hence, 1:1 resonance is expected.

To understand the dynamical responses of the system at different forcing parameters the first step is to distinguish between the locked and unlocked responses of the system for each measurement point, or in other words to determine the location of the 1:1 entrainment band in the forcing amplitude - frequency parameter plane. For this analysis the phase differences between the external forcing and the time dependent coefficients of the KL spatial modes of $U_{PP} - < U_{PP} >_x$, as well as the phase relation of the forcing signal to the time series of the spatially uniform mode are determined.

The spatiotemporal patterns that appear in different parameter regions, inside and outside of this entrainment band exhibit a large variety of responses which will be discussed in detail in the following sections.

4.2.1 Determination of the entrained region

The phase difference between the forcing signal and the time series of the KL spatial modes of $U_{PP} - < U_{PP} >_x$, and the oscillating spatially uniform mode are calculated as explained in the introduction of this chapter and the advances of theses phase differences with time are used to discriminate between the locked and quasiperiodic responses.

Figure 4.7 shows an overview of the parameter combinations of forcing frequency and forcing amplitude at which measurements were carried out. The designation I, II and III refers to the forcing amplitudes 20, 40 and 80 mV, respectively. At each forcing strength the values of f_f/f_0 discussed in the text are marked with a letter. Although the KL decomposition and analysis of the advances of the $\Delta\Phi_0$, $\Delta\Phi_1$ and $\Delta\Phi_2$ are performed for all points, only those $\Delta\Phi$ evolutions which are important for the discussion are presented.

A) Forcing amplitude 20 mV

For the forcing strength of 20 mV the variations of $\Delta\Phi_0$, $\Delta\Phi_1$ and $\Delta\Phi_2$ are depicted in figures 4.8, 4.9 and 4.10, respectively. It can be observed in all three figures that except for point I-d and I-e, the phase differences between the forcing signal and

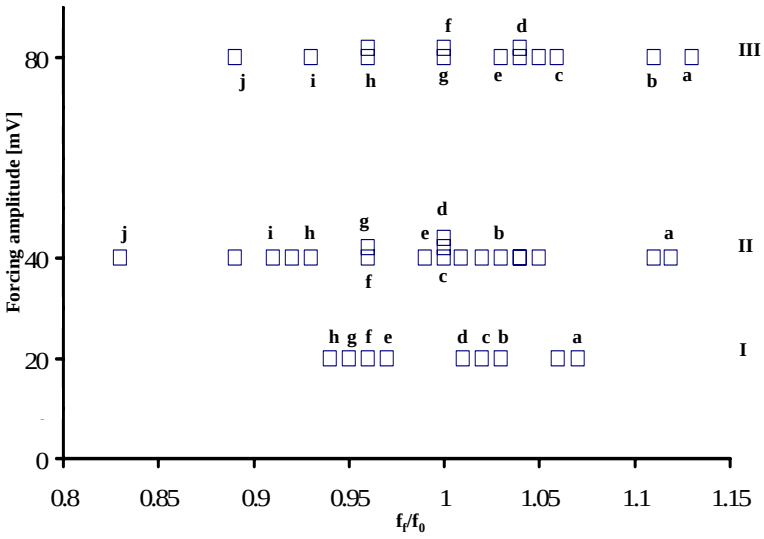

Figure 4.7: *Location of the experimentally measured points in the amplitude - frequency parameter space.*

the three spatial modes grow unboundedly in positive or negative directions. This indicates that the forcing fails to entrain the system at these points and they are located in the quasiperiodic region. At point I-d and I-e, on the other hand, the phase differences stay constant, thus the system exhibits synchronous behavior and two points lie in the resonance regime.

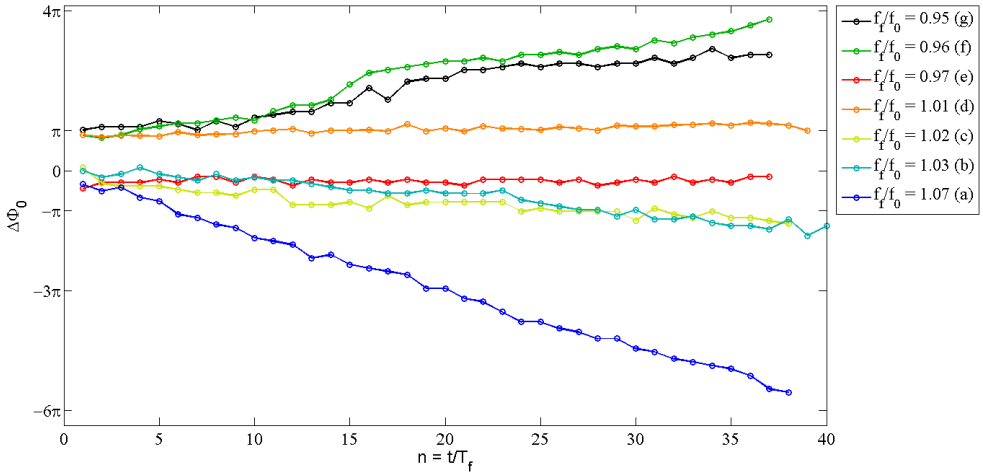

Figure 4.8: *20 mV forcing amplitude: Phase difference between the sinusoidal forcing signal and the spatially uniform mode vs. time. The letters in the caption correspond to the points in figure 4.7.*

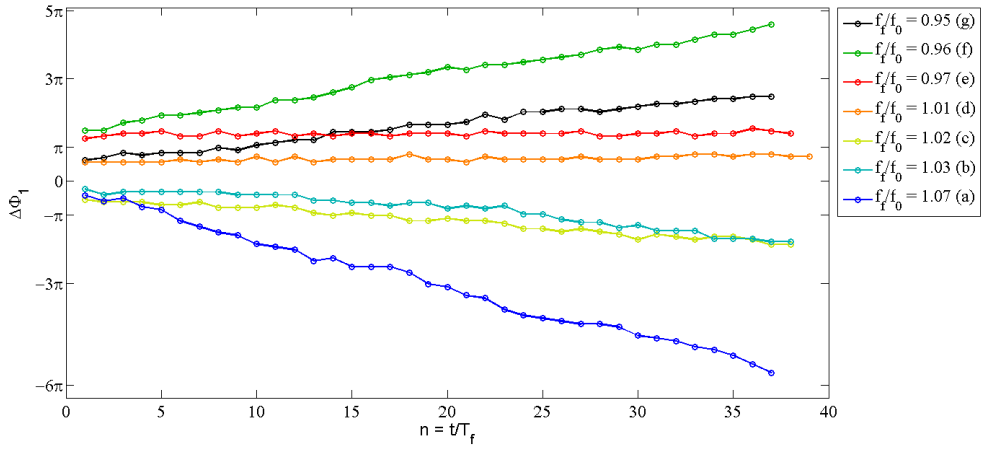

Figure 4.9: *20 mV forcing amplitude: Phase difference between the external signal and the time series of the first KL mode, $a_1(t)$ vs. time. The letters correspond to the marked measurement points in figure 4.7*

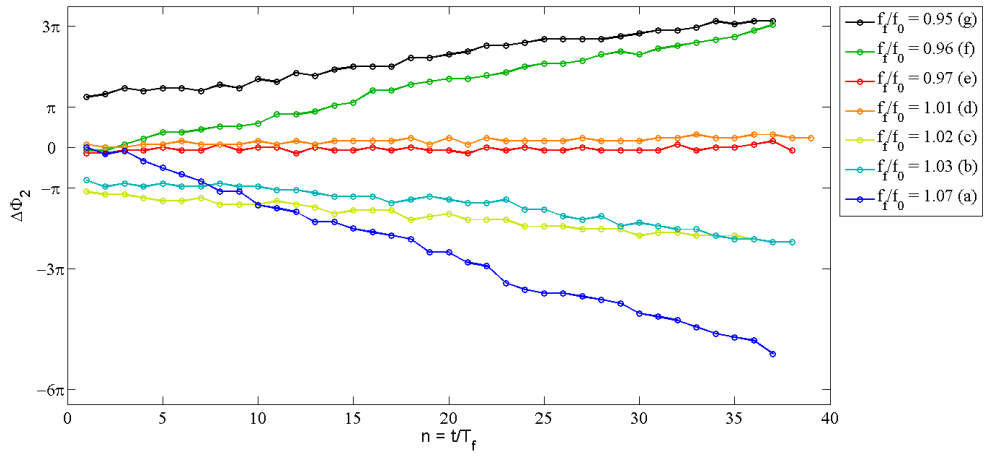

Figure 4.10: *20 mV forcing amplitude: Phase difference between the external signal and the time series of the second KL mode, $a_2(t)$ vs. time. The letters correspond to the marked measurement points in figure 4.7*

As summarized in section 2.5, within the quasiperiodic region in the vicinity of the synchronous regime, phase slips between quasi-stationary states are expected to occur. However, in figures 4.8, 4.9 and 4.10 it can be seen that the advances of $\Delta\Phi_0$, $\Delta\Phi_1$ and $\Delta\Phi_2$ drift continuously and no phase slips appear. To study the transition between the quasiperiodic region and the entrained region further, power spectra of $a_1(t)$ and $a_2(t)$ were determined. In each power spectrum the frequency with the highest intensity was identified as the response frequency of that time series. The

response frequency of $a_1(t)$ was equal to that of $a_2(t)$ at all parameter values. The green curve in figure 4.11 shows a plot of f_r-f_f vs. f_0-f_f. The blue curve in figure 4.11 is the diagonal where $f_0 = f_f$, and thus on this line the periodic perturbation does not affect the base frequency of the forced system. The two points where the f_r-f_f is zero correspond to the entrained responses at I-d and I-e. One can see in the figure that except for the adjacent point on the left side of the entrained region and the last measurement point on the right hand side which lie above the green line in the rest of the parameter region all quasiperiodic points fall in a line on the diagonal. Hence, except for the two points where the response frequency is larger than f_0, the times series of all responses stay unaffected by the forcing and oscillate with the natural frequency of the system. Considering this fact, the data does not contain evidence of a square-root like pushing of the frequency towards the forcing frequency as a characteristic behavior of dynamical systems which go through a saddle-node bifurcation at the borders of the synchronization regime (compare to figure 2.14). This is perfectly in line with the missing phase slips in figures 4.8, 4.9 and 4.10.

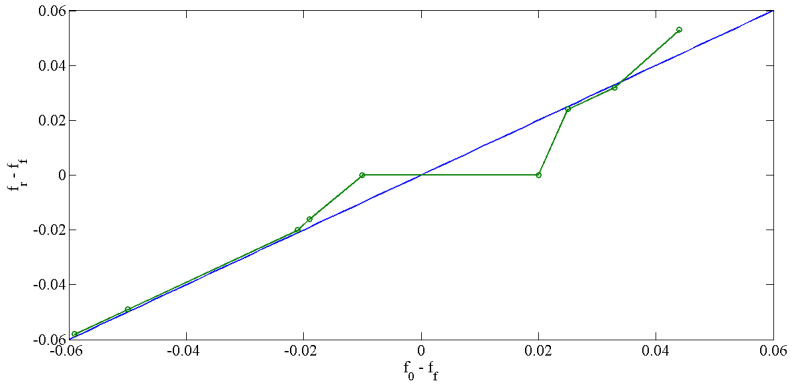

Figure 4.11: *20 mV forcing amplitude: The green curve shows the variations of the difference between the response frequency of a_1 and the forcing frequency with changing detuning. The blue line has a slope of 1 and is added for comparison.*

B) Forcing amplitude 40 mV

Figures 4.12, 4.13 and 4.14 display the phase shifts between of the external perturbation and the time series of the coefficients of the uniform mode and the first two KL modes of the non-uniform part of the interfacial potential, respectively.

From the constant phase difference between the forcing signal and the time series of the spatially uniform mode in figure 4.12 it can be deduced that a forcing strength of 40 mV is strong enough to lock the uniform mode of the driven system to the

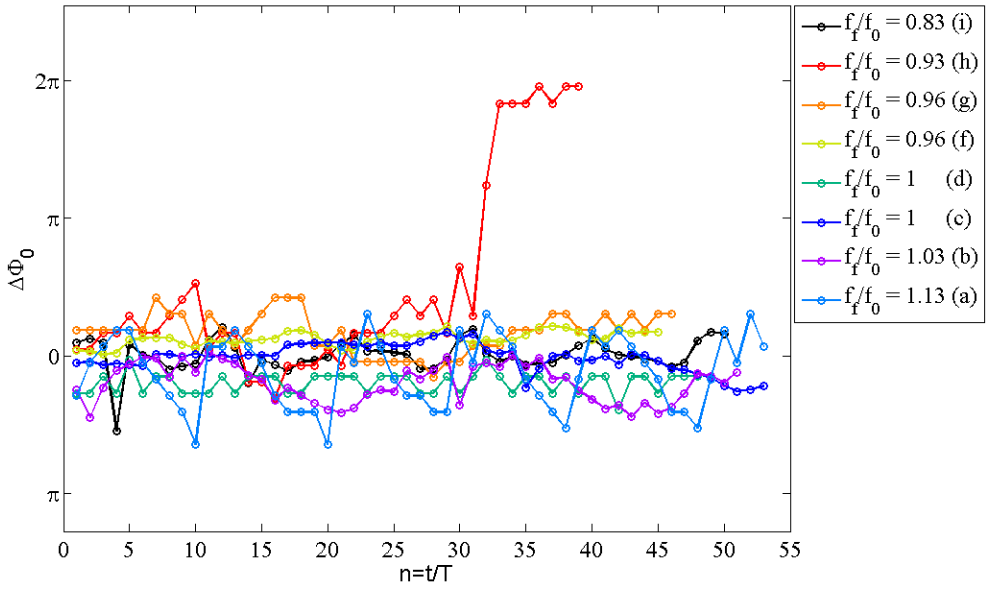

Figure 4.12: *40 mV forcing amplitude: The phase difference between the sinusoidal modulation and the spatially uniform mode a_0 for different measurement points marked on figure 4.7.*

forcing in the entire investigated f_f interval. However, at $f_f/f_0 = 0.93$, due to noise or internal changes $\Delta\Phi_0$ makes a 2π jump from the state of constant phase difference and again establishes a constant phase relation to the forcing signal.

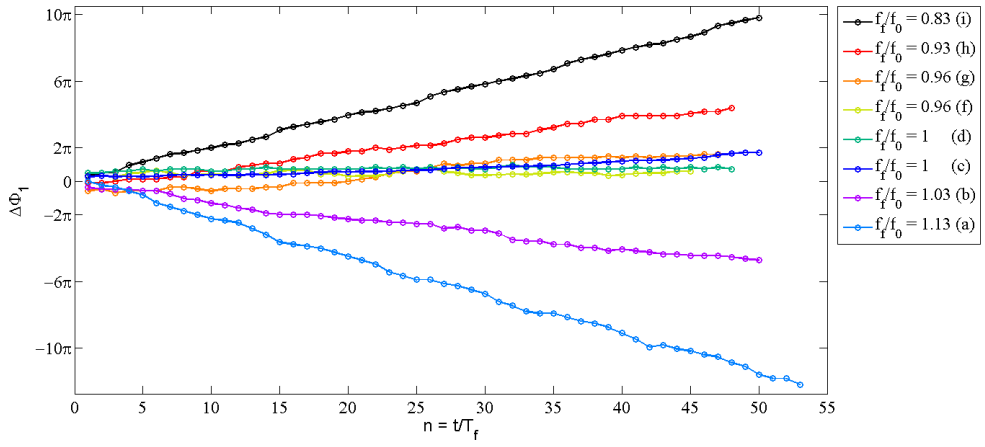

Figure 4.13: *40 mV forcing amplitude: The advances of $\Delta\Phi_1$ for different measurement points marked in figure 4.7.*

From figure 4.13 and 4.14 the boundaries between the resonance regime and the quasiperiodic region can be determined on both sides. In the parameter region between point II-f ($f_f/f_0 = 0.96$) and II-d ($f_f/f_0 = 1$) the system is entrained by

the forcing, since all three spatial modes lock to the external modulation. However, at $f_f/f_0 = 1$ and $f_f/f_0 = 0.96$ we observe also time series with a continuous and slow drift of $\Delta\Phi_1$ and $\Delta\Phi_2$ with time (curves (g) and (c) in figures 4.13 and 4.14). This points to the existence of a bistability between entrained and quasiperiodic responses at these two parameter points.

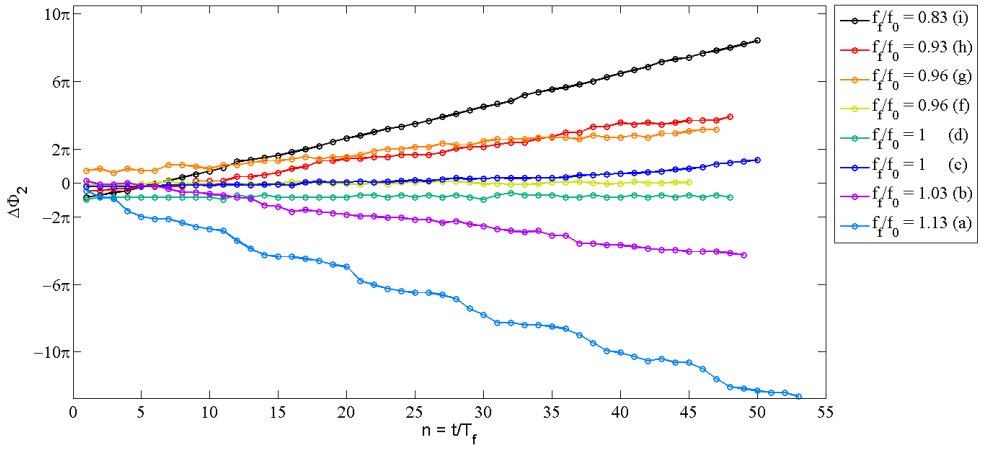

Figure 4.14: *40 mV forcing amplitude: Phase difference between the external signal and the time series of the second KL mode, $a_2(t)$ vs. time. The letters correspond to the marked measurement points in figure 4.7.*

Similar to the responses to 20 mV forcing amplitude, at 40 mV forcing amplitude no phase slips can be observed in the growth of $\Delta\Phi_1$ and $\Delta\Phi_2$. However, to investigate the influence of the detuning on the response of the dynamical system and the presence of critical slowing down in the system, the dependence of f_r-f_f on the detuning is shown in the green curve in figure 4.15. The blue curve marks again the curve for $f_r = f_0$.

Since the synchronous region is not symmetric around $f_f/f_0 = 1$, the green curve in figure 4.15 is not symmetric around zero either. In the parameter area close to the boundaries of the synchronization regime f_0 is pulled towards f_f and hence, f_r lies between f_f and f_0 and the variations of f_r are not linear. Contrary to the responses observed for 20 mV forcing amplitude, here only for high detuning the points come close to the diagonal. Hence, except for high detuning, the driven system is influenced by the external forcing. However, this influence does not follow any trend in the increase or decrease of the response frequency of the points adjacent to the entrainment area. Therefore, one cannot find any evidence of the existence of critical slowing down in the system. This is again in agreement with the missing phase slips during the advances of $\Delta\Phi_1$ and $\Delta\Phi_2$.

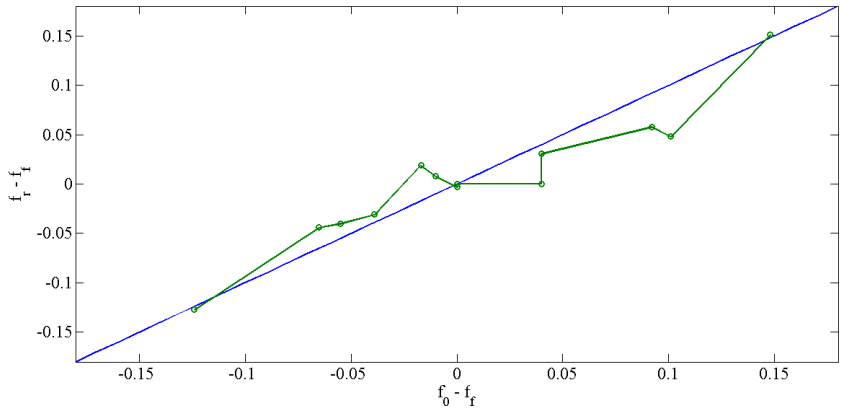

Figure 4.15: *40 mV forcing amplitude: Variations of the difference between the response frequency of a_1 and the externally applied forcing frequency vs. the detuning.*

C) Forcing amplitude 80 mV

At this forcing strength, the spatially uniform mode locks to the forcing signal within the entire parameter region and the phase difference of a_0 to the sinusoidal perturbation signal remains nearly unchanged at zero. This constant phase relation of this spatial mode to the forcing signal can be observed in figure 4.16.

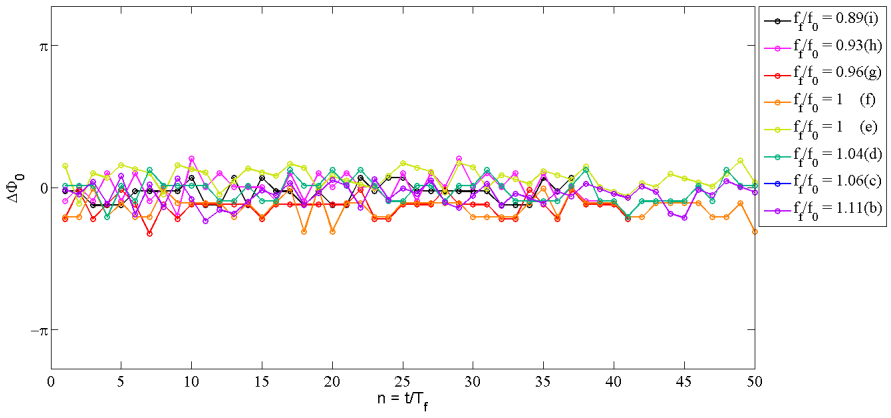

Figure 4.16: *80 mV forcing amplitude: Advances of the phase difference between the external modulation and the spatially uniform mode. The letters correspond to different points in figure 4.7.*

The phase relation of $a_1(t)$ and $a_2(t)$ to the external sinusoidal signal exhibited two types of responses. In the first type of response, the time series of the coefficients of the first and second KL spatial modes of $\mathrm{U_{PP}} - < \mathrm{U_{PP}} >_x$, oscillate periodically

with the forcing frequency and establish a constant phase relation to the forcing signal and thus, are phase locked. The time series of $a_1(t)$ and $a_2(t)$ of the second type exhibit amplitude modulations which are more pronounced in the oscillations of $a_2(t)$. Due to this amplitude modulations, at some measurement points such as III-f and III-d, determination of the exact maxima of $a_2(t)$ and therefore, of the phase difference between this coefficient and the forcing signal was not possible. The growth of $\Delta\Phi_1$ and $\Delta\Phi_2$ at these measurement points, as far as they could be determined, together with the FFT analysis of the time series of $a_1(t)$ and $a_2(t)$ suggest that the responses of the system at these measurement points are not locked to the external forcing. Later in this chapter it will be shown that the responses of the driven system at these points are intermittent or irregular.

In the negative detuning regime, where the $f_f > f_0$, both locked and unlocked responses emerge and at measurement points III-d and III-f a bistability of entrained and unlocked patterns occurs. Since the unlocked responses only appeared in a parameter range with negative detuning, the left border between the synchronous and asynchronous regime cannot be determined. In contrast to the previously discussed results at lower forcing amplitude, the drift of $\Delta\Phi_1$ and $\Delta\Phi_2$ of the unlocked responses with time is not uniform, but strongly modulates, some modulations arising from 2π or 3π phase slips.

Figure 4.19 summarizes the results of the analysis for all measured parameter val-

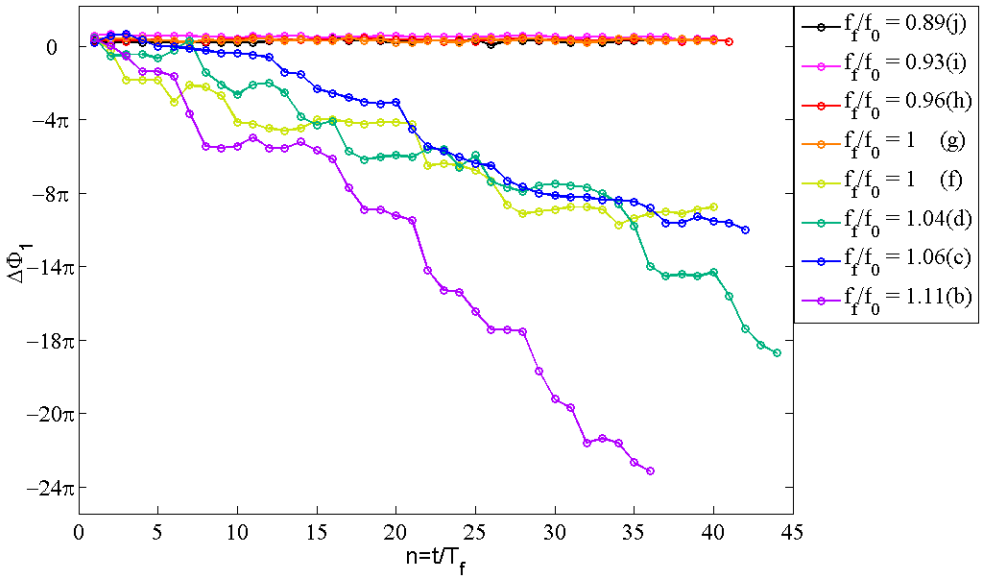

Figure 4.17: *80 mV forcing amplitude: The changes of the phase difference between the external modulation and the time dependent coefficients of the first KL mode of the non-uniform part of U_{PP} for different measurement points in figure 4.7.*

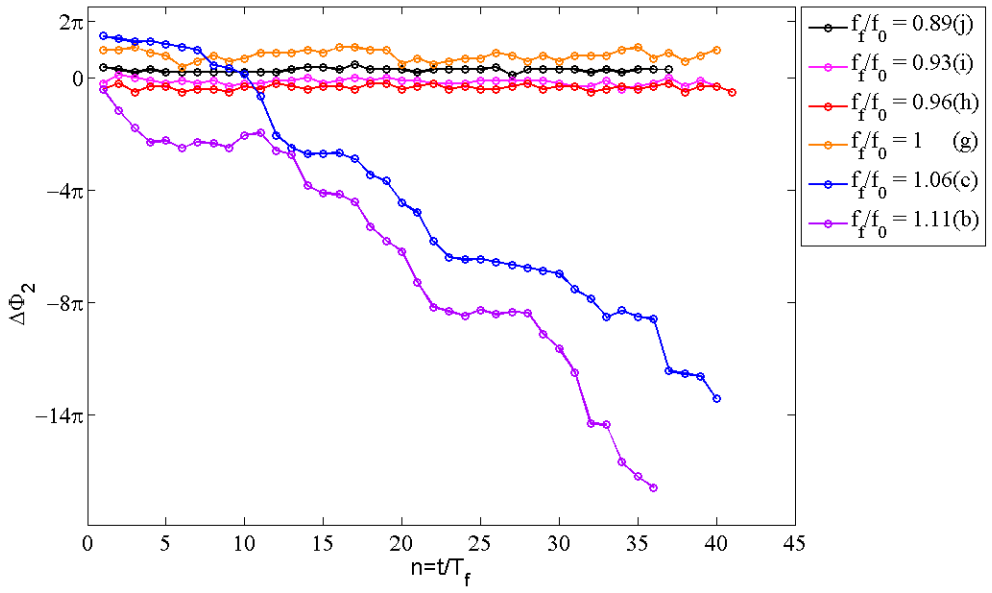

Figure 4.18: *80 mV forcing amplitude: Phase difference between the external signal and the time series of the second KL mode, $a_2(t)$ vs. time. The letters correspond to the marked measurement points in figure 4.7.*

ues. In this figure, the unlocked and locked measurement points are distinguished by filled diamonds and circles, respectively. Different colors, are used to distinguish between various qualitatively different behaviors of the system.

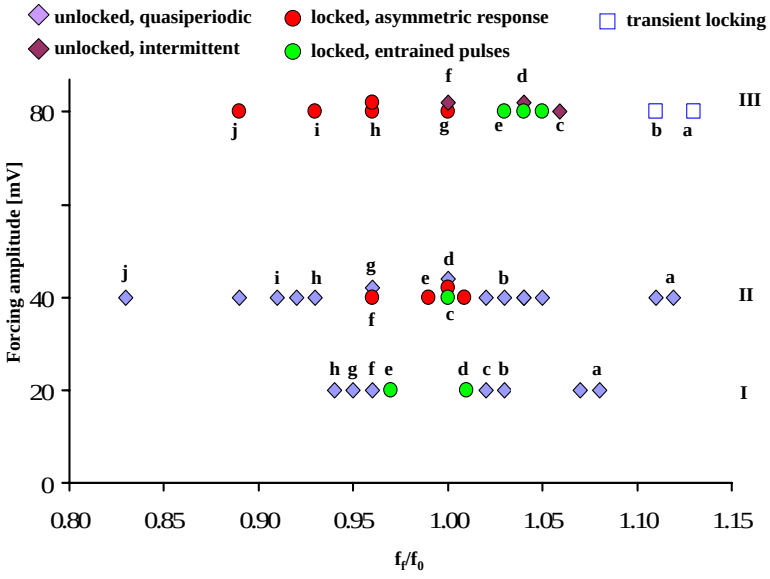

Figure 4.19: *Different responses of the system around the 1:1 resonance tongue.*

4.2.2 Entrained behavior

Within the 1:1 resonance region a variety of qualitatively different entrained behavior established. However, from the results of the KL decomposition of U_{PP} it can be deduced that despite the qualitative differences between the entrained responses of the system to the external modulation, the first two KL eigenvectors of U_{PP} are always sufficient to describe the space-time evolution of U_{PP} at all entrained measurement points. Figure 4.20(a), (b) and (c) display the contribution of the first eight KL spatial modes of U_{PP} for three entrained responses.

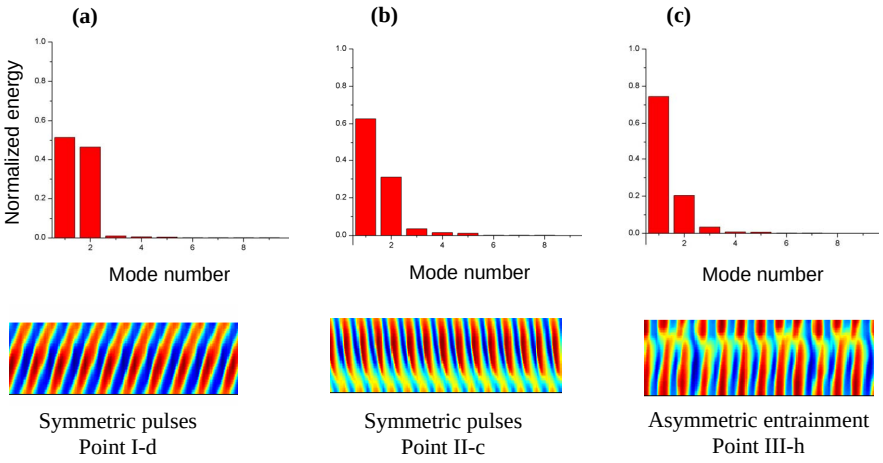

Figure 4.20: *Energy distributions of first eight KL modes of U_{PP} of three examples of entrained responses in the synchronous regions of the 1:1 tongue.*

The analysis of the inhomogeneous part of U_{PP} sheds light on the phenomenological differences between the observed entrained responses. Based on the specific features of different locked responses, such as the response of each pulse mode to the external forcing, the relative contribution of each of the two spatial modes to the total dynamics, or the influence of the external forcing on the oscillations of the uniform mode, they can be classified into three types: Symmetric responses with suppressed uniform mode, Symmetric responses with 'breaking point' behavior and asymmetric entrained responses. The characteristics of each type and the dynamics that lead to the appearance of these patterns will be discussed in the following.

A) Symmetric entrainment

i) Suppression of the spatially homogeneous mode

The type of entrained response at which the external forcing suppresses the spatially homogeneous mode is only observed at low amplitude (20 mV) forcing, at measurement point I-d ($f_f/f_0 = 1.01$).

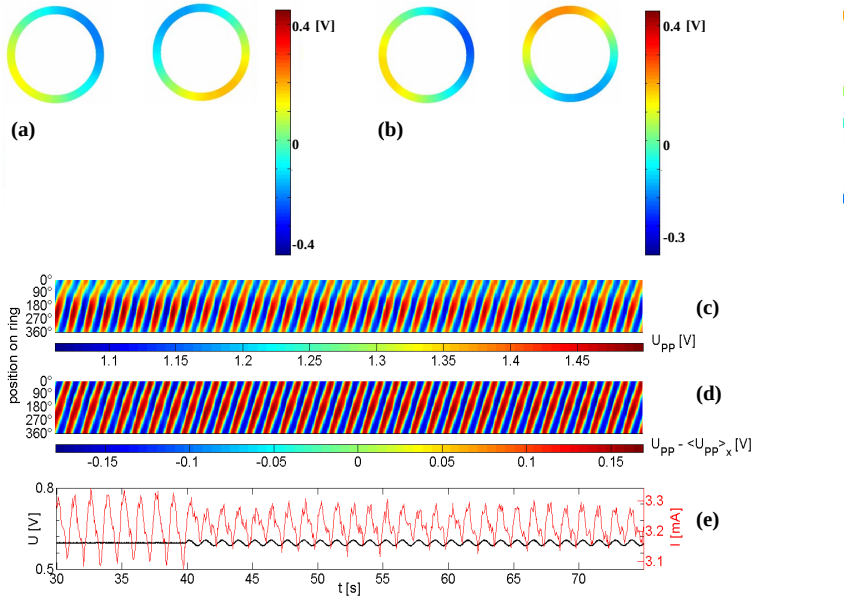

Figure 4.21: *Point I-d in figure 4.19: (a) and (b) The first two KL spatial modes of U_{PP} before and after applying the external forcing, respectively, (c) the time-space evolution of the U_{PP}, (d) spatiotemporal evolution of $U_{PP} - < U_{PP} >_x$, (e) red curve I(t) and black curve U(t). $U_0 = 0.6$ V. $R_c = 300\Omega$, $R_\Omega = 540\Omega$.*

Figure 4.21(e) displays the variations of applied voltage (the black curve) and current (the red curve) with time. One can see that adding the sinusoidal signal to the voltage at t = 40 s results in the decrease of the current amplitude. Since current and electrode potential Φ_{dl} are related by the potentiostatic control by U = IR + Φ_{dl}, the total current is directly proportional to the contribution of the uniform mode to the dynamics. Therefore, the reduction of the current amplitude in the red curve in figure 4.21(e) is equivalent to the reduction of the oscillation amplitude of the coefficient of the uniform mode, thus the homogeneous oscillations of the electrode potential are suppressed through the time-periodic forcing. The reduction of the uniform oscillations can also be seen in the orange curve in figure 4.8 which

depicts the phase relation between the forcing signal and the spatially homogeneous mode for point I-d. In this figure one can see that the two signals oscillate out of phase and keep the constant phase shift of π which leads to the suppression of the spatially homogeneous mode. It should be noted that since the current and the spatially homogeneous potential mode always oscillate out of phase, the phase difference between the external signal and the current oscillations is zero.

The effect of external perturbation on the uniform mode is also reflected in the change of the energy distribution between the KL full spatiotemporal signal before and after switching on the forcing. Figure 4.21(a) and (b) show that because of the suppression of the uniform mode and thus, reduction of its influence on the dynamics of the system after addition of the external perturbation, the offset on the first KL spatial mode becomes smaller.

Investigating the spatiotemporal pattern in more detail, we see that after subtracting the spatially uniform mode, the inhomogeneous part of U_{PP} (shown in figure 4.21(d)) is hardly affected by the forcing and the pulse solution is stable during the forcing.

ii) The 'breaking point' behavior

The measurement points at which the frequency locked systems exhibits a so-called breaking point in the spatiotemporal evolution of U_{PP} are marked with red and green filled circles in figure 4.19. The latter figure shows that this spatiotemporal pattern is observed for all three forcing amplitudes. Figure 4.22(a) and (b) depict two examples of such spatiotemporal patterns.

Here it can be seen that the response of the system consists of traveling structures with a local 'breaking line' in the pulse or a position where the pulse width becomes very narrow. These 'defects' are practically invisible when subtracting the uniform signal from the data, as can be seen in figure 4.22(c) and (d). The KL decomposition of the inhomogeneous part of the data confirms that the overall signal can be described by a superposition of the uniform mode and a traveling pulse. Figure 4.23(a) and (b) depict the distribution of normalized energy from the data of figure 4.23(b) at point II-c, together with the two dominant modes, respectively. Clearly, the two first modes carry a nearly equal contribution of the energy of the inhomogeneous part of the system and the two KL spatial modes are sine-shaped and shifted by $\pi/2$ with respect to each other. These two spatial modes are correlated to two time dependent, phase-shifted coefficients which exhibit regular and periodic oscillations with time, displayed in figure 4.22(e), (f), (g) and (h). The time series of a_1 and a_2

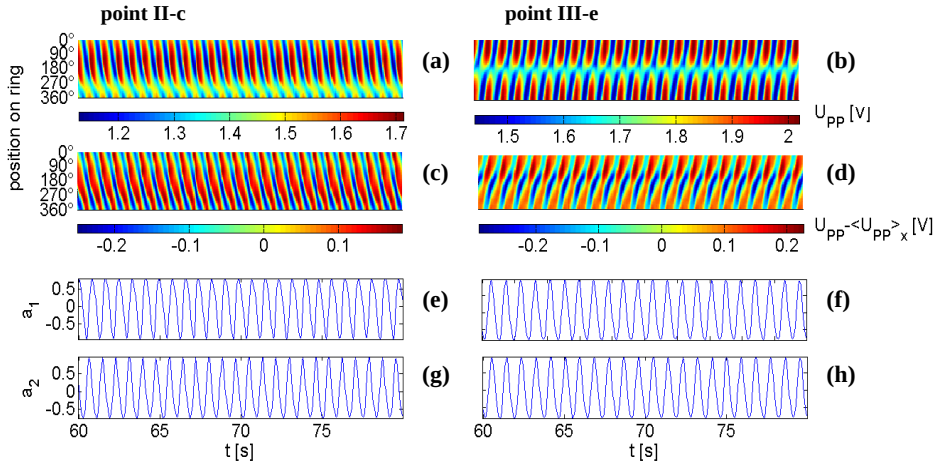

Figure 4.22: *Points II-c and III-e in figure 4.19 as examples of entrained responses with local breaking or narrowing point: (a) and (b) the spatiotemporal evolution of U_{PP} at (c) and (d) $U_{PP} - < U_{PP} >_x$, (e) and (f) the time series of the first KL coefficients (g) and (h) time series of the second KL coefficient. Figures on the right hand side correspond to point III-e and figures on the left hand side to point II-c. $U_0 = 0.4$ V (point III-e) and 0.35 V (point II-c). $R_c = 300\Omega$, $R_\Omega = 540\Omega$.*

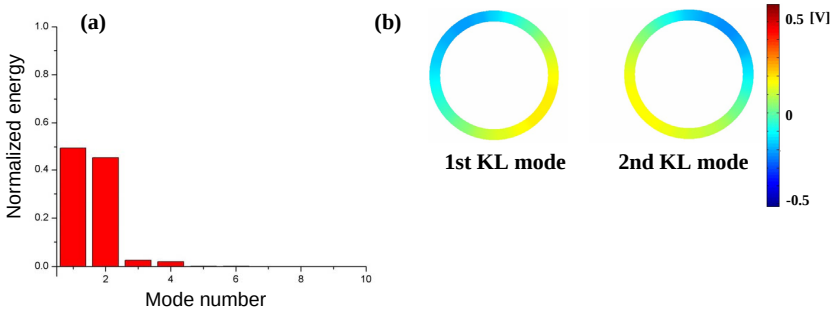

Figure 4.23: *Point II-c in figure 4.19: (a) The energy distribution of the first 8 KL modes of $U_{PP} - < U_{PP} >_x$, (b) the first two spatial modes of $U_{PP} - < U_{PP} >_x$.*

have equal amplitudes and are time-shifted by $\pi/2$. Thus, 'breaking point behavior' is the result of a linear superposition of a traveling pulse and a uniform oscillation.

B) Asymmetric entrainment

The measurement points where the so-called asymmetric entrainment was found are marked by red filled circles in figure 4.19. This class of response occurs only at moderate and high forcing amplitudes. At both 40 mV and 80 mV forcing strength the asymmetric entrainment occurs in the positive detuning regime, $f_f/f_0 \leq 1$.

The spatiotemporal evolution of U_{PP} look phenomenologically similar to the breaking point dynamics. As figure 4.24(c) shows, also at these parameters the traveling structures possess a local breaking or narrowing line. However, the subtraction of the uniform mode from U_{PP} does not result in a traveling pulse solution, as can be seen in figure 4.24(d).

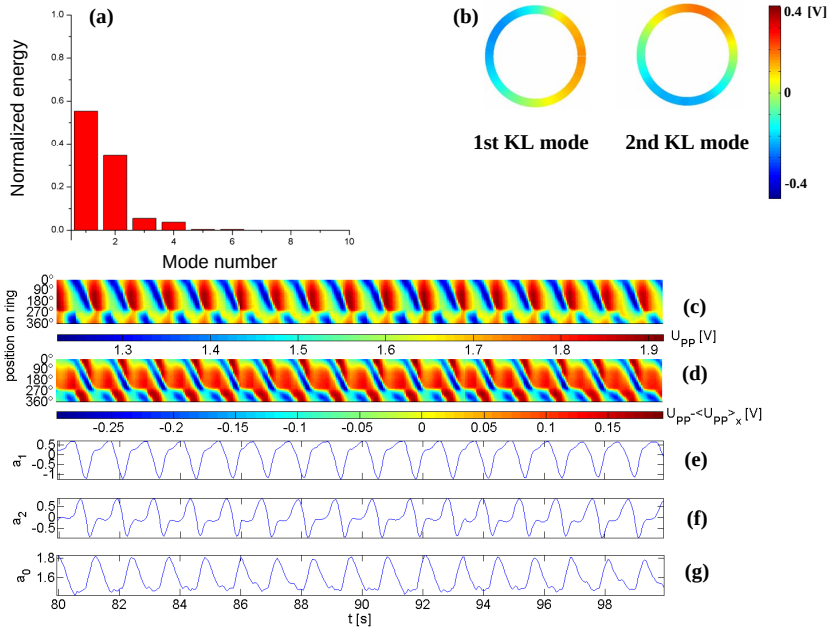

Figure 4.24: *Point II-f in figure 4.19: (a) Distribution of the normalized energy between the first 8 KL spatial modes of $U_{PP} - < U_{PP} >_x$, (b) the first two KL spatial modes of (a), (c) and (d) the space-time evolution of U_{PP} and $U_{PP} - < U_{PP} >_x$ respectively, (e) and (f) time series of the coefficients of the first and second KL spatial mode, respectively, (g) oscillations of the spatially uniform mode with time. $U_0 = 0.35$ V,at $f_f/f_0 = 0.96$. $R_c = 300\Omega$, $R_\Omega = 540\Omega$.*

The results of the KL decomposition of $U_{PP} - < U_{PP} >_x$ shown in figure 4.24(a) and (b), reveal that the spatial eigenmodes are still sine-shaped pulse pairs, i.e. the two spatial structures are $\pi/2$ phase shifted with respect to each other, but their

contribution to the dynamics differs strongly. From figure 4.24(e) and (f) it is evident that the oscillations of the time dependent coefficients, $a_1(t)$ and $a_2(t)$ not only have different amplitudes, but also different shapes. Hence, here the symmetry of the two first inhomogeneous modes is broken. Therefore, we denote such behavior as asymmetric entrainment.

Figures 4.25 and 4.26 present how the difference between the amplitude of $a_1(t)$ and $a_2(t)$ changes within the resonance region, for forcing amplitudes of 40 mV and 80 mV, respectively. For the measurements depicted by green squares in figures 4.25 and 4.26 the amplitudes are only slightly different. However, when forcing with 40 mV, at $f_f/f_0 = 1.01$ and for forcing amplitude of 80 mV at $f_f/f_0 = 1.03$, the difference between the amplitudes becomes larger. This effect can be attributed to a pitchfork bifurcation that takes place at these parameter points where due to the external forcing the symmetric response of the dynamical system changes to an asymmetric entrained response. A pitchfork bifurcation is common in physical systems with symmetry. Pitchfork bifurcations are the generic bifurcations when a symmetric solution changes its stability and which two fixed points with a broken symmetry bifurcate. Both fixed points are either stable (supercritical pitchfork bifurcation) or unstable (subcritical pitchfork bifurcation) [97]. In the bifurcation diagrams shown in figure 4.25 and 4.26 the red square symbols stand for the asymmetrically entrained responses and the points marked with green squares for the entrained pulses. The slight differences between the amplitude of a_1 and a_2 of the symmetrically entrained responses is caused by the presence of slight imperfections in the pulse structure. The filled green triangle in figure 4.25, stands for a response which was not experimentally measured, but its occurrence is predicted by the bifurcation scenario.

Observing that at 40 mV forcing amplitude and $f_f/f_0 = 1$, bistability of both symmetric and symmetry broken states was experimentally measured, the bifurcation scenario presented in figure 4.25 suggests that at this parameter range a subcritical pitchfork bifurcation takes place. At $f_f/f_0 = 1.01$ a saddle-node bifurcation gives rise to the appearance of a stable and unstable fixed points suggesting that within the parameter regime marked with the green line the coexistence of the two qualitatively different stable solutions is possible.

The bifurcation diagram at the higher forcing amplitude of 80 mV, is a nice example of a supercritical pitchfork bifurcation that takes place close to $f_f/f_0 = 1.03$. At the bifurcation point, the symmetry between the response of the traveling wave spatial mode to the external forcing breaks and hence, the symmetric entrained response of the dynamical system becomes unstable.

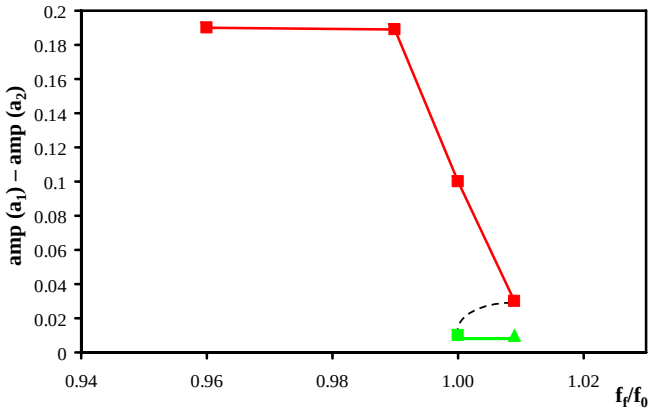

Figure 4.25: *The bifurcation diagram for entrained responses at 40 mV forcing amplitude.*

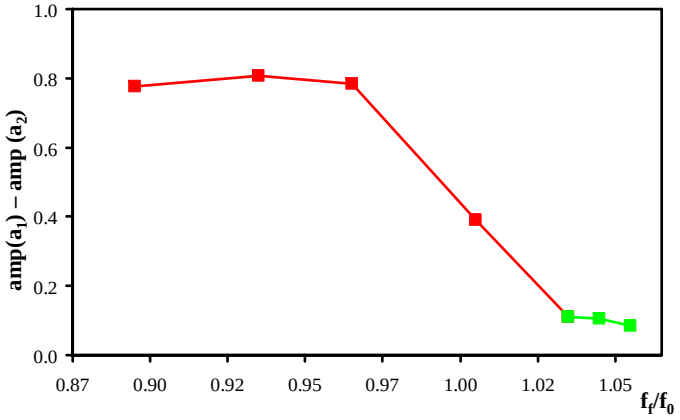

Figure 4.26: *The bifurcation diagram for entrained responses at 80 mV forcing amplitude showing a supercritical pitchfork bifurcation.*

With increasing distance from the bifurcation point, the asymmetry between the responses of the two spatial modes becomes more evident. This effect is also reflected in the difference between the normalized energy of the two modes, which increases with increasing distance from the bifurcation point.

4.2.3 Changes of phase shifts between forcing and response signal within the entrainment band

The phase shifts between the periodic force and the oscillating time series of the three active modes do not only help discriminating parameter regions with entrained and quasiperiodic responses, they also reveal much insight into the dynamics of the entrained regions. Therefore, the behavior of $\Delta\Phi_0$, $\Delta\Phi_1$ and $\Delta\Phi_2$ when passing through the 1:1 Arnold tongue is studied in more detail below.

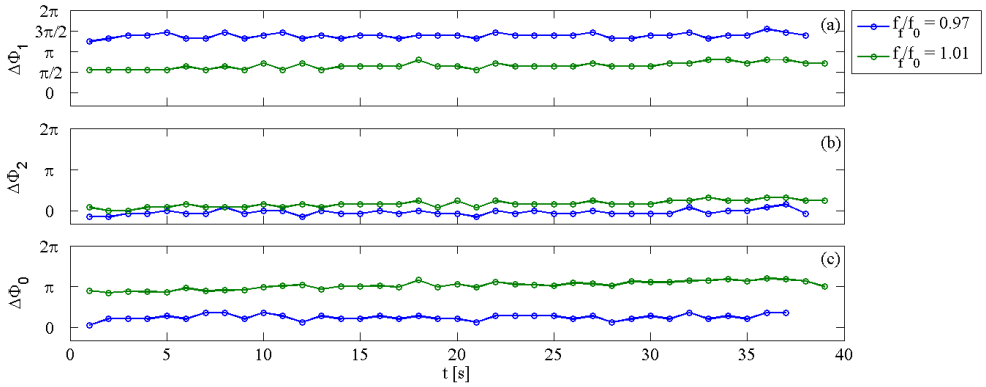

Figure 4.27: *20 mV forcing amplitude: The phase difference between the forcing signal and (a) $a_1(t)$, (b) $a_2(t)$ and (c) the spatially uniform mode. The blue and green curve correspond to the measurement point I-e and I-d, respectively.*

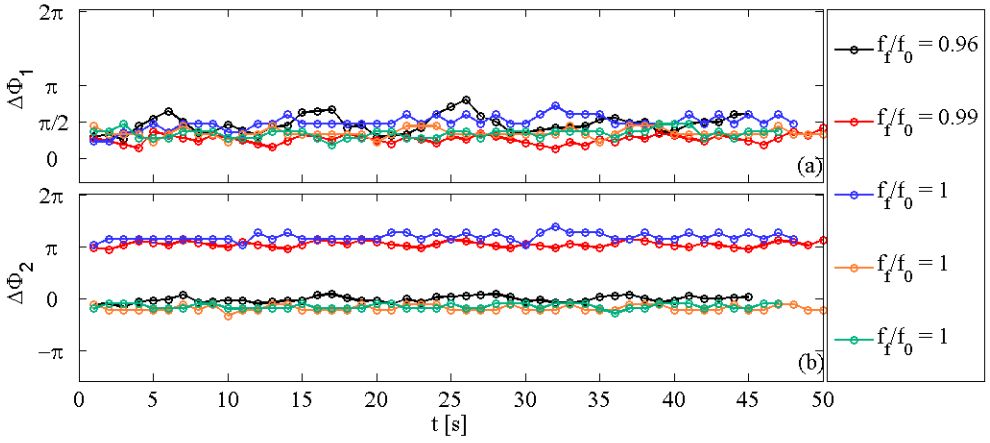

Figure 4.28: *40 mV forcing amplitude: The phase difference between the forcing signal and (a) a_1 and (b) a_2 for entrained responses which mark the boundaries of the synchronization region.*

Figures 4.27, 4.28 and 4.29 show how the phase difference between the forcing signal and a_0, a_1 and a_2 change when moving within the resonance region at 20, 40

and 80 mV forcing amplitudes, respectively. One can see in these three figures that at all forcing strengths the phase difference between the forcing signal and one of the traveling wave spatial modes is always constant (figures 4.27(b), 4.28(a) and 4.29(a)). However, for the phase difference between the forcing signal and the other traveling wave spatial mode a phase shift of π is observed at some measurement points (figures 4.27(a), 4.28(b) and 4.29(b)). This phase shift appears due to the phase invariance of the pulse modes, i.e. $a_1(t)\sin(x)$ and $-a_1(t)\sin(-x)$ are equivalent KL spatial modes and hence, the phase difference of 0 and π between the forcing signal and the corresponding time dependent coefficient of that KL spatial mode are equivalent too. Therefore, the change observed for the latter phase differences are not related to their position within the tongue. As a result, one can see that when moving from one border of the entrainment band to the other, only the phase difference between the forcing signal and the uniform mode at 20 mV forcing amplitude changes by π and $\Delta(\Delta\Phi_1)$ and $\Delta(\Delta\Phi_2)$ stay zero.

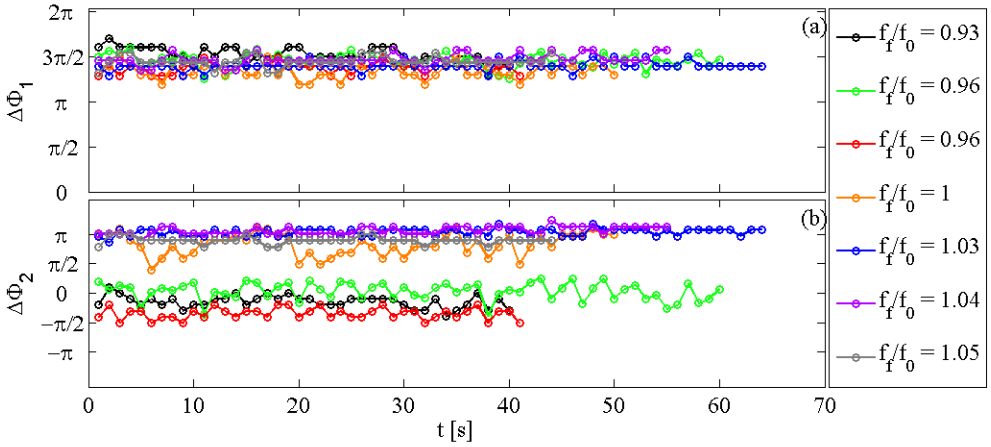

Figure 4.29: *80 mV forcing amplitude: The phase difference between the forcing signal and (a) a_1 and (b) a_2 for entrained responses to 80 mV forcing. The left boundary of the resonance region is not experimentally measured.*

4.2.4 Quasiperiodic behavior

At low and moderate forcing strengths the space-time evolution of the interfacial potential gives rise to quasiperiodic patterns which are similar in the entire parameter region outside the resonance regime. The measurement points that exhibit

quasiperiodic behavior are marked with purple diamond symbols in figure 4.19.

Figure 4.30(a) and (b) present an example of the space-time evolution of U_{PP} and the current oscillations with time (the black curve), respectively. The red curve in figure 4.30(b) displays how the response of current changes when the forcing signal is switched on at t = 33 s.

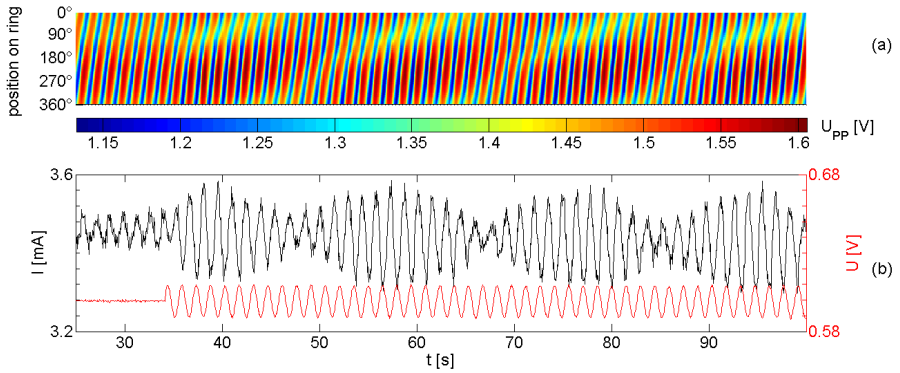

Figure 4.30: *Point I-a in figure 4.19: (a) The time-space evolution of the interfacial potential, (b) the time series of the total current (black curve) and time series of the applied voltage (red curve) for point I-a.* $U_0 = 0.6$ *V.* $R_c = 300\Omega$, $R_\Omega = 540\Omega$.

The occurrence of beat oscillations characterizes all quasiperiodic responses. The beat oscillations correspond to the oscillations of the slowly varying envelope of the fast oscillations. They can be identified easily in the time series of the current (black curve in figure 4.30(b)) and in the time series of a_1 and a_2, shown in figure 4.31(a) and (b), respectively.

The beat frequency is the difference between the response frequency and the forcing frequency. This frequency appears with a low intensity in the power spectrum of the time series of a_1 and a_2, displayed in figure 4.31(c). Power spectrum of a_2 is identical to the one shown in figure 4.31(c) and therefore has not been displayed.

From the results of the frequency analysis of the time series of the coefficients of the first and second KL spatial modes of $U_{PP} - < U_{PP} >_x$ shown in figure 4.31(c) it can be deduced that the coefficients mainly oscillate with a response frequency which lies between f_f and f_0. In addition to f_r, f_f, f_0 and $f_r + f_f$ are also present in the oscillations, however, with considerably lower intensity compared to f_r. In the example depicted in figure 4.31 the response frequency is equal to $\frac{f_f + f_0}{2}$. Hence, here and in similar examples, the time series can be understood as a linear superposition of two oscillations, one with the forcing frequency and one with the autonomous

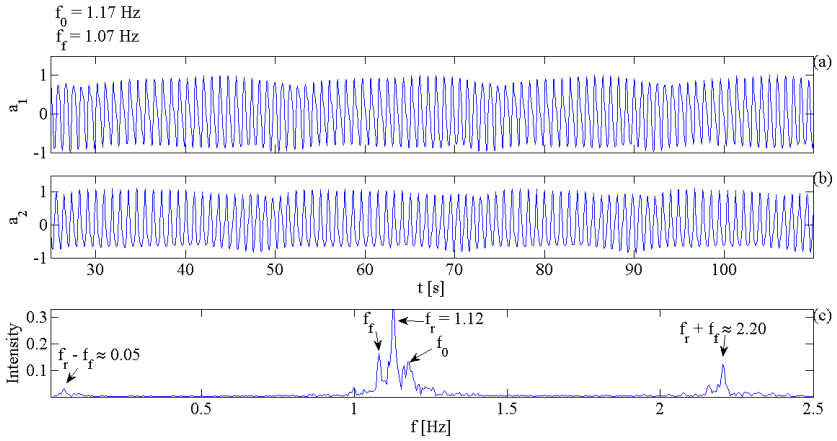

Figure 4.31: *Point II-i in figure 4.19: (a) and (b) The time series of the coefficients of the first and second KL spatial modes of* $U_{PP} - < U_{PP} >_x$*, respectively, (c) Frequency spectrum of (a).* $U_0 = 0.35$ *V.* $R_c = 300\Omega$, $R_\Omega = 540\Omega$.

frequency.

The results of the KL decomposition of U_{PP} shed more light on the dynamics of the system in this parameter range. The energy distribution between the first 8 KL spatial modes of U_{PP} shows that the first three spatial modes capture over 95 % of the total energy and are therefore the main eigenvectors constructing the spatiotemporal data of U_{PP}. The spatially uniform mode appears as an offset on one, two or all of them.

After subtracting the spatially uniform mode, the remaining patterns are traveling spatial structures with width modulations. The width modulations are the result of the excitation of the traveling mode pair by both the forcing and the autonomous frequency. Figure 4.32(b) and (a) display the first and second KL spatial modes of the traveling wave and their corresponding contribution to the construction of the $U_{PP} - < U_{PP} >_x$, respectively.

From the results of the KL decomposition of U_{PP} for entrained and quasiperiodic responses it becomes evident that outside the resonance region three KL eigenvectors are required for capturing the spatiotemporal response of the system whereas within the synchronous regime the first two spatially coherent modes are sufficient to describe the spatiotemporal data. This observation elucidates that entrainment by the external modulation reduces the active degrees of freedom in the system from three to two.

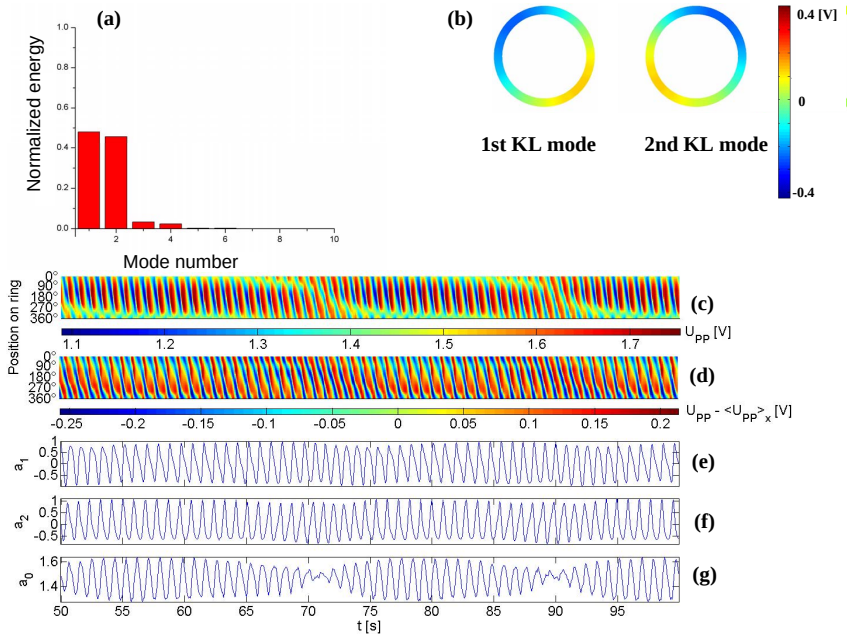

Figure 4.32: *Point II-i in figure 4.19: (a) Distribution of the normalized energy between the first 8 KL spatial modes of* $U_{PP}- < U_{PP} >_x$*, (b) the first two KL spatial modes, (c) and (d) the space-time evolution of* U_{PP} *and* $U_{PP}- < U_{PP} >_x$*, respectively, (e) and (f) time series of the coefficients of the first and second KL spatial mode, respectively, (g) oscillations of the spatially uniform mode with time.* $U_0 = 0.35$ *V.* $R_c = 300\Omega$*,* $R_\Omega = 540\Omega$*.*

4.2.5 Intermittent responses

In section 4.2.1 it was shown that when the system is forced with 80 mV forcing amplitude unlocked responses appear in the negative detuning region. For these states the coefficients of the spatial modes exhibit strong amplitude modulations. The measurement points with such a response are marked with dark purple diamond symbols in figure 4.19.

To gain more insight into the characteristics of this type of responses, the time series of the coefficients of the first and second spatial modes of $U_{PP}- < U_{PP} >_x$ and the spatially homogeneous mode were analyzed by means of a Hilbert transform. The Hilbert transform describes an oscillatory time series through the temporal evolution of phase, $\Phi(t)$, and amplitude, $\rho(t)$, respectively. However, when investigating an externally forced system it is useful to follow the changes of $\Phi(t)$ and $\rho(t)$ of the coefficients at fixed phases of the external forcing. To obtain this stroboscopic mapping, the phase and amplitude obtained from the Hilbert transform are observed at $t_k = k \cdot T_f$ where T_f is the forcing period and $k = 1, 2, 3, ...$ Plotting $\cos(\Phi(t_k))$ ver-

sus $\sin(\Phi(t_k))$ presents the distribution of the phase at times which are multiples of the forcing period on the unit circle. Multiplying the $\cos(\Phi(t_k))$ and the $\sin(\Phi(t_k))$ by the time dependent amplitude, $\rho(t_k)$, and plotting them provides a presentation of the stroboscopic phase and amplitude of the time series. Figure 4.33 presents an example of the two latter graphs which are obtained from the time series of the coefficients of the first and second KL spatial mode of $U_{PP} - < U_{PP} >_x$ and the spatially homogeneous mode at point III-c. The time dependent coefficients and the spatially uniform mode at point III-c are depicted in figure 4.34(c), (d) and (e), respectively. In figures 4.33(a) and (c) it can be seen that the time dependent phase of the first and second KL spatial modes are somewhat inhomogeneously distributed but fill almost the whole unit circle. The chaotic modulations of the amplitudes of the a_1 and a_2 manifest itself in the scattered points in figure 4.33(b) and (d), respectively. The results of the Hilbert transform analysis of the spatially uniform mode which are shown in figure 4.33(e) and (f), show that the variations of the phase are confined to a certain region of phases, which is a manifestation of the fact that this mode is synchronized by the forcing.

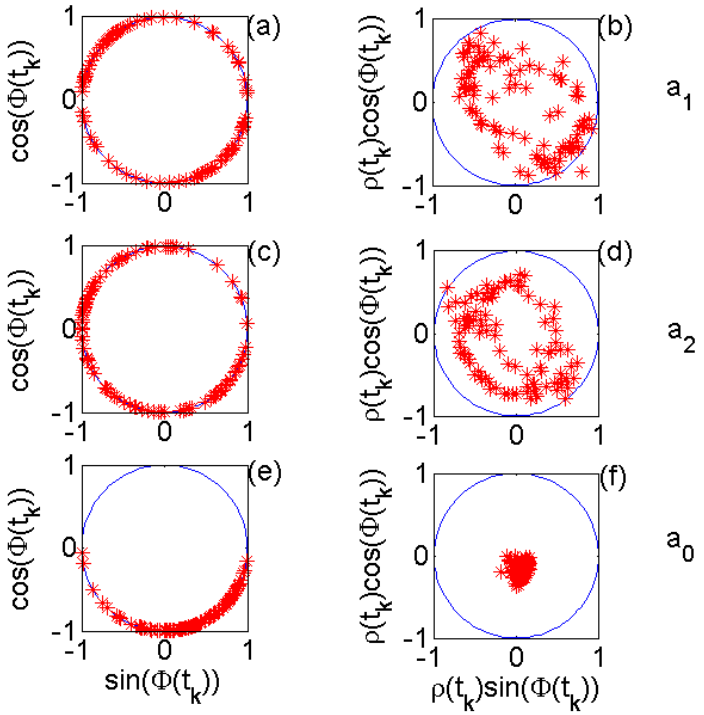

Figure 4.33: *Point III-c in figure 4.19: (a), (c) and (d) distribution of stroboscopically measured phase on unit circle obtained from a_1, a_2 and a_0, respectively. (b), (d) and (f) stroboscopic image of distribution of time dependent phase and amplitude obtained from a_1, a_2 and a_0, respectively.*

The results of the Hilbert transform analysis for all marked points are very similar to those shown for points III-c in figure 4.33. This confirms that, the measurement points marked with dark purple in figure 4.19 are not entrained by the forcing.

The response of the dynamical system at measurement points III-c, III-d and III-f show an intermittency between regular and irregular spatiotemporal patterns. At measurement point III-c, for instance, pulses with a traveling breaking point are interrupted by bouts of irregular patterns and return to the breaking point behavior again, which can be seen in figures 4.34(a). Figure 4.34(b) shows that the intermittency is preserved after subtracting the spatially homogeneous mode. Therefore, the intermittent behavior is also reflected in the oscillations of the time series of the coefficients of the first and second spatial modes of the inhomogeneous part of U_{PP}. The time series of a_1 and a_2 in figure 4.34(c) and (d) reveal that the chaotic modulation of a_1 and a_2 amplitudes in regions where irregular pattern appear are followed by periodic oscillations with nearly equal amplitudes that gives rise to the intermittent traveling pulses.

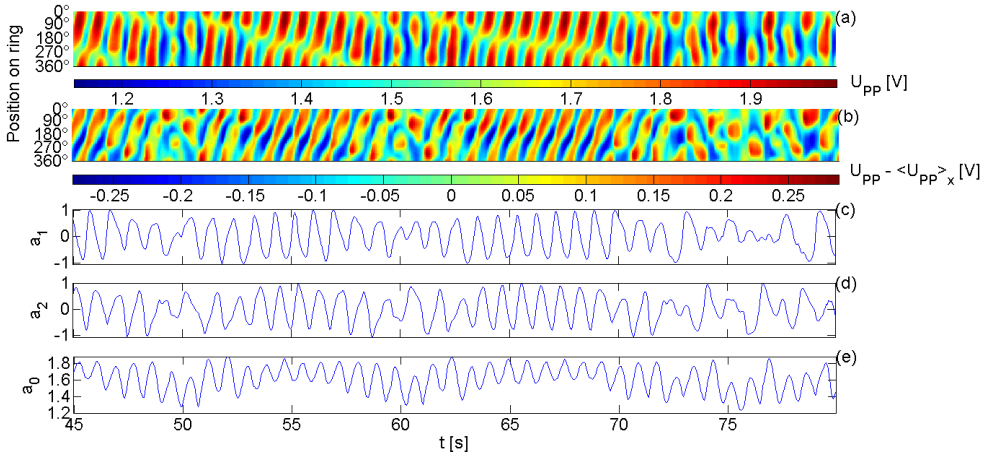

Figure 4.34: *Point III-c in figure 4.19: (a) and (b) The space-time evolution of the U_{PP} and $U_{PP} - < U_{PP} >_x$ respectively, (c), (d) and (e) oscillations of the coefficients of the first and 2nd KL spatial modes and the spatially homogeneous mode, respectively. $U_0 = 0.40$ V. $R_c = 300\Omega$, $R_\Omega = 540\Omega$.*

Figure 4.35(a) and (b) present the space-time evolution of U_{PP} and $U_{PP} - < U_{PP} >_x$ at measurement point III-f, as another example of the intermittent behavior in this parameter range. The switching on and off of one of the coefficients, and the amplitude modulations which cause the irregular patterns are also observed in figure 4.35(b) and (c).

At point III-a and III-b long periods of entrained standing pattern were followed

by long periods of unlocked solutions. This suggests that there exists a heteroclinic loop in the phase space between these two patterns. Figure 4.36(a) and (b) display the space-time evolution of U_{PP} and $U_{PP} - < U_{PP} >_x$ while the dynamical system is close to the locked state. A closer look at the time series of the coefficients of the first and second KL spatial modes of $U_{PP} - < U_{PP} >_x$ in figures 4.36(c) and (d) reveals that the first KL spatial mode of $U_{PP} - < U_{PP} >_x$ oscillates with half of the forcing frequency whereas the coefficient of the second KL spatial mode oscillates with f_f and exhibits period-2 oscillations. Hence, the first and second KL spatial modes of the system are influenced by different resonances and are locked to the 2:1 and 1:1 forcing, respectively.

After a short transient time, the periodic oscillations of $a_1(t)$ and $a_2(t)$ become irregular oscillations with apparently chaotic amplitude modulations. The unlocked irregular response observed at measurement points III-a and III-b are similar. The spatiotemporal pattern of the system at this state and the time dependent coefficients of the corresponding spatial modes are displayed in figure 4.37 for point III-b. It is worth while to investigate whether the unlocked response is deterministic chaotic. To elucidate the existence of chaos in the unlocked responses at measurement points III-a and III-b next-maximum mapping is used. A next-maximum map, which is obtained by plotting the maximum of $a_1(t_{n+1})$ (and $a_2(t_{n+1})$) versus the

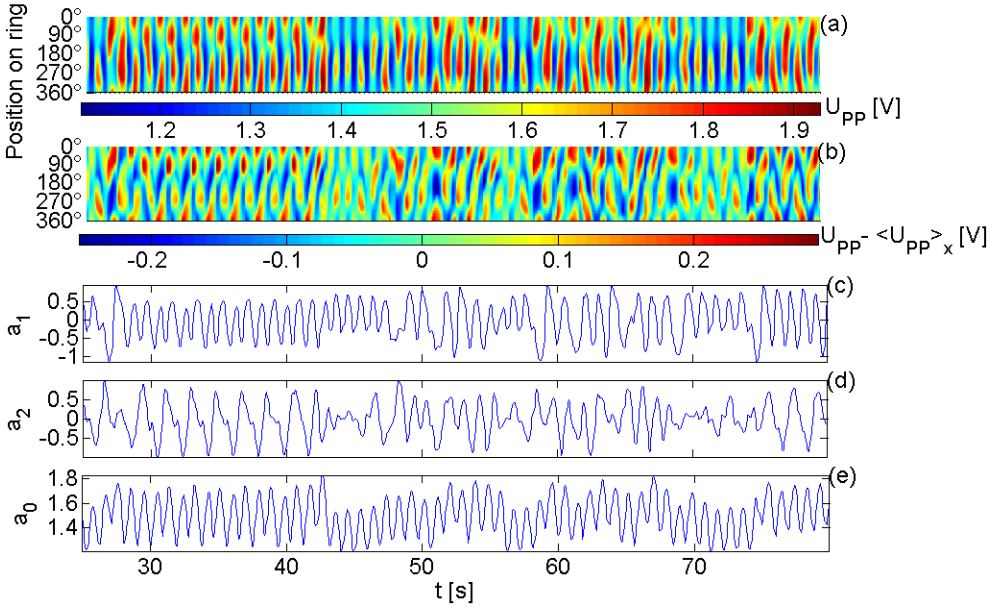

Figure 4.35: *Point III-f in figure 4.19: (a) $U_{PP}(x,t)$, (b) $U_{PP} - < U_{PP} >_x (x,t)$, (c) and (d) the coefficients of the first and second KL spatial modes of the inhomogeneous part of U_{PP}, (f) the time series of the spatially uniform mode. $U_0 = 0.40$ V. $R_c = 300\Omega$, $R_\Omega = 540\Omega$.*

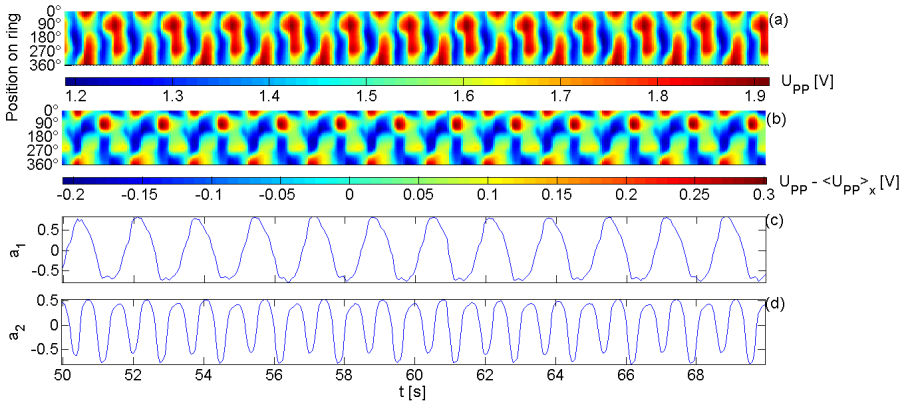

Figure 4.36: *Point III-a in figure 4.19: (a) $U_{PP}(x,t)$, (b) $U_{PP} - < U_{PP} >_x (x,t)$, (c) and (d) time dependent coefficients of the first and second KL modes of $U_{PP} - < U_{PP} >_x$. $U_0 = 0.4$ V. $R_c = 300\Omega$, $R_\Omega = 540\Omega$.*

maximum at t_n, reduces the time-continuous dynamics to a time-discrete map. Specific structures of this map point to the existence of a certain behavior in the system such as period-2 oscillations or chaotic behavior. They are therefore, finger prints of specific dynamics. Figure 4.38(a) and (b) depict the next-maximum maps obtained from the time series of a_1 and a_2 in figure 4.37(c) and (d), respectively. However, from both figures it is clear that the maps possess no distinguishable structures, such as a unimodal map, which could be attributed to a low dimensional chaotic system.

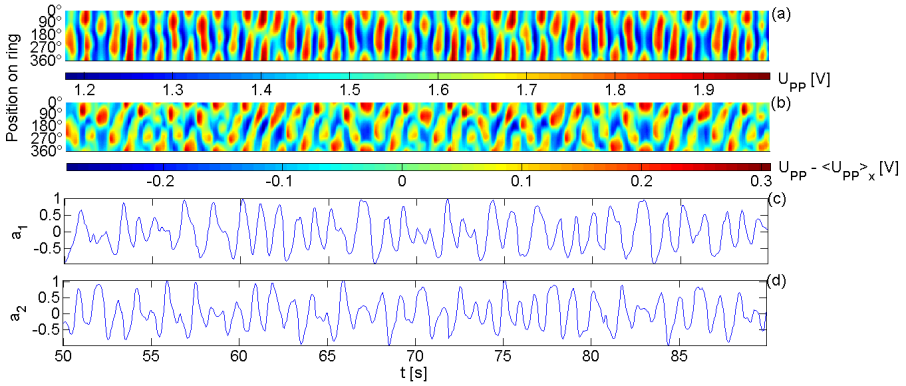

Figure 4.37: *Point III-b in figure 4.19: (a) The spatiotemporal evolution of U_{PP}, (b) the spatiotemporal evolution of $U_{PP} - < U_{PP} >_x$, (c) and (d) the coefficients of the first and second KL spatial modes of the inhomogeneous part of $U_{PP} - < U_{PP} >_x$. $U_0 = 0.40$ V. $R_c = 300\Omega$, $R_\Omega = 540\Omega$.*

The results of the Hilbert transform analysis of a_1 and a_2 also do not show any

specific structure which could provide evidence of the existence of chaos.

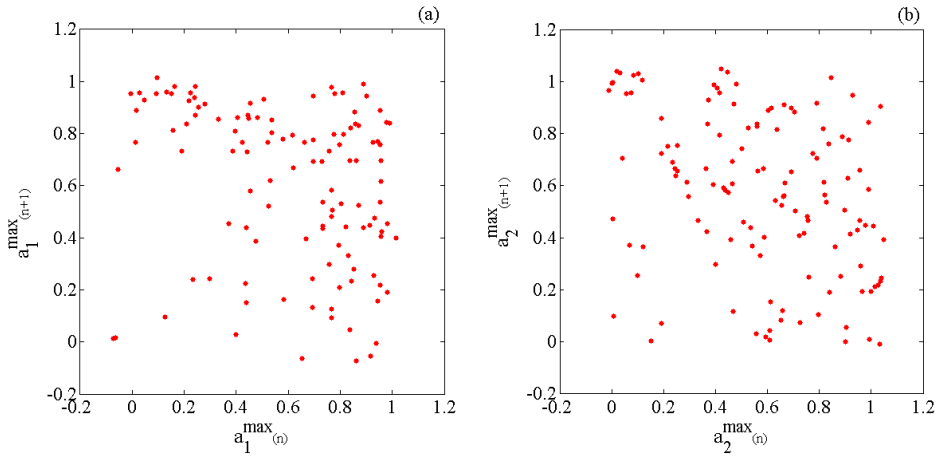

Figure 4.38: *The next-maximum maps for (a) $a_1(t)$ and (b) $a_2(t)$ shown in figure 4.37(c) and (d), respectively.*

The energy distribution between the first 8 KL spatial modes of U_{PP} shows that similar to the quasiperiodic responses, the unlocked intermittent responses of the system in this parameter region require three eigenvectors to capture the spatiotemporal dynamics phenomenologically. As it was observed for the quasiperiodic response, also here either the second or the third KL spatial mode contains an offset caused by the spatially uniform oscillations.

4.3 The 2:1 Arnold Tongue

In this section the response of the oscillatory system to a time-periodic forcing at a frequency about twice as large as the one of the unforced systems is presented. In the following, after determination of the entrainment regions for the 2:1 forcing with 20, 40 and 80 mV forcing amplitudes, the different locked dynamical responses of the system within this resonance regime will be studied. Furthermore, the behavior of the system outside the resonance region is investigated.

4.3.1 Determination of the entrained region

The determination of the resonance region was carried out similarly to the procedure described for the 1:1 tongue. Also here, at each forcing amplitude the results of the KL decomposition of the inhomogeneous part of U_{PP} together with the response of the spatially uniform mode are used to distinguish between locked and unlocked responses. However, to obtain the correct phase relation for the 2:1 external forcing, the phase is calculated for $f_f/2$, i.e. the phase difference is given by $\frac{2\pi}{2T_f}(\Delta t)$, where Δt is the time difference between every second maximum of the forcing signal and a local maximum of the coefficients of the spatial modes. A phase advancement of 2π of the forcing is defined to occur in $2T_f$ and thus, the phase at half of the forcing frequency is compared to that of the KL mode coefficients. When the spatial modes oscillate with the forcing frequency, as it was found for the uniform mode, the phase differences are calculated as explained for the 1:1 tongue.

Figure 4.39 shows all the parameter values at which measurements were carried out. Like in the experiments of the 1:1 resonance regime, the forcing has been applied with three forcing amplitudes.

A) Forcing amplitude 20 mV

Figure 4.40, 4.41 and 4.42 depict the advances of the phase difference between the spatially uniform mode, the first and the second coefficients of the KL spatial mode of $U_{PP} - < U_{PP} >_x$, and the sinusoidal forcing signal, respectively, for a forcing amplitude of 20 mV.

For all the measurement points the phase shifts between the spatially uniform mode and the sinusoidal forcing signal stay constant. This can be seen in figure 4.40 where $\Delta\Phi_0$ is depicted for several measurement points. Thus, the forcing entrains the uniform mode of the system independent of the forcing frequency. The time

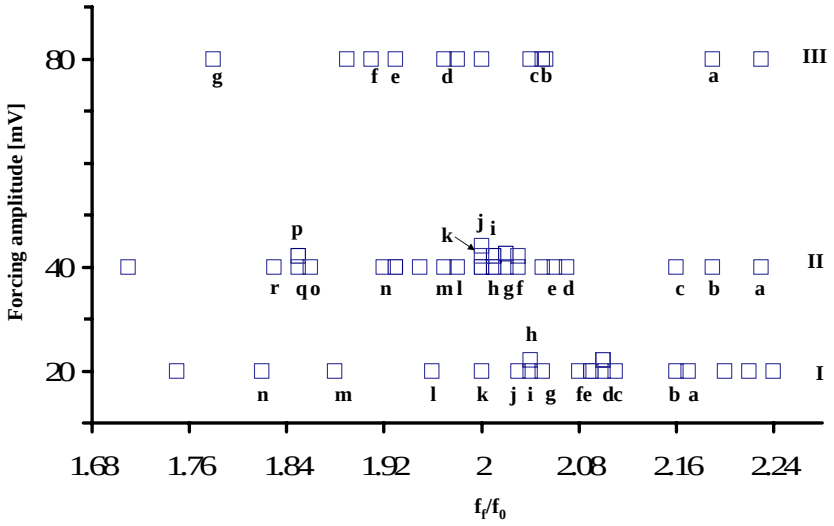

Figure 4.39: *The experimentally measured points plotted in the amplitude - frequency parameter plane.*

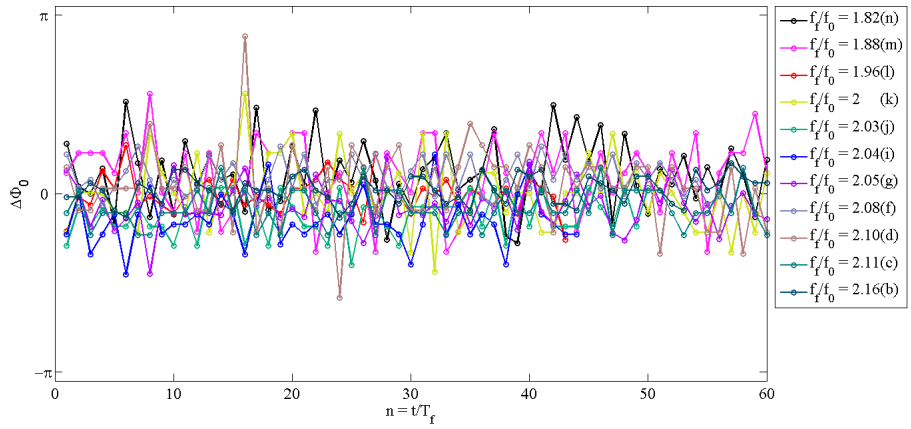

Figure 4.40: *20 mV forcing amplitude: Advances of the phase difference of the spatially uniform mode to the forcing signal for measurement points marked on figure 4.39.*

series of the spatially uniform mode show that this mode oscillates with the forcing frequency, hence the phase relations of this spatial mode to the forcing signal were calculated identically to the 1:1 resonance regime.

The response of the spatially uniform mode to the forcing signal with 20 mV am-

plitude distinguishes the behavior of the system at this forcing parameters from the responses around the 1:1 resonance where the forcing was not strong enough to entrain the spatially homogeneous mode.

From figures 4.41 and 4.42 it is clear that the response of the first and second KL spatial modes of $U_{PP} - < U_{PP} >_x$, depends on the forcing frequency. The coefficient a_1 is locked to the forcing at points I-h, I-i, I-g, I-f, I-e, I-c and I-a and the rest of the measured points are unlocked. Figure 4.41 depicts the evolution of $\Delta\Phi_1$ with time for some of the measurement points. For the advances of $\Delta\Phi_2$ one finds that at point I-h, I-i, I-g and I-a the phase difference between a_2 and the forcing signal is not constant and thus, the second KL spatial mode of these measurements are not entrained by the forcing signal. This can be observed in figure 4.42 for measurement points I-i and I-g. This phenomenon of *half entrainment* results in the appearance of modulated standing anti-phase oscillations and will be discussed later in this section in detail.

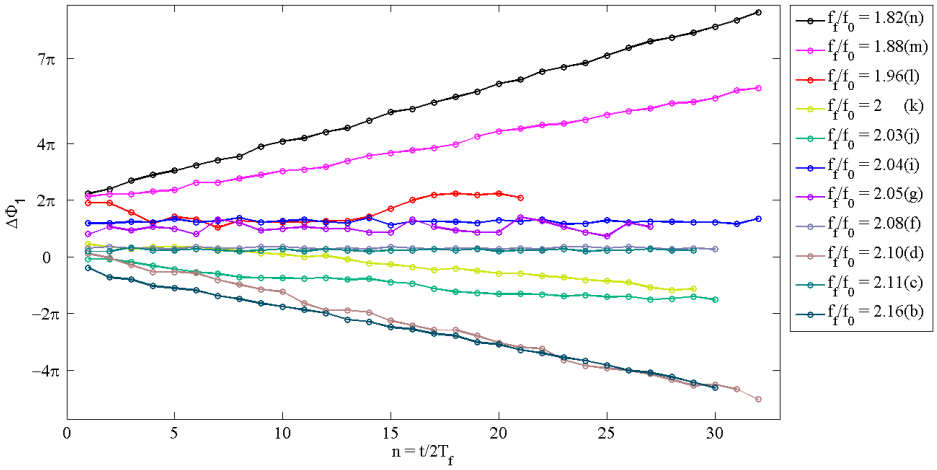

Figure 4.41: *20 mV forcing amplitude: Evolution of the phase difference between the forcing signal and the coefficient of the first KL spatial mode with time for measurement points that are marked on figure 4.39.*

There are two points which deserve special attention. According to the results of the KL decomposition for point I-c, which will be presented below, the first KL spatial mode of $U_{PP} - < U_{PP} >_x$ is sufficient to describe the behavior of the system at this point hence, $\Delta\Phi_2$ of this point is not depicted in figure 4.42. At point I-l we observe in figure 4.41 that $\Delta\Phi_1$ is nearly constant during the time interval 4x2T_f and 12x2T_f. Figure 4.42 shows that in the same period of time, $\Delta\Phi_2$ exhibits a pronounced drift, but subsequently remains nearly constant. Hence, we see that at this point there is an exchange in the entrainment of the KL coefficients. This

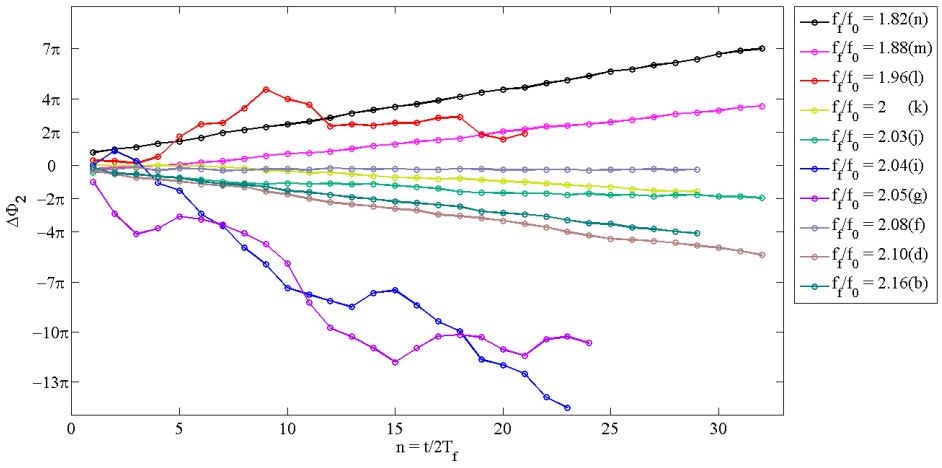

Figure 4.42: *20 mV forcing amplitude: Evolution of $\Delta\Phi_2$ with time for different measurement points in figure 4.39.*

phenomenon which is caused by intermittency in the system will also be explained in detail below.

These results show that when forcing the system with low forcing amplitude, the entrainment region is very narrow. Moreover, unlocked responses were observed in between the entrained responses.

B) Forcing amplitude 40 mV

Similar to the responses at 20 mV forcing, when applying a sinusoidal perturbation with an amplitude of 40 mV the spatially uniform mode oscillates with the forcing frequency and thus, is entrained by the external perturbation at all measurement points. The phase shift of the time series to the sinusoidal signal is always close to zero, as in the case of 20 mV forcing amplitude (see figure 4.40). Hence, this spatial mode oscillates in-phase with the forcing in the entire detuning range considered in this section.

For several of the experimentally measured points the phase differences of a_1 and a_2 to the sinusoidal external modulation are displayed in figures 4.43 and 4.44, respectively. At points II-q, II-g and II-e the constant phase difference between forcing signal and a_1 suggests that the system is entrained by the external perturbation. Measurement points II-q and II-e correspond to a standing pattern which is described only by the first KL spatial mode, thus due to the low contribution of a_2, the corresponding $\Delta\Phi_2$ are not depicted in figure 4.44. At measurement points where the system fails to lock to the external modulation, a continuous phase drift

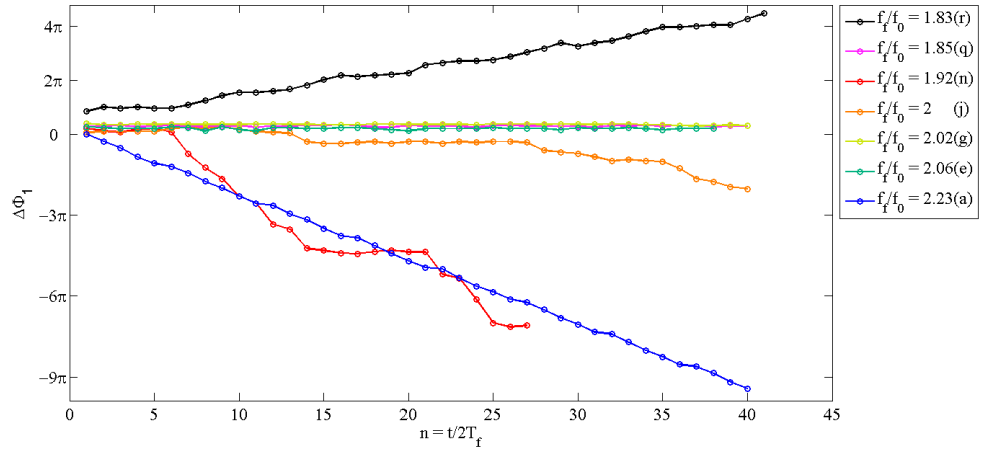

Figure 4.43: *40 mV forcing amplitude: Advances of the phase difference of the spatially uniform mode to the forcing signal with time for measurement points marked in figure 4.39.*

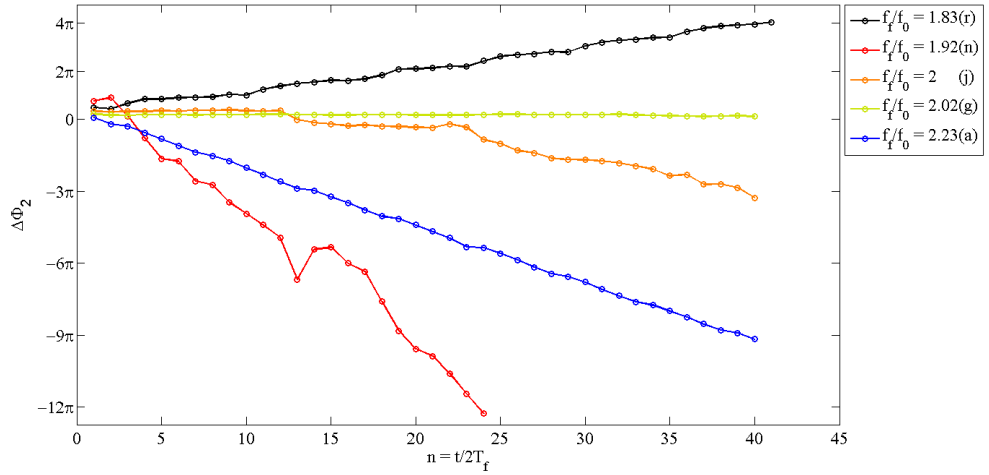

Figure 4.44: *40 mV forcing amplitude: Growth of $\Delta\Phi_2$ with time for different measurement points in figure 4.39.*

is observed and the system exhibits no phase slips.

C) Forcing amplitude 80 mV

When forcing the system with 80 mV amplitude, the spatially uniform mode is entrained by the forcing throughout the entire measured frequency range and thus, the uniform mode oscillates again in-phase with the forcing signal. The advances of $\Delta\Phi_1$ and $\Delta\Phi_2$ are depicted in figures 4.45 and 4.46, respectively, for representative values of the forcing frequency. The figures show that at all measurement points the advances of $\Delta\Phi_1$ and $\Delta\Phi_2$ are unbounded, indicating that all the experimentally

measured points are located outside the resonance region. Moreover, in the entire frequency interval between $f_f/f_0 = 1.76$ and 2.24, $\Delta\Phi_1$ and $\Delta\Phi_2$ grow only in negative direction, independent of the sign of the detuning. This is in contrast to the expected phase advancement for positive detuning. An analysis of the time series of the KL mode coefficients, $a_1(t)$ and $a_2(t)$, by fast Fourier transform (FFT), (see figure 4.47) reveals that the main oscillation frequency present in the time series are indeed lower than $f_f/2$ which is in line with the determined negative slope $\frac{d(\Delta\Phi_1)}{dn}$ and $\frac{d(\Delta\Phi_2)}{dn}$.

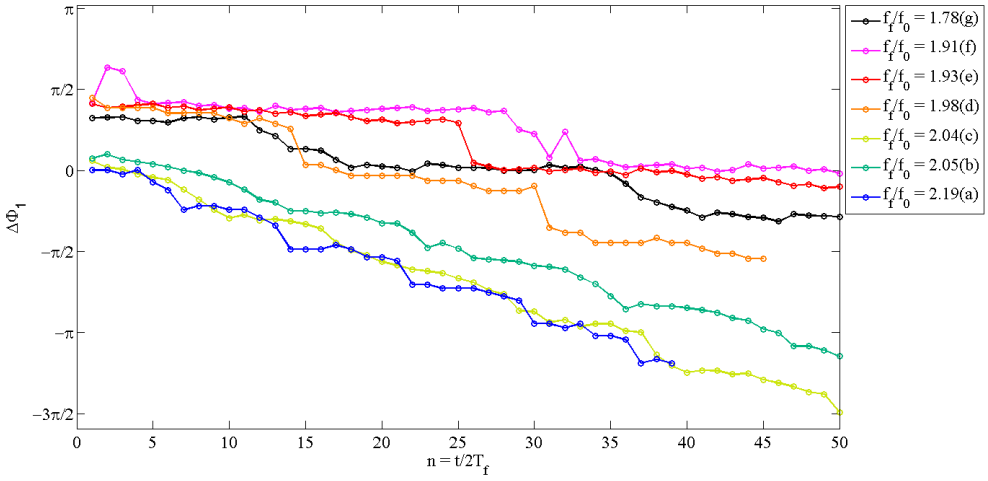

Figure 4.45: *80 mV forcing amplitude: The advances of $\Delta\Phi_1$ with time for different measured points marked at figure 4.39.*

In contrast to the behavior at a moderate forcing strength of 40 mV, where only continuous phase drifts were observed, at 80 mV forcing amplitude $\Delta\Phi_1$ and $\Delta\Phi_2$ make phase slips of about $\pi/3$ between quasi-locked regions at certain ranges of forcing frequency. Plotting $\Delta\Phi_2(n)$ on the unit circle (see figure 4.48) provides a clear picture of the phase slips of the system and also the phase drifts.

Figures 4.45 and 4.46 show that at positive detuning ($f_f/f_0 < 2$) the system is in a quasi-locked state for a long time, but once in a while undergoes fast phase slips by about 60 °. This is shown for $\Delta\Phi_2$ at three parameter values in figure 4.48 (upper row). The advances of $\Delta\Phi_1$ and $\Delta\Phi_2$ in the positive detuning region are continuous and exhibit non-uniformities but no clear phase slips. This can be seen clearly in figure 4.48 where the advancement of $\Delta\Phi_2$ exhibit uniform modulations which results in scattered phase differences on the unit circle (figure 4.48 (lower row)).

From the three accumulation centers in the upper plate of figure 4.48 it can be seen

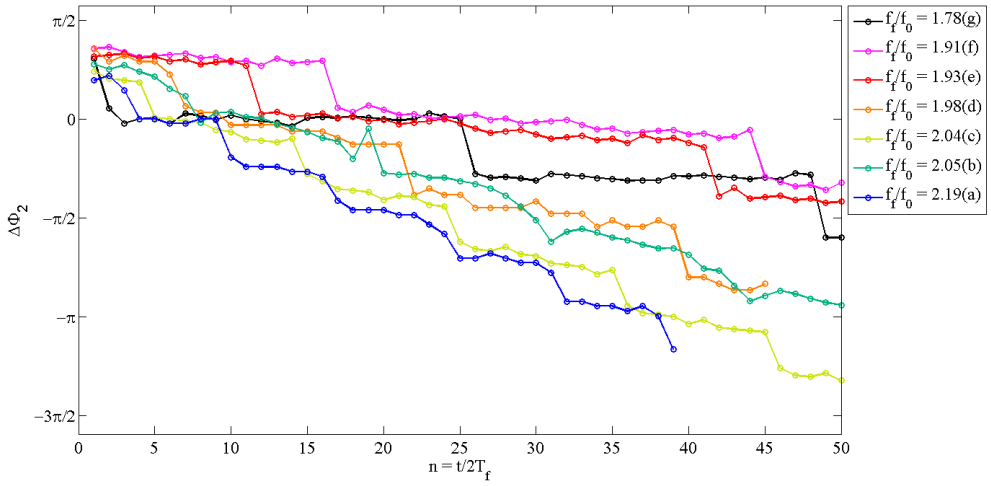

Figure 4.46: *80 mV forcing amplitude: Evolution of the phase difference between the forcing signal and the time series of a_2 with time for different measured points marked in figure 4.39.*

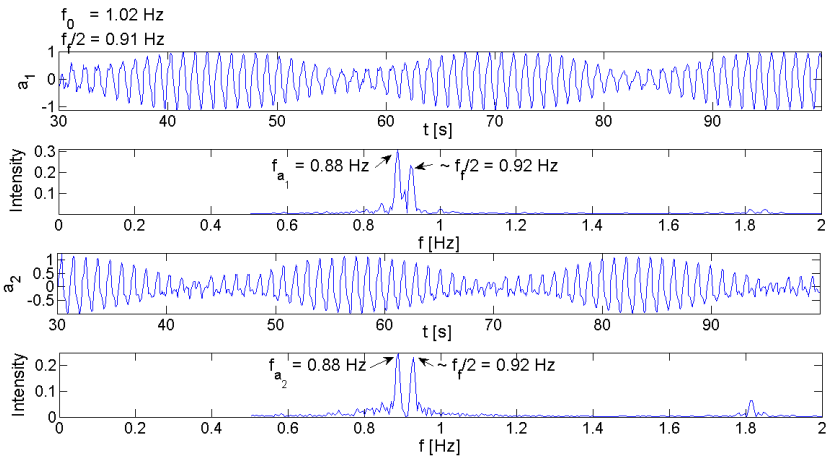

Figure 4.47: *Point III-g in figure 4.39: First and third plate: time series of the first two KL mode coefficients, respectively, second and fourth plate: frequency power spectra corresponding to a_1 and a_2, respectively.*

that when the system is forced with positive detuning, at 80 mV forcing amplitude, it possesses three quasi-stationary fixed points between 0 and π. Together with their counter parts, these three quasi-stationary fixed points result in the presence of 6 quasi-stationary fixed points in the second iterate on the Poincaré map. Each accumulation center represents a point on the invariant circle where a saddle-node bifurcation would be expected and hence, is the *ghost* of a saddle-node bifurcation of a period-6 orbit.

Figure 4.49 gives an overview, where synchronous and asynchronous behavior is

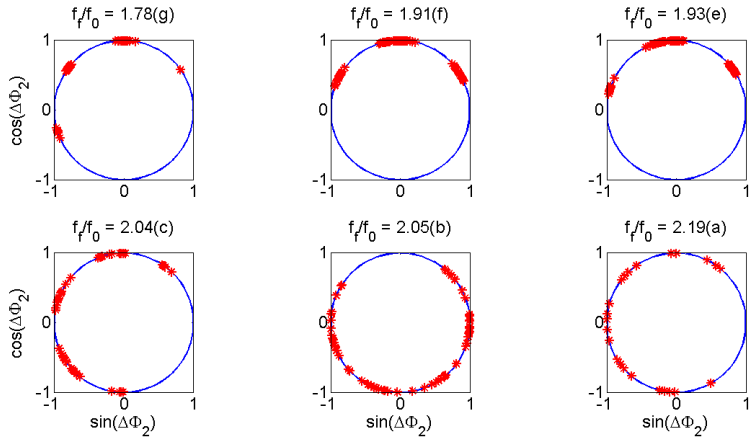

Figure 4.48: $\Delta\Phi_2$ *of several of the measurement points shown in figure 4.45 plotted on the unit circle.*

found in the forcing amplitude - forcing frequency parameter plane. The locked responses are marked with filled circles and the unlocked responses are shown with filled diamonds. The measurement points marked with filled triangles designate the parameter regions where the system exhibits transient or intermittent behavior which will be explained later in this section.

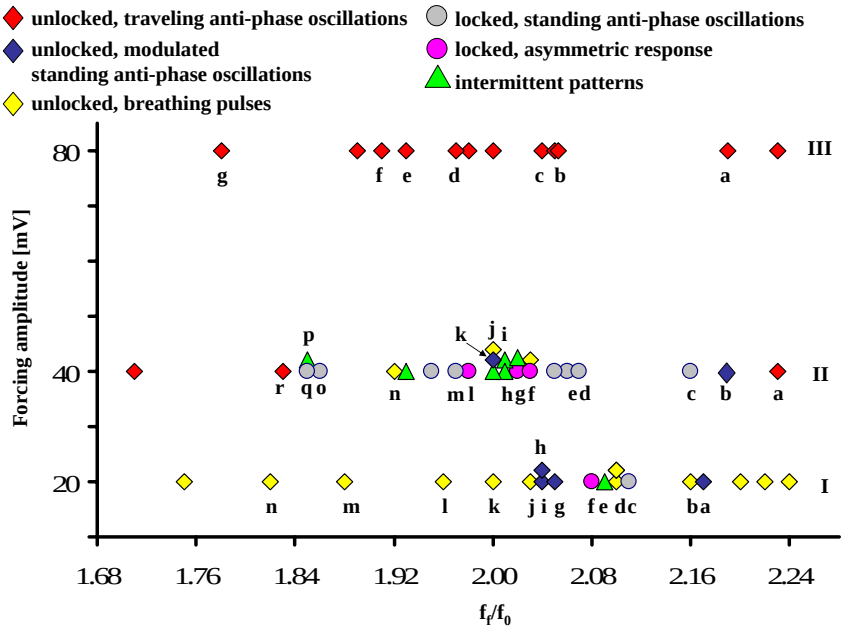

Figure 4.49: *2:1 resonant tongue depicted in the forcing frequency to natural frequency - amplitude parameter plane.*

4.3.2 Entrained behavior

In this section the qualitatively different entrained patterns observed in the 2:1 tongue are discussed in detail.

(A) Standing anti-phase oscillations

The measurement points which exhibit standing anti-phase oscillations are marked with filled gray circles in figure 4.49. This synchronous response is the most common type of entrained behavior at 40 mV and it also appears at one measurement point at 20 mV forcing strength. Figure 4.50 depicts the dominant KL modes together with the energy distribution for the full data (4.50(a)) and the inhomogeneous part of it (4.50(b)). The results of the KL decomposition at these points reveal that the standing spatiotemporal pattern of U_{PP} is dominated by one sinusoidal spatial structure and the spatially uniform mode. Figure 4.50(a) and (c) confirm that the third spatial mode which is the 90° space-shifted version of the first spatial mode, hardly contributes to the energy of this data set.

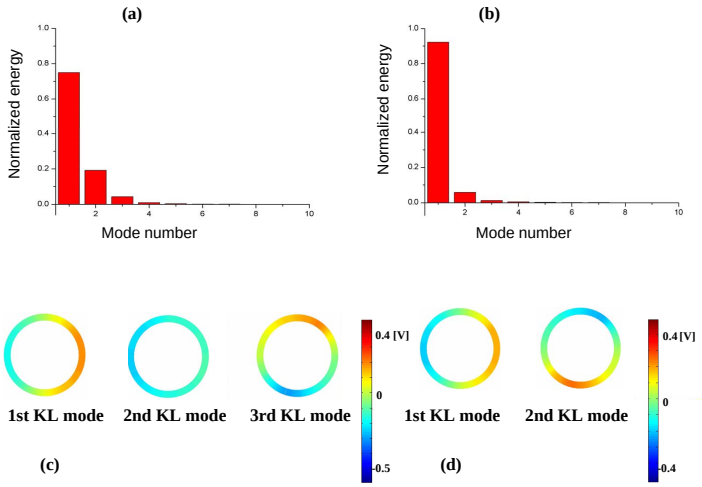

Figure 4.50: *Point II-q in figure 4.49: (a) and (b) Distribution of the normalized energy of the KL spatial modes of U_{PP} and $U_{PP}- < U_{PP} >_x$, respectively, (c) and (d) the KL spatial modes corresponding to (a) and (b), respectively.*

The energy distribution of the KL modes of $U_{PP}- < U_{PP} >_x$ confirms that one of the spatial modes of the pulse pair contains nearly all the energy and the second one is suppressed.

Figure 4.51(a) shows the standing anti-phase oscillations formed by the space-time

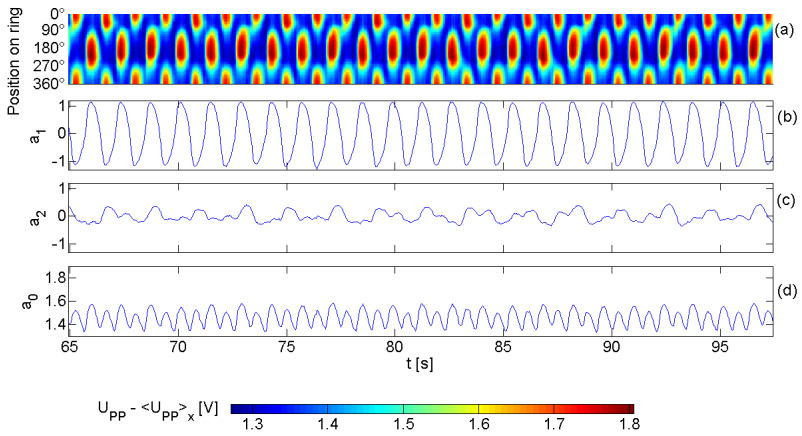

Figure 4.51: *Point II-c in figure 4.49: (a) $U_{PP}- < U_{PP} >_x$ as a function of ring position and time, (b) and (c) time series of the coefficients of the first and second KL spatial mode of $U_{PP}- < U_{PP} >_x$, (d) time series of the spatially uniform mode. $U_0 = 0.32$ V. $R_\Omega = 550\Omega$, $R_c = 350\Omega$.*

evolution of the inhomogeneous part of the interfacial potential. The time dependent coefficients of the KL spatial modes, (see figure 4.50(d)) are depicted in figure 4.51(b) and (c). The difference between the amplitudes of the oscillations of $a_1(t)$ and $a_2(t)$ confirms that the second spatial mode of the traveling wave pair has a very low contribution to the pattern.

(B) Asymmetric entrainment

At measurement points marked with filled pink circles in figure 4.49, the driven system is locked to the forcing but the response of the traveling wave spatial modes to the external perturbation is asymmetric. This type of synchronous response is similar to the asymmetric entrainment that occurs in the 1:1 resonance region. At these forcing parameters, the externally applied forcing breaks the symmetry between the two spatial modes of the traveling wave and results in spatiotemporal patterns, which deviate from the pulse behavior. However, in contrast to the behavior found in the 1:1 Arnold tongue, here an asymmetrically locked response occurs also at 20 mV forcing amplitude whereas in the 1:1 resonance regime entrained pulses were the only locked response that appeared.

A typical example of an asymmetrically entrained response is depicted in figure 4.52(c) and (d). The space-time evolution of $U_{PP}- < U_{PP} >_x$ (4.52(d)) exhibits a traveling structure with strong modulations in width and height during one circulation around the ring. The spatial profile of the KL modes of $U_{PP}- < U_{PP} >_x$ (figure 4.52(b)) and the distribution of the energy between them (figure 4.52(a)) give some

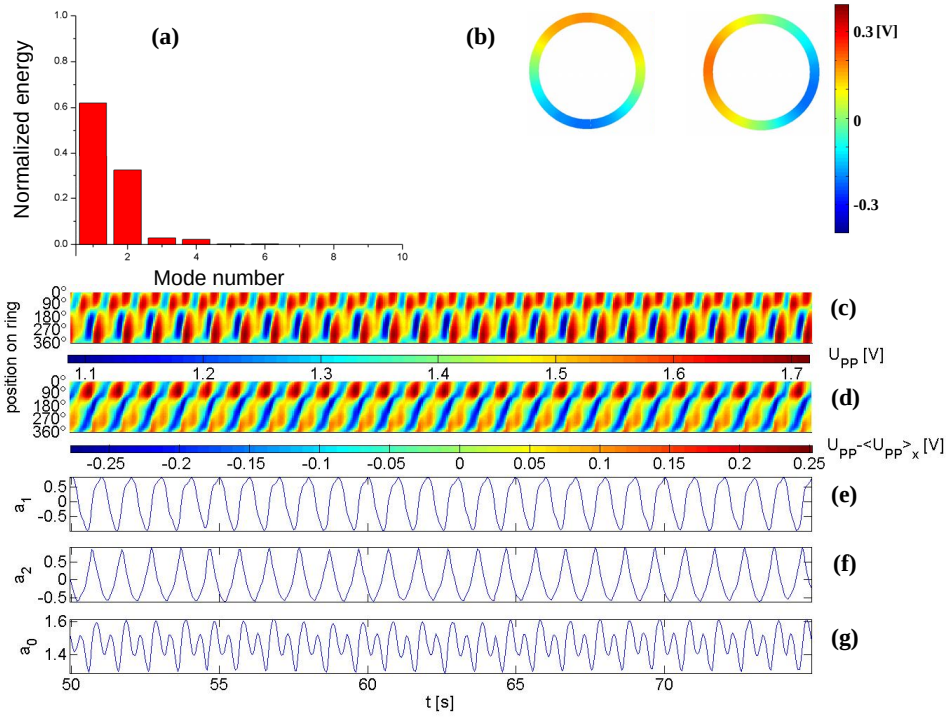

Figure 4.52: *Point II-l in figure 4.49: (a) The energy distribution of the KL spatial modes of* $U_{PP} - < U_{PP} >_x$*, (b) the first two KL spatial modes of* $U_{PP} - < U_{PP} >_x$*, (c)* $U_{PP}(x,t)$*, (d)* $U_{PP} - < U_{PP} >_x (x,t)$*, (e) and (f) time series of the coefficients of the spatial modes shown in (b), (g) time series of the spatially uniform mode.* $U_0 = 0.35$ *V.* $R_\Omega = 540\Omega$*,* $R_c = 300\Omega$*.*

insight into this dynamics. Although the pattern is constructed by a sin(x) and its 90 ° space-shifted profile, the contribution of the modes to the total energy differs considerably. Furthermore, the oscillations of the coefficients of the spatial modes shown in figure 4.52(e) and (f) deviate from sinusoidal behavior. This is more pronounced in the oscillations of the second coefficient, a_2. One can also see that the time series of a_1 and a_2 are not $\pi/2$ phase-shifted. It is clear that both entrained coefficients oscillate with $1/2f_f$, while the spatially uniform mode exhibits period-2 oscillations with the dominant frequencies of f_f and $1/2f_f$ (figure 4.52(g)).

The asymmetric spatiotemporal responses that form in the 2:1 resonance tongue are similar to those observed for the symmetric and asymmetric entrained responses in the 1:1 tongue. Also here, the system exhibits pulses with the so-called breaking point or a narrowing line. Examples of these type of patterns can be observed in figures 4.52(c), 4.53(a). One can see this resemblance by comparing the latter figures with figures 4.22(a) and 4.24(c). However, since the homogeneous mode exhibits

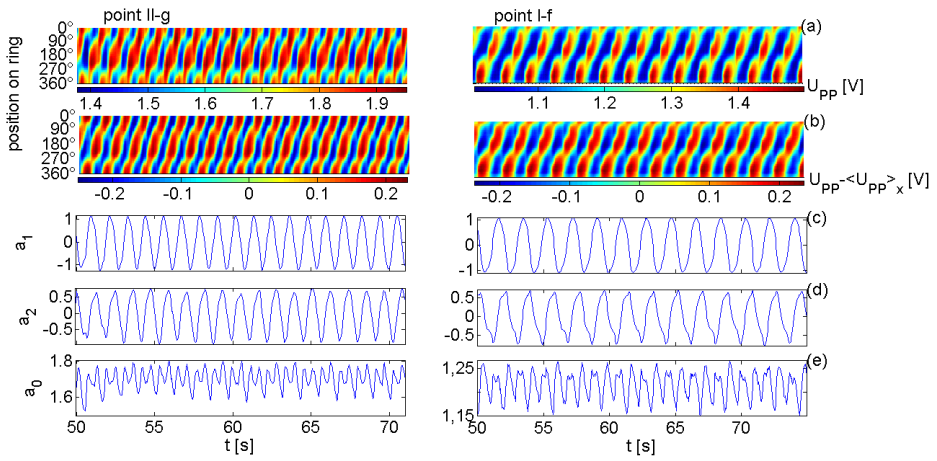

Figure 4.53: *Point II-g and I-f in figure 4.49: (a) U_{PP}(x,t), (b) $U_{PP}- < U_{PP} >_x$ as a function of ring position and time, (c) and (d) time series of the first and the second KL spatial mode, respectively, (e) time series of the spatially uniform mode. $U_0 = 0.21$ V (point I-f) and 0.32 V (point II-g). $R_\Omega = 530\Omega$, $R_c = 350\Omega$.*

period-2 oscillations within the 2:1 resonance tongue, the linear superposition of this spatial mode with the pulse modes gives rise to the formation of two breaking points or narrowing lines.

4.3.3 Half entrained responses

At measurement points marked by dark blue symbols in figure 4.49 the response is *half entrained*, i.e., only one of the two time series of a_1 and a_2 locks to the forcing signal. Phenomenologically the spatiotemporal behavior can be described as irregularly *modulated standing anti-phase oscillations*.

Figure 4.54 shows a typical example, depicting the spatiotemporal evolution of $U_{PP}- < U_{PP} >_x$ (4.54(b)), the time series of the coefficients of the first and second KL spatial modes (4.54(c) and (e)) and the spatially uniform mode (4.54(g)) together with their corresponding phase shifts to the forcing signal (4.54(d), (f) and (h)).

In figure 4.54(b), no particular structure can be distinguished in the spatiotemporal evolution of $U_{PP}- < U_{PP} >_x$. The irregular patterns that form are neither similar to the standing structures observed in the previous section, nor do they resemble the traveling spatiotemporal structures that form outside the entrainment band (for an example of the latter see figure 4.58(a)).

The energy distributions between the first and the second KL modes of $U_{PP} - < U_{PP} >_x$ sheds light on the origin of this phenomenon. Figure 4.54(a) shows that the first spatial mode contains nearly 70% and the second KL mode less than 30% of the information. Here, the second spatial mode acts as an unlocked modulation superimposed on the entrained first KL mode and prevents the system from forming a standing anti-phase pattern as observed in figure 4.51 at point II-c ($f_f/f_0 = 2.16$). The resulting phenomenon is best termed as irregularly modulated standing anti-phase oscillation.

The time series of the first KL coefficient and of the spatially uniform mode, a_0, oscillate with $f_f/2$ and f_f, respectively. Hence, the changes of their phase difference to the external sinusoidal signal are minor and bounded, indicating that these two modes are entrained by the external modulation. However, the unbounded advances of $\Delta\Phi_2$ shows that the forcing fails to entrain to the forcing. Figures 4.54(d), (f) and (g) depict the phase relations of a_1, a_2 and a_0 to the forcing frequency.

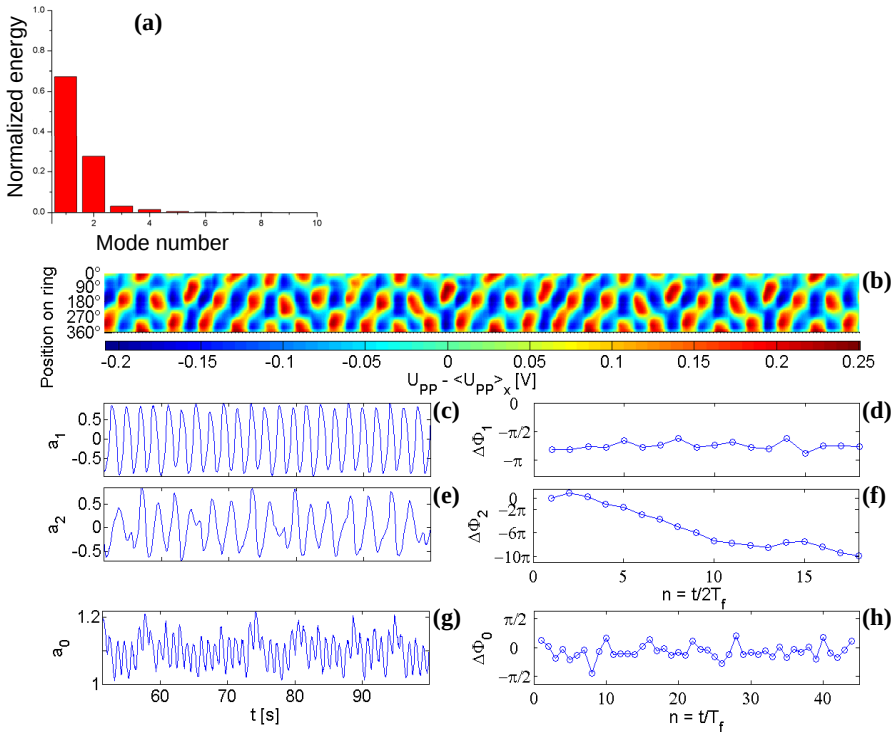

Figure 4.54: *Point I-i in figure 4.49: (a) Energy distribution between the KL spatial modes of $U_{PP} - < U_{PP} >_x$, depicted for the first 8 ones, (b) $U_{PP} - < U_{PP} >_x$ as a function of ring position and time, (c) $a_1(t)$, (e) $a_2(t)$, (g) $a_0(t)$, (d), (f) and (h) the phase difference of (c), (e) and (g) to the forcing signal respectively. $U_0 = 0.21$ V. $R_\Omega = 530\Omega$, $R_c = 350\Omega$.*

A FFT analysis of the time series of $a_2(t)$ shows that the main oscillation frequency of this spatial mode is much lower than $f_f/2$ and hence, the changes of $\Delta\Phi_2$ with time are faster than expected for the position of the corresponding measurement points in the resonance region. This can be well seen in figure 4.42 where the advances of $\Delta\Phi_2$ are shown for 2:1 forcing parameters at 20 mV amplitude.

4.3.4 Changes of phase shifts between forcing and response signal within the entrainment band

To gain more understanding of the dynamics of the driven system it is helpful to follow the behavior of $\Delta\Phi_1$ and $\Delta\Phi_2$ as the frequency is varied within the entrainment band.

Figure 4.49 shows that at constant forcing amplitude of 20 mV in the parameter region between the two entrained responses, I-c and I-f, unlocked and intermittent responses appear, hence,the borders between the synchronous and asynchronous regions are not exactly clear. However, since at measurement points II-h, II-i, II-g and II-a half entrained responses emerge, whose first KL spatial modes are entrained, the changes of $\Delta\Phi_1$ can be followed in the parameter range between points II-h at $f_f/f_0 = 2.04$ and II-a at $f_f/f_0 = 2.18$. Figure 4.55 depicts the variations of $\Delta\Phi_1$ at the latter points with time. Similar to the entrained responses within the 1:1 entrainment band, also here the π phase difference between $\Delta\Phi_1$ at points II-f ($f_f/f_0 = 2.08$) and II-c ($f_f/f_0 = 2.11$) and the other data is due to the phase invariance of the results of the KL decomposition. Hence, at 20 mV forcing amplitude the phase difference between the forcing signal and $a_1(t)$ of the entrained and half entrained responses stays approximately constant as the forcing frequency changes.

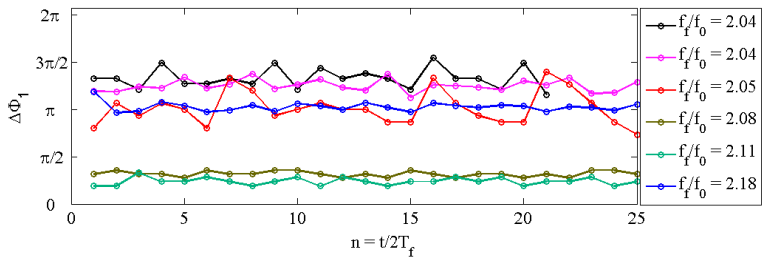

Figure 4.55: *Variations of $\Delta\Phi_1$ with increasing detuning, measured at 20 mV forcing amplitude.*

When the driven system is forced with a higher amplitude of 40 mV, a synchronization region exits between $f_f/f_0 = 1.85$ and 2.16. Figure 4.56 shows the changes of $\Delta\Phi_1$ within this synchronous region at constant forcing amplitude of 40 mV. Also here, $\Delta\Phi_1$ does not change considerably when moving from one border of the entrainment band to the other.

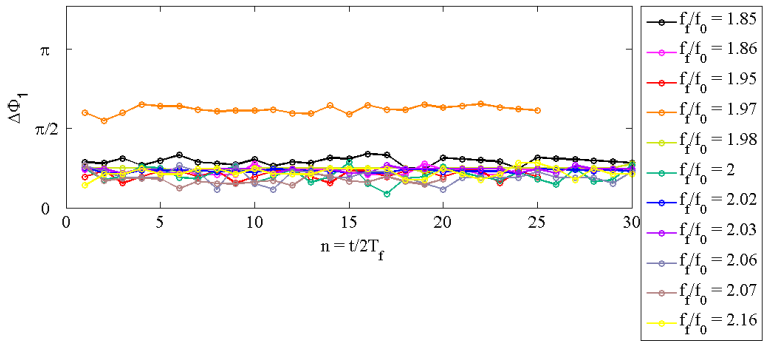

Figure 4.56: *Changes of the phase difference between the forcing signal and the time series of a_1 within the synchronization region at constant forcing amplitude of 40 mV.*

It is obvious from figure 4.49 that for a forcing strength of 80 mV no resonance region was experimentally measured.

4.3.5 Unlocked responses

The measurement points where the unlocked responses appeared are marked with diamond symbols in figure 4.49. Outside the 2:1 resonance region mainly three types of unlocked behavior appear. The half entrained modulated standing anti-phase oscillations have already been discussed, the traveling anti-phase oscillations and the breathing pulses will be presented in the following.

The KL decomposition of U_{PP} of the three types of unlocked responses show that similar to the unlocked responses to the 1:1 forcing parameters, three spatial modes have the main contribution to the spatiotemporal pattern and hence, the system has three active degrees of freedom. Figure 4.57(a) shows the energy distribution between the KL spatial modes of U_{PP} for point II-r, as a representative example. Figure 4.57(b) displays the three spatial modes which capture nearly all the energy. When the forcing strength is increased to 80 mV, the sequence of the KL spatial modes which carry most of energy is slightly different than that shown in figure 4.57(b) and the traveling wave spatial modes (which may contain an offset caused

by the spatially uniform mode) are the second and third KL modes. The spatial mode with the highest contribution is either a spatially homogeneous mode or a spatial mode with a low amplitude structure.

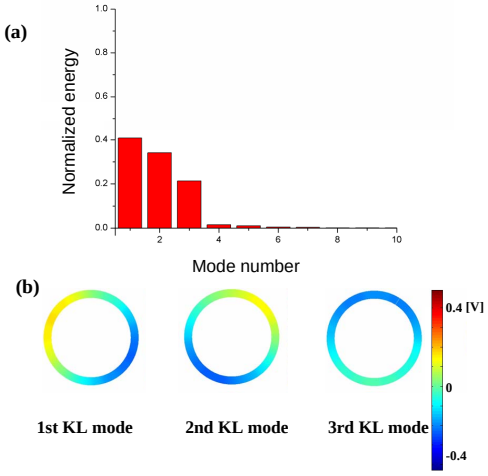

Figure 4.57: *Point II-r in figure 4.49: (a) Energy distribution between the first 8 KL spatial modes of U_{PP}, (b) the first three KL spatial modes depicted in (a).*

(A) Traveling anti-phase oscillations:

The red colored diamond symbols in figure 4.49 stand for the appearance of traveling anti-phase oscillations.

Figure 4.58(a) presents the spatiotemporal pattern of the inhomogeneous part of U_{PP} for point II-r, where traveling anti-phase oscillations occur. In figure 4.58(b) and (c) the time series of the coefficients of the first and second KL modes of the inhomogeneous part of the U_{PP} are displayed. Here it can be observed that a_1 and a_2 exhibit quasiperiodicity in their time series and that the corresponding changes of the amplitude stay within the same range for both coefficients. The oscillations of the spatially uniform mode, which are depicted in figure 4.58(d), are not quasiperiodic but oscillate with the forcing frequency.

The traveling anti-phase oscillations at 80 mV and 40 mV forcing amplitudes can be easily distinguished by looking at the spatiotemporal pattern of U_{PP} and $U_{PP} - < U_{PP} >_x$. One can see in figures 4.58(b) and (c) that whenever a_1 oscillations have the largest amplitude, a_2 oscillates with the lowest amplitude, which give rise to the appearance of cluster patterns seen in figure 4.58(a). However, at 80 mV forcing

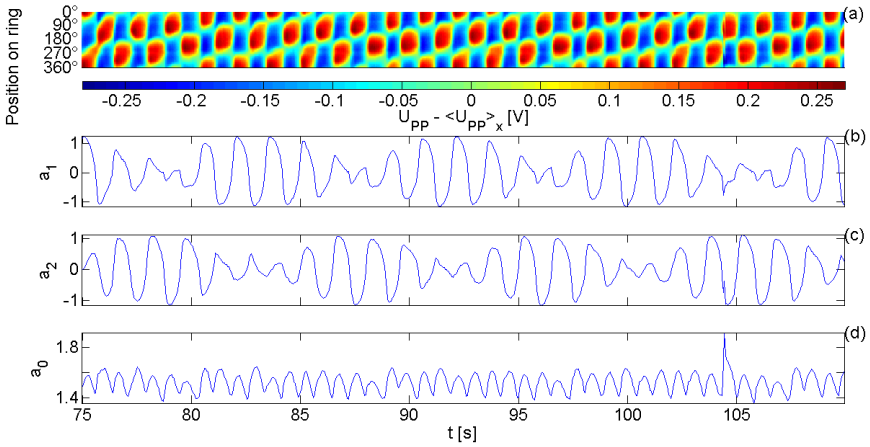

Figure 4.58: *Point II-r in figure 4.49: (a) The spatiotemporal evolution of the inhomogeneous part of the interfacial potential, (b) the time series of the coefficients of the first two KL modes of the $U_{PP}- < U_{PP} >_x$ and the spatially homogeneous mode, (c) the corresponding phase differences of the time series in (b) to the forcing signal. $U_0 = 0.32$ V. $R_\Omega = 550\Omega$, $R_c = 350\Omega$.*

strength the amplitude modulations in the times series of a_1 and a_2 (figures 4.59(b) and (c)) are less pronounced than the modulations observed in figures 4.58(b) and (c) and leading to a pattern between propagating pulses and traveling anti-phase oscillations. Moreover, due to the higher strength of the forcing amplitude when applying the forcing with 80 mV, f_f appears with a higher intensity in the power spectrum of a_1 and a_2 of the traveling anti-phase oscillations. This can be easily seen in the time series of a_1 and a_2 in figures 4.59(b) and (c) where due to the presence of f_f with high intensity small structures appear on the low amplitude oscillation peaks.

The beat frequency present in the quasiperiodic oscillations that appear at 40 and 80 mV applied forcing amplitudes is equal to $2f_r$-f_f, which is similar to the responses to the 1:1 tongue, when considering the 2:1 relation of f_f and f_0 in these forcing parameter range.

(B) Breathing pulses:

The filled yellow diamond symbols in figure 4.49 represent the third type of unlocked response that appears when applying a 2:1 external forcing. The spatiotemporal patterns observed at these measurement points are structures which exhibit repeated width narrowing followed by a thickening during one rotation on the ring-electrode and are therefore called *breathing pulses*.

Analyzing the KL decomposition of the system after subtraction of the spatial aver-

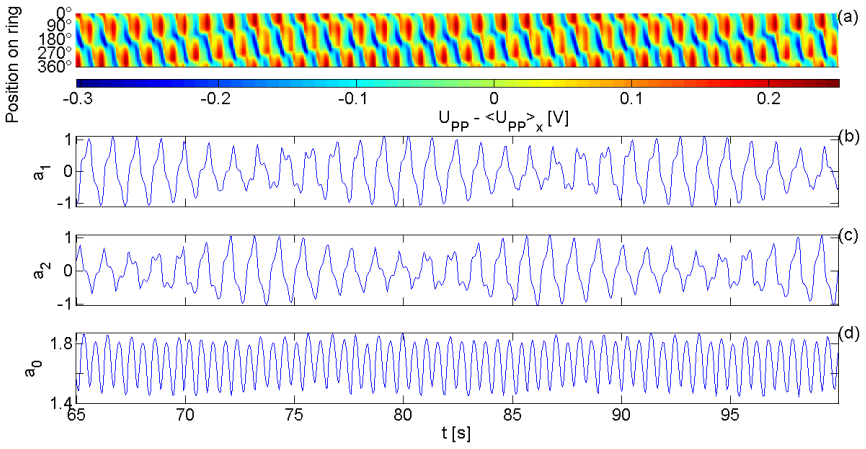

Figure 4.59: *Point III-b in figure 4.49: (a) ($U_{PP}- < U_{PP} >_x$)(x,t), (b) and (c) the time series of the coefficients of the first two KL modes of the $U_{PP}- < U_{PP} >_x$,(d) time series of the spatially homogeneous mode. $U_0 = 0.35$ V. $R_\Omega = 550\Omega$, $R_c = 350\Omega$.*

age from the interfacial potential shows that the inhomogeneous part of the system consists of two spatial modes, a sine shaped profile and the 90 ° space-shifted version of it whose contributions to the total energy differ considerably. The energy distribution between the KL spatial modes of the inhomogeneous part of U_{PP} show that at point II-j the first KL spatial mode of $U_{PP}- < U_{PP} >_x$ carries about 58% of the normalized energy whereas the second spatial mode contains about 32% of it. At measurement points with 20 mV forcing amplitude the difference is lower but still clearly distinguishable.

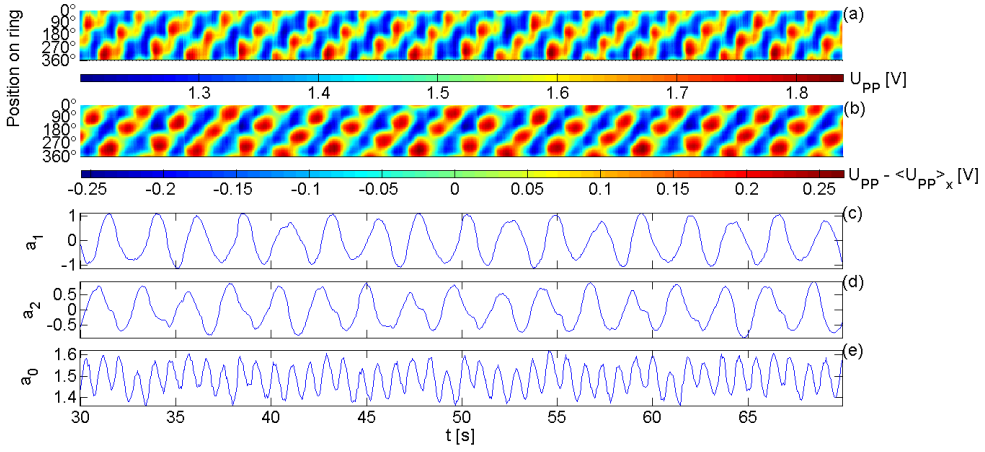

Figure 4.60: *Point II-j in figure 4.49: (a) U_{PP}(x,t), (b) ($U_{PP}- < U_{PP} >_x$)(x,t), (c) and (d) the time series of the coefficients of the first two KL modes of the $U_{PP}- < U_{PP} >_x$,(e) time series of the spatially homogeneous mode. $U_0 = 0.29$ V. $R_\Omega = 530\Omega$, $R_c = 350\Omega$.*

Figure 4.60(c) and (d) depict the time series of a_1 and a_2 at point II-j. One can see that contrary to the traveling anti-phase oscillations, the oscillation amplitude exhibits only slight modulations. Therefore, instead of the cluster patterns of figure 4.58(a) and 4.59(a), traveling structures appear with a strongly modulated width.

Moreover, the coefficient of the second KL spatial mode oscillates with a slightly lower frequency than the coefficient of the first mode, as a result the phase difference between the forcing signal and a_2 grows faster than $\Delta\Phi_1$, which can be seen in figures 4.43 and 4.44 for points II-n and II-j. Therefore, the phase difference between $\Delta\Phi_2$ and $\Delta\Phi_1$ drifts continuously or make phase slips of several periods and increases with time. However, $\Delta\Phi_2$-$\Delta\Phi_1$ corresponding to traveling anti-phase oscillations oscillates periodically, with bounded amplitudes not larger than $\pi/2$. This can be observed in figure 4.61 where the phase relation between a_1 and a_2 are shown for traveling anti-phase oscillations (points II-a and II-r) and breathing pulses (point II-j and II-n).

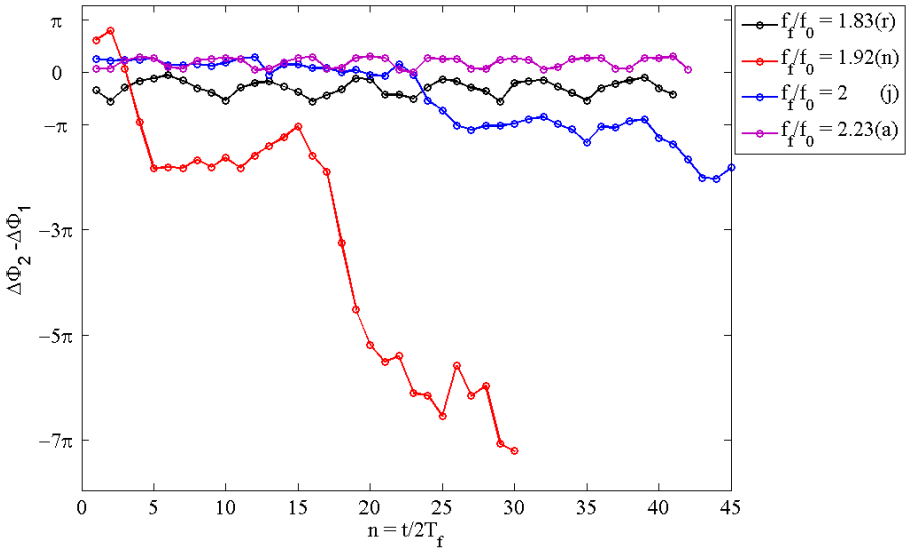

Figure 4.61: *The phase shift between the time series of the coefficients of the second and the first KL spatial mode of* $U_{PP} - < U_{PP} >_x$.

4.3.6 Intermittent responses

The parameter values at which intermittent responses occur are marked with green triangles in figure 4.49. From this figure it is evident that within the forcing parameters of this tongue, the intermittent patterns appear only at low and moderate forcing amplitudes whereas in the 1:1 resonance regime the intermittent dynamics

due to the forcing appeared exclusively for a forcing amplitude of 80 mV.

When looking at the spatiotemporal pattern of the interfacial potential at each marked point, it can be seen that the time scales of the change between the intermittent patterns differ from one measurement point to the other. Figure 4.62(a) shows the space-time evolution of $U_{PP} - < U_{PP} >_x$ at point II-p. This response is a good example of intermittent responses where a certain pattern, here traveling structures with width modulation, is repeatedly interrupted by another pattern for a short time. The coefficients of the first and second KL spatial modes of $U_{PP} - < U_{PP} >_x$, which are shown in figure 4.62(b) and (d) for point II-p, reflect this interruption well. As it can be seen in both figures, during the quasi-stationary intervals both coefficients a_1 and a_2 oscillate periodically in time, which gives rise to the appearance of the traveling pattern. However, after several periods of oscillations, the second coefficient misses one oscillation period which causes the appearance of the short bursts that interrupt the traveling pulses. The missing oscillation appears as phase slips of about π (measured with the second iterate, $2T_f$) in the plot of $\Delta\Phi_2$ in figure 4.62(e).

Studying the time series of the coefficients of the first and second KL spatial modes of similar intermittent responses shows that whenever few periods of irregular oscillations appear as repeated bursts between regular oscillations where the system is at a quasi-stationary state, the occurrence of the interruptions in the pattern are due to the changes in oscillation period or strong variations in the amplitude of $a_2(t)$. The time series of the first KL spatial mode and the spatially homogeneous mode exhibit moderate or strong amplitude modulations, but no changes in the periods of their oscillations.

In the intermittent responses discussed above, the occurrence of a base pattern is interrupted by comparatively short bursts. At measurement points II-h and II-i (both at $f_f/f_0 = 2.01$), however, the dynamical system changes back and forth between an entrained response that is stable over many periods of oscillations and an asynchronous pattern that also appears for a long time. This repeated exchange between the locked and unlocked states suggests that the presence of a heteroclinic loop between the latter states. Figure 4.63(a) presents the space-time evolution of $U_{PP} - < U_{PP} >_x$ for point II-h, where the change from locked behavior to unlocked at about 95 seconds can be easily seen. Figure 4.63(c) and (d) display that after about 95 seconds the periodic oscillations of a_1 and a_2 change to quasiperiodic ones. The spatially uniform mode possesses period-2 oscillations as the system is locked to the forcing which are replaced by strong amplitude modulations as the system enters the asynchronous state.

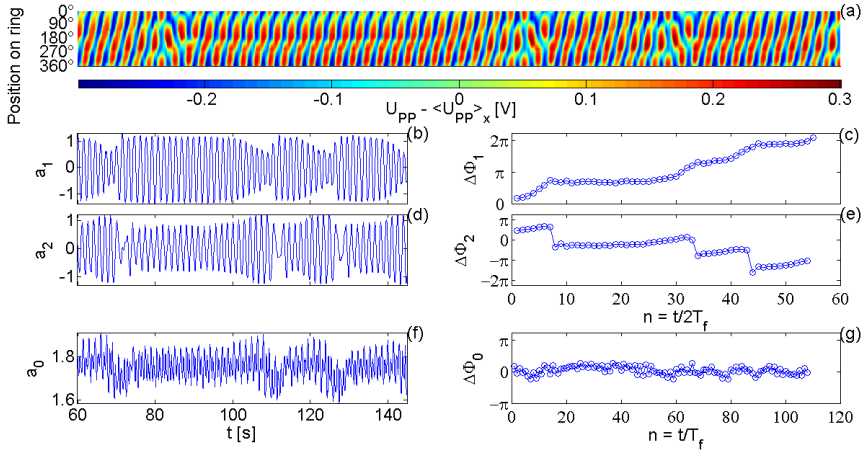

Figure 4.62: *Point II-p in figure 4.49: (a) Spatiotemporal evolution of* $U_{PP} - < U_{PP} >_x$*, (b) the coefficients of the 1st and 2nd KL mode of* $U_{PP} - < U_{PP} >_x$ *and the oscillations of the spatially homogeneous mode, (c) the phase differences* a_1*,* a_2 *and* a_0 *to the forcing signal.* $U_0 = 0.32$ *V.* $R_\Omega = 550\Omega$*,* $R_c = 350\Omega$*.*

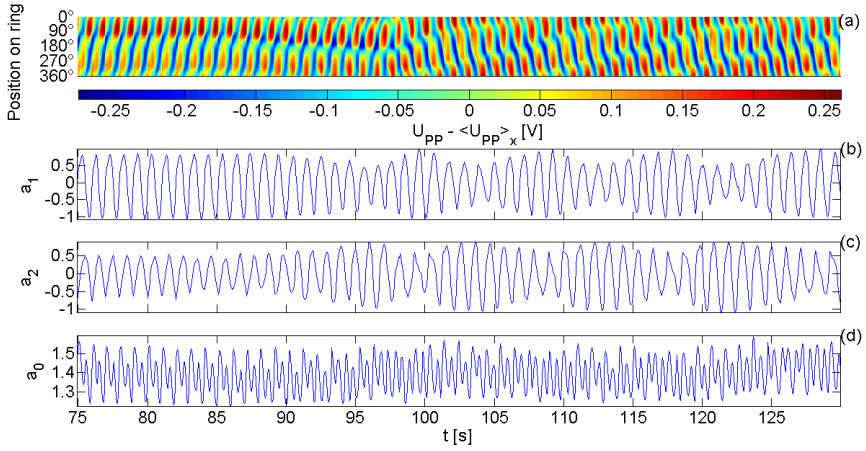

Figure 4.63: *Point II-h in figure 4.49: (a) Spatiotemporal evolution of the inhomogeneous part of the interfacial potential,* $U_{PP} - < U_{PP} >_x$*, (b) and (c) oscillations of the first and second KL mode coefficients with time, (d) the time series of the spatially uniform mode.* $U_0 = 0.35$ *V.* $R_\Omega = 540\Omega$*,* $R_c = 300\Omega$*.*

Further study of the intermittent spatiotemporal patterns that appear when forcing the systme with 40 mV, one can see that at several measurement points the external modulation seems to support successive changes in the propagation direction of the traveling pulse. Thus, the perturbation seems to change the phase of one of the two coefficients of the KL spatial modes by π. An example of this phenomenon is depicted in figure 4.64.

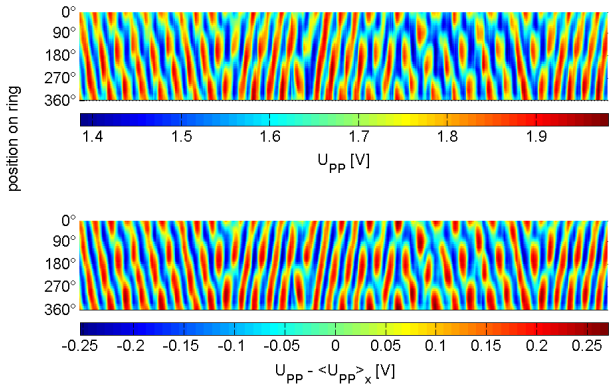

Figure 4.64: *Point I-e in figure 4.49 as an example for repeated change of propagation direction in pulses due to the external forcing. Upper plate:* U_{PP}(x,t)*, Lower plate:* $(U_{PP} - < U_{PP} >_x)(x,t)$.

4.4 The 1:2 Arnold Tongue

In this section the dynamical response of the oscillating system to an external forcing with approximately half of the natural frequency is investigated. Figure 4.65 gives an overview of the parameter values which were experimentally investigated, close to the 1:2 subharmonic resonance.

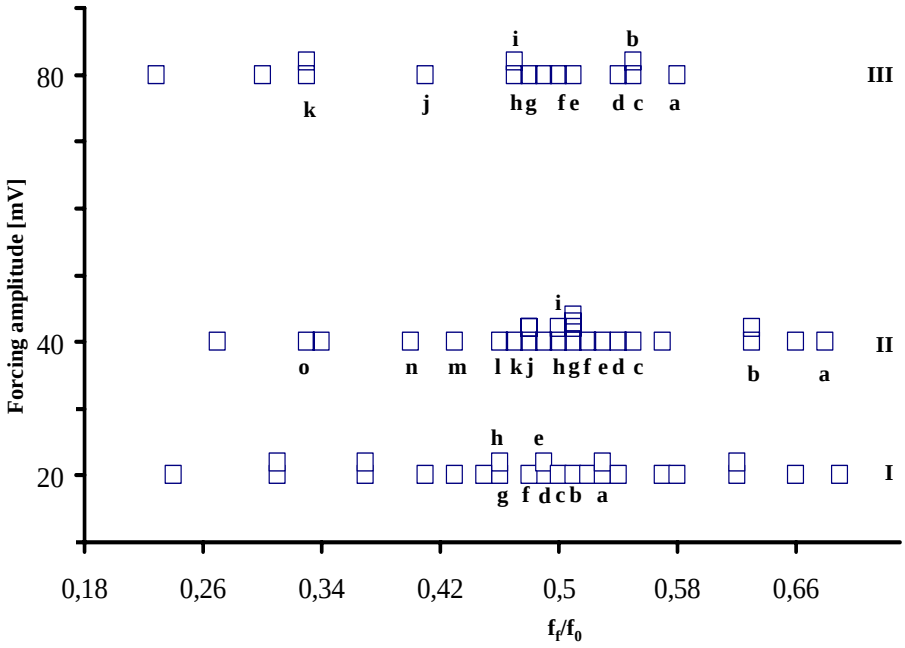

Figure 4.65: *The experimentally measured points in the amplitude - frequency parameter plane.*

4.4.1 Determination of the entrained region

When the system is forced with nearly half the natural frequency, the phase difference between the forcing signal and the coefficients of the KL spatial modes are determined by calculating the time difference between the n^{th} local maximum of the forcing signal and the $2n^{th}$ maximum of the time series of the KL spatial mode coefficients. Whenever the oscillation frequency of the response is equal to f_f, the phase relation between the forcing signal and the response is obtained as shown for the responses to the 1:1 resonance.

(A) Forcing amplitude 20 mV

When applying a 1:2 forcing to the system, a forcing strength of 20 mV is sufficient

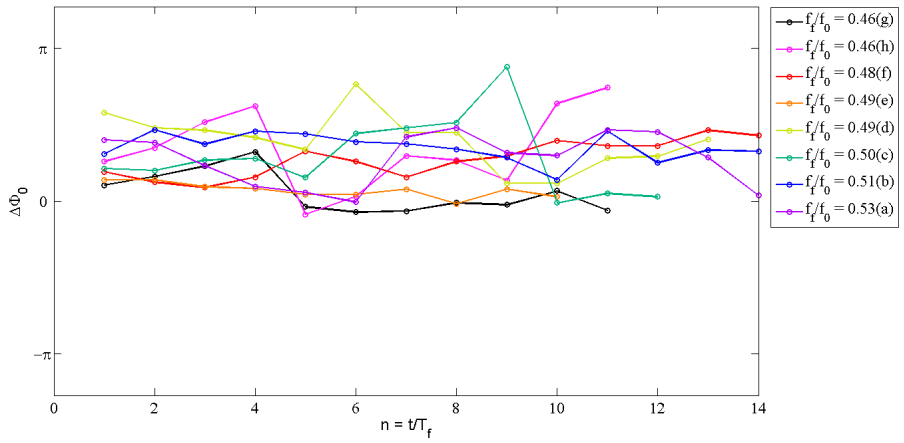

Figure 4.66: *20 mV forcing amplitude: The phase difference between the forcing signal and the time series of the spatially uniform mode.*

to entrain the spatially uniform mode of the oscillating system. Hence, as figure 4.66 shows, the phase difference between the sinusoidal forcing signal and the time series of the spatially uniform mode stays constant at about zero in the entire forcing parameter regime. However, although the time series of the spatially uniform mode of the forced system oscillates with f_f, the frequency power spectra of the time series show that it also contains the superharmonics and in several cases additional noise from the measurement setup, which makes the determination of the exact local maximum of each peak difficult. This results in slight variations in the phase relation between the forcing signal and the spatially uniform mode, like in points I-h, I-f and I-c in figure 4.66.

Figures 4.67 and 4.68 show the advances of the phase difference between the forcing signal and a_1 and a_2. The nearly constant value of $\Delta\Phi_1$ and $\Delta\Phi_2$ at points I-f and I-e indicate that the system locks to the forcing at these two measurement points.

At point I-g an initial increase in the values of $\Delta\Phi_1$ and $\Delta\Phi_2$ is followed by a plateau which starts at $n = 5$. This type of behavior suggests that the system goes through a transition from an unlocked to a locked state.

At the remaining measurement points the advances of the phase difference between the sinusoidal external signal and the two coefficients drift continuously, in positive or negative direction showing that these measurement points are located outside the resonance region.

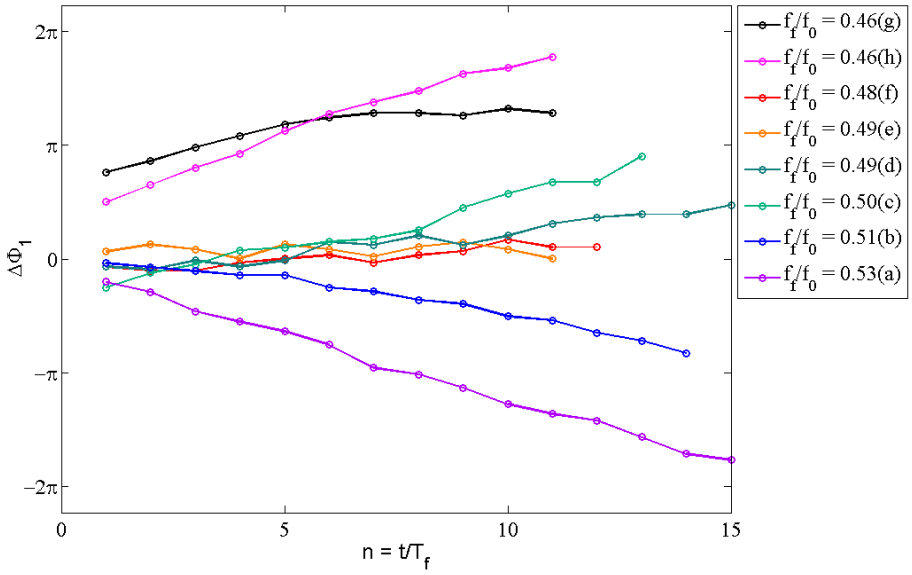

Figure 4.67: *20 mV forcing amplitude: Variations of $\Delta\Phi_1$ with time at constant forcing amplitude measured for points marked on figure 4.65.*

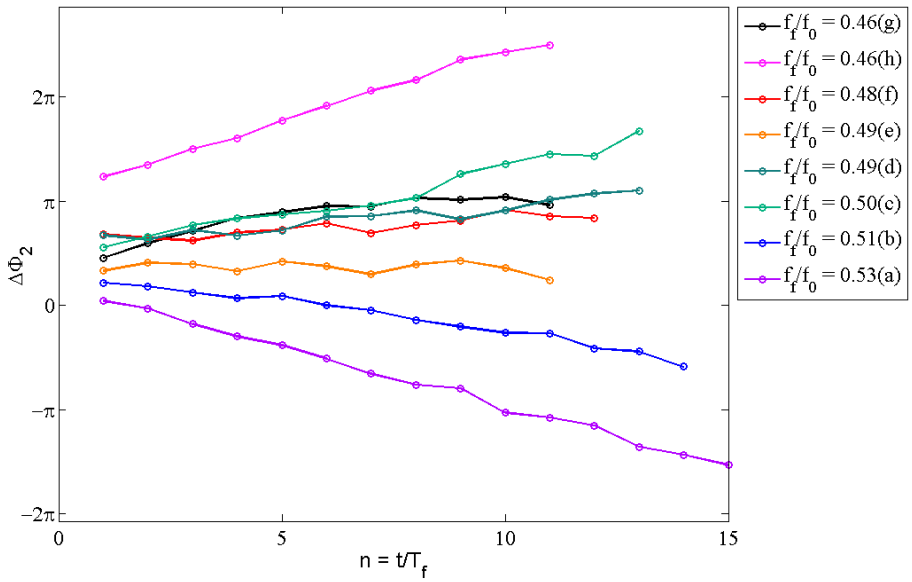

Figure 4.68: *20 mV forcing amplitude: Advances of $\Delta\Phi_2$ at different measurement points in figure 4.65.*

(B) Forcing amplitude 40 mV

When the system is forced with 40 mV forcing amplitude, the time series of the spatially uniform mode shows that this spatial mode oscillates with f_f. The constant phase difference of zero between the forcing signal and the time series of the spatially uniform mode reveals that the external modulation is in-phase with this spatial mode of the system.

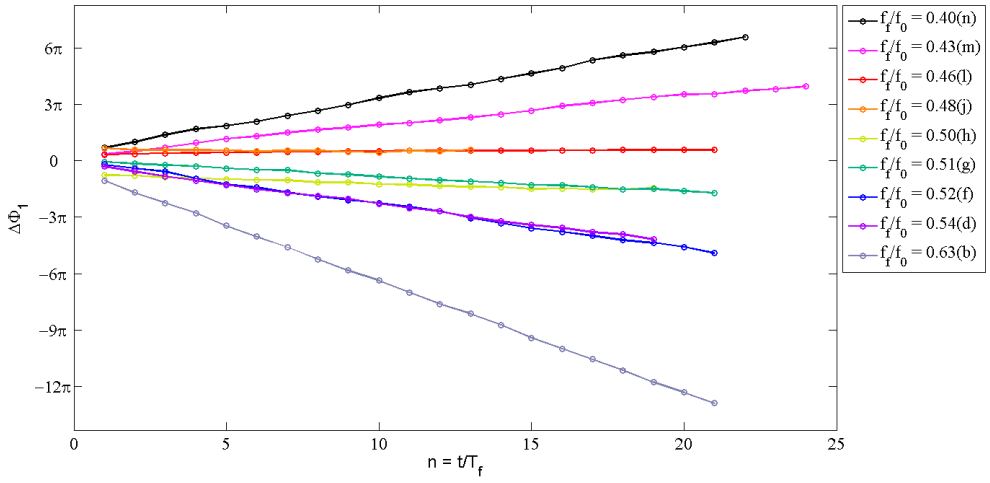

Figure 4.69: *40 mV forcing amplitude: Advances of $\Delta\Phi_1$ measured for points marked in figure 4.65.*

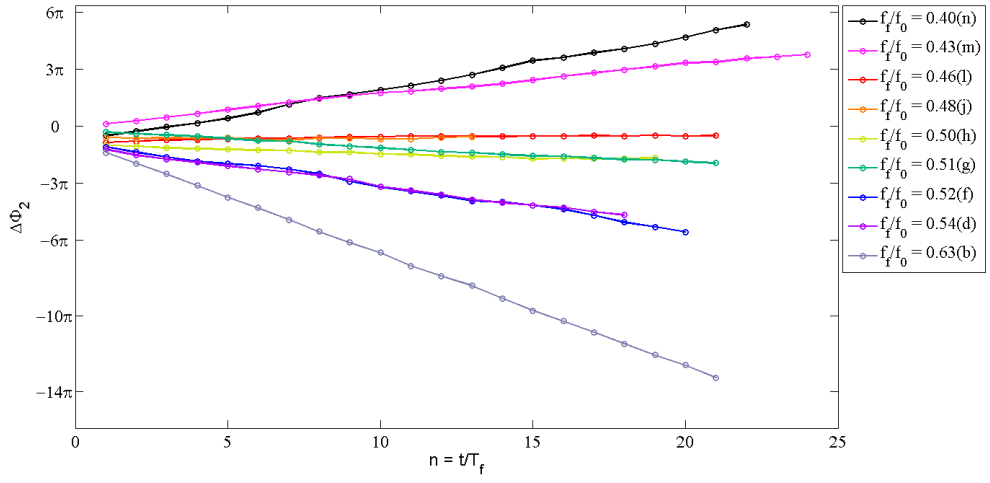

Figure 4.70: *40 mV forcing amplitude: Variations of $\Delta\Phi_2$ with time at constant forcing amplitude for several different measurement points in figure 4.65.*

The advances of $\Delta\Phi_1$ and $\Delta\Phi_2$ are depicted in figures 4.69 and 4.70, respectively. The analysis of the KL spatial modes of $U_{PP} - < U_{PP} >_x$ and the spatially homoge-

neous mode show that at this forcing parameters only at measurement points II-l, II-h and II-j the systems entrains to the forcing. However, within this parameter region unlocked responses appear too.

Both figures 4.69 and 4.70 show that the phase difference between the forcing signal and a_1 and a_2 for the unlocked responses drift continuously and for none of the measurement points a phase slip is observed. In order to get insight into the existence of critical slowing down close to zero detuning, where $1/2f_0$-$f_f = 0$, it is helpful to investigate the changes of the response frequency as the detuning changes. Therefore, the variations in the difference between $1/2f_r$ and f_f versus detuning is plotted in green in figure 4.71. It is clear that for the entrained responses $1/2f_r$-$f_f = 0$. Figure 4.71 shows that for the unlocked responses f_r grows almost linearly as detuning increases in positive and negative direction. The blue curve in figure 4.71 has a slope of one and thus comparing the green curve with the blue curve suggests that the response frequency of the driven system is always smaller than its natural frequency and even at large values of detuning f_r does not become equal to f_0.

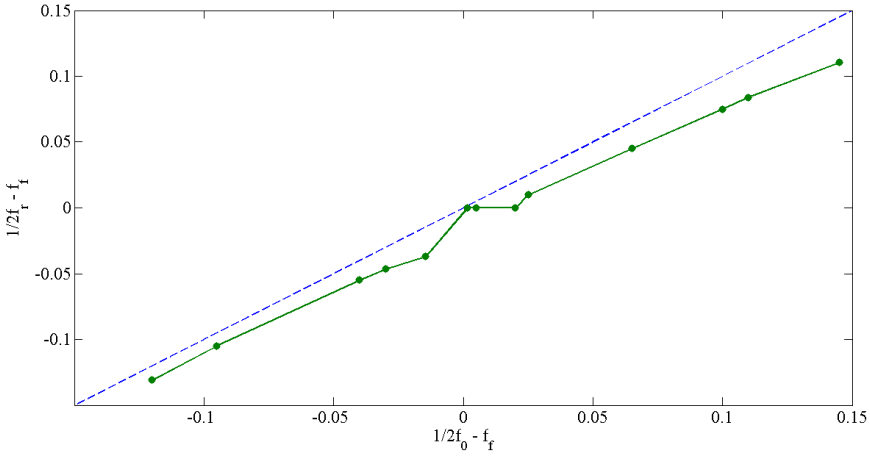

Figure 4.71: *40 mV forcing amplitude: Variations of the difference between the response frequency and the forcing frequency versus detuning.*

(C) Forcing amplitude 80 mV

Similar to the response of the spatially homogeneous mode to external forcing with low and moderate forcing amplitudes, the spatially uniform mode oscillates in-phase with the forcing frequency. Thus, the phase difference of its oscillations to the forcing signal does not grow with time and at 80 mV forcing amplitude the spatially uniform mode stays entrained within the entire measured region.

Figures 4.72 and 4.73 depict the advances of the phase difference between the externally applied sinusoidal signal and the coefficients of the first and second KL modes. The figures show that between point III-j and III-h the growth of the phase relation between the forcing signal and a_1 and a_2 changes sign, which indicates that within this parameter region the system locks to the forcing and thus these points are located close to the border of the synchronization regime.

Due to the strong amplitude modulations and presence of several different frequencies in the time series of a_2 at the measurement point III-f, at $f_f/f_0 = 0.50$, determination of the exact maxima was not possible. At the measurement point III-d ($f_f/f_0 = 0.54$) intermittent standing patterns appear and the amplitude of the a_2 oscillations are very low, which makes the determination of maxima difficult, too. Thus, the changes of the phase could not be obtained for these points and are correspondingly not shown in figure 4.73.

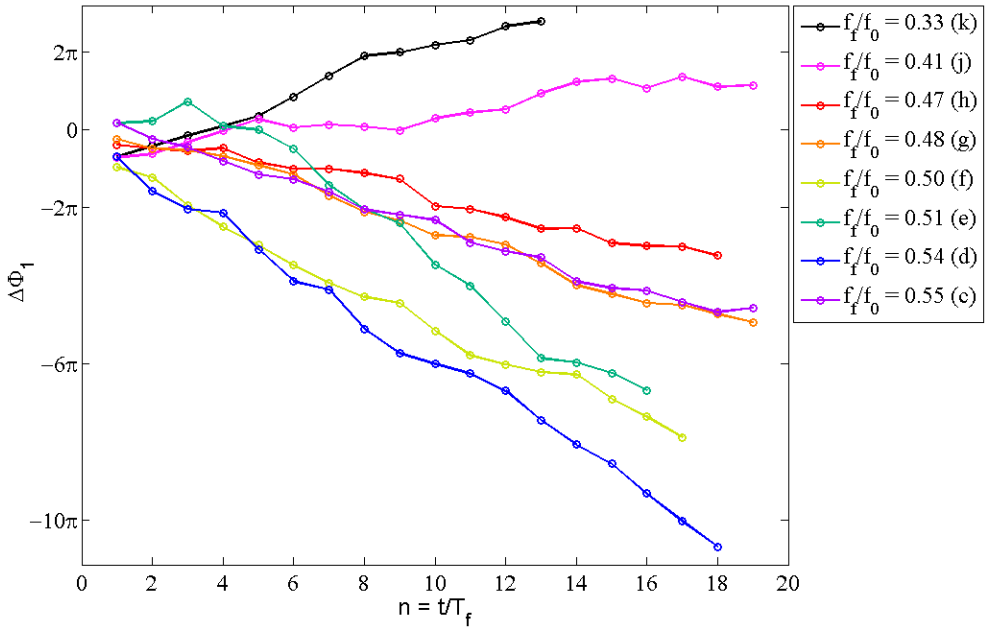

Figure 4.72: *80 mV forcing amplitude: The advances of the phase difference between the forcing signal and the time dependent coefficients of the first KL spatial mode for several measurement points marked on figure 4.65.*

Figure 4.74 summarizes the results of the above presented analysis for the 1:2 forcing parameters. On the figure the entrained responses are marked by filled circles and the unlocked responses are designated by filled diamond symbols.

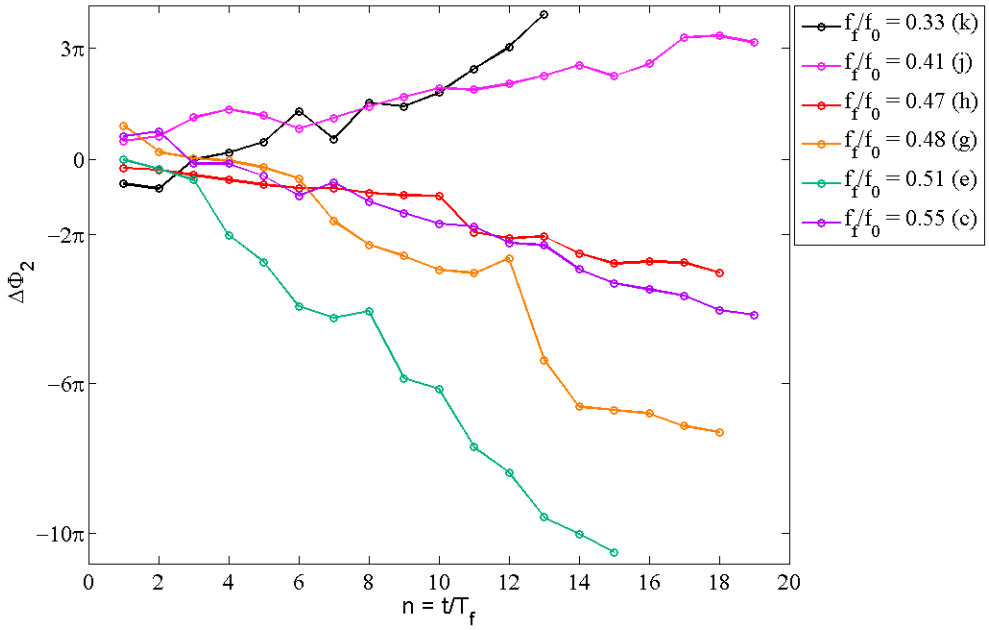

Figure 4.73: *80 mV forcing amplitude: The changes of $\Delta\Phi_2$ for different measurement points marked on figure 4.65.*

4.4.2 Breathing pulses

When the system is forced with 20 mV and 40 mV forcing amplitudes the synchronous and asynchronous patterns that appear are phenomenologically very similar. The results of KL decomposition of U_{PP} show that at low and moderate forcing strengths independent of the behavior of the system with respect to entrainment, the description of the space-time evolution of U_{PP} at each measurement point requires three spatial modes. Hence, unlike the dynamical behavior of the system within the 1:1 and 2:1 resonance regimes, entrainment does not influence the number of spatially active coherent modes that govern the spatiotemporal patterns. This can be seen in figure 4.75 which depicts the energy distribution between the first 8 KL spatial modes of U_{PP} (figure 4.75(a)) and the first three KL spatial modes (figure 4.75(b)) that construct the entrained response shown in 4.75(c). Hence, the synchronous and asynchronous responses can only be distinguished by monitoring the growth of the phase relations of the forcing signal with a_0, a_1 and a_2 and the frequencies that are present in the time series of these three spatial modes. In figure 4.74 the locked responses are marked with filled light blue circles and the unlocked responses with filled red diamonds.

The spatiotemporal patterns that arise in this parameter regime are pulse like structures which go through a width narrowing followed by a thickening, and hence are termed breathing pulses. However, the pulses that appear in two successive circu-

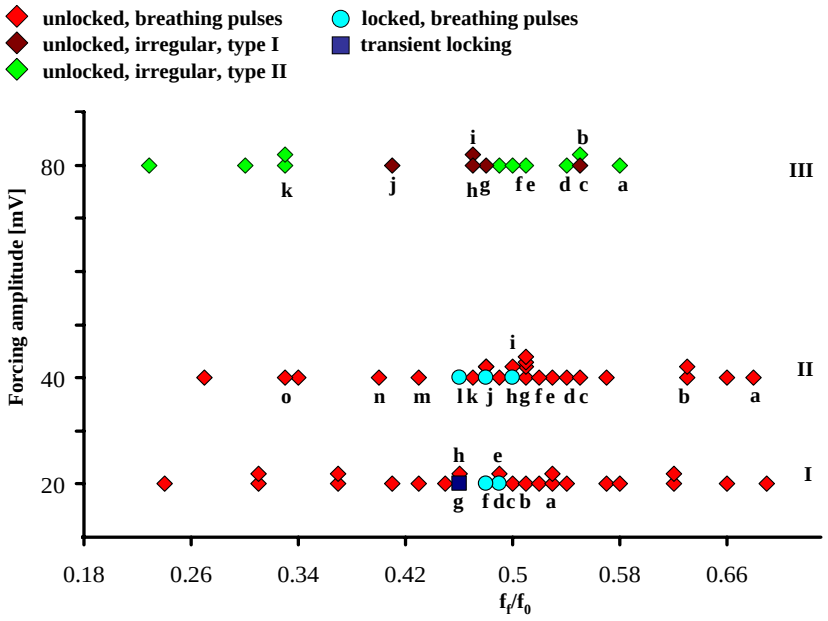

Figure 4.74: *The 1:2 resonance region depicted in the amplitude - frequency parameter space.*

lations around the ring look slightly different and can be differentiated from each other, which results in the appearance of spatiotemporal period-2 pattern in U_{PP}. Examples of such patterns that result from the space-time evolution of U_{PP} are displayed in figures 4.75(c) and 4.77(c). However, in figure 4.75(c), due to the stronger influence of the spatially homogeneous mode on the KL spatial modes of U_{PP}, the local narrowing has changed to a breaking point. The higher strength of the spatially homogeneous mode can be recognized in figure 4.75(b) where the spatially uniform mode appears as an offset to the second KL spatial mode of U_{PP}.

The KL decomposition of the inhomogeneous part of the interfacial potential shows that at all measured points the system consists of a traveling wave pair, a sinusoidal profile and its 90° space-shifted version. However, the influence of the externally applied forcing on the response of the pulse modes depends on the applied forcing frequency and is not equal in the entire parameter range. This can be clearly seen when comparing the space-time evolution of $U_{PP} - < U_{PP} >_x$ at point II-l ($f_f/f_0 = 0.46$) in figure 4.76(c) with that of the point II-a ($f_f/f_0 = 0.68$) in figure 4.77(d). Studying the results of the KL decomposition of the inhomogeneous part of U_{PP} indicates that in a parameter regime with negative detuning the inhomogeneous part of U_{PP} is almost unaffected by the external perturbation and the response is nearly a linear superposition of the pulse and the spatially uniform mode. However, when

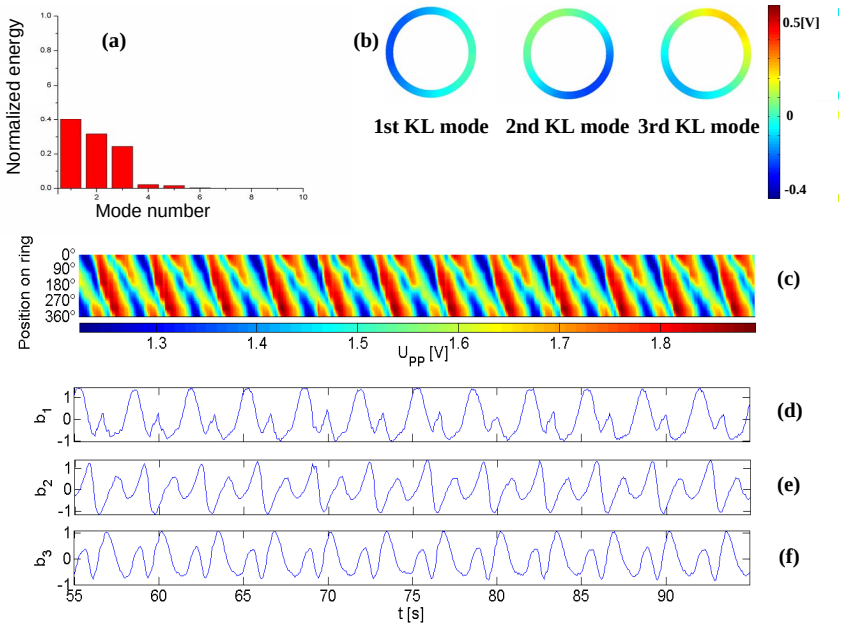

Figure 4.75: *Point II-h in figure 4.74: (a) Energy distribution of the first 8 KL modes of U_{PP}, (b) the first three KL spatial modes, (c) U_{PP}(x,t), (d), (e) and (f) the time dependent coefficients of the KL spatial modes shown in (b). $U_0 = 0.28$, $f_f/f_0 = 0.46$. $R_\Omega = 550\Omega$, $R_c = 350\Omega$.*

the detuning is positive, the interaction of the pulse solution with the forcing causes an unequal distribution of the normalized energy between the two traveling wave spatial modes, as it can be seen in figure 4.76(a). Hence, the response is asymmetric and deviates from a pulse behavior. Figures 4.76(d) and (e) depict the time series of the coefficients of the two KL spatial modes of $U_{PP} - < U_{PP} >_x$ where both time series exhibit a periodicity of 2.

Studying the frequency analysis of the time series of a_1 and a_2 of the responses in the entire parameter region sheds light on how the external forcing affects the responses to these forcing parameters. Figure 4.78(a) shows the space-time evolution of the inhomogeneous part of the interfacial potential at constant forcing strength of 40 mV for different applied forcing frequencies, where the change from period-2 patterns to traveling pulses can be observed. The corresponding power spectra of the time series of the first and second KL spatial mode coefficients show that at positive detuning, the time series of a_1 and a_2 contain two extra frequencies f_0+f_f and f_0-f_f, which appear with very low intensity in the frequency power spectra of the coefficients of the responses when the detuning is negative. In figure 4.78(b) the intensity of the two frequencies f_0+f_f and f_0-f_f are plotted versus f_f/f_0. It is

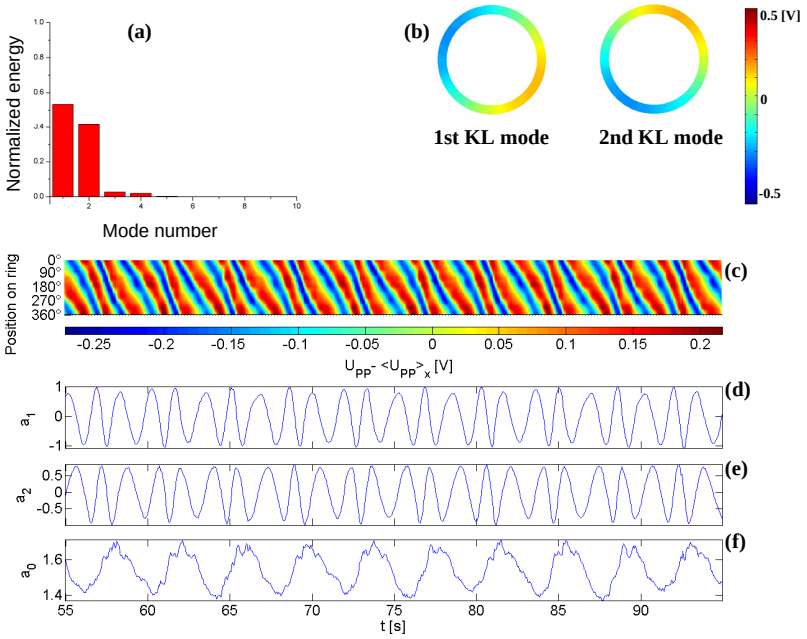

Figure 4.76: *Point II-l in figure 4.74: (a) Energy distribution of the first 8 KL modes of* $U_{PP}- < U_{PP} >_x$*, (b) the first three KL spatial modes, (c)* $(U_{PP}- < U_{PP} >_x)(x,t)$*, (d)* $a_1(t)$*, (e)* $a_2(t)$*, (f) the time series of the spatially homogeneous mode.* $U_0 = 0.28$*.* $R_\Omega = 550\Omega$*,* $R_c = 350\Omega$*.*

obvious that the intensity decreases as the positive detuning becomes smaller. This trend continues as one goes through the 1:2 tongue to negative values of detuning. Hence, the strong influence of the external forcing, which manifests itself in the time-space evolution of $U_{PP}- < U_{PP} >_x$, causes the excitation of oscillations with frequencies f_0+f_f and f_0-f_f in the time series of a_1 and a_2.

It is interesting to notice that when the detuning is positive both locked and unlocked responses experience a strong influence of the forcing. Examples can be observed in figure 4.78(a) point II-j where the system is entrained and at points II-o and II-n where the responses are unlocked.

4.4.3 Irregular responses

Irregular responses only appear when the system is forced with 80 mV amplitude. In figure 4.74 green and dark red diamonds mark the parameter values where irregular patterns were observed. It was already shown in the first part of this section that all the measured responses of this system to a 1:2 external forcing with 80 mV

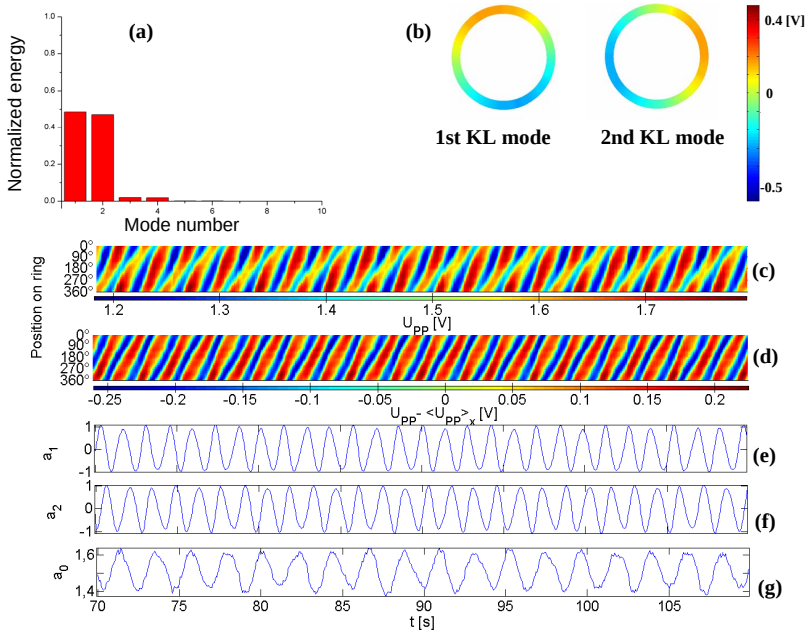

Figure 4.77: *Point II-a in figure 4.74: (a) Energy distribution of the first 8 KL modes of* $U_{PP}- < U_{PP} >_x$*, (b) the first three KL spatial modes, (c)* $(U_{PP}- < U_{PP} >_x)(x,t)$*, (d)* $a_1(t)$*, (e)* $a_2(t)$*, (f) the time series of the spatially homogeneous mode.* $U_0 = 0.28$*.* $R_\Omega = 550\Omega$*,* $R_c = 350\Omega$*.*

amplitude are unlocked.

When looking at the spatiotemporal patterns of the interfacial potential at different parameter values, it seems that two types of irregular responses can be distinguished, according to their phenomenology. Figure 4.79 presents examples of the two patterns. The irregular pattern shown in figure 4.79(a) contains fragments of the a pulse and is more coherent compared to the spatiotemporal structures displayed in figure 4.79(b) where fractions of space that are quasi-uniform pop up at irregular moments in time and at different positions in space with variable width.

The distribution of the two types of irregular patterns on the forcing amplitude-frequency plane indicates that the type of irregular pattern that appears at a measurement point is not determined by the forcing frequency at each point. The occurrence of the two different types of patterns is a result of the slight changes of the surface, which manifests itself in the structure of the traveling pulses of the reference state. Figure 4.80(c) and (d) show the pulses before applying the external perturbation, for the experiments shown in figure 4.79(a) and(b). In the type I unforced traveling pulses, displayed in figure 4.80(c), the results of the KL decom-

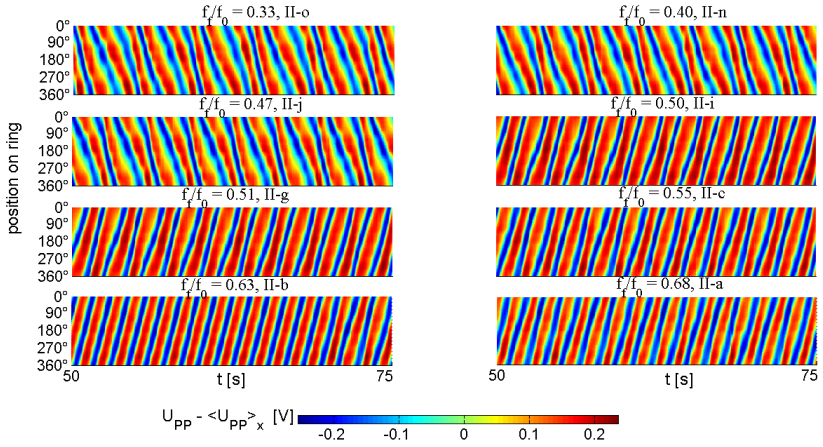

(a)

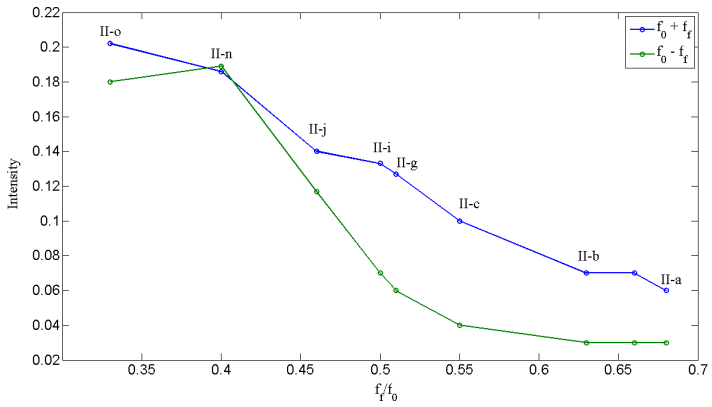

(b)

Figure 4.78: *(a) The spatiotemporal evolution of $U_{PP} - < U_{PP} >_x$ for measurement points at different forcing frequencies (b) the intensity of the $f_f + f_0$ and $f_f - f_0$ frequencies in the oscillations of a_1 with time.*

position reveal that the first two KL eigenvectors of the system contain over 99% of the information and the higher modes hardly play a role in the reconstruction of the traveling pulse. The type II pulses, on the other hand, are constructed by spatial sine and cosine profiles but the higher modes capture more than 10% energy. The third spatial mode of the type II unforced pulses is either completely or mostly spatially homogeneous, the forth and fifth spatial pair correspond to sin(2x) and cos(2x). This difference in the reference state results in the appearance of the two types of irregular responses, shown in figure 4.79. However, to determine possible qualitative differences between the two types of pattern it is necessary to study and compare the results of the KL decomposition for each type.

The results of the KL decomposition of U_{PP} for an example of each pattern is presented in figure 4.81. The KL decomposition of U_{PP} at all measured points shows

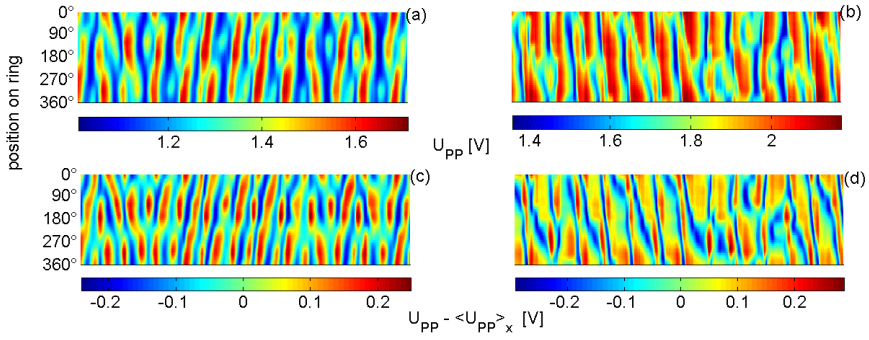

Figure 4.79: *Point III-g and III-e in figure 4.74: (a) and (b) Spatiotemporal evolution of the interfacial potential at $f_f/f_0 = 0.48$ and 0.51, respectively, (c) and (d) spatiotemporal evolution of the inhomogeneous part of the interfacial potential for the same two measurement points. Measured at (a) $U_0 = 0.28$ V and (b) $U_0 = 0.33$ V. $R_\Omega = 550\Omega$, $R_c = 350\Omega$.*

that in the presence of forcing the system can be described by three spatial modes where the spatial mode which possesses the highest energy is uniform. An example of the first three KL modes is displayed in figure 4.81(e). Figure 4.81(c) shows that the contribution of the second KL mode to the construction of structures presented in 4.81(b) is considerably lower than the structures in figure 4.81(a).

Comparing figures 4.82(a) and (b) with 4.81(a) and (b) shows that subtraction of the spatially uniform mode does not considerably change the irregular spatiotemporal patterns that appear. The inhomogeneous part of U_{PP} consists of a sinusoidal and its 90° space-shifted spatial profiles. Yet, figure 4.82(c) and (d) show that in the type II irregular patterns (figure 4.82(b)) the eigenvalues corresponding to the two dominant modes are more similar in the type II irregular patterns than the type I patterns.

Figure 4.83 and 4.84 present the time series of the coefficients of the KL spatial modes of $U_{PP} - < U_{PP} >_x$, for points III-c and III-d in figure 4.74 as representative examples of the two types of irregular patterns. Figure 4.83(b) and (c) show that at point III-c, the second coefficient of $U_{PP} - < U_{PP} >_x$ has lower amplitudes and larger amplitude modulations than the first coefficient. However, at point III-d, the amplitudes of a_1 and a_2 in figure 4.82(b) and (c) have nearly equal amplitudes and exhibit similar amplitude modulations, which may point to higher correlations between a_1 and a_2 at point III-d ($f_f/f_0 = 0.54$) compared to point III-c ($f_f/f_0 = 0.55$).

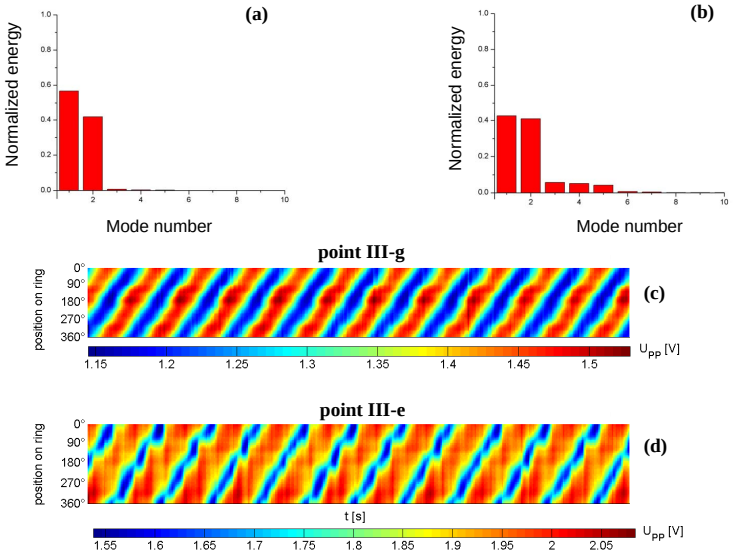

Figure 4.80: *Two different types of traveling pulses prevailed by the unforced electrochemical system at point III-g and III-e: (a) and (b) The energy distribution of the first 8 KL modes of U_{PP} at points III-g and III-e, respectively, (c) and (d) the spatiotemporal evolution of U_{PP} at point III-g and III-e, respectively. Measured at (a) $U_0 = 0.28$ V, (b)$U_0 = 0.33$ V. $R_\Omega = 550\Omega$, $R_c = 350\Omega$.*

To gain a quantitative measure of the correlation between the two KL mode coefficients of $U_{PP} - < U_{PP} >_x$ the cross correlation function is calculated. The normalized cross correlation function is defined as shown in equation 4.4 [98] and provides a measure of how closely two signals are related to each other.

$$\rho_{XY}(\tau) = \frac{1}{N} \sum_n (X(t_n)Y(t_{n+\tau})) \tag{4.4}$$

where the lag, τ, is an integer multiple of the sampling interval.

Figure 4.85(e) and (f) display the cross correlation of a_1 and a_2 for points III-c and III-e in figure 4.74, respectively. The natural frequency of the reference state of the system at point III-c, which is also the main oscillation frequency of a_1, is 0.51 Hz. From figure 4.85(e) it can be observed that the cross correlation function of a_1 and a_2 of a type I irregular pattern oscillates with a frequency close to f_0, whereas $\rho_{a_1 a_2}(\tau)$ at point III-e in figure 4.85(f) contains additional frequencies other than $f_0 = 0.55$ Hz and exhibits period-2 oscillations during the first 12 seconds. Furthermore, since the first two eigenvectors of the inhomogeneous part of U_{PP} are the traveling wave

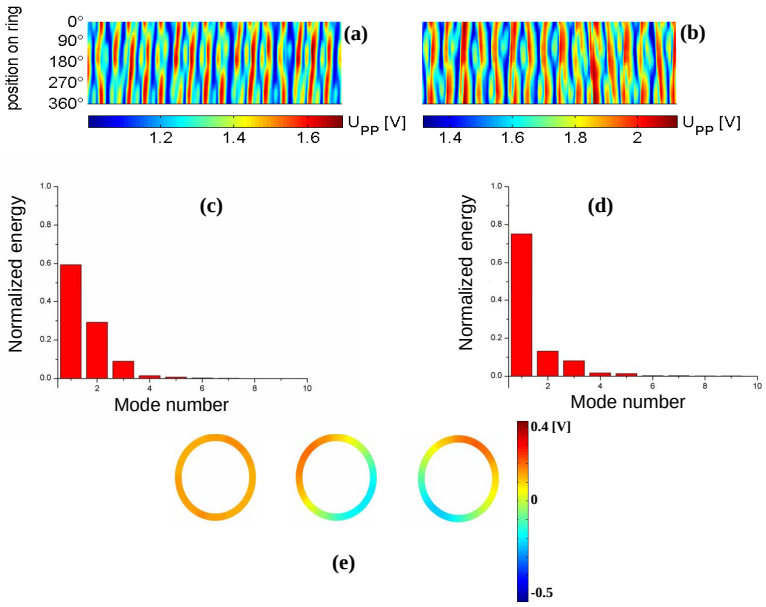

Figure 4.81: *Point III-c and III-f in figure 4.74: (a) and (b) Spatiotemporal evolution of U_{PP} at point III-c and III-f, respectively, (c) and (d) the energy distribution of the first 8 KL modes of U_{PP} for (a) and (b) respectively, (e) the first three KL modes of (a). Measured at (a) $U_0 = 0.28$ V, (b) $U_0 =$ at 0.33 V. $R_\Omega = 550\Omega$, $R_c = 350\Omega$.*

spatial modes, sin(x) and cos(x), the comparison of the cross correlation between a_1 and a_2 with corresponding one of the unforced pulse, provides us a measure of how much of the original pulse is left in the response. The blue curve in figure 4.86(a) and (b) display the cross correlation functions for the unforced traveling pulses at the measurement points III-c ($f_f/f_0 = 0.55$) and III-e ($f_f/f_0 = 0.51$), respectively. The comparison with $\rho_{a_1 a_2}(\tau)$ of the responses to the external forcing (the green curves) shows that the blue and green curve in figure 4.86(a) oscillate with the same frequency whereas the green curve in figure 4.86(b), presenting the correlation function of a_1 and a_2 of the response at point III-e oscillates with a different frequency than its reference state. Hence, the results confirm that the irregular response at point III-c, as an example of type I irregular patterns, preserves more of the original pulse than the response at point III-e, which is representative for the type II irregular responses.

In addition to the above mentioned characteristics of the two types of irregular responses, each type exhibits dynamical features which are not observed for the other one. At first glance, oscillations of a_1 with time, shown in figure 4.83(b), seem to possess an intrinsic period, however, the amplitudes of the oscillations are irregularly

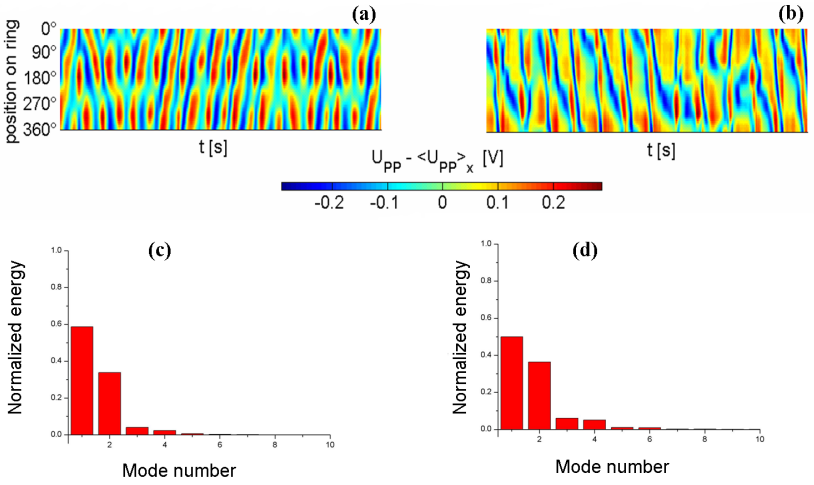

Figure 4.82: *Point III-c and III-d in figure 4.74: (a) and (b) Spatiotemporal evolution of* $U_{PP}- < U_{PP} >_x$ *at point III-c and III-d, respectively, (c) and (d) the energy distribution of the first 8 KL modes of* $U_{PP}- < U_{PP} >_x$ *for (a) and (b) respectively. Measured at (a)* $U_0 = 0.28$ *V, (b)* $U_0 =$ *at 0.33 V.* $R_\Omega = 550\Omega$, $R_c = 350\Omega$.

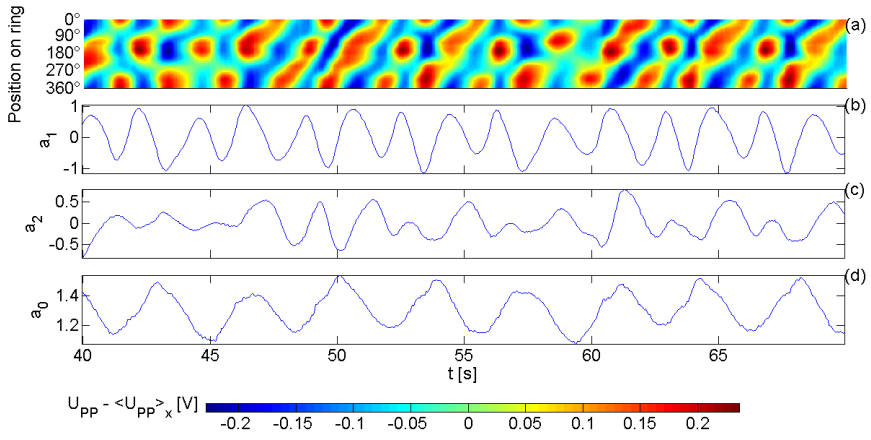

Figure 4.83: *Point III-c in figure 4.74: (a)* $(U_{PP}- < U_{PP} >_x)(x,t)$ *(b) and (c) time dependent coefficients of the first and second KL modes (d) time series of the spatially uniform mode.* $U_0 = 0.28$ *V.* $R_\Omega = 550\Omega$, $R_c = 350\Omega$.

modulated and resemble time series observed for Rössler-type chaotic systems. The Rössler system is a set of three differential equations which possess one nonlinear term and exhibits a strange attractor [60].

To obtain a measure for comparing the type I irregular response of the system with the Rössler system, the next-maximum map of the present system can be compared to that of a Rössler system. For obtaining the next-maximum map, the succes-

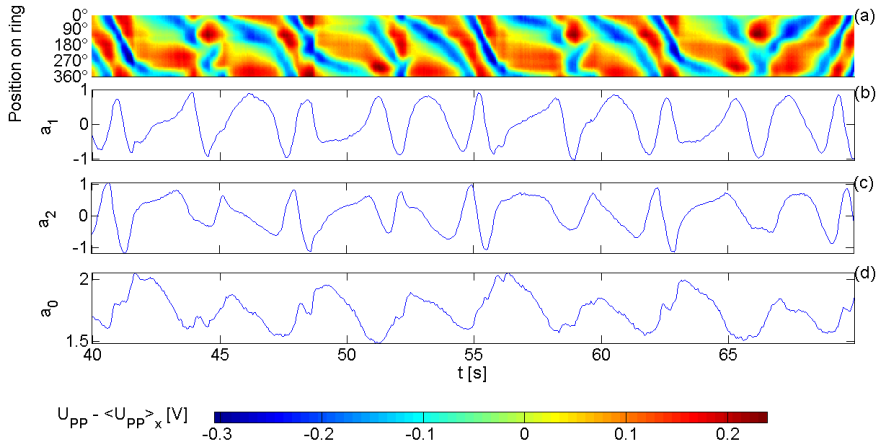

Figure 4.84: *Point III-d in figure 4.74: (a) The time-space evolution of the inhomogeneous part of U_{PP}, (b) and (c) the time dependent coefficients of the first and second KL mode, respectively, (d) the oscillations of the spatially uniform part of U_{PP} with time. $U_0 = 0.33$ V. $R_\Omega = 550\Omega$, $R_c = 350\Omega$.*

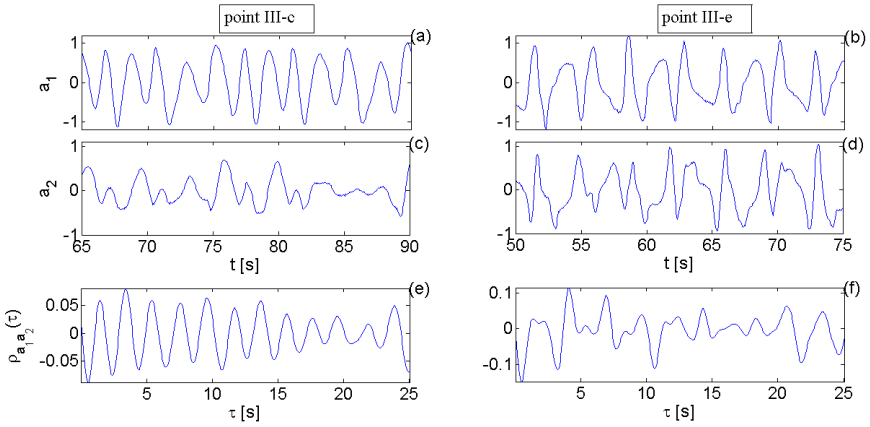

Figure 4.85: *Point III-c and III-e in figure 4.74: (a) and (c) The time series of the first and second KL coefficients of $U_{PP} - < U_{PP} >_x$ for measurement point III-c, (e) the cross correlation between (a) and (c), (b) and (d) the first and second time dependent KL coefficients of $U_{PP} - < U_{PP} >_x$ for measurement point III-e, (f) the cross correlation between (b) and (d). Point III-c ($f_f/f_0 = 0.55$) measured at $U_0 = 0.28$ V and point III-e ($f_f/f_0 = 0.51$) at $U_0 = 0.33$ V.*

sive local maxima of $a_1(t)$ are recorded and then $a_1^{max_{(n+1)}}$ is plotted vs. $a_1^{max_{(n)}}$ where $a_1^{max_{(n)}}$ denotes the nth local maximum of $a_1(t)$. Figure 4.87 depicts the next-maximum map of a_1 for the measured point III-c at $f_f/f_0 = 0.55$, shown in figure 4.83(b). It is known that [60] the next-maximum map of systems which possess a Rössler-type attractor, lie on a unimodal map whereas in figure 4.87 and the other maps of the type I data no specific structure can be distinguished. This shows

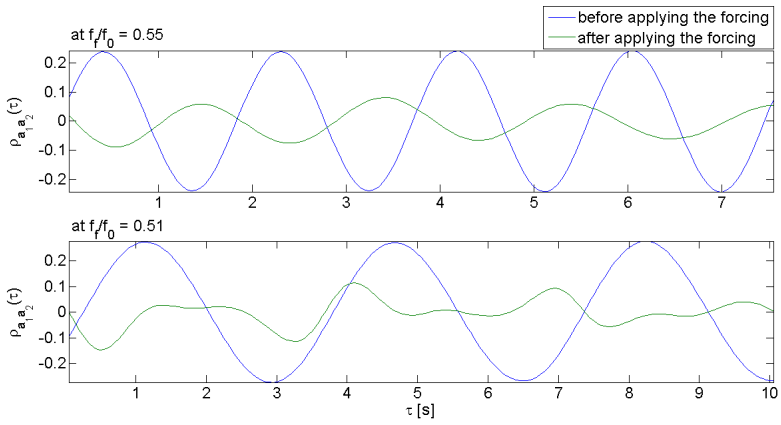

Figure 4.86: *Comparison between the cross correlation of the KL spatial mode coefficients of the inhomogeneous part of the traveling pulse before applying the perturbation and the cross correlation of the coefficients of the first two KL spatial modes of the response to forcing.*

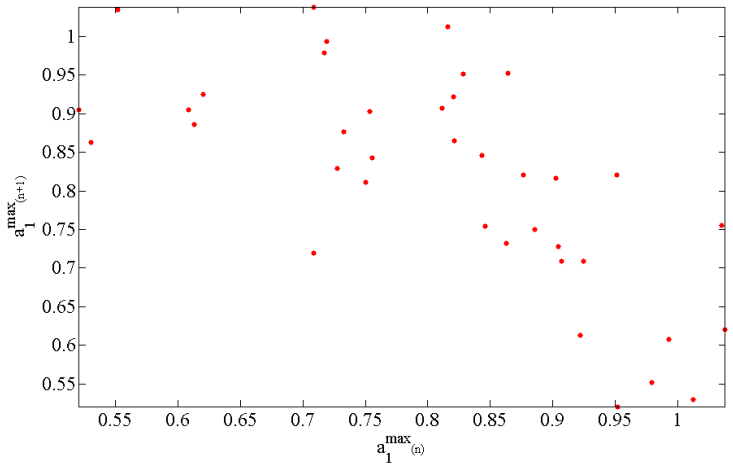

Figure 4.87: *A representative example of a next-maximum map of the coefficient of the first KL mode of $U_{PP}- < U_{PP} >_x$ for type I irregular patterns.*

that the irregular type-I patterns cannot be classified as Rössler-type chaotic system.

The type II irregular dynamics exhibits intermittent intervals that is not observed for the type I irregular dynamics. Here, the system switches from an irregular to a standing pattern. Figure 4.88(a) displays the intermittent spatiotemporal pattern observed at point III-d ($f_f/f_0 = 0.54$). The time series of the first two KL modes, which are shown in figure 4.88(b) and (c) show how the changes in the dynamics give rise to the standing patterns. Between 40 and 75 seconds a_1 and a_2 oscillate in a complicated manner and the oscillations of the uniform mode exhibit chaotic amplitude modulations. As the forcing continues, the internal alternations of the

dynamics give rise to a reduction in the amplitude of a_2, which prevails standing patterns. Moreover, the oscillations of a_1 and the spatially uniform mode become periodic and regular. This coherent state occurs only intermittently, and after some time the system gets back to the irregular state. Similar behaviors are observed at point III-b ($f_f/f_0 = 0.55$) and III-a ($f_f/f_0 = 0.58$).

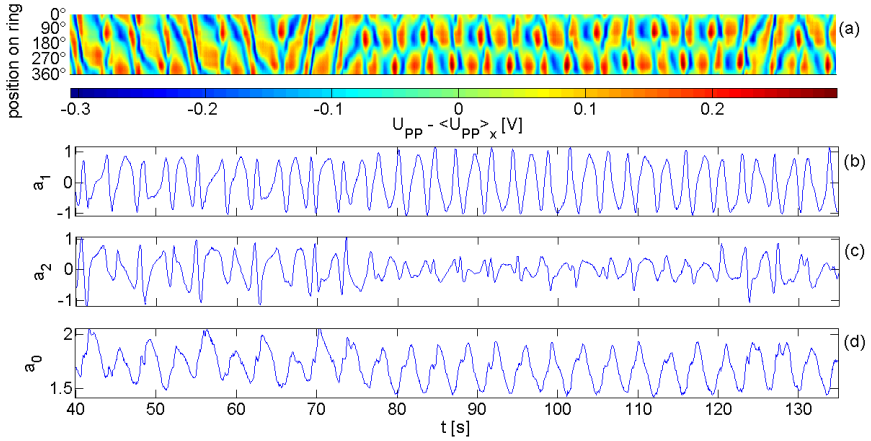

Figure 4.88: *Point III-d in figure 4.74: (a) ($U_{PP}- < U_{PP} >_x$)(x,t), (b) and (c) the time series of the first and second KL mode coefficients of $U_{PP}- < U_{PP} >_x$, (d) the oscillations of the spatially uniform mode with time. $U_0 = 0.33$ V. $f_f/f_0 = 0.54$. $R_\Omega = 550\Omega$, $R_c = 350\Omega$.*

The phenomenological difference between the type I and type II irregular patterns is also clearly reflected in the advances of the phase difference between the forcing signal and the first and second KL coefficients of $U_{PP}- < U_{PP} >_x$, depicted in figures 4.72 and 4.73. One can see in these two figures that the phase difference of the type I responses to the forcing signal grows with a lower slope than the phase difference of the type II responses to the forcing signal (compare the advances of $\Delta\Phi_1$ and $\Delta\Phi_2$ at point III-f with point III-c). This shows that the frequencies of a_1 in type I irregular responses are closer to $2f_f$.

4.5 Discussion

Before we start the discussion, we summarize the most important observations of our studies:

- The reference state of the system was a traveling pulse on a ring-electrode, i.e., in a spatially quasi 1-dimensional domain with periodic boundary conditions, superimposed by a uniform oscillation. The period of the uniform oscillation was always equal to the time of one circulation of the pulse around the ring. The pulse was induced by a negative global coupling and emerged in a non-trivial Hopf bifurcation with wave number 1. Thus, from a more theoretical point of view, the studies can be classified as investigations of the impact of periodic perturbations on an oscillatory medium where the base instabilities leading to the oscillations is a non-trivial Hopf bifurcation, and mode selection stabilizes a traveling wave solution. The experimental evolution of the spatiotemporal dynamics could be phenomenologically captured by the evolution of three spatial modes, the uniform mode and a sinusoidal 'pulse pair', $\sin(\frac{2\pi x}{L} + \phi)$ and $\cos(\frac{2\pi x}{L} + \phi)$ with L being the circumference of the ring-electrode.

- The additive harmonic forcing applied to the reference state gave rise to four base types of entrainment: none, one, two or three of the active spatial modes were observed to lock to the forcing. The system was classified as being entrained when all modes locked to the external signal, half entrained when two modes locked to it and as not entrained when just one or none of the modes locked.

- The suppression of the oscillations of both pulse modes leading to uniformly oscillating responses was never observed. A suppression of the uniform mode occurred only at low forcing strength within the 1:1 tongue.

- The transition into the entrained regions was not accompanied by a critical slowing down and no experimental evidence existed showing that the Arnold tongue is bounded by saddle-node bifurcations, as characteristic for forced individual oscillators. This includes the behavior of the phase difference between the driving force and the time series of the coefficients of the three spatial modes, inside the entrainment band. For a simple forced oscillator the phase difference changes by π/m in a $m : n$ entrainment band. In our experiments, however, the phase differences stayed approximately constant when transversing the tongue. Again, there is one exception to this statement at low forcing

strength in the 1:1 tongue, where the phase difference between the forcing signal and the uniform mode changed by π, between the two sides of the tongue while those of the coefficients of the spatial modes were not affected.

- The uniform mode was synchronized to the external forcing at nearly all parameter values with a phase difference of around zero to the forcing signal. Only at low forcing strength around the 1:1 tongue it oscillated quasiperiodically.

- The patterns that prevailed in the Arnold tongues depended on the resonance region as well as the forcing parameters.
  - Forcing around a 1:1 resonance mainly results in the appearance of entrained pulses and asymmetrically entrained patterns. Asymmetric entrainment is referred to the state where applying the external forcing breaks the symmetry between the two equivalent traveling wave spatial modes. In this situation, the contribution of the two traveling waves to the construction of the pattern is not equal anymore. This difference in the contribution of the spatial modes manifests itself in the amplitude difference between the time series of their corresponding coefficients, $a_1(t)$ and $a_2(t)$.
  - Within the 2:1 entrainment band standing anti-phase oscillations are the most commonly observed synchronous response of the system to the external forcing. Moreover, the asymmetrically entrained responses occur in this forcing parameter regime too. A characteristic feature of the 2:1 resonance region is the appearance of half entrainment which gives rise to the occurrence of modulated standing anti-phase oscillations. However, the half entrained responses are considered unlocked, since only one of the two traveling wave spatial modes is entrained by the forcing.
  - The resonance region due to applying a 1:2 forcing is very narrow, compared to the other two measured entrainment bands. The resonant patterns that appear in this parameter regime are breathing pulses. The term breathing pulses is referred to traveling pulses whose width modulates in such a way that a decrease in the width is followed by an increase, during one rotation of the pulse along the ring-electrode.

The experimental investigations of this work are a continuation of several experimental and theoretical works, which focused on the study of the influence of external forcing on spatially distributed systems. An overview of the studies in the context of chemical reactions was presented in 2.5. The oscillations of the unforced system of the dynamical systems in theses studies emerge through an instability of a uniform stationary state where the wave number of the most unstable mode is zero, i.e., a 'trivial' Hopf bifurcation. These oscillations can be spatially uniform or non-uniform such as the rotating spiral waves observed in the experiments [13, 15–17, 66]. With

the assumption that the forced system is close to the bifurcation point, most of the theoretical investigations were based on the forced complex Ginzburg-Landau equation [18–20, 74–76].However, in the above presented chapter it was shown in detail that the reference state of this work consists of non-uniform oscillations which arise through a non-trivial Hopf bifurcation with wave number one, superimposed with uniform oscillations. Examples of applying a temporal forcing to traveling waves have been reported in the convection and fluid dynamics experiments where traveling waves that arise through a Hopf bifurcation are subjected to time-periodic forcing [12, 32]. However, no evidence for the oscillation of the spatially uniform mode during the propagation of the traveling pulses was found in these works.

Therefore, due to this fundamental dynamical difference between the reference states of the system studied in this thesis and the previous investigations, the work presented here sheds new light on the dynamics of driven spatially extended systems.

The spatiotemporal responses caused by forcing traveling pulses with frequencies very close to their natural frequency, provide the best example for understanding the important role of the negative global coupling on the dynamics of the driven system. When oscillations which arise through a 'trivial' Hopf bifurcation are subject to external forcing the system establishes a defined phase relation to the forcing signal and around the 1:1 resonance their response is similar to the behavior of single oscillators subject to external forcing. Experimental and theoretical works in the literature show that when applying an external forcing with 1:1 frequency ratio to uniform oscillations and rotating spiral waves, an entrained, homogeneous state with no spatial structure is stable [13, 16, 19, 66, 74]. However, it was shown in 4.2 that when traveling waves are externally forced due to the different phase relations of the different spatial modes to the external forcing two qualitatively different entrained responses appear which are not spatially uniform.

The theoretical investigations of the 2:1 resonance region showed that forced complex Ginzburg-Landau equation has both resonant spatially uniform solutions and resonant two-phase standing wave pattern solutions. The boundaries of the resonance region where the spatially uniform solutions appear coincides with the Arnold tongues of single forced oscillators. Similar to single oscillators, two stable uniform phase-locked solutions are formed in a pair of saddle-node bifurcations, which mark the border of the synchronization regime [78]. However, the parameter range of resonant standing wave patterns does not always coincide with the tongue of spatially uniform oscillations and occurrence of bifurcations can influence the range of frequency locking of standing waves. The standing patterns consist of two spatially uniform domains that oscillate with half of the forcing frequency and are phase

shifted by π. Similar to these studies, during the experiments of this thesis standing anti-phase oscillations appeared as the most common entrained response of the system to 2:1 forcing. Also here, the traveling wave modes oscillated with half the forcing frequency.

Theoretical and experimental reports in show that the occurrence of nonequilibrium Ising-Bloch bifurcation causes the resonant standing wave patterns lose stability and non-resonant Bloch-front spiral waves prevail [76,78]. Similarly, it was observed during the experiments of our work that at the breakdown of synchronization standing anti-phase oscillations lost stability and unlocked traveling anti-phase oscillations appeared. However, for positive frequency detuning, half entrained responses occurred on the boundary between the standing and traveling anti-phase oscillations. Furthermore, in our system standing anti-phase oscillations are not the only entrained responses that occur. Experimental results showed that in a narrow parameter region inside the 2:1 entrainment band asymmetrically entrained responses appear too. Contrary to the standing anti-phase oscillations, the asymmetrically entrained responses are traveling structures. At the fixed forcing strength of 40 mV close to $f_f/f_0 = 1.97$ (see figure 4.49) a transition from standing anti-phase oscillations to traveling asymmetrically entrained responses takes place. The latter entrained responses then change to standing patterns again at about $f_f/f_0 = 2.04$. Hence, in addition to the transition from resonance standing patterns to unlocked traveling patterns which was already reported in the literature, a transition from standing to traveling entrained responses is observed within the 2:1 resonance region. However, the mechanism of none of the latter transitions is yet understood.

In addition to the studies above where the standing waves appeared as a result of applying an external forcing to spiral waves [13, 15] during the experiments with nematic liquid crystals traveling waves were externally forced which also gave rise to the appearance of standing waves [33]. However, also here, no reports on the existence of traveling entrained patterns were found.

Moreover, despite the diversity of the numerous theoretical and experimental works that have focused on the study of the dynamics of externally driven spatially extended systems, to the current knowledge of the author of this work, no results on the responses of these systems around a 1:2 resonance regime were found in the literature and thus, the above presented studies are the first reports on the dynamics of a spatially extended system with forcing parameters $f_f = \frac{1}{2} f_0$.

4.5.1 A prototypical model equation

We have seen that in our experiments the oscillations emerge through a non-trivial Hopf bifurcation with wave number 1. Close to a Hopf bifurcation all oscillatory media exhibit universal dynamics which can be described by the complex Ginzburg-Landau equation. In the presence of a sinusoidal forcing it reads:

$$\partial_t \mathrm{W} = (1 + i\nu)W - (1 + i\mathrm{c}_2)\,|W|^2\,W + (1 + i\mathrm{c}_1)\partial_x^2 \mathrm{W} + \delta_m \cdot W^{*(m-1)} \qquad (4.5)$$

Here, the first two terms on the right hand side describe the local oscillator, the third one the diffusive coupling and the forth one accounts for the periodic force. δ_m is the strength of the forcing, W^* the complex conjugate of the complex order parameter W and m denotes the nominator of the resonance tongue $m : n$ under investigation. The system is in a rotating reference frame with the frequency of the external forcing. The parameter ν accounts for the frequency mismatch between the autonomous and forcing frequencies.

In Eq. 4.5 diffusion is the only spatial coupling present in the system hence, to account for the influence of the negative global coupling present in the dynamical system of this work Eq. 4.5 is modified to

$$\partial_t \mathrm{W} = (1+i\nu)W+\gamma < W >_x -(1+i\mathrm{c}_2)\,|W|^2\,W+(1+i\mathrm{c}_1)\partial_x^2 \mathrm{W}+\delta_m \cdot W^{*(m-1)} \quad (4.6)$$

where the second term on the right hand side represents the global coupling. Here, γ is the coupling strength.. For negative global coupling $\gamma < 0$. The term $< W >_x$ stands for the spatially uniform mode. The presence of the negative global coupling only affects the spatially uniform mode such that the trivial Hopf bifurcation is delayed and the modes with wave number k_n for $n = \pm 1$ are the first to become unstable through a non-trivial Hopf bifurcation.

The simulations of Eq. 4.6 were carried out using a pseudo spectral method. The basic idea of a pseudo spectral method is that the solution can be represented in the spectral domain by a set of orthogonal eigenfunctions, such as Fourier series with time dependent coefficients. The simulations presented here were performed with 256 Fourier modes. Discretization of a partial differential equation using a Fourier spectral method results in the separation of the equation to a linear part, which is diagonal and a nonlinear part. This equations were then solved using an exponential time stepping algorithm [99]. The program used in this thesis was written in Matlab by Dr. V. García-Morales.

4.5.2 The reference state

The reference state of our experiments was traveling pulse, which was superimposed by a uniform oscillation with the pulse frequency.

As the first step to gain more understanding of the experimental results a corresponding reference state has to be established. In a parameter range where $c_1 = -0.9$, $c_2 = 0.5$, $\gamma = -1.11$ and the system length, L is equal to 10, traveling pulses with constant shape and speed emerge as the stable solution of Eq. 4.6. Figure 4.89(a) displays these traveling pulses and figures 4.89(b) and (c) present r_n, the moduli of the complex order parameter $|W_n|$, for the modes with $n = 0$ and $n = 1$, respectively.

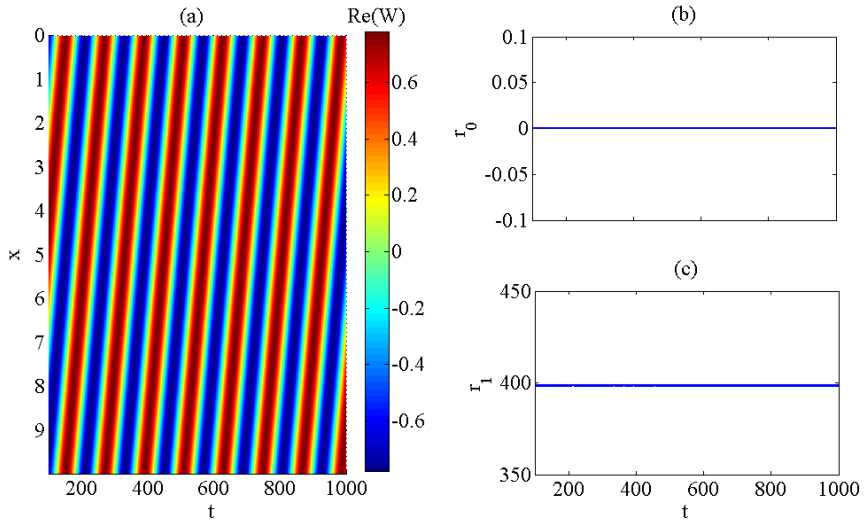

Figure 4.89: *(a) The space-time evolution of the real part of $W(x,t)$ which appear as traveling pulses, (b) and (c) the moduli of the spatially homogeneous mode and the traveling wave spatial mode with $n = 1$, respectively. $c_1 = -0.9$, $c_2 = 0.5$, $\gamma = -1.11$, $L = 10$, $\delta = 0$ and $\nu = 0$.*

From figure 4.89(b) it is clear that the spatially homogeneous mode does not oscillate. The same result was obtained with a realistic model for the electrooxidation of hydrogen in the presence of poisons and negative global coupling [48, 100]. This physical model is based on four variables; the surface coverages of the anions and cations, Φ_{dl} and the copper concentration in front of the electrode. The model also predicts that traveling pulses with constant width and velocity appear at sufficiently large coupling strength and a stationary current density [23, 30]. As already mentioned, this is in contrast to our and former experimentally observed traveling pulses which exhibited slight modulations in width during one rotation along the ring-electrode, accompanied by current oscillations with the same frequency as the

traveling pulses. These modulations were attributed to slight inhomogeneities in the geometry of the ring-electrode or the catalytic activities of the electrode surface [30, 49]. Since in none of our simulations or the previous simulaitons involving the physical model modulated pulses could be obtained, we introduced in the following an inhomogeneity of the local dynamics.

As already mentioned, the parameter c_2 describes the dependency of the frequency of local oscillators on the amplitude of the oscillations. By adding an inhomogeneity this parameter changes to $c_2(x) = c_0 + b(x)$. The inhomogeneity b, was chosen as a Gaussian and is thus described by:

$$b(x) = \eta \cdot \frac{1}{\sqrt{2\pi\sigma^2}} \cdot exp(\frac{-x^2}{2\sigma^2}) \tag{4.7}$$

where σ and η control the width and the height of the inhomogeneity, respectively. Figure 4.90 depicts how c_2 varies in space for $\eta = 1$ and $\sigma = 1$.

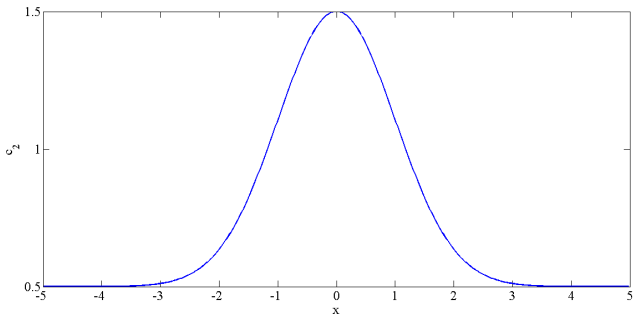

Figure 4.90: *Parameter $c_2(x)$ after addition of a Gaussian function $b(x)$ to account for the local surface inhomogeneities on the ring-electrode which is assumed to have a length L.*

After introducing the space dependence in c_2 into Eq. 4.6, in a wide range of parameters modulated traveling pulses with oscillations of the spatially homogeneous mode appear as the stable solution. Figure 4.91(a) shows an example of such traveling pulses with $\eta = 1$ and $\sigma = 1$. Figure 4.91(c) depicts that the spatially homogeneous mode with $n = 0$, has a non-zero modulus and hence, oscillates. As expected, decreasing the inhomogeneity reduces the modulations. This can be seen in figure 4.91(b) where η and σ are reduced while the other parameters are kept constant. Comparing figures 4.91(c) and (d) reveals that the amplitude of the oscillations of the spatially uniform mode is also influenced by the strength of the inhomogeneity. This leads to smaller amplitudes of $< W >_x$.

Traveling wave solutions can be described as $a_1(\mathrm{t})\sin(\frac{2\pi x}{L}) + a_2(\mathrm{t})\cos(\frac{2\pi x}{L})$, where $a_1(t) = a_2(t \pm T/4)$. When using this presentation, it becomes obvious that the presence of the local inhomogeneity results in slight amplitude differences of about 10% between the amplitudes of the $a_1(t)$ and $a_2(t)$, respectively.

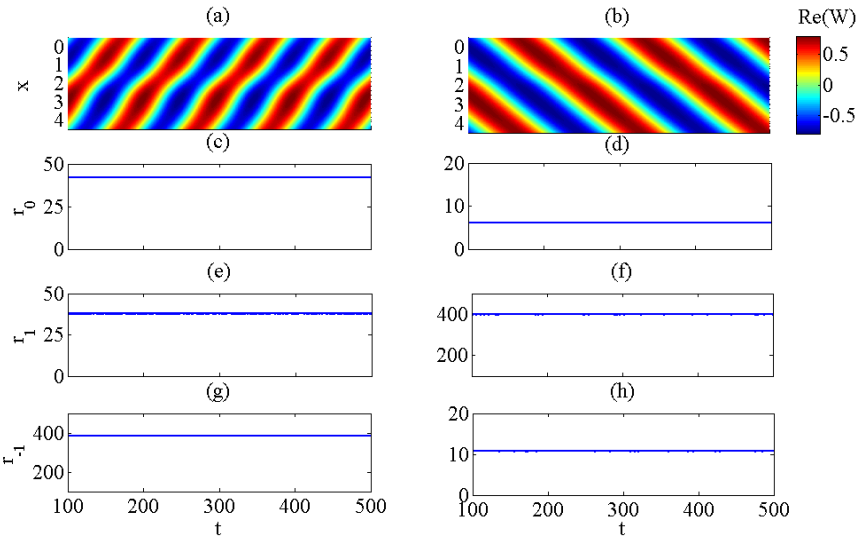

Figure 4.91: *Upper plate: The real part of $W(x,t)$ presenting modulated traveling pulses (a) with large surface inhomogeneity $\eta = 1$ and $\sigma = 1$ and (b) with small inhomogeneity $\eta = 0.2$ and $\sigma = 0.5$. (c) and (d) present the moduli of periodic solutions with $n = 0$, (e) and (f) show the moduli of periodic solutions with $n = 1$ and (g) and (h) show the moduli of periodic solutions with $n = -1$, corresponding to (a) and (b). $c_1 = -0.9$, $c_0 = 0.5$, $\gamma = -1.11$, $L = 10$, $\delta = 0$ and $\nu = 0$.*

Figure 4.92(a) and (b) depict traveling pulses resulting from the simulations in the presence of a local inhomogeneity and a typical example of traveling pulses which appeared in the experiments during the oscillations of the unforced electrochemical system, respectively. One can see that the simulated traveling pulses reproduce the width modulations and the slight non-uniformities in the height of the experimentally measured pulses well. The slight difference between the oscillation amplitude of $a_1(t)$ and $a_2(t)$ was also observed experimentally.

The simulations reveal also that the presence of slight inhomogeneities on the surface results in the activation of spatial modes with $n > 1$ (or $n < -1$), however, with a small amplitude. Figures 4.93(a) and (b) depict the time evolution of the diffusion term in Eq. 4.6 in the Fourier space, for the first 10 spatial modes of the spatiotemporal pattern, in the absence and presence of a local inhomogeneity, respectively. One can see that before introducing the local unevenness except for the spatial mode

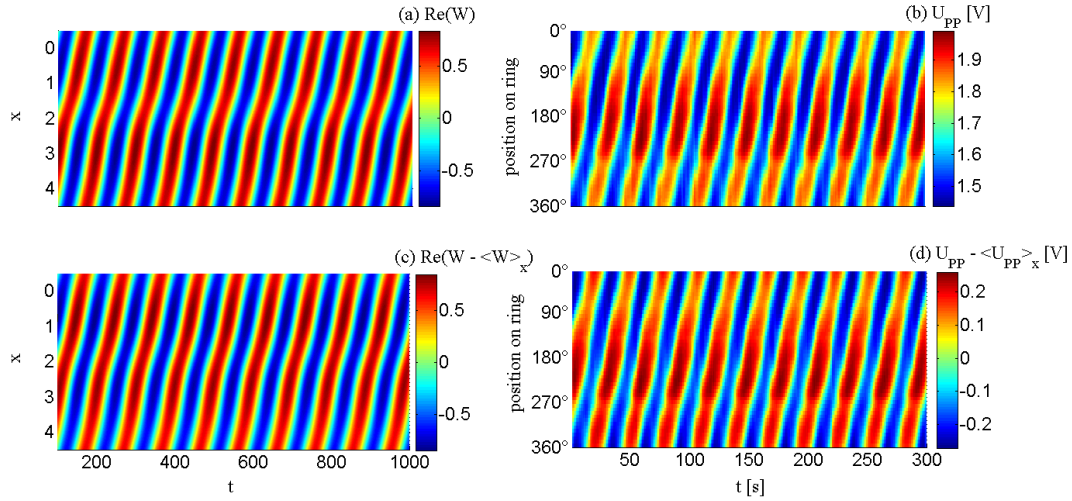

Figure 4.92: *Traveling pulses (a) obtained in the simulation in the presence of surface inhomogeneity:* $\eta = 1$ *and* $\sigma = 1$*, before applying a forcing, (b) observed experimentally for the unforced electrochemical oscillating system in the presence of negative global coupling, (c) and (d) after subtraction of the spatially uniform mode corresponding to (a) and (b), respectively.* $c_1 = -0.9$, $c_0 = 0.5$, $\gamma = -1.11$, $L = 10$, $\delta = 0$ *and* $\nu = 0$.

with $n = 1$ all other modes have no contribution to the inhomogeneous part of the equation and their diffusion term is zero. However, figure 4.93(b) reveals that in the presence of the local inhomogeneity, in addition to the mode with $n = 1$, the 3 following higher modes with $n = 2, 3$ and 4 are also activated and thus, have a small contribution to the traveling waves dynamics. Hence, despite the low contribution of the spatial modes with $n > 1$ to the dynamics, compared to the spatial modes with $n = \pm 1$, considering their influence is necessary for describing the system.

The above presented simulation results confirm the assumption presented in the literature [30,49], that for a perfectly uniform surface the spatially homogeneous mode is not excited by a traveling pulse (figure 4.89(b)). Only when introducing a local surface inhomogeneity, the spatially homogeneous mode starts oscillating. In figures 4.91(e) and (h) one can see that the presence of the inhomogeneity also activates the traveling pulse which propagates in the opposite direction and hence, the contribution of the traveling pulse with an opposite wave number is larger than zero. It is the interaction between the traveling wave with the opposite wave number and the spatially uniform mode which excites the oscillation of the spatially uniform mode. However, comparing figures 4.92(a) and (b) with figures 4.92(c) and (d) which display traveling pulses with and without the spatially uniform mode, indicates that the subtraction of the spatially uniform mode decreases the width modulations of

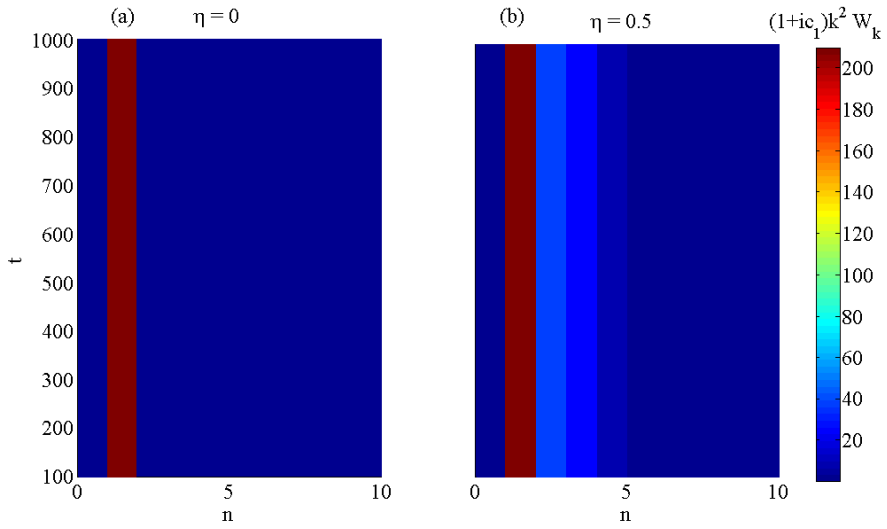

Figure 4.93: *The time evolution of the diffusion term in Fourier space, with* $k_n = \frac{2\pi n}{L}$*, for modes with* $n = 0...10$*, where* $n = 0$ *represents the spatially homogeneous mode, (a) in the absence of the local inhomogeneity and (b) in the presence of a local inhomogeneity with* $\eta = 0.5$ *and* $\sigma = 1$*.* $c_1 = -0.9$*,* $c_0 = 0.5$*,* $\gamma = -1.11$*,* $L = 10$*,* $\delta = 0$ *and* $\nu = 0$*.*

the pulse during one rotation, but it does not eliminate them. The remaining modulations can be attributed to the influence of the spatial modes with higher wave numbers which are activated due to the presence of the local inhomogeneities (figure 4.93(b)).

4.5.3 The 1:1 resonance region

In order to investigate the response of the oscillating system to a time-periodic external forcing, the forcing strength,γ, and the frequency mismatch, ν, are varied. For the 1:1 resonance tongue $m = 1$ in Eq. 4.5 and thus the forcing term is the constant δ. The simulations were performed in a parameter region where $c_1 = -0.9$, $c_0 = 0.5$, $\gamma = -1.11$ and $L = 10$, unless mentioned otherwise.

Figure 4.94 depicts 1:1 resonance tongue calculated for the spatially uniform system. Standing waves are the only locked solutions of Eq. 4.6. Outside the resonance region, when the frequency mismatch, ν, is negative the system exhibits only traveling patterns whereas for positive ν close to the border of the entrainment band the unlocked solutions are standing patterns and only at higher values of frequency mismatch unlocked traveling patterns appear. Considering the variety of qualitatively different entrained solutions which were experimentally observed inside the

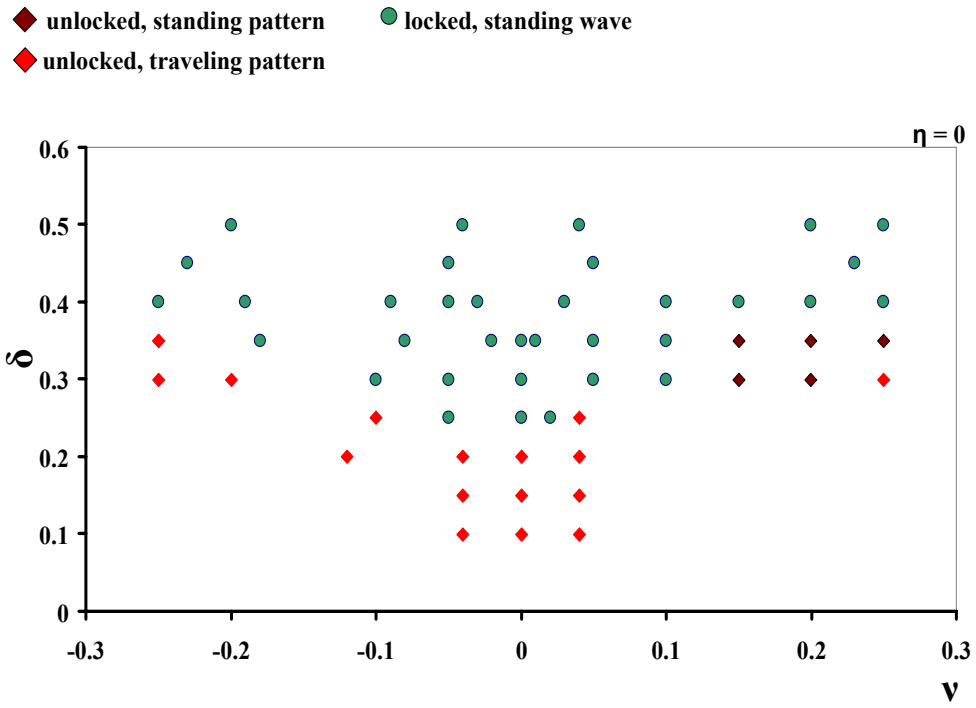

Figure 4.94: *Different responses of the system in the 1:1 resonance region, depicted in the frequency mismatch-forcing strength plane measured for a homogeneous electrode surface.* $\eta = 0$.

1:1 resonance regime, the entrainment band in figure 4.94 is not in agreement with the experimentally observed results shown in this chapter. This confirms that a perfectly uniform surface does not represent the experimental condition.

Now, the important question is to find the right parameters η and σ which resemble the surface inhomogeneities that reproduce the experimental conditions. Hence, the response of the dynamical system to a 1:1 forcing was investigated for different inhomogeneity values. Figure 4.95 depicts the 1:1 entrainment band for a small surface unevenness with $\eta = 0.2$ and $\sigma = 0.5$.

When the externally applied forcing is weak, entrained pulses are the only locked response that is prevailed by the system. By increasing the forcing strength, asymmetrically entrained responses and standing waves appear too. At moderate forcing strength, standing waves are only observed at one side of the resonance regime, while at higher values of δ standing waves appear on both sides. Above a certain forcing strength, standing waves are the only entrained response observed for the system. At moderate and high forcing strength half entrained responses occur in addition. The tongue shaped entrainment band is asymmetric, in terms of the width

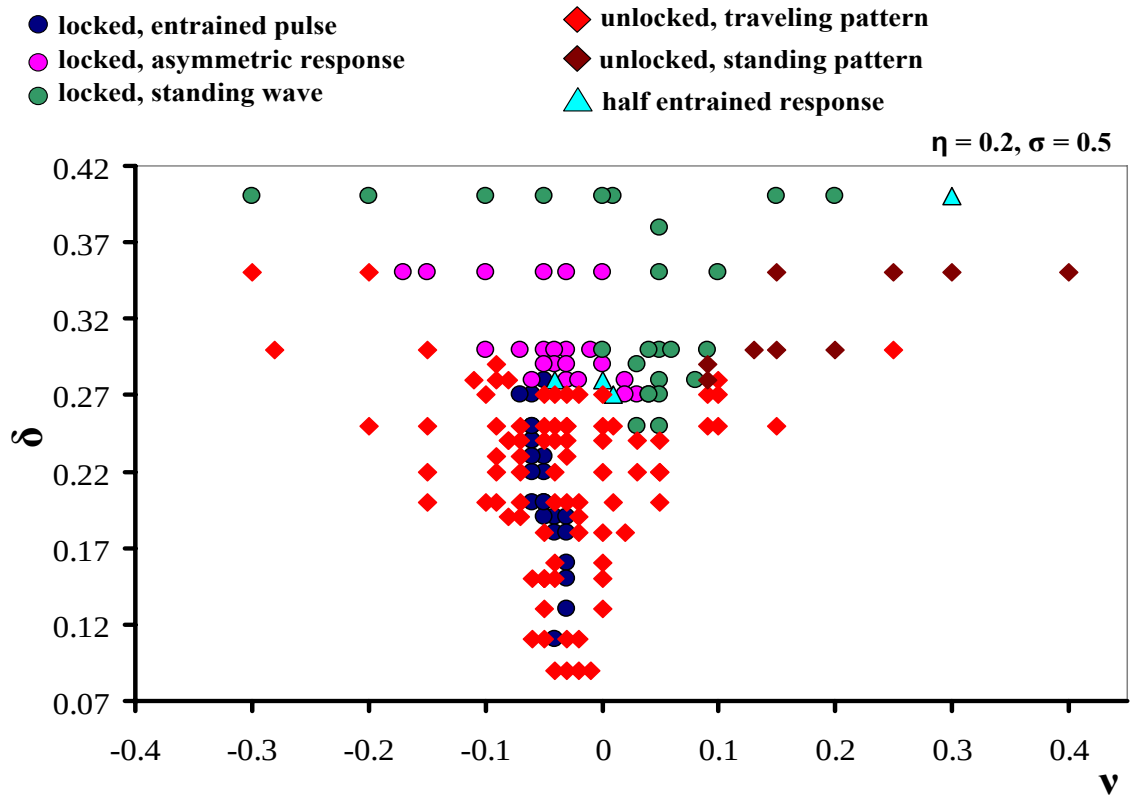

Figure 4.95: *Different responses of the system in the 1:1 resonance region, depicted in the frequency mismatch-forcing strength plane, in the presence of surface inhomogeneity:* $\eta = 0.2$ *and* $\sigma = 0.5$.

of the entrainment regimes around $\nu = 0$, and also in terms of the types of responses that appear. The experimentally observed entrained pulses and the asymmetrically entrained responses also appeared in the 1:1 entrainment band. Hence, in contrast to a uniform medium, a Gaussian distribution of local parameters reproduces these features. However, as shown in figure 4.19 in the experiments at a constant forcing amplitude both entrained pulses and asymmetric responses were found whereas in figure 4.95 at a given forcing strength either entrained pulses or asymmetrically entrained responses occur. The only exception is seen at $\delta = 0.28$ where asymmetrically entrained responses appear in a very narrow region, close to entrained pulses. Moreover, contrary to the experimentally measured 1:1 resonance region, the entrainment band in figure 4.95 does not become broader with increasing forcing strength. Another clear difference between the responses in figure 4.95 and the experimentally measured ones is the appearance of unlocked responses within the resonance region at $\delta = 0.27$. These points indicate that with the selected inhomogeneity parameter values many experimental observations cannot be reproduced.

In the following the impact of the inhomogeneity parameters on the dynamics is investigated further. Figure 4.96 depicts the 1:1 entrainment band which results from introducing a broader local inhomogeneity with $\sigma = 1.5$ and $\eta = 0.2$. One can see that the stable synchronous solutions of the system are similar to those observed in figure 4.95, and also in this parameter regime, the simultaneous existence of entrained pulses and asymmetrically entrained responses at a fixed forcing strength is not observed.

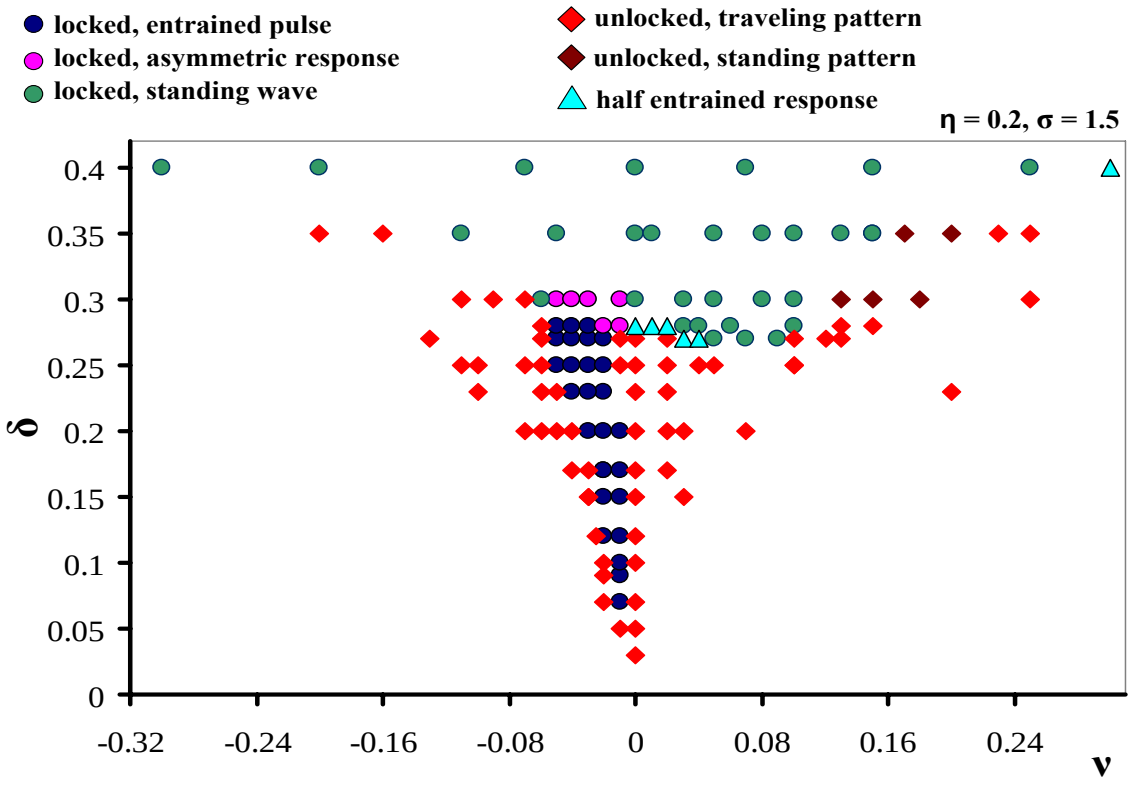

Figure 4.96: *Different responses of the system in the 1:1 resonance region, depicted in the forcing strength-frequency mismatch plane in the presence of surface inhomogeneity:* $\eta = 0.2$ *and* $\sigma = 1.5$.

Figure 4.97 shows another 1:1 resonance region, simulated with $\eta = 1$ and $\sigma = 1$. Comparing this figure with figures 4.95 and 4.96 it becomes evident that the width and height of the local inhomogeneity do not influence the types of stable entrained solutions that appear. However, one can see that at larger unevenness (figure 4.97) entrained pulse solutions appear in a broader region at fixed values of forcing strength. Furthermore when the forcing strength is between $\delta = 0.2$ and 0.37, variation of frequency at a fixed forcing strength results in the appearance of both entrained pulses and asymmetrically entrained responses. When $\delta < 0.2$ entrained

pulses are the only stable solution of the system. These results are in good agreement with the experimental observations shown in figure 4.19.

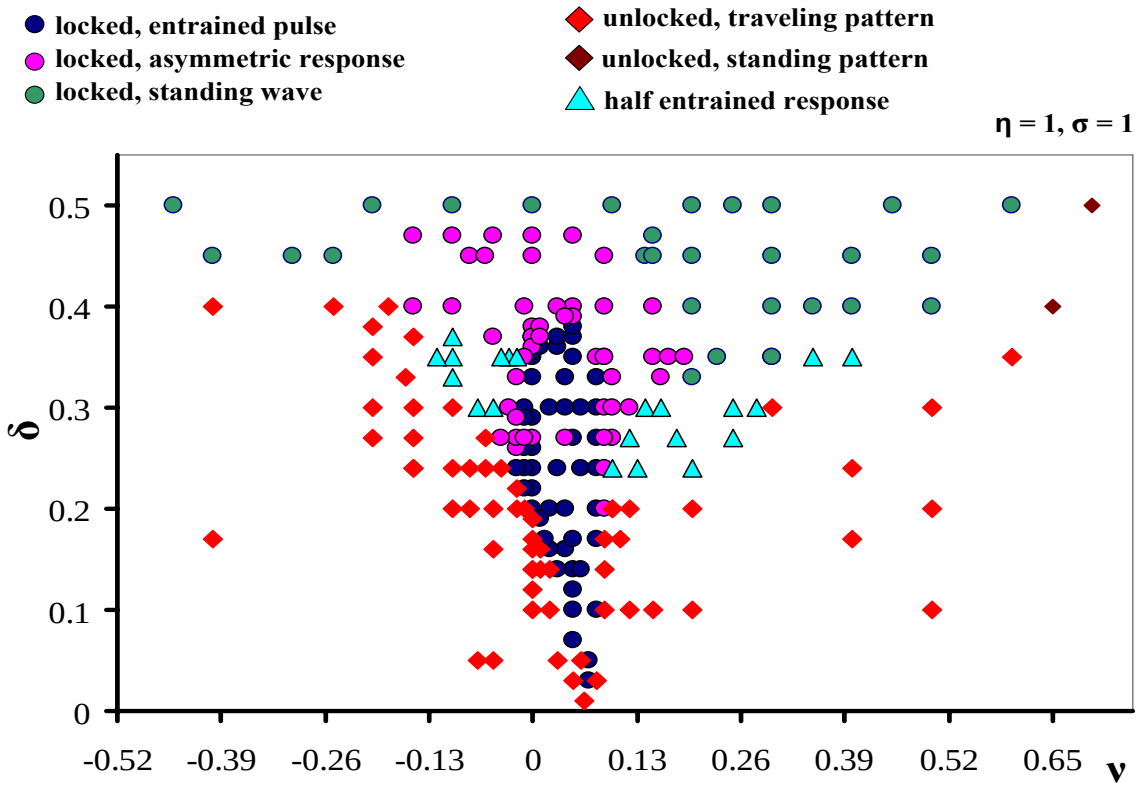

Figure 4.97: *Different responses of the system in the 1:1 resonance region, depicted in the frequency mismatch-forcing strength plane, in the presence of surface inhomogeneity:* $\eta = 1$ *and* $\sigma = 1$.

As can be seen in figure 4.97 for the forcing strengths between 0.20 and 0.25, the asymmetrically entrained responses appear only at one side of the entrainment band close to the border. When increasing the forcing strength they appear on both sides but still only close to the borders of the synchronization region. Interestingly, in this parameter range the transition from synchronous to asynchronous behavior happens through the appearance of half entrained responses whereas at lower forcing strength the entrained pulses change to unlocked traveling structures as the border is crossed. At higher forcing strengths standing waves appear within the 1:1 entrainment band, too. Comparing these theoretical predictions with our experimental results, we observe a discrepancy. The half entrained responses and the standing waves are not observed in the experiments. The reason may be that the half entrained responses occur only within a narrow parameter region on the border, where no measurements where performed. Moreover, apparently the highest experimentally applied forcing

strength was still not high enough for the occurrence of the standing waves observed in figure 4.97.

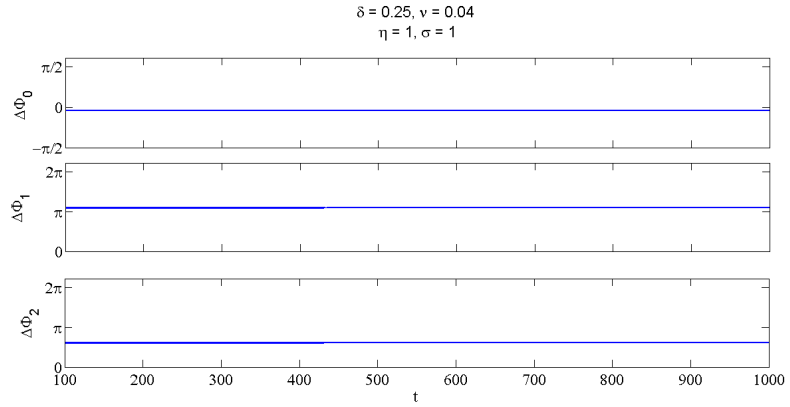

Figure 4.98: *The time evolution of the phase difference between the forcing signal and (a) the spatially homogeneous mode, (b) and (c) the time dependent coefficients of the first and second traveling wave spatial modes, respectively which correspond to an entrained pulse obtained in a parameter region with.* $\eta = 1$, $\sigma = 1$, $\delta = 0.25$ *and* $\nu = 0.04$.

Figure 4.98(a), (b) and (c) show the evolution of the phase difference between the forcing signal and the spatially homogeneous mode, $a_1(t)$ and $a_2(t)$ for an entrained pulse from figure 4.97, respectively. As expected for entrained pulses, the phase difference between $\Delta\Phi_1$ and $\Delta\Phi_2$ is 90 °, however, the amplitude of $a_1(t)$ and $a_2(t)$ are not exactly equal, due to the imperfection caused by the local inhomogeneity in the unforced pulse. Still, the asymmetrically entrained responses can be distinguished from the entrained pulses by the considerably large amplitude difference between $a_1(t)$ and $a_2(t)$.

A noticeable feature of the experimental 1:1 resonance regime was that outside the resonance tongue the homogeneous mode was entrained for higher forcing strength but not at low forcing strength. The evolution of the phase difference between the forcing signal and the spatially homogeneous mode in simulations with $\delta = 0.1$ outside the resonance region is unbounded. However, at $\delta = 0.17$ the spatially homogeneous mode locks to the forcing in the entire frequency region. Figure 4.99 and 4.100 show the advances of $\Delta\Phi_0$ for forcing strengths of 0.1 and 0.17, respectively.

Figure 4.101 and 4.102 depict the advances of the phase difference between the forcing signal and $a_1(t)$ and $a_2(t)$ with time, for the responses shown in figure 4.97, at $\delta = 0.17$. These two figures are comparable with those obtained experimentally for the 1:1 forcing parameters (figures 4.13 and 4.14). In both experiments and simu-

lations the growth rate of $\Delta\Phi_1$ and $\Delta\Phi_2$ increase with increasing distance from the resonance region. However, it was shown in the experiments that the system did not exhibit critical slowing down close to the resonance tongue. The phase difference between the forcing signal and the coefficient of the traveling wave spatial modes grew continuously, with slight non-uniformities but without exhibiting clear phase slips. This observation is obviously in contrast to the well known scenario for single oscillators, where the saddle-node bifurcation that takes place at the borders of the synchronous regime results in the occurrence of critical slowing down (see section 2.5). Another contradiction to this scenario is the absence of π phase shift of $\Delta\Phi_1$ and $\Delta\Phi_2$ when moving from one border of the entrainment band to the other. Figure 4.28 and 4.29 showed that within the 1:1 entrainment band $\Delta\Phi_1$ and $\Delta\Phi_2$ stay constant, independent of the applied forcing frequency. The π phase shift was only observed for $\Delta\Phi_0$ at low forcing amplitude (figure 4.27). Hence, these observations suggest that the transition from the synchronous to the asynchronous state does not take place through a saddle-node bifurcation. In contrast, in the simulations indications that the border of the resonance tongue is formed by a saddle-node bifurcation, are obtained. The growths of $\Delta\Phi_1$ and $\Delta\Phi_2$ with time are highly non-uniform and exhibit phase slips of about $3\pi/2$ and slow motion of the trajectory over a phase angel of $\pi/2$. These phase slips can be clearly seen in figure 4.103. For larger values of ν the growth becomes less non-uniform and the phase slips become smaller. Yet, there are also features which cannot be understood immediately. When transversing the resonance region, $\Delta(\Delta\Phi_1)$ and $\Delta(\Delta\Phi_2)$ are non-zero, but not equal to π, as expected for systems which lose or gain synchronization through a saddle-node bifurcation at the borders. Furthermore, the values of $\Delta(\Delta\Phi_1)$ and $\Delta(\Delta\Phi_2)$ are

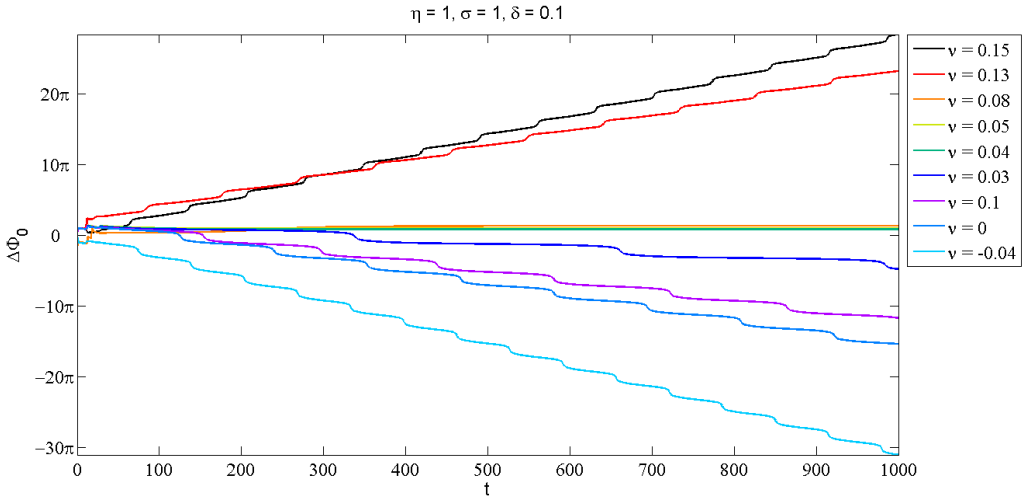

Figure 4.99: *Advances of the phase difference between the spatially uniform mode and the forcing signal, calculated for $\eta = 1$, $\sigma = 1$ (figure 4.97), for $\delta = 0.1$.*

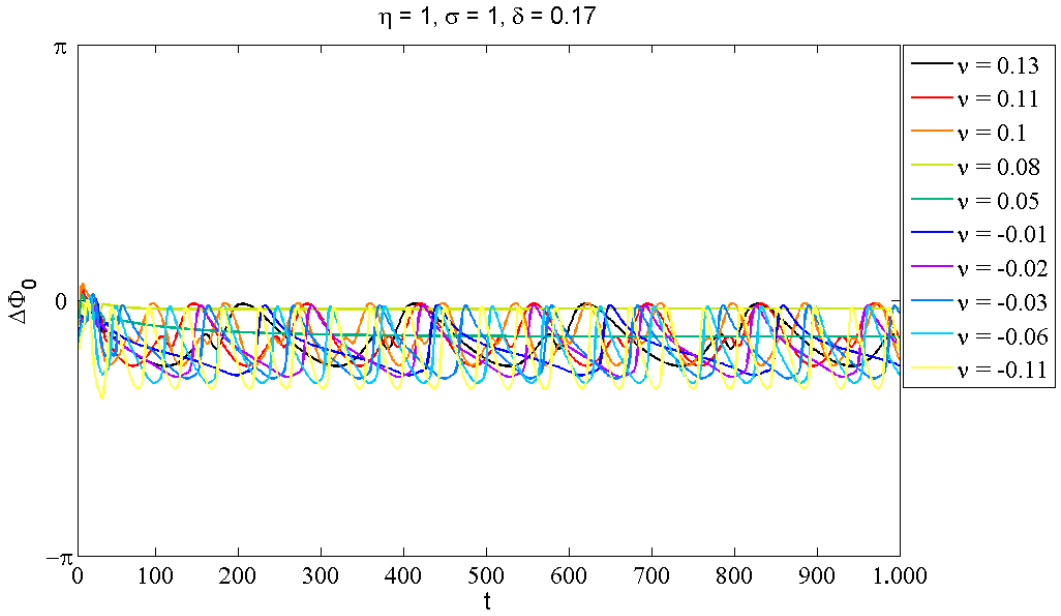

Figure 4.100: *Advances of the phase difference between the spatially homogeneous mode and the forcing signal, calculated for* $\eta = 1$, $\sigma = 1$ *(figure 4.97), for* $\delta = 0.17$.

different at different forcing strengths. The experimentally observed π phase shift of $\Delta(\Delta\Phi_0)$ was not theoretically found either.

These results show that although the theoretical observations exhibit similarities to the dynamics observed for single oscillators, both experimental and theoretical results exhibit features that differ from it and their understanding requires further experimental and theoretical investigations which were beyond the scope of this thesis.

Another experimentally observed feature of the 1:1 resonance region which is worth investigating theoretically, is the existence of a pitchfork bifurcation within the entrainment band (figures 4.25 and 4.26). Figure 4.104 presents the changes of the difference between the amplitude of $a_1(t)$ and $a_2(t)$ with ν, for the entrained responses at $\delta = 0.27$ in figure 4.97. From this figure it is obvious that a supercritical pitchfork bifurcation takes place within the simulated 1:1 resonance region, depicted in figure 4.97. Here it should be mentioned that, the experimental results as well as the results of the simulations show that the effect of the local inhomogeneities, and correspondingly the width modulations, is also reflected in the amplitudes of the time dependent coefficients of the sine and cosine-shaped spatial profiles, a_1 and a_2. Due to the presence of the inhomogeneities, the amplitudes of a_1 and a_2 differ about 5% for symmetric pulses, whereas in the absence of the inhomogeneities the amplitudes of the two time dependent coefficients are equal, as expected for perfect

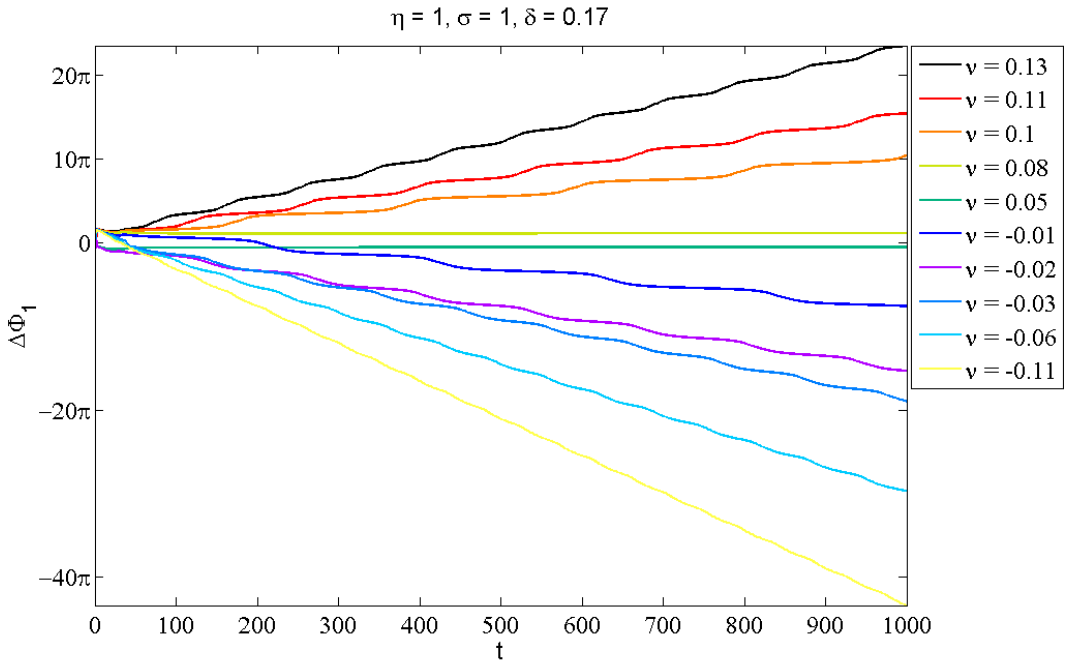

Figure 4.101: *Advances of the phase difference between the first traveling wave spatial mode and the forcing signal, calculated for $\eta = 1$, $\sigma = 1$ (figure 4.97), for $\delta = 0.17$.*

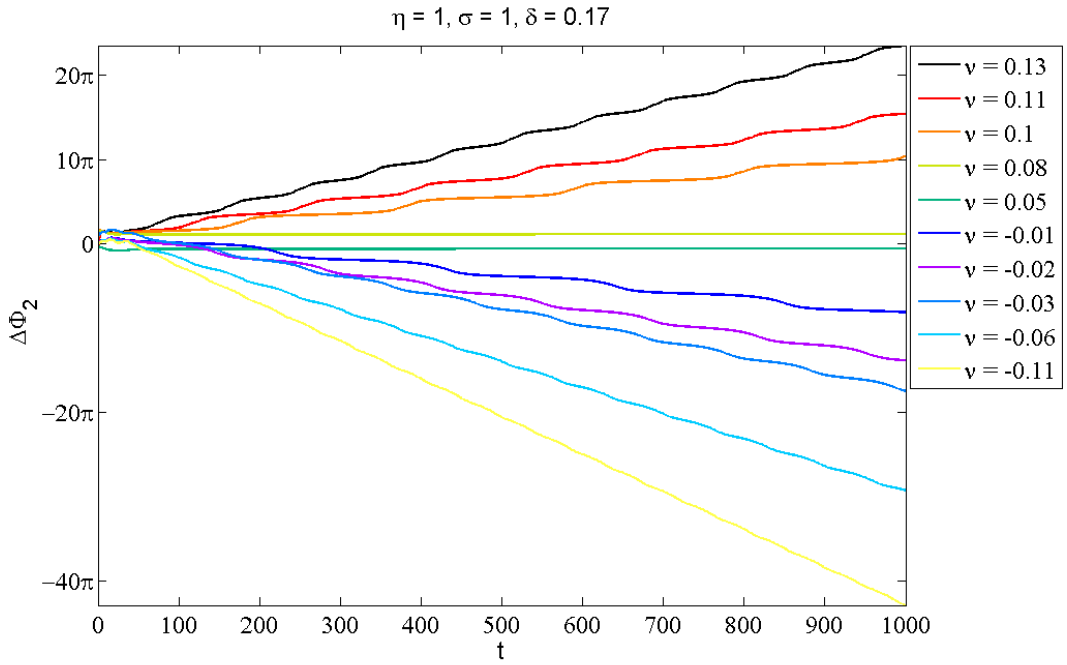

Figure 4.102: *Advances of the phase difference between the second traveling wave spatial mode and the forcing signal, calculated for $\eta = 1$, $\sigma = 1$ (figure 4.97), for $\delta = 0.17$.*

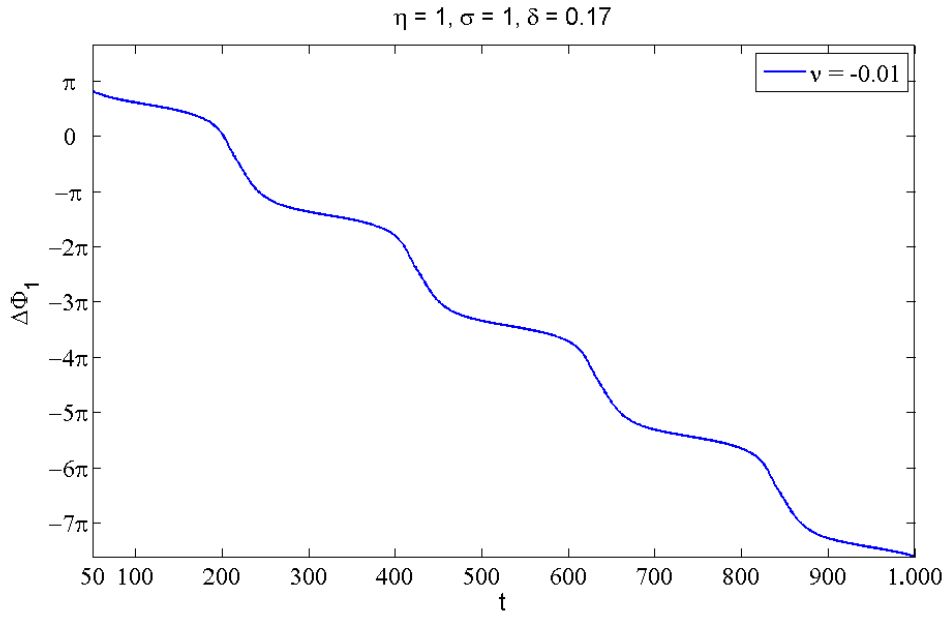

Figure 4.103: *Phase slips observed close to the border of the entrainment band depicted for* $\nu = -0.01$ *in figure 4.101.*

traveling pulses. This slight asymmetric behavior of a_1 and a_2 can be easily observed in the experimentally and theoretically obtained bifurcation diagrams (figures 4.26 and 4.104) since the values marked in green, which correspond to the entrained pulses, are larger than zero. The bistability between the asymmetrically entrained responses and the locked pulses which appears at $f_f/f_0 = 1$ for forcing amplitude of 40 mV, in figure 4.19 was not reproduced in the simulations. Hence, the subcritical pitchfork bifurcation observed for forcing strength of 40 mV was not found either. Moreover, one can see in figure 4.104 that the growth of the amplitude difference in the theoretically obtained bifurcation diagram does not follow the square root behavior, as it was observed in the experiments and is expected for a pitchfork bifurcation.

4.5.4 The 2:1 resonance region

The dynamics of the forced system inside the 2:1 resonance region was found to be by far less sensitive to the applied forcing amplitude than in the 1:1 Arnold tongue. Within the 2:1 entrainment band standing anti-phase oscillations are the most common locked solutions of the system. Asymmetrically entrained responses were also observed in a narrow parameter region.

With Eq. 4.6, the 2:1 resonance region of this system can be theoretically studied as well. It is clear that when the forcing frequency is twice the natural frequency, m

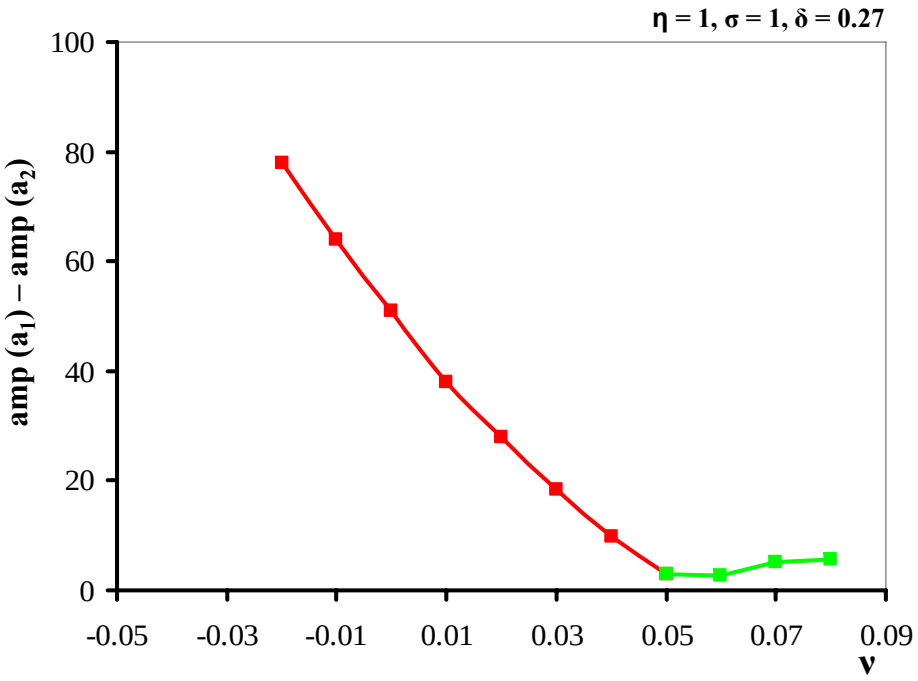

Figure 4.104: *The bifurcation diagram depicting the pitchfork bifurcation observed within the 1:1 resonance regime calculated for $\eta = 1$, $\sigma = 1$ (figure 4.97), for forcing strength of $\delta = 0.27$. The red square symbols stand for the asymmetrically entrained responses and the green points represent the entrained pulses.*

in Eq. 4.6 is equal to 2. Thus, the forcing term is $\delta \cdot W^*$. Figure 4.105 presents the tongue shaped 2:1 entrainment band for the inhomogeneity parameters that best fit the experimentally observed results.

Figure 4.105 shows that the resonant patterns predicted by the simulations are in good agreement with those observed experimentally and depicted in figure 4.49. However, the behavior of the spatially uniform mode marks a significant difference between the experimentally and theoretically obtained results. It was shown that during the experiments, the spatially homogeneous mode always oscillated in phase with the external forcing, in the entire frequency region inside and outside the entrainment band (figure 4.40). This locking behavior is not found in the simulations. The results of the simulations showed that the spatially homogeneous mode only locks within the 2:1 entrainment band.

Considering the behavior of the system close to the borders of synchronization region, the experimental and theoretical observations are very similar to the what was

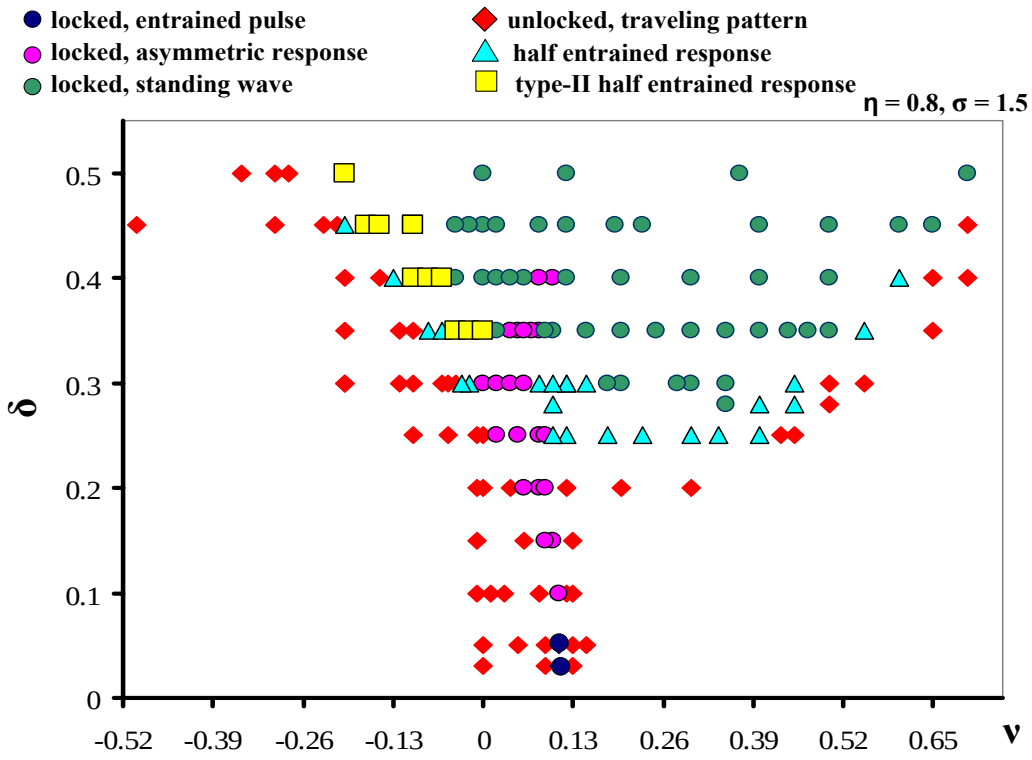

Figure 4.105: *Different responses of the system in the 2:1 resonance region, depicted in the frequency mismatch-forcing strength plane, in the presence of surface inhomogeneity:* $\eta = 0.8$ *and* $\sigma = 1.5$.

shown for the 1:1 entrainment band. The advances of $\Delta\Phi_0$, $\Delta\Phi_1$ and $\Delta\Phi_2$ outside the 2:1 entrainment band show the same trends shown for the 1:1 entrainment band in figures 4.99, 4.101 and 4.102. Also here, in the vicinity of the 2:1 resonance regime the growth of $\Delta\Phi_0$, $\Delta\Phi_1$ and $\Delta\Phi_2$ are highly non-uniform, exhibiting phase slips and thus, critical slowing down. However, figure 4.106 depicts that close to the 2:1 entrainment bands the phase slips are slightly larger than $\pi/2$ which, together with the slowly moving period amounts the π phase slips observed for single oscillators close to the border of the 2:1 entrainment band. When moving from one side of the entrainment band to the other side $\Delta(\Delta\Phi_0)$, $\Delta(\Delta\Phi_1)$ and $\Delta(\Delta\Phi_2)$ are non-zero but also not equal to the $\pi/2$ phase shift which is observed for single oscillators. Hence, similar to the theoretical results of the 1:1 resonance regime the occurrence of phase slips and critical slowing down in the vicinity of the 2:1 entrainment band suggests the occurrence of a saddle-node bifurcation at the synchronization borders. Yet, the changes of the phase differences $\Delta(\Delta\Phi_1)$ and $\Delta(\Delta\Phi_2)$ are different than expected and cannot be explained yet.

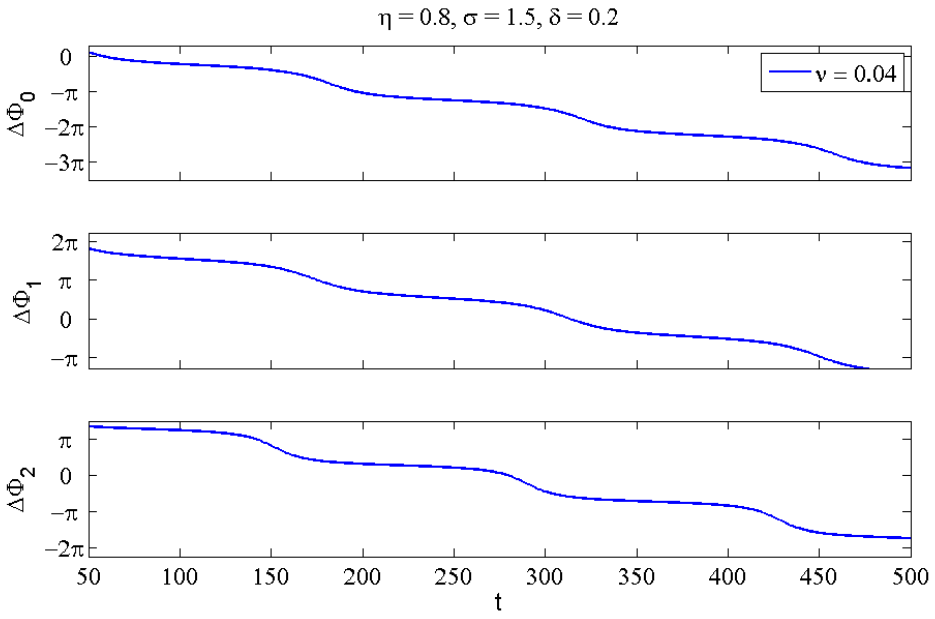

Figure 4.106: *Phase slips observed close to the border of the 2:1 entrainment band depicted for the response at $\delta = 0.2$ and $\nu = 0.04$ in figure 4.105.*

Figure 4.105 shows that the transition from synchronous to asynchronous behavior is through the occurrence of half entrained responses. However, for forcing strength higher than $\delta = 0.35$ a new type of response is found theoretically which was not observed during the experiments. This new type is termed as the *type-II half entrainment* and is marked with yellow squares in figure 4.105. Here, the response corresponding to a standing wave, which locks to the forcing is superimposed by an unlocked uniform mode.

The occurrence of the type-II half entrained responses at the border between the entrained standing patterns and the half entrained responses indicates that in this parameter regime the spatially uniform mode is the first mode to loses synchronization. This is then followed by the lose of synchronization by one of the traveling wave modes, which gives rise to half entrainment. With increasing ν the second traveling wave mode cannot be entrained by the forcing either, resulting in the unlocked traveling structures.

As one can see in figure 4.105 the type-II half entrained behavior only appears at one side of the 2:1 entrainment band. In contrast, the half entrained responses are found on both sides of the entrainment band at the border between the synchronous and asynchronous regions. However, the half entrained responses that appear at negative frequency detuning can be distinguished from those that occur at positive values of ν. Due to the early loss of synchronization in the spatially uniform mode

at negative values of ν, the spatially uniform mode of the half entrained responses in this region is unlocked whereas at positive detuning this spatial mode of the half entrained responses is entrained by the forcing. It is evident that since the spatially uniform mode is always entrained by the forcing during the experiments this phenomenon was not observed experimentally.

At moderate forcing strength such as at $\delta = 0.3$, the half entrained responses also appear at the border between the asymmetrically entrained and standing wave responses. A similar behavior was found during the experiments with 20 mV forcing amplitude. The spatially uniform mode of the theoretically obtained half entrained responses in this region are entrained.

Although the applied forcing amplitude does not affect the type of resonant patterns that appear within the 2:1 entrainment band, it has an influence on the behavior of the system in the asynchronous parameter regime. It was shown in figure 4.49 that outside the 2:1 entrainment band two types of unlocked behavior can be distinguished. The traveling anti-phase oscillations appear only at higher forcing amplitudes whereas for the forcing strength of 20 mV, only breathing pulses prevail. However, in the theoretically obtained unlocked responses only traveling anti-phase oscillations were found.

4.5.5 The 1:2 resonance region

The entrainment region that results from applying a forcing frequency with approximately half of the natural frequency is very narrow at low forcing amplitude. At moderate forcing strength asynchronous responses appear in between locked solutions and hence,it is difficult to distinguish an entrainment region. When the forcing amplitude increases to 80 mV, only unlocked behavior is observed. Comparing the responses to an applied forcing of 20 and 40 mV with that of 80 mV, shows that the dynamics of the driven system at low and moderate forcing amplitudes are almost identical, whereas higher forcing strength of 80 mV changes the behavior of the driven system drastically, such that only irregular spatiotemporal patterns appear. Furthermore, at the latter parameter region two types of irregular responses appear that can be differentiated phenomenologically. The difference between the two types arises due to the differences in their corresponding unforced reference states, where slight changes in the surface quality has increased the local inhomogeneities, which in turn has activeted the higher spatial modes as can be seen in figure 4.80.

The most interesting characteristic of the 1:2 resonance region is that the synchronous and asynchronous spatiotemporal patterns that appear at low and mod-

erate forcing amplitudes are identical and cannot be distinguished only through observing the spatiotemproal patterns. The KL decomposition of the inhomogeneous part of U_{PP} confirms that this spatiotemporal pattern, shown in figure 4.75(c) consists of three spatial modes (figure 4.75(a) and (b)). This feature, distinguishes the 1:2 resonance band from the previously shown 1:1 and 2:1 entrainment regions, where the spatiotemporal patterns of the entrained and unlocked responses looked clearly different from each other and that locking reduced the number of active degrees of freedom in the system from three to two.

Chapter 5

Dynamics in the Presence of Br^- Ions: Stochastic Excursions

In this chapter experiments in the presence of Br^- ions ($Pt|H_2SO_4,Br^-,Cu^{2+}|H_2$) will be presented. The phenomena encountered in these experiments demonstrate differences to measurements carried out with Cl^- ions in a similar parameter range. This points to an active role of the nature of the anion. Here, we observe the random occurrence of global uniform oscillations of the double layer potential and local excursions that are confined to some regions of the ring-electrode. These stochastic phenomena are observed for both the negatively globally coupled and the uncoupled HOR system. In the first section of this chapter different types of oscillations that prevail in this parameter range are introduced. In the second and third section the phenomena of emergence of burst oscillations and the stochastic emergence of the uniform and non-uniform excursions will be presented and discussed qualitatively. The last section sheds light on the influence of external forcing on the stochastic dynamics. The specific experimental details are presented in the caption of the corresponding figures.

5.1 Non-stationary long term dynamics

The HOR system with Br^- as electrosorbing anion exhibits a variety of oscillations. They appear in transient experiments in which the potential is slowly ramped and also in stationary experiments at constant potential. The system is quasi-stationary over 100-200 oscillations, however, when the experiment is run several hours a slight change of parameters in time can be observed. This drift can be best followed by measuring the cyclic voltammogram of the system at different points of time during one measurement day. The alternation of the cyclic voltammograms with time shows a similar trend in all experiments and indicates changes in the dynamics due to the

slow drift of some parameters.

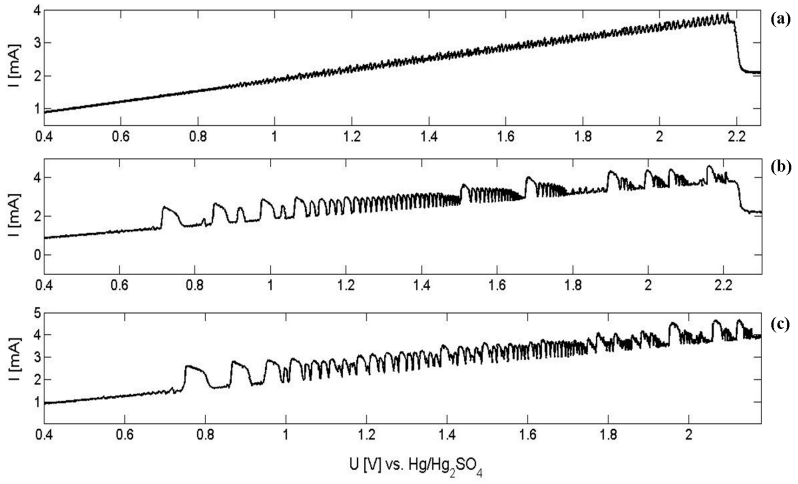

Figure 5.1: *Cyclic voltammograms of a Pt electrode in H_2 saturated electrolyte consisting 0.5 mM H_2SO_4, 0.1 mM $CuSO_4$ and 0.01 mM KBr in the absence of negative global coupling. Scan rate 20 mV/s. (a), (b) and (c) show the changes in the dynamics in the measured sequence. A typical time difference between (a), the first measured and (c), the last measured cyclic voltammogram during one experiment day is is about 7 hours. Intermittent type behavior such as (b) is observed at several times during one measurement day.*

Figure 5.1 displays examples of the cyclic voltammograms recorded at different times. In the beginning, the system either exhibits small fluctuations or low amplitude oscillations. Here, as demonstrated in figure 5.1(a), the oscillation amplitude takes larger values with increasing voltage, which points to an emergence of a limit cycle through a Hopf bifurcation. The decrease in the signal to noise ratio with time, makes the noise dominant and suspends the low amplitude oscillations in further stages of the experiment. The low amplitude oscillations, depicted in figure 5.2(a), are irregular. As already explained in chapter 2, in this parameter range, in the vicinity of the Hopf bifurcation, the self-organized spatiotemporal phenomena of the system are described by the complex Ginzburg-Landau equation (CGLE) and the instability that underly the transition from uniform to spatially instable oscillations are called the Benjamin-Feir (BF) instabilities. At the onset of the oscillations, where the low amplitude oscillations appear, the system can be Benjamin-Feir unstable and is in a weak turbulent regime which can explain the irregularities observed in the low amplitude oscillations [101].

Figure 5.1(b) and (c) show how current-potential scan changes in the course of time. In particular, the onset of oscillations is qualitatively different. Instead of low amplitude oscillations, large amplitude, periodic relaxation oscillations (figure 5.2(d))

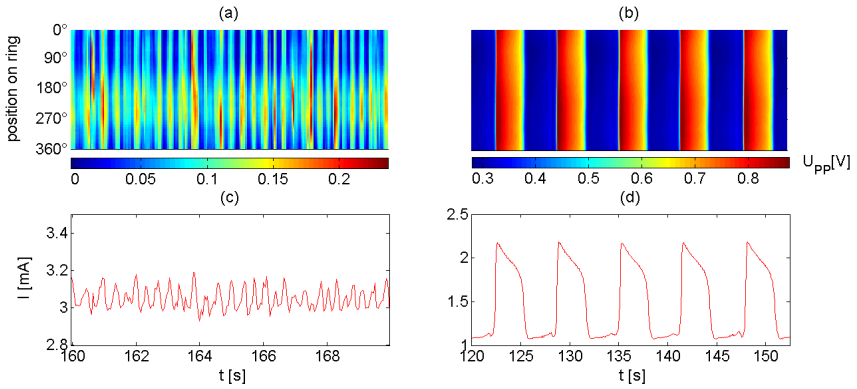

Figure 5.2: *Upper plates: spatiotemporal evolution of U_{PP} for (a) low amplitude oscillations observed at the beginning of a measurement day and (b) relaxation oscillations observed after 4-5 hours, Lower plates: time series of current (c) corresponding to (a) and (d) to (b). Both time series acquired at onset of oscillations. For other experimental details see figure 5.1.*

mark the beginning of the oscillatory regime. Figures 5.2(a) and (b) depict the spatiotemporal patterns that appear during the occurrence of the irregular oscillations and the relaxation oscillations, respectively. One can see that the large amplitude relaxation oscillations (5.2(b)) are spatially homogeneous whereas during the low amplitude irregular oscillations (5.2(a)) some spatial inhomogeneities, though with a low amplitude, occur.

To understand the alternation in dynamics with time, two parameters can be taken into account. It has been shown [24] that the formation and dissolution of oxide layers on Pt surface changes the morphology of the surface and makes it rougher. Thus, the surface quality changes slightly with time. The interaction of the nonlinearities with the inhomogeneities of the surface could give rise to the changes in the dynamics.

On the other hand, while on the surface of the WE Cu^{2+} ions compete with Br^- ions and H_2 for free Pt sites, on the CE, Cu^{2+} is deposited as the counter reaction to that on the WE. This deposition could change the copper concentration in the electrolyte with time and cause changes in the type and origin of oscillations. Wolf et al. presented a series of experiments which confirms this assumption [10]. In their measurements the Cu^{2+} concentration was changed as the concentration of the anion (Cl^-) was kept constant. The resulting cyclic voltammograms showed that for a Cu^{2+} concentration of $1.5\text{x}10^{-4}$ M only irregular small amplitude oscillations are observed. Only by reducing the concentration to $3\text{x}10^{-5}$ M regular, periodic oscillations started to appear. They observed relaxation oscillations at the onset

the oscillations, when the Cu^{2+} concentration was $1.5x10^{-6}$ M. However, calculating the change of Cu^{2+} concentration during the experiments of this work is not straightforward. When the Cu current is diffusion limited the potentiostat shifts the electrode potential to negative values such that H^+ is reduced and hence it is difficult to determine the copper deposition current.

5.2 Burst oscillations

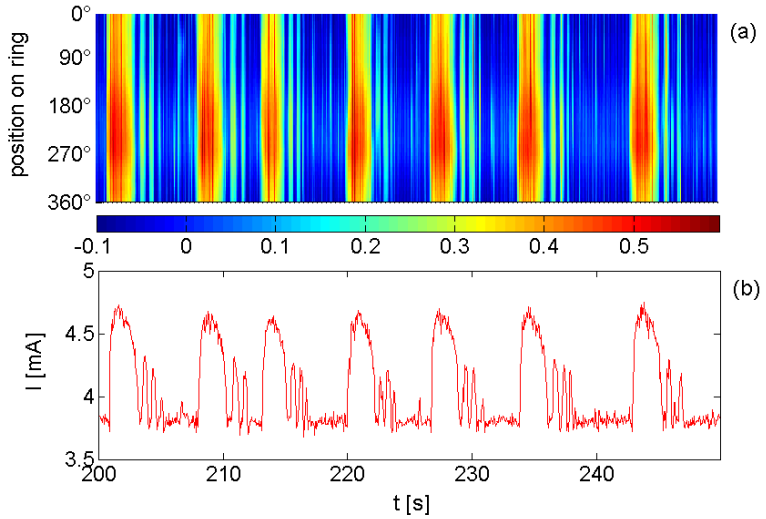

Figure 5.3: *Burst oscillations: (a) Spatiotemporal variations of U_{PP} as a function of time and ring position during the oscillations, (b) the current time series corresponding to (a). Distance from the onset of oscillations 1.25 V. For other experimental details see figure 5.1.*

Looking closer at figure 5.1(b) and (c), we see that at potentials about 1.5 V, oscillations emerge which are a characterized by a first large amplitude uniform peak, followed by a series of high frequency oscillations with lower amplitudes. These type of oscillations are termed burst oscillations. The 'bursting' type periodic behavior is characterized by flares of high frequency oscillations, where oscillations take the form of bursts of action potential, regularly spaced from each other by phases of quiescence [102]. One of the best-characterized examples of this mode of oscillatory behavior is provided by a biological system by the R15 neuron of Aplysia [103, 104]. Other examples can be found during electrodissolution of metals [105, 106]. In phase space the trajectory associated with bursting oscillations takes the form of a limit cycle with several loops, corresponding to as many existing successive peaks.

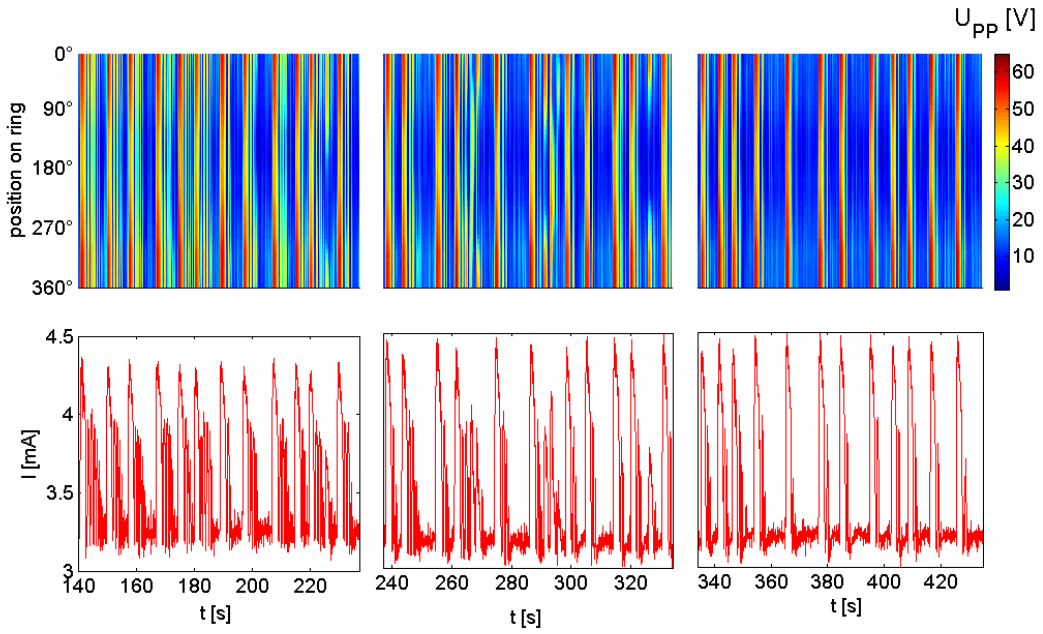

Figure 5.4: *Homogeneous oscillations followed by high frequency oscillations appear as transients. The top row displays the time evolution of the double layer potential as a function of ring position and the bottom row presents the current oscillations with time. The Br^- concentration is $5x10^{-6}$ M and $\gamma = -0.17$. For the other experimental details see figure 5.1.*

Figure 5.3(b) shows an example of burst oscillations observed during the HOR in the presence of Br^-. Emergence of the burst oscillations starts at the intermittent time stage of the experiments, as can be seen in figures 5.1(b) and (c). One can see in figure 5.3(a) and 5.4 (top row) that the fast oscillations which follow the high amplitude oscillation, are spatially uniform.

Inducing a negative global coupling to the system, during the appearance of the burst oscillation and changing the coupling strength showed that the emergence and stability of burst oscillations is not influenced by a desynchronizing coupling.

Furthermore, experiments which were carried out over a long time showed that the burst oscillations appear to be long transients in which we observe a progressive decrease in the number of small peaks that follow the large amplitude spike, with time. Figure 5.4 displays the transition from burst oscillations to uniform high amplitude spikes.

5.3 Stochastic global and local excursions

To gain further understanding of the behavior of the dynamical system in the presence of Br^- ions, in addition to the non-stationary measurements several stationary experiments were carried out in which the potential was kept at a constant value and the current response was recorded. Figure 5.5(c) shows a typical current time series observed during a stationary measurement.

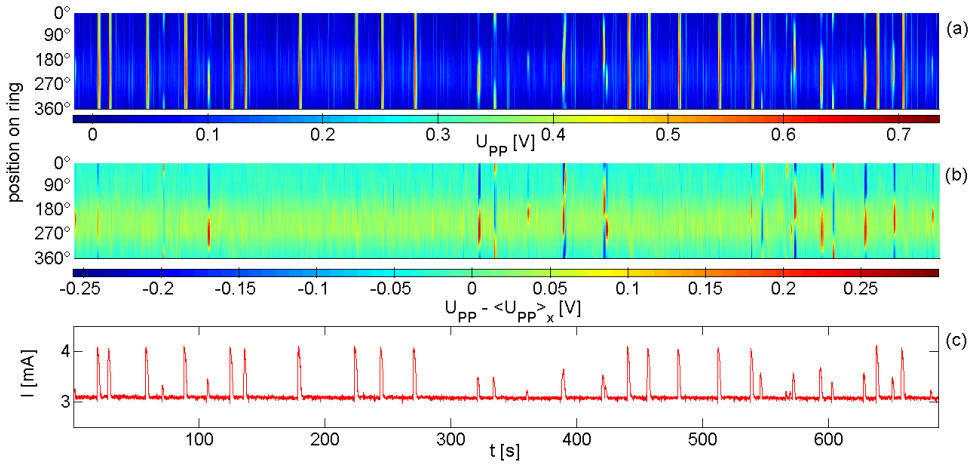

Figure 5.5: *A long stationary measurement showing (a) $U_{PP}(x,t)$, (b) $(U_{PP} - < U_{PP} >_x)(x,t)$ and (c) the current time series corresponding to (a) and (b). Distance from the onset of oscillations: 1 V. For other experimental details see figure 5.1.*

Considering the time series presented in figure 5.5(c) and several similar ones, at different potentials with respect to the onset of oscillations, the oscillation peaks can be mainly divided into two classes, with respect to their amplitudes and the corresponding spatiotemporal pattern that appears during their occurrence. The first type are relaxation like excursions with a high amplitude which are spatially uniform. One current oscillation begins with a sharp and steep increase whose decrease starts slowly and continues fast and gives rise to two flanks that each exhibit sinusoidal structures. During one high amplitude oscillation the entire electrode area makes an excursion and stays spatially uniform. Hence, this type of peaks will be referred to as *global*. The second type, on the other hand, can be easily distinguished by their amplitude which is considerably lower compared to that of the globally uniform excursions. The low amplitude oscillations exhibit a spatial pattern which is confined to a portion of the electrode. Therefore, this type of excursions are termed as *local*. Examples of both globally uniform and local excursions are depicted in figure 5.6. The global and local nature of the patterns are very well observed in figure 5.6(a).

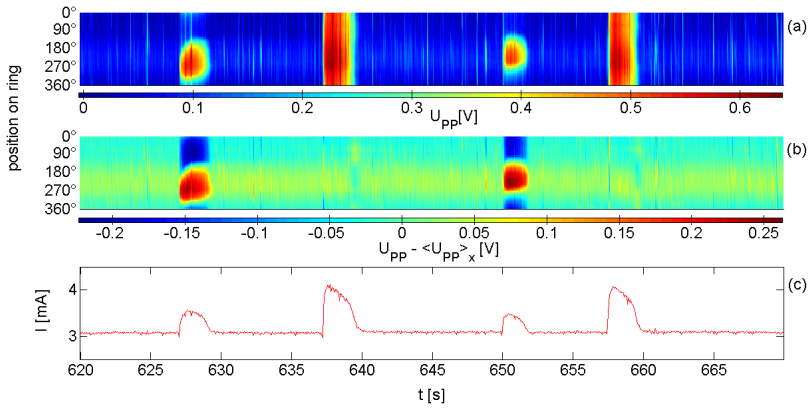

Figure 5.6: *The global and local excursions observed during the oscillations in the presence of Br^-: (a) $U_{pp}(x,t)$, (b) $(U_{pp}- < U_{pp} >_x)(x,t)$, (c) the current time series showing the high and low amplitude current oscillations. Distance from the onset of oscillations: 1 V. For other experimental details see figure 5.1.*

By observing the behavior of the dynamical system in this parameter region over a long period of time it can be elucidated that the appearance of the two types of peaks is a random phenomenon, and hence, contrary to the oscillations observed in the presence of Cl^- ions, these oscillations possess no intrinsic frequency. This in turn, indicates that in phase space no limit cycle exists for this system, in this parameter range. Another interesting aspect of this stochastic phenomenon is the equal possibility of observing spatially uniform global excursions and the spatiotemporal patterns that are confined to a certain region of the ring-electrode. Current time series such as the one shown in figure 5.5(c), which are measured over a long time, provide good statistics of the latter random events. Based on the statistics data, one can study the influence of different parameters on initiation of the excursions and also the favored emergence of a specific type of excursions.

Figure 5.7 shows how the mean frequency value of excursions is influenced by the value of the applied potential i.e., the distance from the onset of oscillations. Moreover, the figure shows how the potential value affects the emergence of the globally uniform and local excursions. One can see as the potential becomes more positive than the onset potential, the total number of excursions increases until a threshold potential difference is reached. At this point the stochastic nature of the excursion vanishes and a periodicity could be observed. A further increase in the difference between the set potential and the onset potential results in the significant decrease of the total number of oscillations, however, the number continues rising with a considerably lower slope. This is depicted in figure 5.7(a) with the blue curve. However, the applied potential does not influence the emergence of a specific type of oscillations. This can be observed in figure 5.7(b) where the ratio of the number of local

excursions to the total number of peaks is depicted. Although in some potential windows the occurrence of the local peaks is favored over the globally uniform ones, no trend could be distinguished.

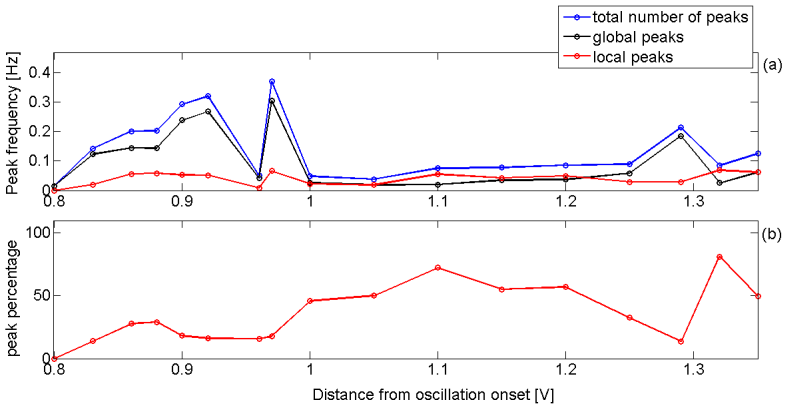

Figure 5.7: *(a) Displays how the occurrence of excursions changes as the potential becomes more positive than the potential at the oscillation onset, (b) shows the change of the ratio of local peaks to the total number of excursions with increasing potential difference. The results were obtained in the absence of NGC.*

5.3.1 Effect of negative global coupling

To gain more knowledge about the parameters that may influence the emergence of the random excursions, or support the occurrence of a certain type of excursion, a negative global coupling was induced to the dynamical system. Considering the desynchronizing effect of a negative global coupling, one could expect that through the addition of a NGC to the system the occurrence of the non-synchronized, local excursions would be favored over the emergence of the globally uniform current spikes. Figure 5.8(a) depicts the mean frequency value of the excursions as the potential increases. Comparing the blue curves in figure 5.7(a) and 5.8(a), it is clear that the mean frequency of the excursions is much less for the coupled system. However, the dependency of the stochastic occurrence of the total number of excursions on the potential shows a similar trend at some parameter range. The total number of excursions (the blue curve in figure 5.8(a)) increases with rather constant slope as the distance to the onset potential becomes larger. It is clear from figure 5.8(b) that despite the high number of global excursions the emergence of local oscillations is favored with increasing potential difference.

Increasing the coupling strength to γ = -0.4, favors the initiation of more excursions and increases the total number of excursions compared to figure 5.8(a). Interest-

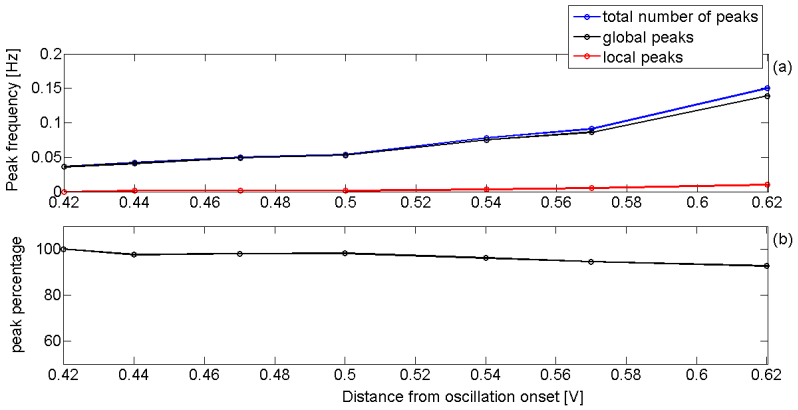

Figure 5.8: *(a) and (b) show the mean peak frequency of random excursions and the ratio of the global peaks to the total number of random oscillations as a function of potential distance from the oscillation onset, respectively. A negative global coupling is added to the system (-0.18 $<\gamma<$ -0.2).*

ingly, at higher desynchronizing coupling, the appearance of local structures is the main phenomenon, hence the ratio of local to global excursions is higher than one in the measured potential windows. Moreover, the presence of the negative global coupling results in inhomogenizing the oscillations such that the high amplitude oscillations are no more spatially uniform and the entire electrode makes a non-uniform excursion. This may show that, a certain strength of the NGC is required for desynchronizing the global uniform excursions and producing more local spatiotemporal patterns. To prove this, however, more experiments with different coupling strengths are required.

5.3.2 Effect of external forcing

In the above mentioned experiments we have observed that in a certain parameter range the HOR system in the presence of Br^- ions demonstrates a reproducible stochastic phenomenon whose occurrence and stability is not significantly influenced by the presence of a destabilizing global coupling. For further understanding of this phenomenon, it would be interesting to know if an opposite effect, namely the addition of an externally applied signal which acts towards the synchronization of the system, affects the stability of the excursions. To investigate that, an external time periodic signal was added to the voltage and the respond of the system was studied. Similar to the experiments presented in chapter 4, the forcing parameters are the frequency and the amplitude of the externally applied signal. A sinusoidal signal with two frequencies, 0.1 Hz and 0.5 Hz, was employed whose amplitudes were changed. It is important to bear in mind that, in the contrary to the HOR system

in presence of Cl^- ions which was discussed in chapter 4, the system studied in this section does not posses an intrinsic frequency and therefore one can not speak of a resonance tongues.

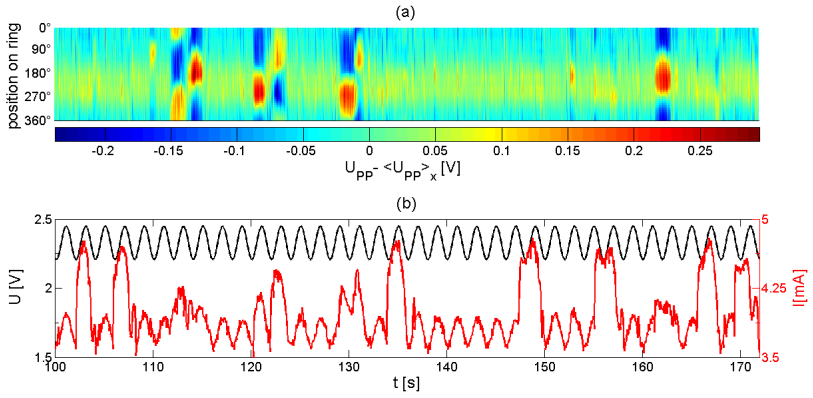

Figure 5.9: *A Sinusoidal signal with 0.5 Hz frequency and 240 mV amplitude was externally added to the voltage. (a) shows the space-time evolution of the inhomogeneous part of the interfacial potential and (b) depicts the external voltage (black curve) and the current time series (red curve). Distance from the onset of oscillations: 1.25 V. For the rest of experimental details see figure 5.1.*

Figure 5.9 shows the response of the globally uncoupled system after adding an external sinusoidal signal to the applied voltage. The sinusoidal signal oscillates with 0.5 Hz and 240 mV amplitude. From this picture it is obvious that neither the spatially uniform peaks nor the local oscillations are influenced by the external perturbation and only the base current is modulated by the forcing. Changing the forcing parameters shows that the external periodic perturbation, which has a global effect, hardly influences the random characteristic of the peak occurrence.

Despite the fact that the system does not entrain to the forcing and the stochastic nature of the phenomenon is preserved, certain forcing parameters seem to favor more frequent excursions. Figure 5.10 displays how the number of excursions changes by increasing the forcing amplitude for the two perturbation frequencies.

At 0.1 Hz, increasing the forcing strength decreases the emergence of the random peaks which contradicts the expected effect of the external forcing. However, by increasing the forcing frequency to 0.5 Hz, the variation with higher forcing amplitudes affects the system and gives rise to more excursions. In this case the potential distance from the onset of the oscillations seems to be less important. The raise in the total number of current spikes can be due to the impact of the variation in the externally applied voltage on the chemical reaction or on the interaction between

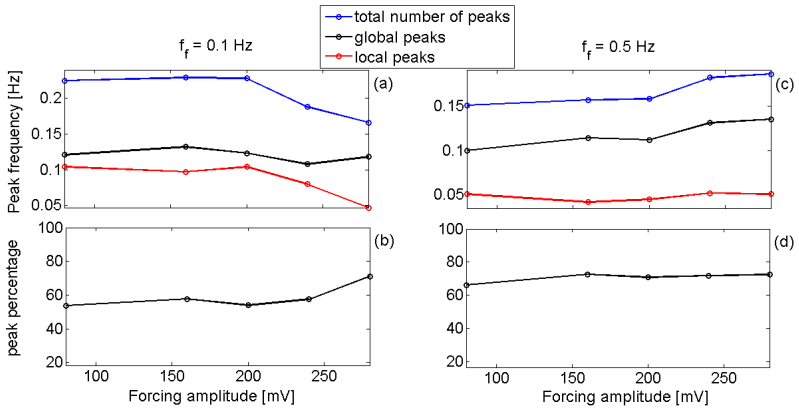

Figure 5.10: *Effect of an externally applied forcing on the occurrence of the random excursions. (a) and (c) show the change in the mean frequency of the excursions with increasing forcing strength, for 0.1 Hz and 0.5 Hz forcing frequencies, respectively, (b) and (d) display the influence of forcing strength on the emergence of global peaks for 0.1 Hz and 0.5 Hz forcing frequencies, respectively. All measurements are performed in the absence of NGC.*

the molecules. This, however, does not impact the type of oscillations and their corresponding spatiotemporal structures at 0.5 Hz.

Another interesting issue to investigate is the response of the dynamical system to the simultaneous presence of a desynchronizing global coupling and an externally applied forcing. Applying the external forcing with low frequency and different amplitudes to the negatively globally coupled system shows that the dynamics of the system are robust against the impacts of the NGC and the external perturbation with 0.1 Hz. In this parameter range, the behavior is very similar to the uncoupled und unforced system and the stochastic phenomenon is preserved. Here, as in the unforced system, the globally coupled system with $\gamma = -0.4$ favors the locally confined patterns over the globally uniform excursions and thus, more local oscillations are observed.

Adding a sinusoidal signal with 0.5 Hz frequency and 80 mV amplitude, keeps the dynamics unchanged and fails to entrain the system. By increasing the forcing amplitude to 160 mV, at a fixed forcing frequency, the system exhibits intermittency between unlocked traveling anti-phase patterns and entrained homogeneous oscillations. The intermittent behavior continues at higher forcing amplitude. Figure 5.11 depicts the traveling anti-phase oscillations observed at forcing strength of 200 mV which are followed by the homogeneous oscillations which oscillate in-phase and with half of the frequency of the forcing signal. The traveling anti-phase patterns observed for this parameter range are very similar to the anti-phase structures dur-

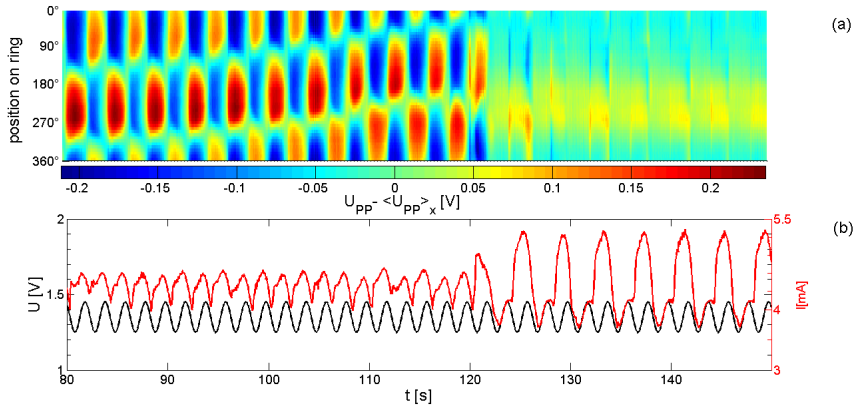

Figure 5.11: *(a) Space-time evolution of ($U_{PP}- < U_{PP} >_x$) showing traveling anti-phase oscillations and homogeneous oscillations, (b) the times series of current (red curve) and voltage (black curve). The externally added sinusoidal signal has a frequency of 0.5 Hz and an amplitude of 200 mV. γ = -0.4. For the rest of the experimental detail see figure 5.1.*

ing 2:1 forcing of the pulses, discussed in chapter 4.

5.4 Summary and Discussion

The focus of the present chapter was the phenomena observed during the electrooxidation of H_2 in the presence of Cu^{2+} and Br^- ions on Pt ring-electrode. During the non-stationary measurements different types of oscillations were observed, which despite slight shifts in the parameters, were persistent. However, observing the stationary behavior of the system indicated that in the presence of Br^- ions, in addition to the burst type oscillations, the oscillations that appear can be classified to two classes: high amplitude, globally spatially uniform and low amplitude excursions which exhibit a spatially confined patterns. These oscillations appear as random events and possess no intrinsic frequency.

The emergence of long amplitude excursions during the oxidation of hydrogen on Pt electrode in presence of Cu^{2+} and Br^- ions is comparable to the behavior of excitable systems. Excitability is a typical dynamic phenomenon of systems far from equilibrium. The common feature of all excitable systems is that they posses a globally attracting rest state where the unperturbed system stays. Addition of a weak perturbation would bring the system away from this state, however, it relaxes back to the resting position without initiating any phenomenon. However, if the perturbation is stronger than a certain threshold, the system leaves the rest state

and makes an excursion in phase space, giving rise to the appearance of spikes, before resting again. As long as the perturbation exceeds the threshold, the amount of it does not influence the spikes [60]. Applying two well separated perturbing signals would give rise to the appearance of two spikes, one after another. Hence, the high amplitude excursions observed in the presence of Br^- ions can be attributed to the large excursions of the system in phase space which is caused by noise. In the excitable systems, if the time interval between the two following perturbations are not large enough, the system does not respond noticeably to the second perturbation and would give rise to the occurrence of a high amplitude spike, followed by a low amplitude peak. The reason is that after each excursion the system takes a certain recovery time before it can react to the second perturbation [107]. However, since the time intervals between the appearance of the global and local oscillations are random, the emergence of low amplitude oscillations cannot be attributed to this effect.

The phenomena observed during the oxidation of hydrogen on Pt ring-electrode in presence of Cu^{2+} and Br^- ions are significantly different from the behavior observed in the presence of Cl^- ions. In chapter 4 it was shown that during the oxidation of hydrogen on Pt ring-electrode in presence of Cu^{2+} and Cl^- ions, nearly uniform, periodic relaxation oscillations appear (see figure 4.1). Although the globally spatially uniform excursions that appear in the presence of Br^- ions are similar to these relaxation oscillations, the emergence of local peaks and, the stochastic nature of the excursions indicates that changing the anion affects the mechanism that gives rise to the oscillations.

Furthermore, experiments in the presence of negative global coupling showed that the stochastic excursions that occurred in the presence of Br^- were not affected by the desynchronizing global coupling significantly, whereas during the oscillations in the presence of Cl^- ions, the presence of a negative global coupling resulted in the appearance of phase pulse which traveled along the ring-electrode.

The response of the dynamical system to an externally applied signal points to another crucial difference between the behavior in the presence of Cl^- and Br^-. In the experiments presented in this chapter it was shown that the synchronizing effect of external forcing does not considerably influence the stochastic phenomenon. This is of course, in contrast to the rich variety of resonant patterns observed in globally coupled electrochemical oscillator in the presence of Cl^- ions. In the presence of Br^- only at high forcing and global coupling strength their simultaneous effect influences the system and gives rise to the appearance of traveling anti-phase oscillations. The traveling anti-phase oscillations are intermittent and are follow by a locked spatially uniform behavior. One can see that contrary to responses observed in chapter 4 ap-

plying the external forcing to this system gives rise to spatially uniform responses. However, one can see that a high strength of the external forcing and the negative global coupling are needed to initiate a change in the dynamics. Considering that in the HN-NDR electrochemical system under the study, the potential takes the role of the activator and that, negative global coupling as well as the external forcing act on the activator, the observations presented in this chapter indicate that the emergence and characteristic features of the globally uniform and local excursions are robust against the perturbations induced to the activator variable of the system.

It should be mentioned that during the few experiments which were performed in a different parameter regime than those presented above, the system exhibited periodic relaxation oscillations and turbulent behavior within various potential windows. However, further experimental studies together with theoretical considerations are required for elucidating the underlying mechanism resulting in the appearance of the stochastic phenomenon and, understanding the role of the anion.

Chapter 6

Summary

The main focus of this work was dedicated to the study of the response of an electrochemical oscillator close to a non-trivial Hopf bifurcation to a spatially uniform, time-periodic external perturbation.

The electrochemical system used to perform the experiments was the oxidation of H_2 on a Pt ring-electrode in the presence of poisons, more precisely Cu^{2+} and Cl^- or Br^- ions. In the presence of Cl^- anions the system exhibits spatially uniform oscillations under potentiostatic measurement control. By compensating part of the cell resistance a negative global coupling induces to the system, which in turn, causes the emergence of traveling phase pulses through a non-trivial Hopf bifurcation of wave number one. The traveling pulses were superimposed by uniform oscillations with the same frequency as the phase pulses. These propagating waves constituted the reference state that was subject to a sinusoidal variations of the applied voltage. The response of the system was studied as a function of frequency and amplitude of the externally applied signal, whereby the focus was on the 1:1, 1:2 and 2:1 resonance regions. Despite of the spatially uniform forcing, the uniform oscillation was never stabilized, in contrast to experiments on oscillatory media close to the trivial Hopf bifurcation [13, 16]. Yet, a Karhunen-Loève decomposition revealed that there were no more than three active degrees of freedom, the spatially uniform mode and the sinusoidal pulse-mode pair, $\Phi(\theta)$ and $\Phi(\theta+\pi/2)$, with θ being the angular variable.

The participation of three spatial modes in the dynamics allowed for four different types of responses: the entrainment of none, one, two or all three spatial modes to the forcing. In this respect, the dynamical system was considered as entrained when all three spatial modes were locked, half entrained when two of the spatial modes were entrained and unlocked when only one or none of the spatial modes was entrained by the external forcing.

Inside as well as outside of the Arnold tongues, the dynamics exhibited unusual features, differing from those found in other forced oscillating systems. The most remarkable of them was the behavior of the phase relation between the oscillations of the coefficients of the three spatial modes and the external forcing. With the exception of a small parameter region close to the 1:1 resonance of low forcing amplitude, the uniform mode always locked in phase to the forcing signal, inside as well as outside of the entrainment bands. The oscillations of the two pulse modes exhibited a constant phase difference to the external forcing inside the entrainment bands. Outside the tongues the phase differences drifted with a constant velocity, thus lacking any sign of a critical slowing down, and, also a saddle-node bifurcation.

Special emphasis was also given to the characterization of the coherent entrained patterns inside the resonance regions. Entrained traveling pulse structures prevailed in the 1:1 region, however in a restricted parameter interval. The loss of the $\pi/2$-time translation symmetry between the oscillations of the pulse-mode pair in a pitchfork bifurcation led to asymmetrically entrained responses. These two types of responses were also observed within the 1:2 entrainment band where they both appeared in the form of breathing pulses. Furthermore, for high forcing amplitudes various intermittent and irregular patterns existed outside the 1:1 and 1:2 entrainment bands, respectively. Within the 2:1 tongue, standing anti-phase oscillations established. In addition, asymmetrically entrained traveling structures were observed within a narrow parameter range inside this resonance regime. Just outside it, half entrained responses with only one of the pulse modes entrained to the external forcing, appeared in the form of modulated standing anti-phase oscillations.

To gain more understanding of the experimental results theoretical simulations were performed, based on the forced complex Ginzburg-Landau equation (FCGLE) on one dimensional domain with periodic boundary conditions. To establish the reference state, a negative global coupling term was added to the CGLE. While a non-trivial Hopf bifurcation could be established that gave rise to a stable pulse solution, the uniform mode was never excited simultaneously with the pulse mode.

A characteristic of the experiments was that the homogeneous mode oscillated always with the propagating frequency of the pulse. This suggested that the electrode surface was not perfectly uniform but exhibited local catalytic variations. When allowing for slight spatial variations of the local oscillator properties in CGLE, the reference state with three active degrees of freedom could be established. In further studies, simulations of the response of this reference system with local parameter variations to time-periodic uniform forcing was investigated.

In the simulations a number of the experimental observations could be reproduced, most noticeably the entrained pulses as well as the pitchfork bifurcation within the 1:1 Arnold tongue, standing anti-phase patterns in the 2:1 Arnold tongue as well as the half entrained responses close to this resonance region. However, there were also discrepancies between simulations and experiments. The most considerable one was the entrainment behavior of the uniform mode. While in the experiments the uniform mode was also entrained outside the 2:1 resonance tongues, this was not the case in the simulations. In contrast, in the simulations also responses with entrained pulse modes but unlocked uniform mode existed. This suggests that the non-uniformities in the reactivity of the ring electrode were not completely captured in the model. Furthermore, in the simulations the transition from quasiperiodic behavior to complete entrainment was accompanied by critical slowing down, indicating that the bifurcations at the entrainment borders differ in experiment and theory. In conclusion, both experiments and simulations showed that a spatially non-uniformly oscillating system respond in a much richer way to a time-periodic forcing than an oscillatory system close to a trivial Hopf bifurcation. Some experimental aspects were satisfyingly understood with the simulations presented here others, however, call for more intricate treatment by theoreticians. Furthermore, the experiments of this work were carried out in a spatially quasi-1 dimensional domain with periodic boundary conditions. Performing similar experiments in a spatially 2-dimensional medium such as on a disc electrode and considering different boundary conditions will shed new light on the influence of geometry, on the dynamics of externally forced spatially extended systems.

Chapter 5 of this work focused on the investigation the qualitative changes in the dynamics of the unforced oscillating system as the Cl^- anions were replaced by Br^-. Exchanging these two anions led to the occurrence of oscillations of a stochastic nature which lacked an intrinsic frequency. Those oscillations occurred either as large amplitude excursions which were spatially uniform or as low amplitude oscillations which connected to the excitation of a confined area of the ring-electrode. Hence, replacing the anion offered us a new reference state of the electrochemical oscillator.

Inducing a negative global coupling to this system did not affect the dynamics qualitatively. It was shown that the globally spatially uniform excursions and the local oscillations were preserved in the presence of negative global coupling. However, above a certain threshold of coupling strength, the desynchronizing coupling favored the occurrence of locally patterned oscillations over globally uniform excursions.

The stochastic large and low amplitude excursions were not significantly influenced by the presence of an externally applied time-periodic perturbation. Furthermore,

the stochastic phenomena proved to be robust against the simultaneous influence of a negative global coupling and an externally applied forcing at low amplitude applied forcing and low coupling strength. Only when the coupling strength and applied forcing amplitude were high enough did the system prevail traveling anti-phase oscillations, such as those observed around the 2:1 entrainment band in chapter 4. These results show that our understanding of forced spatially extended oscillatory media is still in its infancy and many exciting studies still lie ahead of us.

Acknowledgements

I would like to thank

Prof. Dr. Katharina Krischer for giving me the opportunity to work in her group. I also appreciate her motivations, help and constant interest in discussions.

Prof. Dr. Adrian Bîrzu for a fruitful collaboration which was a great help during the work of this thesis. His constant and friendly support and insightful comments are also acknowledged.

Dr. Vladimir García-Morales for an excellent team-work and for taking time to answer my questions. I would also like to thank **Robert Hölzel** for his useful comments on the theoretical part of my work.

People of the group E19a for making the working in this group an enjoyable experience. Specially, I would like to acknowledge the great company of my office mates **Dr. Iljana Miethe, Robert Hölzel, Kathrin Kostorz and Andreas Heinrich**. Their continuous interest in 'language games' was a good motivation to improve my German!

Kamila Wilson for helping me with all administrative problems and for her kind concern for my work.

Dr. Babak Sedghi for being generous with his time and giving me a hand in Matlab programming.

Nima Nooshi for his unconditional help and support, combined with patience and constant motivations in the time of writing this thesis.

My family for their emotional support and understanding during the work of this thesis, as well as in other periods of my life.

Bibliography

[1] C. Huyghens, *Oeuvres completes des Christian Huyghens*. Societ'e Hollandaise des Sciences, Hague, Netherlands, 1983.

[2] L. Glass and M. C. Mackey, *From Clocks to Chaos: The Rhythms of Life*. Univ. Press, Princeton, NJ, 1988.

[3] T. Allen, "On the arithmetic of phase locking: Coupled neurons as a lattice on R^2," *Physica D*, vol. 6, p. 305, 1983.

[4] I. I. Blekhman, *Synchronization in Science and Technology*. ASME Press, New York, 1988.

[5] M. H. Jensen, P. Bak, and T. Bohr, "Transition to chaos by interaction of resonances in dissipative systems. i. circle maps," *Phys. Rev. A*, vol. 30, p. 1960, 1984.

[6] L. Glass and J. Sun, "Periodic forcing of a limit-cycle oscillator - fixed points, arnold tongues, and the global organization of bifurcations," *Phys. Rev. E*, vol. 50, p. 5077, 1994.

[7] V. I. Arnold, *Geometrical methods in the theory of ordinary differential equations*. Springer-Verlag, New York, 1983.

[8] A. Pikovsky, M. Rosenblum, and J. Kurths, *Synchronization*. Cambridge University Press, Cambridge, 2001.

[9] E. Ott, *Chaos in dynamical systems*. Cambridge University Press, Cambridge, 1992.

[10] L. Glass, "Synchronization and rhythmic processes in physiology," *Nature*, vol. 410, p. 277, 2001.

[11] M. Eiswirth and G. Ertl, "Forced oscillations of a self-oscillating surface reaction," *Phys. Rev. Lett.*, vol. 60, p. 1526, 1988.

[12] I. Rehberg, S. Rasenat, J. Fineberg, M. de la Torre Juarez, and V. Steinberg, "Temporal modulation of traveling waves," *Phys. Rev. Lett.*, vol. 61, p. 2449, 1988.

[13] V. Petrov, Q. Ouyang, and H. L. Swinney, "Resonant pattern formation in a chemical system," *Nature*, vol. 388, p. 655, 1997.

[14] P. Coullet and K. Emilsson, "Strong resonances of spatially distributed oscillators: a laboratory to study patterns and defects," *Physica D*, vol. 61, p. 119, 1992.

[15] A. L. Lin, M. Bertram, K. Martinez, H. L. Swinney, A. Ardelea, and G. F. Carey, "Resonant phase patterns in a reaction-diffusion system," *Phys. Rev. Lett.*, vol. 84, p. 4240, 2000.

[16] A. L. Lin, A. Hagberg, E. Meron, and H. L. Swinney, "Resonance tongues and patterns in periodically forced reaction-diffusion systems," *Phys. Rev. E*, vol. 69, p. 066217, 2004.

[17] A. L. Lin, A. Hagberg, A. Ardelea, M. Bertram, H. L. Swinney, and E. Meron, "Four-phase patterns in forced oscillatory systems," *Phys. Rev. E*, vol. 62, p. 3790, 2000.

[18] E. Meron, "Phase fronts and synchronization patterns in forced oscillatory systems," *Discrete Dyn. Nat. Soc.*, vol. 4, p. 217, 2000.

[19] H. K. Park, "Frequency locking in spatially extended systems," *Phys. Rev. Lett.*, vol. 86, p. 1130, 2001.

[20] C. Hemming and R. Kapral, "Turbulent fronts in resonantly forced oscillatory systems," *Faraday Discuss.*, vol. 120, p. 371, 2002.

[21] K. Krischer, "Spontaneous formation of spatiotemporal patterns at the electrode|electrolyte interface," *Journal of Electroanalytical Chemistry*, vol. 501, p. 1, 2001.

[22] N. Mazouz, G. Flätgen, and K. Krischer, "Tuning the range of spatial coupling in electrochemical systems: From local via nonlocal to global coupling," *Phys. Rev. E*, vol. 55, p. 2260, 1997.

[23] H. Varela, C. Beta, A. Bonnefont, and K. Krischer, "A hierarchy of global coupling induced cluster patterns during the oscillatory H_2-electrooxidation reaction on a pt ring-electrode," *Phys. Chem. Chem. Phys.*, vol. 7, p. 2429, 2005.

[24] H.Varela, *Spatiotemporal pattern formation during electrochemical oxidation of hydrogen on platinum.* PhD thesis, Freie Universität Berlin: Berlin, 2003.

[25] K. Krischer, N. Mazouz, and P. Grauel, "Fronts, waves, and stationary patterns in electrochemical systems," *Angew. Chem., Int. Ed.*, vol. 40, p. 851, 2001.

[26] P. Grauel, J. Christoph, G. Flätgen, and K. Krischer, "Stationary potential patterns during the reduction of peroxodisulfate at ag ring electrodes," *J. Phys. Chem. B*, vol. 102, p. 10264, 1998.

[27] P. Grauel and K. Krischer, "Fronts and stationary domains during electrochemical H_2 oxidation on pt: The impact of the position of the reference electrode on the spatiotemporal behaviour," *Phys. Chem. Chem. Phys.*, vol. 3, p. 2497, 2001.

[28] J. Lee, J. Christoph, P. Strasser, M. Eiswirth, and G. Ertl, "Spatio-temporal interfacial potential patterns during the electrocatalyzed oxidation of formic acid on bi-modified pt," *J. Chem. Phys.*, vol. 115, p. 1485, 2001.

[29] P. Strasser, J. Christoph, W. F. Lin, M. Eiswirth, and J. L. Hudson, "Standing wave oscillations in an electrocatalytic reaction," *J. Phys. Chem. A*, vol. 104, p. 1854, 2000.

[30] P. Grauel, H. Varela, and K. Krischer, "Spatial bifurcations of fixed points and limit cycles during the electrochemical oxidation of H_2 on pt ring-electrodes," *Faraday Discuss.*, vol. 120, p. 165, 2001.

[31] J. Christoph, R. Otterstedt, M. Eiswirth, N. I. Jaeger, and J. Hudson, "Negative coupling during oscillatory pattern formation on a ring electrode," *J. Chem. Phys.*, vol. 110, p. 8614, 1999.

[32] J. Lega and J. M. Vince, "Temporal forcing of traveling wave patterns," *J. Phys. I France*, vol. 6, p. 1417, 1996.

[33] D. Walgraef, "Temporal forcing of wave patterns," *Journal of Statistical Physics*, vol. 64, p. 969, 1991.

[34] F. Plenge, H. Varela, M. Lübke, and K. Krischer, "Quantitative modeling of the oscillatory electrooxidation of hydrogen on pt in the presence of poisons," *Z. Phys. Chem.*, vol. 217, p. 365, 2003.

[35] A. J. Bard and L. R. Faulkner, *Electrochemical methods: Fundamentals and applications.* New York: Wiley, 1980.

[36] R. Parsons, "Electrical double layer: Recent experimental and theoretical developments," *Chem. Rev.*, vol. 90, p. 813, 1990.

[37] P. Strasser, M. Eiswirth, and M. T. M. Koper, "Mechanistic classification of electrochemical oscillators - operational experimental strategy," *J. Electroanal. Chem.*, vol. 90, p. 813, 1990.

[38] M. T. M. Koper, "The theory of electrochemical instabilities," *Electrochim. Acta*, vol. 37, p. 1771, 1992.

[39] A. N. Frumkin, "Adsorptionserscheinungen und elektrochemische kinetik," *Z. Elektrochem.*, vol. 59, p. 807, 1955.

[40] W. Wolf, J. Ye, M. Purgand, M. Eiswirth, and K. Doblhofer, "Modeling the oscillating electrochemical reduction of peroxodisulfate," *Ber. Bunsenges. Phys. Chem.*, vol. 96, p. 1797, 1992.

[41] K. Krischer, "Principles of spatial and temporal pattern formation in electrochemical systems," *B. E. Conway, J. O. Bockris, and R. White, editors, Modern Aspects of Electrochemistry, Kluwer Academic/Plenum, New York*, p. 1, 1999.

[42] Y. Kuramoto, *Chemical oscillations, waves, and turbulence.* Berlin: Springer Verlag, 1984.

[43] G. F. N. Mazouz and K. Krischer, "Tuning the range of coupling in an electrochemical system: From local via nonlocal to global coupling," *Phys. Rev. E*, vol. 55, p. 2260, 1997.

[44] J. Christoph, P. Strasser, M. Eiswirth, and G. Ertl, "Remote triggering of waves in an electrochemical system," *Science*, vol. 248, p. 291, 1999.

[45] J. Christoph, *Musterbildung auf elektrodenoberflächen.* PhD thesis, Freie Universität Berlin: Berlin, 1999.

[46] K. Krischer, "New directions and challenges in electrochemistry - spontaneous formation of spatiotemporal patterns at the electrode vertical bar electrolyte interface," *J. Electroanal. Chem.*, vol. 501, p. 1, 2001.

[47] K. Krischer, *Nonlinear dynamics in electrochemical systems*, vol. 8 of *Advances in Electrochemical Science and Engineering, R. C. Alkire and D. M. Kolb, Editors.* Weinheim: Wiley-VCH, 2003.

[48] F. Plenge, *Theory of electrochemical pattern formation under global coupling.* PhD thesis, Technische Universität Berlin: Berlin, 2003.

[49] K. Krischer, H. Varela, A. Bîrzu, F. Plenge, and A. Bonnefont, "Stability of uniform electrode states in the presence of ohmic drop compensation," *Electrochim. Acta*, vol. 49, p. 103, 2003.

[50] K. Krischer, N. Mazouz, and G. Flätgen, "Pattern formation in globally coupled electrochemical systems with an s-shaped current-potential curve," *J. Phys. Chem. B*, vol. 104, p. 7545, 2000.

[51] S. Fukushima, S. Nakanishi, Y. Nakato, and T. Ogawa, "Selection principle for various modes of spatially non-uniform electrochemical oscillations," *J. chem. phys.*, vol. 128, p. 014714, 2008.

[52] R. D. Otterstedt, P. J. Plath, N. I. Jaeger, and J. L. Hudson, "Rotating waves on disk and ring electrodes," *J. Chem. Soc.-Faraday Trans.*, vol. 92, p. 2933, 1996.

[53] J. C. J. Lee, P. Strasser, M. Eiswirth, and G. Ertl, "Existence regions of spatiotemporal patterns in the electro-oxidation of formic acid," *Phys. Chem. Chem. Phys.*, vol. 5, p. 935, 2003.

[54] S. Fukushima, S. Nakanishi, K. Fukami, S. Sakai, T. Nagai, T. Tada, and Y. Nakato, "Observation of synchronized spatiotemporal reaction waves in coupled electrochemical oscillations of an ndr type," *Electrochemistry Communications*, vol. 7, p. 411, 2005.

[55] J. O. M. Bockris, *Modern Aspects of Electrochemistry*, vol. 1 of *Chapter 4., ed. J.O.M. Bockris and B.E. Conway.* Butteworths, London, 1954.

[56] B. E. Conway and B. V. Tilak, "Behavior and characterization of kinetically involved chemisorbed intermediates in electrocatalysis of gas evolution reactions," *Adv. Catal.*, vol. 38, p. 1, 1992.

[57] B. E. Conway and B. V. Tilak, "Interfacial processes involving electrocatalytic evolution and oxidation of H_2, and the role of chemisorbed h," *Electrochim. Acta*, vol. 47, p. 3571, 2002.

[58] G. Jerkiewicz, "Hydrogen sorption at/in electrodes," *Prog. Surf. Sci.*, vol. 57, p. 137, 1998.

[59] K. Krischer, M. Eiswirth, and G. Ertl, "Periodic perturbation of oscillatory co oxidation on pt (110): Model calculations," *J. Chem. Phys.*, vol. 97, p. 307, 1992.

[60] S. Strogatz, *Nonlinear dynamics and Chaos.* Preseus Books Publ., 1994.

[61] P. Rehmus and J. Ross, "Analysis of periodic perturbation of limit cycles," *J. Chem. Phys.*, vol. 78, p. 3747, 1983.

[62] G. Dewel and P. Borckmans, "Critical slowing down in periodically perturbed chemical oscillators," *J. Phys. Chem.*, vol. 92, p. 6483, 1988.

[63] I. R. Epstein and K. Showalter, "Nonlinear chemical dynamics: Oscillations, patterns, and chaos," *J. Phys. Chem.*, vol. 100, p. 13132, 1996.

[64] R. Kapral and E. K. Showalter, *Chemical waves and patterns*. Kluver Academic Publishers, Dordrecht, 1995.

[65] I. R. Epstein and J. A. Pojman, *An Introduction to Nonlinear Chemical Dynamics*. New York: Oxford University Press, 1998.

[66] K. Martinez, A. L. Lin, R. Kharrazian, X. Sailer, and H. L. Swinney, "Resonance in periodically inhibited reaction-diffusion systems," *Phys. D*, vol. 168-169, p. 1, 2002.

[67] P. Glansdorff and I. Prigogine, *Thermodynamic theory of structure, stability and fluctuations*. Wiley-Interscience, London, 1977.

[68] R. J. Field, E. Koros, and R. M. Noyes, "Oscillations in chemical systems. ii.thorough analysis of temporal oscillation in the bromate-cerium-malonic acid system," *J. Am. Chem. Soc.*, vol. 94, p. 8649, 1970.

[69] R. J. Field and R. M. Noyes, "Oscillations in chemical systems. iv. limit cycle behavior in a model of a real chemical reaction," *J. Chem. Phys.*, vol. 60, p. 1877, 1974.

[70] O. Steinbock, V. Zykov, and S. Müller, "Control of spiral-wave dynamics in active media by periodic modulation of excitability," *Nature*, vol. 366, p. 322, 1993.

[71] C. Elphick, A. Hagberg, and E. Meron, "Multiphase patterns in periodically forced oscillatory systems," *Phys. Rev. E*, vol. 59, p. 5285, 1999.

[72] A. M. Zhabotinsky, "Periodic processes of the oxidation of malonic acid in solution (study of the kinetics of belousov's reaction)," *Biophysics*, vol. 9, p. 329, 1964.

[73] B. P. Belousov, *Collections of Abstracts on Radiation Medicine*, vol. 1. Medgiz, Moscow, 1958.

[74] H. Chate, A. Pikovsky, and O. Rudzick, "Forcing oscillatory media: phase kinks vs. synchronization," *Physica D*, vol. 131, p. 17, 1999.

[75] J. Kim, J. Lee, and B. Kahng, "Harmonic forcing of an extended oscillatory system: Homogeneous and periodic solutions," *Phys. Rev. E*, vol. 65, p. 046208, 2002.

[76] B. Marts, A. Hagberg, E. Meron, and A. L. Lin, "Resonant and nonresonant patterns in forced oscillators," *CHAOS*, vol. 16, p. 037113, 2006.

[77] H.-K. Park and M. Bär, "Spiral destabilization by resonant forcing," *Europhysics Letters*, vol. 65, p. 837, 2003.

[78] A. Yochelis, C. Elphick, A. Hagberg, and E. Meron, "Two-phase resonant patterns in forced oscillatory systems: boundaries, mechanisms and forms," *Physica D*, vol. 199, p. 201, 2004.

[79] A. Yochelis, C. Elphick, A. Hagberg, and E. Meron, "Frequency locking in extended systems: The impact of a turing mode," *Europhys. Lett.*, vol. 69, p. 170, 2005.

[80] M. C. Cross and P. C. Hohenberg, "Pattern formation outside of equilibrium," *Rev. Mod. Phys.*, vol. 65, p. 851, 1993.

[81] A. S. Mikhailov, *Foundations of Synergetics I.* Berlin: Springer Verlag, 1994.

[82] V. Garcia-Morales and K. Krischer, "The complex ginzburg-landau equation: an introduction," *Contemporary Physics*, vol. 53, p. 79, 2012.

[83] A. S. Mikhailov and A. Y. Loskutov, *Foundations of Synergetics II.* Berlin: Springer Verlag, 1996.

[84] T. B. Benjamin and J. E. Feir, "Disintegration of wave trains on deep water. 1. theory," *J. Fluid Mech.*, vol. 27, p. 417, 1967.

[85] E. Lorenz, *Empirical orthogonal functions and statistical weather prediction.* Cambridge: MIT, Department of Meteorology, Statistical Forecasting Project, 1956.

[86] M. D. Graham, S. L. Lane, and D. Luss, "Proper orthogonal decomposition analysis of spatiotemporal temperature patterns," *J. Phys. Chem.*, vol. 97, p. 889, 1993.

[87] K. Krischer, R. Rico-Martinez, I. G. Kevrekidis, H. H. Rotermund, J. L. Hudson, and G. Ertl, "Model identification of a spatiotemporally varying catalytic reaction," *AICHE J.*, vol. 39, p. 89, 1993.

[88] Z. Fei, B. J. Green, and J. L. Hudson, "Spatiotemporal patterns on a ring array of electrodes," *J. Phys. Chem. B*, vol. 103, p. 2178, 1999.

[89] P. F. Panter, *Modulation, Noise and Spectral Analysis.* McGraw Hill, New York, 1965.

[90] A. S. Pikovsky, M. G. Rosenblum, G. V. Osipov, and J. Kurths, "Phase synchronization of chaotic oscillators by external driving," *Physica D*, vol. 104, p. 219, 1997.

[91] G. Tremiliosi-Filho, G. Jerkiewicz, and B. E. Conway, "Characterization and significance of the sequence of stages of oxide film formation at platinum generated by strong anodic polarization," *Langmuir*, vol. 8, p. 658, 1992.

[92] J. Siegmeier, "Local nonlinear dynamics and pattern formation in the H_2/CO mixed system on platinum," Master's thesis, Technische Universität München: München, 2005.

[93] I. Miethe, "Raum-zeitliche musterbildung bei der anodischen elektrooxidation von silizium in flußäurehaltigen elektrolytlösungen," Master's thesis, Technische Universität München: München, 2004.

[94] M. Eiswirth, M. Lübke, K. Krischer, W.Wolf, J. L. Hudson, and G. Ertl, "Structural effects on the dynamics of an electrocatalytic oscillator," *Chem. Phys. Lett.*, vol. 192, p. 254, 1992.

[95] K. Krischer, M. Lübke, W. Wolf, M. Eiswirth, and G. Ertl, "Oscillatory dynamics of the electrochemical oxidation of H_2 in the presence of Cu^{2+}: Structure sensitivity and the role of anions," *Electrochimica Acta*, vol. 40, p. 69, 1995.

[96] K. Krischer, M. Lübke, W.Wolf, M. Eiswirth, and G. Ertl, "Chaos and interior crisis in an electrochemical reaction," *Ber. Bunsenges. Phys. Chem.*, vol. 95, p. 820, 1991.

[97] S. Wiggins, *Introduction to applied nonlinear dynamical systems and chaos*. Springer, 2003.

[98] G. Jenkins and D. Watts, *Spectral analysis and its applications*. San Francisco: Holden-Days, 1968.

[99] S. Cox and P. Matthews, "Exponential time differencing for stiff systems," *Journal of Computational Physics*, vol. 176, p. 430, 2002.

[100] F. Plenge, H. Varela, and K. Krischer, "Pattern formation in stiff oscillatory media with nonlocal coupling: A numerical study of the hydrogen oxidation reaction on pt electrodes in the presence of poisons," *Phys. Rev. E*, vol. 72, p. 066211, 2005.

[101] V. Garcia-Morales and K. Krischer, "Nonlocal complex ginzburg-landau equation for electrochemical systems," *Phys. Rev. Lett.*, vol. 100, p. 054101, 2008.

[102] A. Goldbeter, *Biochemical oscillations and cellular rhythms.* Cambridge: Cambridge university press, 1996.

[103] B. Alving, "Spontaneous activity in isolated somata of aplysia pacemaker neurons," *J. Gen. Physiol.*, vol. 51, p. 29, 1968.

[104] W. Adams and J. Benson, "The generation and modulation of endogenous rhythmicity in the alpysia bursting pacemaker neurone r15," *Progr. Biophys. Mol. Biol.*, vol. 46, p. 1, 1985.

[105] L. Organ, I. Z. Kiss, and J. L. Hudson, "Bursting oscillations during metal electrodissolution: Experiments and model," *J. Phys. Chem. B*, vol. 107, p. 6648, 2003.

[106] A. Karantonis, D. Koutsaftis, and N. Kouloumbi, "Synchronization properties of coupled electrochemical bursters rhythmic electrodissolution/passivation of iron electrode assemblies in acidic electrolyte containing chloride ions," *J. Appl Electrochem*, vol. 40, p. 989, 2010.

[107] B. Lindnera, J. Garcia-Ojalvob, A. Neimand, and L. Schimansky-Geiere, "Effects of noise in excitable systems," *Physics reports*, vol. 392, p. 321, 2004.